UAB
Universitat Autònoma de Barcelona

Integrated energy storage solutions: from novel polyoxovanadate hybrid nanomaterials to electrical grid applications

Anukriti Pokhriyal

Doctoral Thesis

Integrated energy storage solutions: from novel polyoxovanadate hybrid nanomaterials to electrical grid applications

submitted by:

Anukriti Pokhriyal

for the degree of Doctor of Philosophy

in Material Science

at the Universitat Autònoma de Barcelona

Director & Tutor:

Prof. Dr. Pedro Gómez Romero

Co-directors:

Dr. José Luis Domínguez García and **Dr. Rosa Maria González Gil**

September 2024

The research work in this thesis has been carried out during the period of August 2019 to September 2024. The research was funded by a DOC-FAM grant. The DOC-FAM project has received funding from the EU's H2020 research and innovation programme under the Marie Skłodowska-Curie grant agreement No. 754397.

Bellaterra, 22 de Septiembre, 2024

Memoria presentada per aspirar al Grau de Doctor per

Anukriti Pokhriyal

Vist i plau

Prof. Dr. Pedro Gómez Romero

Group Leader

Novel Energy Oriented Materials Group

ICN2 - CSIC

Dr. José Luis Domínguez-García

Group Leader

Power Systems Group

IREC

Dr. Rosa Maria González Gil

Postdoctoral Researcher

Novel Energy Oriented Materials Group

ICN2

To my guardian Àngel,

for always looking after me...

Abstract

This thesis presents an integral approach to the development of novel materials, electrodes, devices and applications in energy storage by researching very different but related areas, all of them necessary to advance towards the consolidation of energy storage in a sustainable energy future.

The research integrates diverse yet interconnected domains, culminating in three parts. The first part, constituting the core contribution, describes the development of novel hybrid electroactive materials made by capacitive carbons and faradaic polyoxovanadate nanoclusters to improve their cyclability. The second part deals with thick (or high mass-loaded) electrode engineering, and the third part on specific possible new applications for the energy storage devices that could be eventually developed and optimised from these materials.

In the first part, the advanced materials synthesised were hybrids of decavanadates ($[V_{10}O_{28}]^{6-}$ or in short, V_{10}) and tetradecavanadophosphates ($[H_4PV_{14}O_{42}]^{5-}$ or PV_{14}) adsorbed on activated carbon (AC). Sodium salts and tetrabutylammonium salts of the polyoxovanadates were used and the materials were characterised by FTIR, ^{51}V NMR, XRD. Electrochemical studies (CVs and GCD) were also extensively used. The asymmetric devices made with AC$\{V_{10}\}$ hybrid materials demonstrated the highest gravimetric and volumetric capacitances of 140 F g^{-1} and 56 F cm^{-3}, respectively, with an improved capacitance retention of 91% after 5,000 cycles.

In the second part, the fabricated electrodes included complex mixtures of the hybrid materials described, together with additional nanocarbon materials, including different ACs, conducting carbon blacks (CSP/CB) or carbon nanotubes (CNTs). Thick electrode fabrication by spray-coating of carbon inks and eventually inks of the hybrid material AC$\{V_{10}\}$ was carried out (on aluminium current collectors). AC-conductive carbon electrodes of mass loading up to 31 mg cm^2 were developed

and showed high capacitances of 2459 mF cm^2. Moreover, the thick electrodes formulated using hybrid AC{V_{10}} materials showed high gravimetric capacitances of 114 F g−1 (5 mg cm^{-2}), superior to AC electrodes. This concept of thick electrodes was extended to novel "nanopastes" with integrated electrolytes and active material mass loadings of up to 50 mg cm^{-2}.

Finally, the last part of the thesis addressed the simulation of a potential ancillary service (frequency regulation) provided by energy storage devices in grids. A comparative analysis of conventional frequency regulation and battery-driven frequency regulation was carried out with emphasis on the advantages of a high power, medium energy system like the one developed in this thesis to address their role in supporting renewable energy integration within emerging energy models.

Resumen

Esta tesis presenta un enfoque integral para el desarrollo de nuevos materiales, electrodos, dispositivos y aplicaciones en el almacenamiento de energía, investigando áreas muy diferentes pero relacionadas, todas ellas necesarias para avanzar hacia la consolidación del almacenamiento de energía en un futuro energético sostenible.

La investigación integra dominios diversos pero interconectados, culminando en tres partes. La primera parte, que constituye la contribución principal, describe el desarrollo de nuevos materiales híbridos electroactivos compuestos de carbones capacitivos y nanoclústeres de polioxovanadatos faradaicos para mejorar su ciclabilidad. La segunda parte se centra en la ingeniería de electrodos gruesos (o con alta carga de masa), y la tercera parte trata sobre nuevas aplicaciones específicas posibles para los dispositivos de almacenamiento de energía que podrían desarrollarse y optimizarse a partir de estos materiales.

En la primera parte, los materiales avanzados sintetizados fueron híbridos de decavanadatos ($[V_{10}O_{28}]^{6-}$ o, en resumen, V_{10}) y tetradecavanadatos fosfatos ($[H_4PV_{14}O_{42}]^{5-}$ o PV_{14}) adsorbidos en carbón activado (AC). Se utilizaron sales de sodio y sales de tetrabutilamonio de los polioxovanadatos, y los materiales se caracterizaron mediante FTIR, ^{51}V RMN y XRD. También se emplearon ampliamente estudios electroquímicos (CVs y GCD). Los dispositivos asimétricos fabricados con materiales híbridos AC$\{V_{10}\}$ demostraron las mayores capacidad gravimétrica y volumétrica, de 140 F g^{-1} y 56 F cm^{-3}, respectivamente, con una mejora en la retención de capacidad del 91% tras 5.000 ciclos.

En la segunda parte, los electrodos fabricados incluían mezclas complejas de los materiales híbridos descritos, junto con materiales adicionales de nanocarbono, como diferentes ACs, negros de carbono conductores (CSP/CB) o nanotubos de carbono (CNTs). Se fabricaron electrodos gruesos mediante la técnica de spray-coating con tintas de carbono y eventualmente tintas del material híbrido AC$\{V_{10}\}$

(sobre colectores de corriente de aluminio). Se desarrollaron electrodos de carbono conductivo con una carga de masa de hasta 31 mg cm^2 que mostraron altas capacidades de 2459 mF cm^2. Además, los electrodos gruesos formulados con materiales híbridos AC$\{V_{10}\}$ mostraron altas capacidad gravimétricas de 114 F g-1 (5 mg cm^{-2}), superiores a los electrodos de AC. Este concepto de electrodos gruesos se extendió a nuevas "nanopastas" con electrólitos integrados y cargas de material activo de hasta 50 mg cm^{-2}.

Finalmente, la última parte de la tesis abordó la simulación de un posible servicio auxiliar (regulación de frecuencia) proporcionado por dispositivos de almacenamiento de energía en redes eléctricas. Se realizó un análisis comparativo de la regulación de frecuencia convencional y la regulación de frecuencia basada en baterías, con énfasis en las ventajas de un sistema de alta potencia y energía media como el desarrollado en esta tesis para abordar su papel en el apoyo a la integración de energías renovables en los modelos energéticos emergentes.

Resum

Aquesta tesi presenta un enfocament integral per al desenvolupament de nous materials, elèctrodes, dispositius i aplicacions en emmagatzematge d'energia, mitjançant la recerca de diverses àrees molt diferents però relacionades, totes elles necessàries per avançar cap a la consolidació de l'emmagatzematge d'energia en un futur energètic sostenible.

La investigació integra diversos dominis, que estan interconnectats, culminant en tres parts. La primera part, que constitueix la contribució central, descriu el desenvolupament de nous materials híbrids electroactius formats per carbons capacitius i nanoclústers de polioxovanadat faradaic per millorar la seva ciclicitat. La segona part tracta sobre l'enginyeria d'elèctrodes gruixuts (o amb alta càrrega de massa), i la tercera part tracta de noves aplicacions específiques possibles per als dispositius d'emmagatzematge d'energia que podrien desenvolupar-se i optimitzar-se a partir d'aquests materials.

A la primera part, els materials avançats sintetitzats van ser híbrids de decavanadats ($[V_{10}O_{28}]^{6-}$ o en resum, V_{10}) i tetradecavanadats fosfats ($[H_4PV_{14}O_{42}]^{5-}$ o PV_{14}) adsorbits sobre carboni activat (AC). Es van utilitzar sals de sodi i sals de tetrabutilamoni dels polioxovanadats i els materials van ser caracteritzats per FTIR, ^{51}V RMN, XRD. També es van utilitzar àmpliament estudis electroquímics (CVs i GCD). Els dispositius asimètrics fets amb materials híbrids AC$\{V_{10}\}$ van demostrar les capacitàncies gravimètriques i volumètriques més altes de 140 F g^{-1} i 56 F cm^{-3}, respectivament, amb una retenció de capacitància millorada del 91% després de 5.000 cicles.

A la segona part, els elèctrodes fabricats incloïen barreges complexes dels materials híbrids descrits, juntament amb materials nanocarbònics addicionals, incloent diferents ACs, negres conductors de carboni (CSP/CB) o nanotubs de carboni (CNTs). Es va fabricar un elèctrode gruixut mitjançant la tècnica de "spray-coating"

d'unes tintes de carboni i, eventualment, de materials híbrids AC{V_{10}} (sobre col·lectors de corrent d'alumini). Es van desenvolupar elèctrodes de carboni conductiu amb una càrrega de massa de fins a 31 mg cm^2 que van mostrar altes capacitàncies de 2459 mF cm^2. A més, els elèctrodes gruixuts formulats utilitzant materials híbrids AC{V_{10}} van mostrar capacitàncies gravimètriques altes de 114 F g−1 (5 mg cm^{-2}), superiors als elèctrodes d'AC. Aquest concepte d'elèctrodes gruixuts es va estendre a noves "nanopastes" amb electròlits integrats i càrregues de massa de material actiu de fins a 50 mg cm^{-2}.

Finalment, l'última part de la tesi va abordar la simulació d'un servei auxiliar potencial (regulació de freqüència) proporcionat per dispositius d'emmagatzematge d'energia en xarxes elèctriques. Es va dur a terme una anàlisi comparativa de la regulació de freqüència convencional i la regulació de freqüència impulsada per bateries, amb èmfasi en els avantatges d'un sistema de gran potència i energia mitjana com el desenvolupat en aquesta tesi, per tal d'abordar el seu paper en el suport a la integració de l'energia renovable en els models energètics emergents.

Contents

List of Acronyms

AC: Activated carbon

BESS: Battery Energy Storage System

BET: Brunauer-Emmett-Teller method

CMC: Carboxymethylcellulose

CNT: Multi-walled carbon nanotubes

CP: Cyclic polarisation

CSP/CB: Carbon SuperP

CV: Cyclic voltammetry

D_2O: Deuterium oxide

DI: Deionised

EESS: Electrochemical energy storage

EDX: Energy-dispersive X-ray spectroscopy

EIS: Electrochemical impedance spectroscopy

EDLC: Electric double-layer capacitor

EVs: Electric vehicles

FTIR: Fourier-transform infrared spectroscopy

GCD: Galvanostatic charge discharge

KB: Ketjen Black

Li-ion: Lithium-ion

MeCN: Acetonitrile

NMR: Nuclear magnetic resonance

POMs: Polyoxometalates

PVDF: Poly(vinylidene) fluoride

PVDF-HFP: Poly(vinylidene fluoride-co-hexafluoropropylene)

RE: Renewable Energy

RFBs: Redox Flow Batteries

SEM: Scanning electron microscopy

SSFBs: Semi-Solid Flow Batteries

TGA: Thermogravimetric analysis

V-POMs: Polyoxovanadates

V-RFBs: Vanadium Redox Flow Batteries

XANES: X-ray absorption near edge structure spectroscopy

XRD: X-Ray diffraction

List of Figures

List of Tables

Publications

Publications resulting from this thesis:

1. Pokhriyal, A.; Domínguez-García, J.L.; Gómez-Romero, P. *Impact of Battery Energy System Integration in Frequency Control of an Electrical Grid with Wind Power. Clean Technologies.* 2022, 4, 972-986.

2. Pokhriyal, A.; Rueda-García, D.; Gómez-Romero, P. *To flow or not to flow. A perspective on large-scale stationary electrochemical energy storage. Sustainable Energy & Fuels.* 2023, 7, 5473-5482.

3. Pokhriyal, A.; González-Gil, R.M.; Bengoa, L.N.; Gómez-Romero, P. *Nanostructured Thick Electrode Strategies toward Enhanced Electrode–Electrolyte Interfaces. Materials.* 2023, 9:3439.

4. Gomez-Romero, P.; Pokhriyal, A.; Rueda-García, D.; Bengoa, L.N.; González-Gil, R.M.. *Hybrid Materials: A Metareview. Chemistry of Materials.* 2024, 36, 1, 8–27.

5. Pokhriyal, A.; González-Gil, R.M.; Bengoa, L.N.; Gómez-Romero, P. *Hybrid Carbon-Decavanadate Electrodes for Energy Storage. Under review.*

1

Introduction

1.1 A case for electrochemical energy storage and development of new technologies

The worldwide need to shift towards cleaner energy generation to mitigate climate change is being fuelled by renewable energy. As the share of renewable energy (RE) keeps increasing, the reliability of the grid becomes an increasing concern. This is because wind and solar are becoming the most common forms of centralised and distributed renewable energy. Since the sun doesn't shine 24 hours and wind speeds may increase or decrease depending on weather conditions, wind and solar energy generation is inherently variable and intermittent by nature. This can cause large fluctuations in the power grid. Therefore, the transition to sustainable energy generation is not possible without the true security of energy supply. Arguably, their much needed expansion and effective utilisation can only take place with simultaneous installation of energy storage systems, especially electrochemical energy storage systems (EESS), such as batteries and supercapacitors, due to their modularity, scalability, high efficiency, ease of set-up and low maintenance.

By the end of 2023, RE accounted for 3870 GW of capacity worldwide, of which solar and wind combined had a majority share of 63% [1]. Yet the installed capacity of EESS technologies by 2022 was only 28 GW [2], clearly showing the huge gap between generation and storage. We believe that this is primarily due to their current high cost (although the prices have sharply dropped in recent years), but also due to the fact that there is not yet an ideal chemistry that meets all the requirements for large-scale storage. Figure 1.1 shows key parameters of EESS and the relative performance of three main EESS technologies.

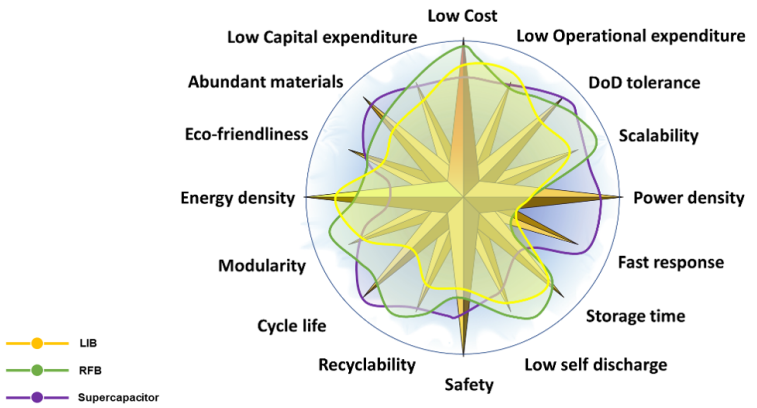

Figure 1.1: *Multiple target features demanded from energy storage technologies and the capabilities of different EESS [3].*

Energy storage had been a neglected piece of our global energy cycle, until the previous century when first lead acid and currently Lithium-ion (Li-ion) emerged as the preferred technologies for rechargeable EESS. We are now witnessing a Cambrian explosion of energy storage variety as present-day demands range from tiny set-and-forget supercapacitors in electronic devices, to electric vehicle batteries, renewable energy storage as well as supercapacitors and batteries for grid balancing. EESS have become the essential hidden components powering our day to day lives. While our reliance on these EESS has significantly increased, it has also become more varied and a creative effort will be needed to properly match these emerging storage needs with storage technologies.

While the industry remains focused on Li-ion technologies and reducing its costs, the research sector is cognizant of the challenges that not only accompany Li-ion but also those that come along with the reliance on a single type of technology. This has fostered the search for beyond Li-ion chemistries such as metal-air, Na, K, Mg, Ca, Zn or Al rechargeable batteries, as well as other technologies, such as supercapacitors, hybrid devices and various types of flow cells which are being researched and developed [4–7].

The evolution of the EESS landscape depends on the potential of each technology to lower costs and improve performance. Presently the per kWh installation costs of a 1 MW/4 h Li-ion battery system are approximately \$448 kWh^{-1} while that for a 10 MW/4 h system is approximately \$411 kWh^{-1}. On the other hand, the installation costs of Vanadium-Redox Flow Batteries (V-RFBs) for 1 MW/4 h and

10 MW/4 h would be \$601 kWh^{-1} and \$554 kWh^{-1}, respectively. By 2030, these costs are expected to grow by at least \$100 kWh^{-1} [8].

The development of any electrochemical storage technology is a complex process and requires convergence of multiple areas for their large-scale implementation, as shown in Figure 1.2. The success of any EESS technology primarily depends on its chemistry but also on the successful scaling up from lab to industrial scale. Next, cell components such as separators, current collectors, or electrodes themselves, need to be fabricated, modified, and improved to ensure optimal integration. Thirdly, a reliable design and assembly of the final device would be required to achieve high performance and efficiency for the transition from research laboratory to the industry while manufacturing and assembly would be tweaked to optimise both material utilisation and costs. In parallel, the practical or final applications for the technology should be explored, energy storage management algorithms should be developed, and the new device should be tested through prototypes and simulations.

Many of these components are linked and depend on each other for successful implementation of EESS. However, the direct lines establishing relationships between cell chemistries, cell/device design and final applications are not yet clearly drawn. This thesis aims to highlight the importance of these relationships and develop new chemistries and devices that fulfil particular application requirements.

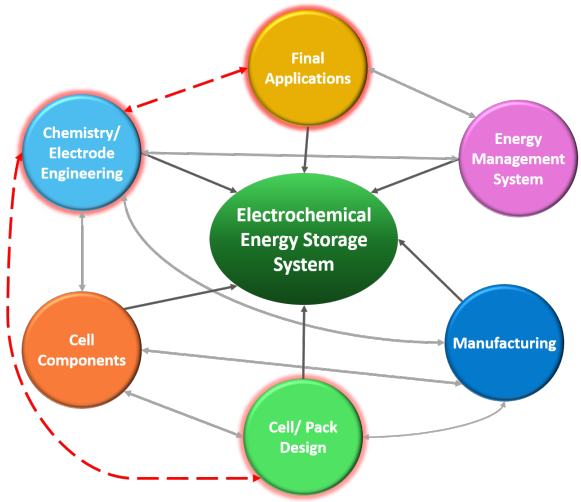

Figure 1.2: *Idea-to-market process considerations for an electrochemical energy storage system and their interdependence marked by grey lines. Highlighted and connected in red are the presently unlinked processes that form the theme of this thesis.*

1.2 Competing chemistries

The nominal power and discharge time for various commercial energy storage technologies is shown in Figure 1.3. Pumped hydro is the only energy storage technology that can be currently implemented on a GW-scale and is ideal for the application of renewable energy storage/arbitrage. But it is feasible only on a large-scale in the utility sector and limited by topographical conditions making it difficult to set up in convenient locations. The relatively "easier to set up" electrochemical energy storage systems are quickly catching up because they are suited for the intermediate 1-100 MW area labelled as "Grid Support" (Figure 1.3). Within the category of EESS, a large number of technologies are available that serve specific storage needs.

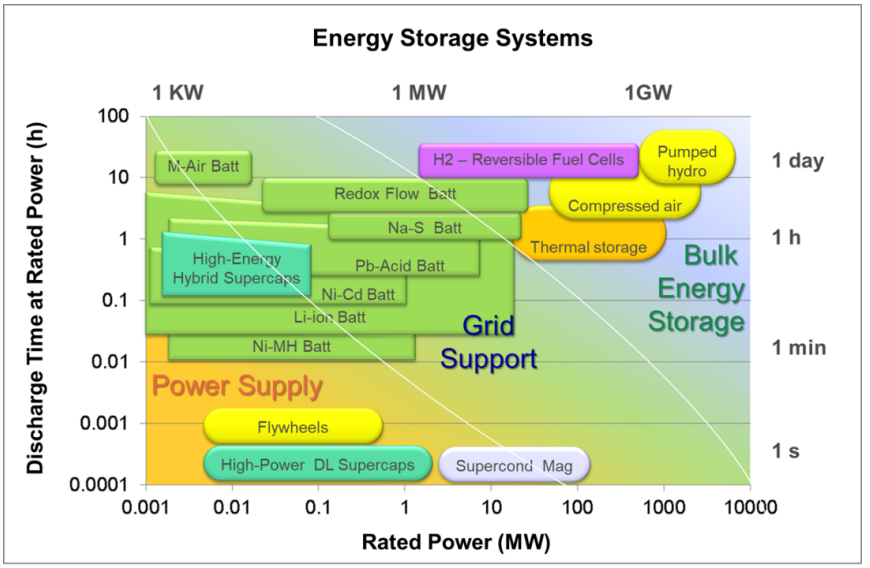

Figure 1.3: *Energy storage technologies as a function of their nominal power and discharge time. Mechanical (yellow), magnetic (light grey) thermal (orange) chemical (purple), electrochemical (green) and electro-physical (blue-green). Image reprinted from our own publication [3] and developed using ref. [9].*

Currently Li-ion batteries are taking over most of these applications, primarily due to the relatively good power and energy densities and reducing costs. Essentially, the same technology that is used to power our cell-phones is also used to store several hundred MWh of RE as well as to power EVs. The other common technology used for stationary applications is RFB, specifically V-RFBs. On the other hand,

supercapacitors service niche applications that require fast response and high power over a very short interval such as wearable electronics, sensors, satellites and even ancillary power services.

Both battery and supercapacitor materials are capable of storing energy through electrochemical mechanisms: redox reactions in the case of batteries and double layer polarisation in the case of supercapacitors. But another important difference is that, in batteries, the redox reactions take place through the bulk of the material and positively charged ions need to diffuse through the whole volume to compensate for the injection of electrons. Thus, batteries operate on a diffusion-controlled mechanism which allows them to store large amounts of energy but prevents fast charge and discharge. On the other hand, the charge storage in supercapcitors takes place at the surface of the material and electrolyte ions can access the active sites without bulk diffusion. Supercapacitors can be broadly divided into electric double layered capacitors (EDLCs) and pseudocapacitors. While EDLCs do not contain any faradaic reactions and operate on the polarisation of ions at the electrode/electrolyte interface (eg. activated carbon), pseudodapacitors involve surface-level redox reactions which allow extremely fast charge and discharge but lower energy densities. The term pseudocapacitance was first described by "Conway" to classify materials that exhibited electrochemical signatures (in cyclic voltammetry and charge-discharge) similar to EDLCs [10]. Many redox pseudocapacitance materials have been studied such as RuO_2, MnO_2, metal oxides, conductive polymers, functional groups on carbons, MXenes, polyoxometalates, etc. [11–13]

We could imagine a supercapacitor as a 200 ml glass and a battery as a large 5 L water jug with a narrow neck. We can quickly pour the water from the glass but it can only hold a limited capacity. If we need to drink more, then the glass must be refilled several times. On the other hand, the narrow-necked water jug would provide more water for a longer time, but it will not be able to provide a fast flow. Between a 200 ml glass and a 5 L water jug we can easily think of an intermediate situation in the form of a 1 L water jar. The question is whether a "water-jar" technology is available in the field of electrochemical energy storage. Or in scientific terms, can we develop energy storage technologies featuring both high energy and power densities? Technologies approaching the capacity and energy of batteries but with the fast response (high power density) and long cyclability of supercapacitors? Such technologies have already been investigated as "Hybrid Supercapacitors" (Figure 1.4).

1.2.1 Hybrid materials and devices

The conventional definition of Hybrid supercapacitors, also called metal-ion capacitors is "energy storage devices composed of one capacitive and one faradaic electrode". This results in a device with the best characteristics of a supercapacitor (high power density, great cyclability fast charge) that incorporates some of the features of batteries (improved energy density and less self-discharge in comparison with EDLC supercapacitors) [14]. This concept can be loosely translated to materials that contain both capacitive and faradaic elements as the one shown in Figure 1.4, which was prepared recently in our group [15]. Such hybrid materials have been developed by combining capacitive activated carbon, reduced graphene oxide, carbon nanotubes, etc., with redox materials such as polyoxometalates.

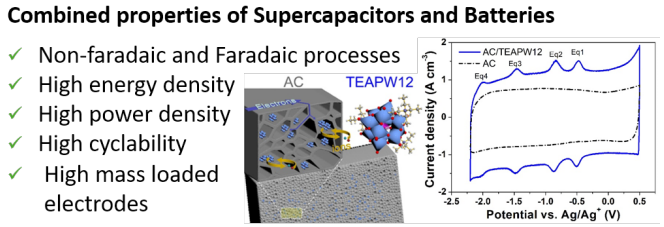

Figure 1.4: *Properties of hybrid materials. Figure modified from ref. [15], copyright 2020, Elsevier.*

Polyoxometalates (POMs) are nano-sized inorganic redox active materials consisting of specific transition metal ions (typically W, Mo, Nb or V) that are linked together by oxygen atoms [16]. Frequently other elements (typically P, Si or most transition metals) can also take part in the structure of POMs. POMs can be classified according to their structures as shown in Figure 1.5. They are capable of very fast reversible redox reactions and have been used as catalysts as well as energy storage material [16]. The first POMs were initially discovered in the late 1700s and characterised by J. F. Keggin in 1933 [17]. Their use as electroactive materials for energy storage is appealing because of their broad range of redox states and valances over which the physical structure experiences very little changes [16]. In fact, their first use as hybrid materials for energy storage dates back to late 1990s [18] and since then this field has expanded greatly [12, 16, 19]. POMs have been used as anode or cathode materials for Li- and Na-ion batteries due to their wide range of redox potentials, but their high molecular weight results in poor gravimetric capacities.

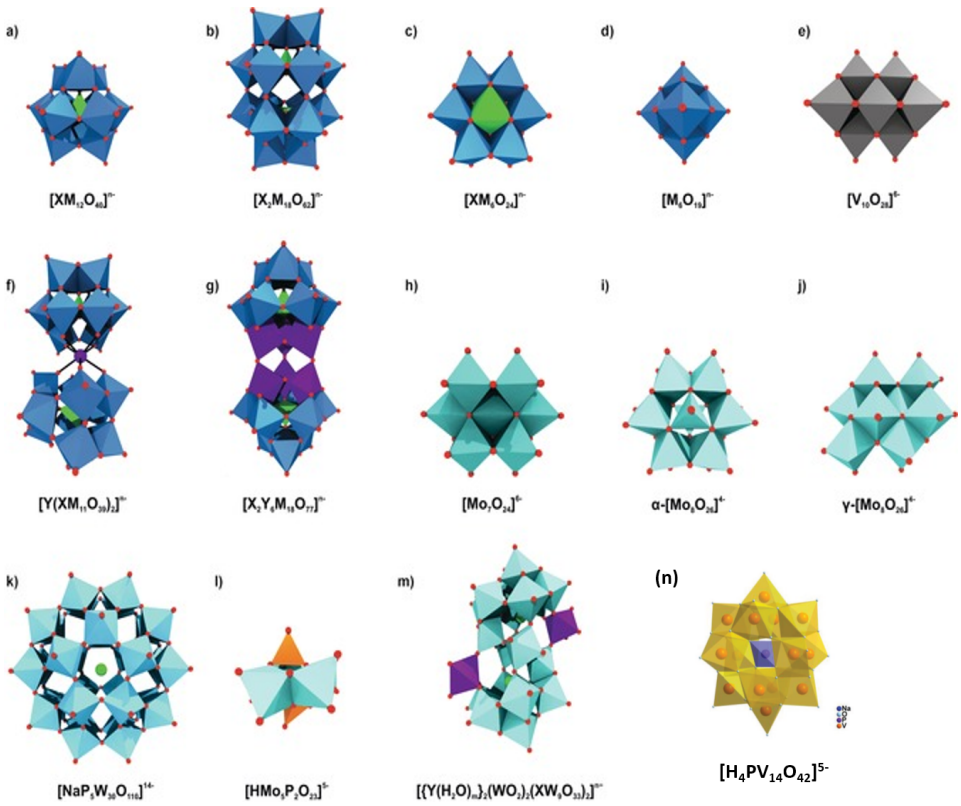

Figure 1.5: *Overview of common POM archetypes. From a to m: a) Keggin, b) Wells–Dawson, c) Anderson, d) Lindqvist, e) decavanadate, f) sandwich Keggin, g) double Keggin, h) heptamolybdate, i) α- and j) γ-octamolybdate, k) Preyssler, l) Strandberg, and m) Krebs-type structure. Blue polyhedra are [MO_6] (M=any addenda atom), light green polyhedra [XO_n] (X=heteroatom), light green spheres sodium, light blue polyhedra [WO_6], light cyan polyhedra [MoO_6], gray polyhedra [VO_6], purple polyhedra and spheres [YO_n] and Y (Y=second heteroatom), orange polyhedra [PO_4], red spheres oxygen, n) Trans-bicapped α-Keggin structure of tetradecavanadophosphates. Figures modified with permission from ref. [20] and [21], copyright John Wiley and Sons, 2018.*

Pure crystallised POMs also suffer from poor conductivity and their multielectron transfers may not always be fully utilised in such a state. Therefore, POMs are best used in composites that allow their anchoring in conductive materials such as activated carbon [15, 22], carbon nanotubes [23], carbon nanopipes [24], graphene [25, 26], conductive polymers [18, 27–30], MXenes [31, 32], etc. This not only isolates and disperses the POMs and prevents their crystallisation; but also allows fast charge transfer due to the contact with conductive materials. Most

importantly, their adsorption into the nano-pores of the conductive matrix or support prevents their dissolution in the electrolyte and drastically improves their cyclability. Such composites or hybrid materials have high capacitances and have even been shown to work in extended potential windows for many thousands of cycles. For example, a pristine AC electrode in a symmetric supercapacitor delivered 186 F g^{-1} in 1 M H_2SO_4, with a maximum voltage window of 1 V. However, when phosphotungstic acid was adsorbed on carbon, this AC-phosphotungstic acid hybrid electrode could extend the working voltage window to 1.6 V and provide a gravimetric capacitance of 254 F g^{-1} in the same electrolyte with 98% capacitance retention over 30,000 cycles [22].

Most of the research on these hybrid materials has previously been concentrated on Tungsten and Molybdenum Keggin-type (polyoxotungstates and polyoxomolybdates) POMs in aqueous electrolytes. This is not surprising due to their commercial availability and crystal stability over long time periods. However, their gravimetric energy density is limited due to the smaller operating voltage window of aqueous electrolytes and the very large atomic mass of Tungsten and Molybdenum. Organic electrolytes and ionic liquids provide a wider window of stability range and hence larger energy densities. However, these POMs are usually incompatible with organic electrolytes because their redox reactions frequently involve protonation reactions. Efforts have been made to substitute the cations to organic cations such as tetraethylammonium, tetrabutyl-ammonium, etc., to promote their redox reactions in organic electrolytes [15]. However, their very large molecular weights makes them competitive only on a volumetric basis and not on a gravimetric basis.

1.2.2 Polyoxovanadates

Other POMs are now being synthesised and tested in batteries and hybrid supercapacitors in organic electrolytes. One such type of POMs that have gained recent traction are "Polyoxovanadates". Polyoxovanadates (POVs or V-POMs) are a subclass of POMs with Vanadium and Oxygen forming anionic nanometer-sized clusters accompanied by charge-balancing cations. These materials have a fascinating history rooted in bio-chemistry. They have previously been tested as potential antidiabetic, anticancer, antimicrobial and antiviral drugs due to the ability of vanadium to interact with proteins [33–35].

Their use in electrochemistry as energy storage materials has been relatively rare and recent. Vanadium features multiple accessible oxidation states: mainly V^{5+}/V^{4+} and more rarely V^{4+}/V^{3+} redox couples. In addition, V-POMs have

much lower atomic weights than other commonly used POMs (V: 50.94 g mol^{-1}; Mo: 95.95 g mol^{-1}; W: 183.84 g mol^{-1}) making them extremely competitive on a gravimetric comparison scale [36]. Meanwhile, despite their advantages as electroactive materials, we must recognise that Vanadium is not the most abundant element and can even be toxic in nature. Therefore, alternative methods to obtain vanadium such as by-products from steel manufacturing, etc., must be used and care must be taken during its disposal and recycling to prevent toxicity. Polyoxovanadates exist in multiple coordination modes such as tetrahedral [VO_4], square-pyramidal [VO_5], and octahedral [VO_6] as shown in Figure 1.6, and have structural flexibility, leading to traditionally "less stable" compounds. This stability challenge is further

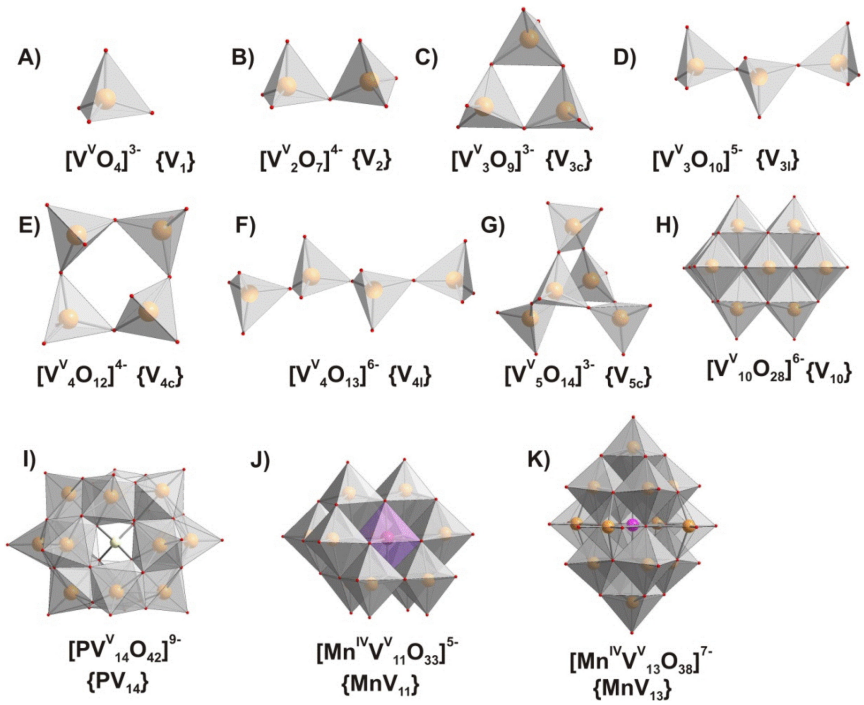

Figure 1.6: *Polyoxovanadate structures with the nuclearity up to 14 addenda atoms and both tetrahedral and octahedral coordination of V. a) Vanadate oxoanion, b) pyrovanadate, c and d) Tri- and tetravanadates are presented in two forms – cyclic ({V_{3c}}, c) {V_{4c}}, e) and linear ({V_{3l}}, d) and {V_{4l}}, f). The linear forms of {V_{3l}} and {V_{4l}} have never been obtained in solid state. In the MnV_{13} structure (k), four equatorial V atoms have 75% occupancy and so in total correspond to three V ions with full occupancy in the sum formula. Color code: {VO_x}, grey; O, red; P, yellow; Mn, pink. The subscript "c" stands for "cyclic", "l" for "linear". Reprinted with permission from ref. [35], copyright 2022, Elsevier.*

exaggerated by their complex protonation chemistry and high redox activity [36].

Commonly used V-POMs for electrochemical energy storage include the decavanadate isopolyoxometalate $[V_{10}O_{28}]^{6-}$ or $\{V_{10}\}$; tetradecavanadophosphate $[PV_{14}O_{42}]^{9-}$ or $\{PV_{14}\}$; and Chloro-dodecavanadate $[V_{12}O_{32}Cl]^{5-}$ or $\{V_{12}\}$ [36]. Decavanadates or $\{V_{10}\}$ are one of the most commonly studied polyoxovanadates in V-POM battery and supercapacitor research as they are most stable polyoxovanadates in acidic media between pH 2 - 6 [35]. Interestingly, these V-POMs have shown fast electron transfer even in organic electrolytes [37]. Moreover, X-ray absorption near-edge spectroscopic (XANES) studies have found that V-POMs intercalate Li- and Na-ions and all ten V^{5+} ions in the cluster can be reversibly reduced to V^{4+} (in the potential range of 4–1.75 V vs. Li^+/Li). [38]

Therefore, decavanadates have shown high initial capacities when used as anode or cathode materials. For example, thermally dehydrated $Li_6[V_{10}O_{28}]$ has been demonstrated as a LIB cathode material, with discharge capacities of about 130 mAh g^{-1} at a current density of 0.2 mA cm^{-2} and $Na_6[V_{10}O_{28}]$ was reported as an anode material with a reversible capacity of about 280 mAh g^{-1} [39]. However, all these devices showed extremely poor cyclability.

Decavanadates are generally synthesised in aqueous media and isolated as hydrated salts, which causes water molecules remaining in the crystal lattice ($M_6[V_{10}O_{28}]\cdot xH_2O$ (where M=Li or Na and x=9-16). The removal of lattice water requires thermal treatment. However, decavanadates can undergo thermally induced structural rearrangements leading to their degradation. For example, the dehydration of lithium decavanadate $Li_6[V_{10}O_{28}]\cdot 16H_2O$ leads to the $LiVO_3$ and LiV_3O_8 oxides, even at low temperatures of about 120 °C [40].

To avoid their degradation and maintain their pH stability ranges, V-POMs have also been tested in aqueous RFBs. An RFB with $H_4[SiW_{12}O_{40}]$) anolyte with $Na_{4.75}H_{4.25}[PV_{14}O_{42}]$ catholyte showing a power output of 50 mW cm^{-2} was developed [41]. In addition $V_6O_7(OMe)_{12}$ and $V_6O_7(OEt)_{12}$ were studied as potential materials for RFBs [42]. However when this PV_{14}-POM is used as a solid electrode, it showed very poor cyclability as well [21]. Recently, organic-cation based decavanadates such as guanidine-V_{10} and TBA-V_{10}, have been tested in Li- and Na-ion batteries to improve their stability. It was observed that while their thermal stability did improve, the cyclability still remained a major issue [43].

The review of literature on polyoxovanadates leads to the following considerations:

1. These materials have a huge potential to provide high gravimetric energy and power densities owing to their low molecular mass and multiple oxidation states.

2. Their synthesis is sensitive to the pH of the solution and depending on the concentrations, more stable V_{10} species may form instead of the desired POM.

3. Their low thermal stability and presence of crystallisation water may lead to their degradation and affect their cyclability.

4. Efforts to synthesise V-POMs with organic cations may improve thermal stability but not necessarily their cyclability.

Therefore, it is clear that the previously mentioned concept of hybridisation must be applied to these materials to fully utilise their electroactivity and also to improve their cyclability. Even though these polyoxovanadates have many advantages over commonly used Mo- or W- POMs, their application as energy storage materials cannot be feasible without addressing their stability and cyclability deficiencies.

1.3 Electrode and cell design

While research on novel energy storage materials is essential to the development of new EESS, other parameters are also of great importance and must also be considered. If we climb up one "level" of the energy storage ladder, we reach the step for electrode and device engineering. While material development is arguably the most essential part of EESS, formulating and forming the electrodes and their effective integration with other components and their containment in a device comes at a close second (or as we will discuss in this thesis, alongside material development).

Currently, two main types of electrodes exist: solid electrodes and flow-electrodes. The former are commercially available as coin cells, pouch cells or even cylindrical or prismatic cells; whereas the latter have special application in flow cells. The choice of cell design and assembly is greatly affected by active material's best utilisation methods, charge transfer through current collectors, as well as ion mobility through membranes and separators. Moreover, battery pack design to regulate temperature can lead to failure or successful commercialisation of a particular cell chemistry.

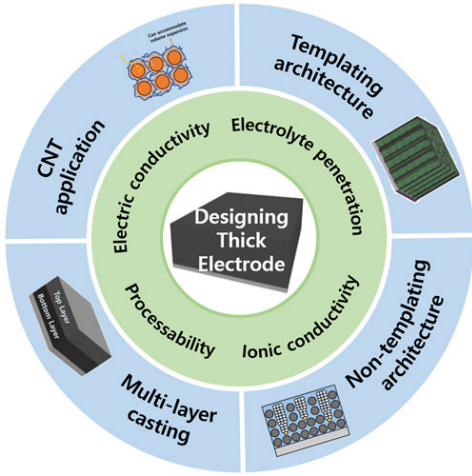

Figure 1.7: *Overview of key factors and various pore structure design methods to improve performance in thick electrodes. Reprinted with permission from ref. [44], copyright Wiley, 2011.*

In this thesis we approach the idea of electrode and cell design from a mass loading perspective. Active material in an EESS can be defined as the materials or compounds that participate in charge storage and discharge. In our case they are activated carbon and V-POMs. The remaining components of the cell such as binder, conductive carbons, separators, electrolyte or even the cell casing itself are "in-active" or passive materials that do not directly participate in charge storage but assist it.

Increasing the amount of active material in a cell seems to be an obvious method to improve the amount of charge stored within a fixed volume. This would also result in lowering costs of passive materials such as separators or current collectors and significantly lower the total weight of the battery. Development of high mass loaded or thick electrode research has been mainly explored in the area of solid electrodes. Many techniques to develop thick electrodes exist (Figure 1.7), each with their advantages and disadvantages [44].

RFBs provide an alternative to solid electrode EESS in the manner of decoupling power and energy since large amounts of electrolytes containing dissolved (or dispersed) active materials can be stored externally to the electrochemical cells. The power would depend on the number of cells and the dimensions of the active area of electrodes. However, even the best commercially available V-RFBs have low active material concentrations. Latest research is focusing on developing electroactive

Nanofluids to increase the effective concentration of electroactive species, while maintaining lower viscosity for efficient flowing [45]. Meanwhile, Semisolid Redox Flow Batteries (SSFBs) and Electrochemical Flow Capacitors (EFCs) could improve electrical conductivity and active species within flow cells [46, 47], but none meet the mark. Therefore, it is clear that increasing electrolyte accessibility to the active electrode sites without losing electrical conductivity would be the most important factor for enhancing power and cyclability without losing capacity and energy density in flow systems. Figure 1.8 highlights the advantages and disadvantages of commercial Li-ion and V-RFBs batteries, and novel SSFBs.

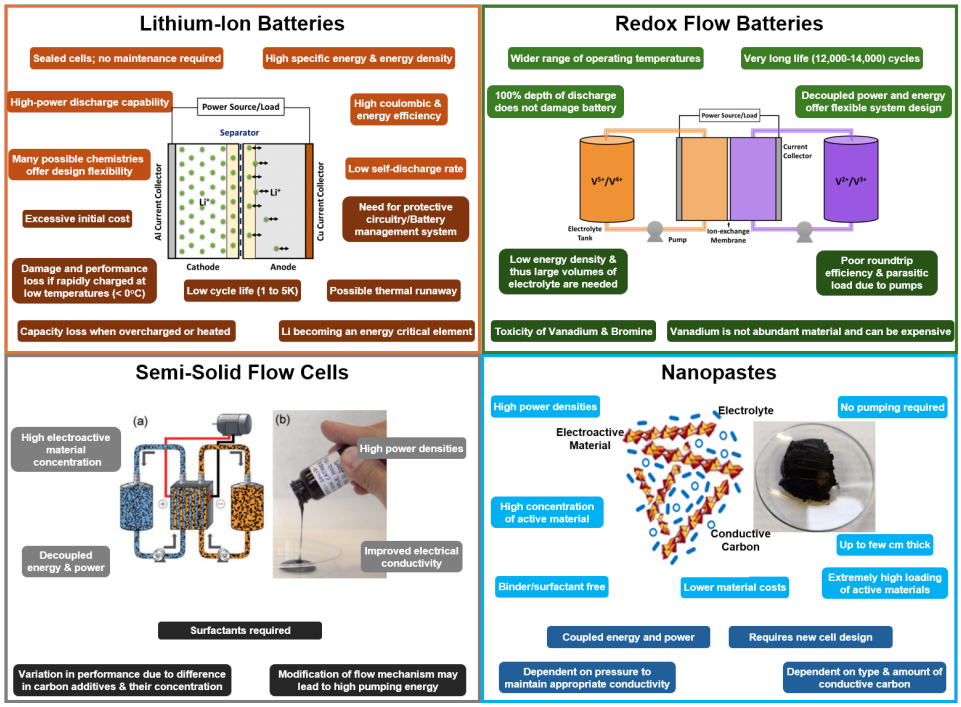

Figure 1.8: *Properties of commercial Li-ion and RFB batteries as well as novel EESS such as semi-solid flow cells and nanopastes. (a,b reprinted with permission from [48], copyright Wiley, 2011).*

The field could thus evolve towards the design of electroactive bulk "nanopastes" (Figure 1.8) which could work as effectively as thick solid electrodes and would not need to be pumped. Nanopaste electrodes could be designed as extra-thick or massive electrodes initiating a battery revolution which rests equally on the integration of materials and components in the devices as well as on the nature of the

materials and components. However, nanopastes are affected by their dependence on pressure of the system or the need to fine tune a compatible electron-conducting network with an electrolyte transport network.

A proof of concept of such non-flowable nanopastes has been developed by our NEO-Energy group in collaboration with its spin-off Napptilus Battery Labs [49, 50]. This alternative design has the potential to significantly lower battery manufacturing costs and promote the development of battery giga-factories. After all, "pastes" are well known by the industry when it comes to primary conventional cells. Why not then for large-scale rechargeable batteries?

1.4 Stationary energy storage applications

One technology fits all vs. customised chemistries

The new and improved cell chemistries and designs should meet the requirements of the final applications where they will be deployed. As per the International Energy Agency, the EESS sector is dominated by Li-ion batteries and between 2015 to 2023, electric vehicles (EVs) accounted for 90% of the increase in new Li-ion demand [51]. Clearly, the expansion in EESS has been overtaken by EVs and grid-scale EESS are not growing at the same rate. This focus seems skewed from an energy security perspective. Therefore, the question is not only to get more storage but also the appropriate type of storage. As the complexity in power grid increases, it becomes increasingly dependent on stable power supply. Depending on these applications, the requirements demanded from the energy storage technology can also differ. Therefore, an in-depth assessment of EESS' final applications has been carried out. The US department of energy defines use-cases for stationary grid connected energy storage on the basis of applications and the sector (that is, utility, residential, industrial, etc.) [52]. Table 1.1 summaries and groups them for the purpose of our perspective.

Each of these applications require specific storage characteristics which will also depend on the sector and the project scale. For example, an ancillary service such as frequency regulation requires an energy storage systems to be sensitive to the frequency variation in the grid and injection of large amounts of power within milliseconds and is required for a few seconds up to a few minutes [53]. The sensitivity of response may lead to many partial charge-discharge cycles which could seriously impact the operable life of an EESS like Li-ion batteries. On the other hand, energy arbitrage can be planned and generally requires longer times of storage

and duration of energy supply. Therefore, the response required from the EESS may not be as sensitive and cyclability requirements can be better estimated. Thus, if the same EESS technology is used in both cases, it would have different responses, ageing and life cycle costs.

Table 1.1: *Applications for grid connected electrochemical energy storage systems*[a]

Application	Description	Requirements
Ancillary services	Provide power over a short duration of time to maintain the balance between electricity supply and demand as well as the frequency of the power grid. That is, the battery serves as a reserve for services such as frequency regulation.	Fast response (ms), high power, good cyclability.
Energy shifting or energy arbitrage	Storing energy when utility prices are low and feeding it back into the grid (or the consumer directly) when the utility prices are high.	Large energy density, low self discharge, low cost.
Renewable energy storage	Storing excess energy generated by either large wind or solar power plants or small residential units. This energy can then be used when generation is not available or not sufficient. For example, to power a house after sunset.	Large energy density, low self discharge, low cost.
Transmission and distribution line deferral	When electricity demand rises, there is a need to upgrade the transmission and distribution (T&D) line network. Batteries could instead be used to meet a short-term incremental increase in power demand instead of upgrading the entire T&D network.	High power and large energy density, low cost.
Uninterrupted power source	Providing power back up to essential services (for example, telecommunication network towers or data centres) requiring power back up in case of a power cut. Batteries can replace the diesel generators that are commonly used for this purpose.	Large energy density, low self discharge, low cost.

[a] Adapted from ref. [3]

Concerning the topic of reliability of electricity supply, the application of ancillary services comes at the forefront since without a reliable grid, other applications for EESS such as energy arbitrage or E-mobility are not possible. Destabilisation of frequency can lead to grid black-outs and long-term power outages [54–56]. Frequency regulation services have strict requirements and an energy storage systems must prevent disruption in frequency by injecting large amounts of power within

milliseconds over and over again. Supercapacitors can be a suitable technology for microgrids since they cannot provide this high power over longer time periods. Meanwhile batteries have limited cyclability and their capacity declines rapidly at fast rates and over repeated cycling. However, our "AC-POM hybrid materials" and particularly AC{V-POM} hybrids may just be the answer to this vital application. With the combination of both surface capacitive and faradaic (but fast) charge storage mechanism, these materials have the possibility to provide high power over a longer time period than ELDCs. Moreover, if their cyclability limits resulting from slow ion diffusion in crystals can be resolved by dispersing the clusters and anchoring them on carbon substrates, their cycle life gets better than not only V-POM batteries but also better than most commercial Li-ion batteries (as we will show in this thesis).

1.5 Motivation and objectives

This thesis aims to develop hybrid materials and devices, driven by their potential applications. The objectives are organised around the three main areas of study:

- **Part I: From Materials to Electrodes.** The primary objective of this thesis is to develop hybrid materials based on AC and polyoxovanadates, specifically focusing on decavanadates- and tetradecaphosphovanadate-based hybrid materials. This involves both in-situ and ex-situ synthesis methods with AC to enhance their gravimetric capacitance and cycling stability in organic electrolytes.
- **Part II: From electrodes to devices.** The next goal is to create high mass-loaded or thick electrodes using scalable methods and integrate AC-polyoxovanadate hybrids to improve capacitance.
- **Part III: From devices to applications.** Finally, the study aims to understand the requirements of electrochemical energy storage systems, such as batteries, for frequency regulation in power grids with high wind penetration, and to apply AC{V-POM} hybrid devices for this purpose.

2

Materials and characterisation methods

2.1 Materials

Table 2.1 presents the starting materials used to prepare the electrodes to be studied. All chemicals were used as received:

Table 2.1: *List of chemicals purchased directly.*

Name	**Chemical Formula**	**Grade**	**Supplier**
Activated carbon (AC)(YP-50F)	C	>99%	Kurary
Activated carbon (YP-80F)	C	>99%	Kurary
Carbon SuperP (CSP)	C	>99%	Thermo Fischer Scientific
Multiwalled carbon nanotubes (CNTs)	C	>99%	Sigma-Aldrich
Ketjen Black (KB)	C	>99%	Akzonobel
Sodium metavanadate	$NaVO_3$	>98%	Sigma-Aldrich
Tetrabutylammonium bromide (TBABr)	$[CH_3(CH_2)_3)]_4N(Br)$	>99%	Sigma-Aldrich
Tetraethylammonium-tetrafluoroborate ($TEABF_4$)	$(C_2H_5)_4N(BF_4)$	>99%	Sigma-Aldrich
Sodium perchlorate (anhydrous)	$NaClO_4$	>98%	Sigma-Aldrich

Continued on next page

Name	Chemical Formula	Grade	Supplier
Acetonitrile (anhydrous)	CH_3CN	>99.8%	Sigma-Aldrich
Polyvinylidene fluoride (PVDF) (Kynar 1810)	$-(C_2H_2F_2)_n-$	>99%	Arkema
Poly(vinylidene fluoride-co-hexafluoropropylene) (PVDF-HFP)	$(-CH_2CF_2-)_x$ $[-CF_2CF(CF_3)-]_y$	reagent grade	Sigma-Aldrich
Sodium carboxymethymcellulose (CMC)	$(C_{12}H_{14}O_9R_6)_n$	>99%	Thermo Fisher Scientific
Diethyl ether	$CH_3CH_2)_2O$	>99%	Sigma-Aldrich
Filter Paper		Grade 4	Sigma-Aldrich
Spray gun		FE-130K	Fengda (amazon.es)

2.2 Physical characterisation techniques

2.2.1 Nuclear magnetic resonance

The molecular structure of a compound can be studied using Nuclear magnetic resonance (NMR) spectroscopy by measuring the interaction of oscillating radio-frequency electromagnetic field with nuclei immersed in strong magnetic field [57]. The properties of the material can be studied when the oscillation frequency matches the intrinsic frequency of the nuclei (resonance). NMR measurements can serve as fingerprints of the POMs and help characterise and identify them. Thus, ^{51}V NMR measurements were performed for all pure POMs and AC{V-POM} hybrid materials.

Bruker Avance NEO 400 MHz spectrometer was used to perform all measurements. 20 mM $NaVO_3$ solution in deuterium oxide (D_2O, 6 ml) was used as reference, with pH corrected to 14 using sodium hydroxide. All pure POMs were dissolved in 6 ml D_2O. Small but adequate quantities of AC{V-POM} hybrids were first dispersed in 7 ml D_2O and then filtered using a nylon membrane filter (pore size: 0.45 µm, diameter 25 mm) attached to a 1 ml syringe. Approximately 6 ml of filtrate solution was obtained with the respective V-POMs (with the excess V-POMs leached out) and transferred to 10 mm sample tubes. Pure V-POMs were once passed through membrane filter to ensure that there was no change in their chemical

shifts due to the filter. All NMR measurements were performed between 2 h and 72 h after synthesis. The samples were spinning in all experiments. No. of scans (ns) between 64 (pure concentrated solutions) and 1024 (filtered hybrids), depending on the sample, were performed to reduce noise.

Brucker TopSpin 4.2.0 software was used to process the spectra. Due to relatively low concentrations of V-POMs in the hybrid materials, in some cases noise elimination was necessary to present the results. An exponential line broadening function (lb 10 to 100) in TopSpin was used to improve the signal to noise ratio.

2.2.2 Fourier-transform infrared spectroscopy

Fourier transform infrared spectroscopy (FTIR) is an analytical technique that uses infrared light to detect specific vibrations of bonds or functional groups in molecules or solids. The absorbed IR radiation is converted into vibrational energy which matches the frequency of the vibration of the specific bond or group, and helps in their identification. The FTIR studies of pure V-POMs and hybrid materials were performed on Brucker Tensor 27 FTIR spectrometer using potassium bromide (KBr) pellets. Background measurements using blank KBr pellets were performed before each set of measurements. 32 scan between the range of 4000 cm^{-1} and 400 cm^{-1} were performed but were cut to 1200 cm^{-1} and 400 cm^{-1} for representing Vanadium and Oxygen bonds.

2.2.3 Powder X-Ray diffraction

X-Ray Diffraction (XRD) is a common technique to identify the crystal structure of a compound as well as to identify its different phases. By scanning a powder sample over a range of diffraction angles, the diffracted signals from all planes can be obtained. The position and intensity of these diffracted peaks can help identify the crystal structure of the compound (Bragg's Law). In case of polyoxovanadates, the crystal structure can vary widely depending on the number of water molecules attached to the POM, and hence XRD patterns may be slightly different depending on treatment of the sample and its environmental conditions (this was also practically observed during initial characterisations).

Nevertheless XRD can be very useful to know whether the sample has crystalline or amorphous nature. Sharp peaks signify crystalline materials with extended long-range order, while broader peaks would indicate nano-sized crystallites, and broad bumps would show an essentially amorphous material. This is extremely

important for synthesising AC-POM hybrid materials since POM crystals on AC surface would mean they have not been incorporated into AC micropores and thus conductivity through the bulk electroactive crystals would be low. Therefore, XRD was not chosen to identify and characterise the V-POMs. NMR and FTIR were better suited techniques. However, XRD was used to identify (and discard) hybrid materials where POMs overgrew into (micro) crystals, showing sharp peaks.

The powder XRD patterns were collected on a PANalytical X′pert Pro-MRD diffractometer with Cu Kα1 radiation (wavelength 1.5406 Å), Ge (440) monochromator and PIXel detector, withscan rate of 0.03 s^{-1} from 3° to 100°. The diffraction patterns were processed using PANalytical X′pert Pro software.

2.2.4 Thermogravimetric analysis

Thermogravimetric Analysis (TGA) is used to characterise the thermal stability and decomposition of a material under different conditions (atmosphere, temperature). The mass of the sample is recorded over time as temperature is increased in a controlled manner. Physical processes such as phase transitions and adsorption or desorption, and chemical processes such as chemisorption, solid-gas reaction and pyrolysis can also be detected and studied under a variety of atmospheric conditions.

The TGA was carried out using NETZSCH-STA 449 F1 Jupiter thermal analysis system. A heating rate of 10 °C min^{-1} from room temperature to 900 °C under air was used to study the decomposition and to identify the mass of POMs in the hybrid materials.

2.2.5 Specific surface area and pore size distribution

The specific surface area was analysed using Brunauer-Emmett-Teller (BET) method through nitrogen adsorption isotherm measurements at 77.150 K. BET is a common method to analyse the active surface area of micro- and mesoporous materials. The measurements were carried out using ASAP 2020 HD micrometrics instrument and temperature was controlled using a liquid nitrogen bath. All samples were degassed at 80 °C for 2 h except AC{TBA-V_{10}} which was degassed at 50 °C for 20 h. The total pore volume (V_{total}) was calculated at P/Po = 0.996 and the t-plot micropore volume was used (V_{micro}).

2.2.6 Scanning electron microscopy

Scanning Electron Microscopy or SEM is a useful technique to study the overall morphology and microstructure of samples. Imaging for magnification length of more than 5 μm was performed on Quante 650 Field-Emission-Gun microscope Quante 650 Field-Emission-Gun microscopy was used and the voltage varied from 2 to 20 kV depending on the sample conductivity to obtain clear images. Cross sections of electrodes observed by mounting them on 70° tabs and the measured thickness was multiplied by a correction factor of 1.06. For smaller particle sizes, high resolution SEM was performed on Magellan 400L XHR between 2 and 10 kV.

Environmental SEM and Cryo-SEM

Environmental SEM and Cryo-SEM were used to study nanopastes. A sample of $(AC)_{1g}$ $(CB)_{0.05g}$ $(CNT)_{0.05g}$ $(1\ M\ Na_2SO_4)_{4.3ml}$ was prepared and pressed in a piston cell (described in Chapter 6), collected and analysed from 100% humidity to approx 30% as well as in cryo-SEM. Environmental SEM was performed on Quante 650 FEG and Cryo-SEM was performed on (VPSEM), HITACHI S-3500N microscope equipped with QUORUM PP3000T system to study cryo-fixed samples.

Energy dispersive X-Ray spectroscopy

Energy Dispersive X-Ray Spectroscopy (EDX) was used to perform qualitative elemental analysis. The Quante 650 FEG microscope was used for EDX measurements at 20 kV.

2.3 Material synthesis, electrode preparation and cell assembly

Due to the vast variety of synthesis methods, materials as well as coating methods used, each chapter contains individual and specific detailed explanations of the synthesis of materials, preparation and coating methods for electrodes as well as cell assembly. All coin cells (CR2032) and swagelock cells were assembled in an argon filled glove box (Jacomex GP with $O_2 < 5$ ppm and $H_2O < 5$ ppm) with cellulose separators (Whatman Grade 4) of 16 mm and 12 mm diameters, respectively.

2.4 Electrochemical characterisation

All electrochemical characterisation was performed on a Biologic VMP3 multichannel potentiostat. The measurements were performed in two modes: three electrodes and two electrodes. In the three electrode configuration, an $Ag/AgNO_3$ reference electrode was used with the supporting electrolyte comprising 0.1 M $TEABF_4$ and 0.01 M $AgNO_3$ in acetonitrile. Carbon cloth loaded with AC (Norit) served as the counter electrode (CE). The three electrodes were assembled using a T-shaped Swagelok cell. The 2 electrode measurements were performed using a coin cell (except paste electrodes) in symmetric and asymmetric configurations. Measurements in the three electrode setup used the term "potential" of working electrode (WE) or CE, while measurements in the two-electrode mode used the term "voltage".

2.4.1 Cyclic voltammetry and cyclic polarisation

Cyclic voltammetry (CV) is one of the most common and useful electrochemical techniques as it is used to study oxidation and reduction processes of a molecular species. In this technique, a WE is placed against the CE with a reference electrode. A potential is applied to the WE with respect to the RE at a given scan rate (mV s^{-1}) and the current passing between the WE and the CE is measured as a function of the potential. The potential measured at the working electrode is without an ohmic drop since there is no current between the WE and RE and thus accurate electrochemical behaviour of different materials can be studied and standardised. In two electrode systems, the CE serves as the reference electrode and the current vs. voltage plot is considered a cyclic polarisation (CP). It is well known that capacitive materials display a mostly rectangular CV or CP plot. On the other hand, redox materials display waves or peaks at their characteristic redox potentials. CVs can be used to calculate the capacitance of the electrode, whereas CPs can be used to calculate capacitance of the cell or device. This is given as:

$$C = \frac{\int I(V)}{2\nu\Delta V} \tag{2.1}$$

Where $\int I(V)$ is the integral area of the CV or CP, ν is the scan rate and ΔV is the voltage window. In case of a symmetric supercapacitor, two identical electrodes are connected in series. Thus the capacitance (C) of the device can be denoted as:

$$\frac{1}{C} = \frac{1}{C_e} + \frac{1}{C_e} \tag{2.2}$$

Therefore capacitance of an electrode, $C_e = 2C$.

The three electrode CVs can also be used to simultaneously test electrochemical properties of both electrodes of a symmetric or asymmetric supercapacitor. This is a less commonly used technique but it can be useful in simultaneously determining the influence of different electrolyte ions on the mechanism or kinetics during charging/discharging reactions [58].

The CVs at various scan rates can also be used to estimate the surface capacitive and diffusion controlled charge contributions in an electrode. The current dependence on the scan rate is given by the following equation [59]:

$$i = a\nu^b \tag{2.3}$$

i is the current of a redox peak at a given scan rate ν and a and b are adjustable parameters. The current is measured at various scan rates and the value of b is determined from the slope of the plot of log i vs log ν:

$$log\, i = log\, a + b\, log\, \nu \tag{2.4}$$

For a diffusion controlled process, $b = 0.5$, the current (i) is proportional to the square root of of the scan rate (ν). On the other hand, for a surface capacitive process $b = 1$ and the current is linearly dependent on the scan rate.

2.4.2 Galvanostatic charge-discharge

Galvanostatic charge-discharge (GCD) is an electrochemical technique in which a constant current is applied to the cell and the potential (or voltage for a two electrode cell) is recorded during the charging and discharging time within a set of pre-determined potential limits. For purely capacitive processes, the potential varies linearly with time, whereas for redox processes, the potential remains nearly constant until the redox process finishes. For a purely capacitive (and in some cases pseudocapacitive materials), the device capacitance can be calculated from the CGD:

$$C = \frac{I\Delta t}{\Delta V} \tag{2.5}$$

Where I is the current, Δt is the discharge time and ΔV is the voltage window (after considering the IR drop). When it comes to pseudocapacitive or hybrid devices involving redox reactions, there is great contention among scholars whether

to use Equation 2.5 to calculate capacitance as the charge/discharge curve does not follow a linear I vs. Q (charge) dependence [60]. A suggested alternative is to use the area under the discharge curve to calculate the device capacitance:

$$C = \frac{I \int V(t) \cdot dt}{\Delta V^2} \tag{2.6}$$

Where $I \int V(t) \cdot dt$ is the integrated area of the discharge curve and ΔV is the total voltage window. However, this is not a commonly used method. In this thesis, Equation 2.5 is generally used to calculate and compare capacitance of difference materials.

Since capacitance of electrode (C_e) is twice the device capacitance C, the gravimetric capacitance (C_g) of the electrode is calculated as:

$$C_g = \frac{C_e}{m} = \frac{2C}{m} \tag{2.7}$$

Where m is the active material mass of one electrode. We can assume the same follows for an asymmetric electrode as the charge (and hence capacitance) of the two electrodes is balanced. However, the normalisation would be made on the basis of the electrode under study (in our case the negative or hybrid electrode).

The areal (C_a) and volumetric (C_v) capacitances are calculated as:

$$C_a = \frac{C_e}{A} = \frac{2C}{A} \tag{2.8}$$

$$C_v = \frac{C_e}{m} = \frac{C}{V_e} \tag{2.9}$$

Where A is the area of electrode and V_e is Volume of electrode. The gravimetric energy is given as:

$$E_g = \frac{C\Delta V^2}{8m} \tag{2.10}$$

The power density is calculated as:

$$P_g = \frac{E_g}{\Delta t} \tag{2.11}$$

Alternatively, it is proposed that the performance of pseudocapacitive materials can also be evaluated using the discharge capacity rather than capacitance [61]:

$$Capacity = I\Delta t \tag{2.12}$$

Part I

Materials to Electrodes: Activated Carbon - Polyoxovanadate Hybrid Materials

Context

Electrode materials used in Electrochemical Energy Storage devices need to fulfil a precise set of conditions to work effectively. They need to be electronic conductors to draw electrons to the electroactive centres that will store them (in batteries and pseudocapacitors), or to polarise the surface (in EDLCs). In the first case, electroactive species are essential, but they also need to be accessible to electrolyte ions to compensate for the charge of electrons injected. This is why intercalation phases with mixed (ionic-electronic) conductivity have been traditionally used as electrode materials. However, it is also possible to fabricate materials in which the functions such as electron conductivity, electroactivity and ion conductivity are provided by different component materials. This is the essential concept behind hybrid materials. But to achieve optimal performance, the interactions between these components must be maintained at the nanometric scale. Only then, the resulting electrode will allow for the full utilisation of electroactive centres while providing fast electron/ion transfer processes and consequently high power.

In this way, hybrid materials present a viable alternative to bridge the gap between supercapacitors and batteries. In theory, they can provide both high power in a short period of time, as well as higher energy at low discharge rates, thus combining the best features of both technologies in just one device. Supercapacitors that incorporate POMs supported on activated carbon electrodes have shown promising performances in recent years [62, 63]. This is because POMs are nano-sized stable structures that can deliver high energy at a fast rate because their active moieties are located at the surface of the cluster [15]. When POMs are properly dispersed, i.e. in the absence of crystals, their redox activity is not limited by diffusion, so in a hybrid material, it is possible to take full advantage of the capacitive effect of activated carbon as well as the faradaic electroactivity of POMs.

This part of the thesis focuses on the novel-materials aspect of energy storage, specifically the synthesis of vanadium based polyoxometalates to bridge the gap between batteries and supercapacitors, taking advantage of the lower mass of vanadium as compared to other heavier (W, Mo) polyoxometalates. Two main types of vanadium-based polyoxometalates are chosen for analysis: decavanadates, based on $Na_6V_{10}O_{28}$ (Na-V_{10}) and $[(C_4H_9)_4N]_3H_3[V_{10}O_{28}]$ (TBA-V_{10}), and sodium tetradecavanadophsphate $Na_5[H_4PV_{14}O_{48}]$ (PV_{14}). V_{10} is an isopolyoxometalate with just V and O in its composition while PV_{14} is a heteropolyanion composed of P, V and O. The structure and pH stability range of V_{10} and PV_{14} is shown in Figure 2.1.

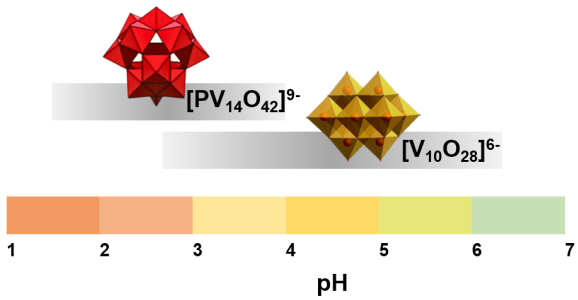

Figure 2.1: *Pictorial representation of the pH stability windows of V_{10} and PV_{14} POMs.*

Chapter 3 describes the synthesis of the sodium and tetrabutylammonium (TBA) salts of decavanadate, their adsorption on AC and the electrochemical investigation of these hybrid electrodes firstly in a symmetric supercapacitor configuration. To take full advantage of the electrochemical activity of the V_{10}-POMs, asymmetric cells AC{V_{10}} were also assembled and tested for these electrodes.

Chapter 4 deals with another vanadium-based polyoxometalate: sodium tetradecavanadophosphate or PV_{14}. Different in-situ syntheses of the AC{PV_{14}} hybrid materials are explained and the partial degradation of PV_{14} into V_{10} is described. The partial degraded materials were characterised and possible solutions to prevent their decomposition are discussed.

3

Hybrid carbon-decavanadate electrodes for energy storage

3.1 Introduction

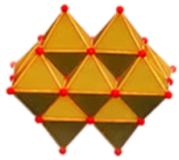

Figure 3.1: *Molecular structure of V_{10} anion. Red dots represent oxygen atoms. V ions are located at the centre of the octahedra.*

Decavanadate POMs have garnered substantial interest as battery active materials due to their lower molecular weights which lead to higher specific capacities. Vanadium is a transition metal with relatively lower mass than Mo or W and with multiple oxidation states (V^{2+} to V^{5+}). This makes Vanadium ideal for energy storage applications and novel decavanadate clusters $[V_{10}O_{28}]^{6-}$ (or V_{10}) are being explored as promising electrode materials. For example, Chen et al. demonstrated sodium decavanadate ($Na_6V_{10}O_{28}$/Na-V_{10}) as active electrode materials in a Li-containing electrolyte with good gravimetric capacitance and rate capabilities [37]. Furthermore, they fabricated asymmetric supercapacitors with activated carbon as positive electrode and Na-V_{10} as negative electrode showing a high energy density of 73 Wh kg^{-1} and a power density of 312 W kg^{-1}. In another study Hartung et al. used Na-V_{10} in a Na-ion battery as an anode material [39]. However, these pure V_{10}-POM materials showed poor cyclability e.g. the Na-V_{10} based supercapacitor had only a 70% capacity retention after 1,000 cycles. To overcome these issues, Ghosh et. al. designed an effective approach to improve stability of these POMs by substituting the Na^+-ion with a larger and more stable organic cluster such as the

TBA-cation [43], which has been previously used to improve POMs compatibility with organic electrolytes [15]. This strategy showed positive results with TBA-V_{10} and Guanidinium-V_{10} as anode materials for Na-ion batteries. Nevertheless, even the best performing Guanidinium-V_{10} had a limited capacity retention of only 83% after 500 cycles, while the TBA-V_{10} electrode had an even lower capacity retention [43]. The latter could be attributed to factors such as the presence of crystal water in the lattice structure, low thermal stability, and their high solubility in many electrolytes [43]. It is clear that V_{10}-POMs possess an enormous potential and advantages over other POMs for their application in energy storage devices, mainly due to their lower molecular weight, and a reduced number of initial reports have proved this. Nonetheless, their cycling stability remains a major limitation, despite recent efforts to solve this issue. For this reason, in this study we propose the use of the previously known concept of "hybridisation" wherein the electroactivity of POMs is utilised by anchoring them on activated carbon. This immobilises the POM on a highly conductive and insoluble support and improves their stability. Using this approach, we develop two AC{V_{10}} hybrid materials, AC{Na-V_{10}} and AC{TBA-V_{10}} through in-situ and ex-situ syntheses that are described in Section 3.2. The electrochemical behaviour of these hybrid materials was characterised in both three- and two-electrode configurations. Symmetric and asymmetric (pure AC electrode vs. AC{V_{10}}) supercapacitor devices were assembled to optimise the voltage operating range of the synthesised materials. Our strategy led to devices with high energy and power density as well as excellent cyclability (>5,000 cycles).

3.2 Preparation of decavanadates and AC{V_{10}} hybrids

The complex polyoxovanadates used in this thesis for the development of hybrid materials were not commercially available and had to be synthesised according to previous reports. It should be noted though that their synthesis is quite intricate, and the final results depend strongly on parameters such as temperature and pH, which is why the procedures are described in detail and conditions different from previously published works are made explicit.

Sodium decavanadate

Pure sodium decavanadate [$Na_6V_{10}O_{28}$] or Na-V_{10} was prepared from the methodology specified in reference [37]. $NaVO_3$ (3 g) was dissolved in deionised (DI) water (100 ml) and 4 M HCl was added dropwise to reduce the pH to 4.8. The solution

was filtered and additional HCl was added to further reduce the pH to 4.5. The solution was stirred for 2 h and ethanol (200 ml, 99%) was added to precipitate Na-V_{10} (orange solid). Na-V_{10} was separated by vacuum filtration using a 0.22 μm filter paper and dried in air (yield of approx. 1.8 g).

Tetrabutylammonium trihydrogen decavanadate

Tetrabutylammonium decavanadate $[(C_4H_9)_4N]_3H_3[V_{10}O_{28}]$ or TBA-V_{10} was synthesised as per the methodology by W. G. Klemperer [64]. $NaVO_3$ (7.5 g) was dissolved in DI water (50 ml). The pH of the solution was reduced to 4.5 using concentrated HCl and stirred for 2 h. Separately tetrabutylammoniumbromide (25 g) was dissolved in DI water (30 ml) then slowly added to the $NaVO_3$ solution and vigorously stirred for approximately 30 min. An orange yellow precipitate was obtained which was collected using vacuum filtration. It was washed successively with DI water (30 ml), ethanol (30 ml) and dried at 50 °C overnight in a vacuum oven. In total 6.3 g of material (characterised as Compound A [unpurified TBA-V10] in Appendix) was obtained. Compound A (5 g) was dissolved in acetonitrile (40 ml) and vacuum filtered through a fine porosity paper to remove insoluble material (characterised as Compound B [TBA-V10 impurity] in Appendix) which was discarded. Anhydrous diethyl ether (90 ml) was added to the filtrate which resulted in a yellow-orange precipitate. This precipitate was further washed with anhydrous diethyl ether (30 ml) and dried in a vacuum oven at 30 °C for 2 h to yield approximately 1.7 g of pure TBA-V_{10}.

In-situ preparation of AC{Na-V_{10}} hybrid material

The hybrid material AC{Na-V_{10}} was prepared by a modification of the methodology in Section 3.2. AC (2 g) was dispersed in DI water (100 ml) by bath sonication for 30 min and then stirred. Meanwhile $NaVO_3$ (2 g) was separately dissolved in DI water (100 ml) by boiling the solution. The $NaVO_3$ solution was slowly cooled down to room temperature and then added to the AC dispersion. Concentrated HCl was added dropwise to reduce the pH to 4.5. The dispersion was stirred for approximately 6 h after which the pH was readjusted and then stirred for approximately another 18 h. The AC{Na-V10} hybrid was isolated through vacuum filtration without washing. The solid was dried in vacuum oven at 80 °C and 2.72 g of AC{Na-V_{10}} hybrid material was obtained.

Ex-situ preparation of AC{TBA-V_{10}} hybrid material

The AC{TBA-V_{10}} hybrid could not be prepared by in-situ synthesis due to the need for purification of the salt obtained after the cation exchange reaction since Na-V_{10} was found to be present as an impurity. Thus, the synthesis was performed in the following two steps: first synthesising TBA-V_{10} as specified in Section 3.2 and second, adsorbing TBA-V_{10} in porous AC.

AC (0.5 g) was dispersed in acetonitrile (25 ml) through stirring. Separately, TBA-V_{10} obtained from Section 3.2 (0.5 g) was dissolved in acetonitrile (25 ml) and stirred for 30 min. The TBA-V_{10} solution was added to AC dispersion and stirred for 24 h. The final solution was vacuum filtered using 0.1 um filter paper and washed with acetonitrile (25 ml). The obtained solid was dried in a vacuum oven at 30 °C for 12 h and 0.86 g of AC{TBA-V_{10}} hybrid material was obtained.

3.3 Electrode preparation and cell assembly

The AC{Na-V_{10}} and AC{TBA-V_{10}} slurries were prepared by mixing the hybrid material, carbon black and PVDF in the ratio 80:10:10 in NMP and stirred for 6 h. The AC electrodes were prepared by mixing AC (YP-80F), CSP and PVDF in the ratio 90:5:5 in NMP. The pure Na-V_{10} and TBA-V_{10} electrodes were prepared by mixing pure V_{10}-POMs, CSP and PVDF in the ratio 70:20:10 in NMP. The slurries were stirred for 6 h, bar coated onto aluminium foil and dried in vacuum at 80 °C to evaporate NMP. Any remaining water from the POMs was assumed to be extracted by NMP and then evaporated during the drying process. Electrodes of 14 mm (coin cells) and 10 mm (Swagelok cells) diameter were cut and pressed (3 t, 5 s). Symmetrical coin cells of AC{V_{10}-POM} hybrids and asymmetric coin cells of AC as positive electrode and AC{V10-POM} hybrids as negative electrodes were assembled in an argon filled glove box with a Whatman 4 separator and 1 M $NaClO_4$ in acetonitrile as electrolyte.

3.4 Characterisation of AC{V_{10}} hybrid materials

^{51}V NMR was performed to characterise and verify the presence of decavanadate species in the hybrid materials. Pure Na-V_{10}, TBA-V_{10} and hybrid AC{Na-V_{10}} powders were dissolved or dispersed in heavy water (D_2O) and the hybrids were filtered using a nylon filtered to remove carbon particles. The ^{51}V-NMR spectra of pure V_{10} (Na and TBA) showed characteristic peaks at -517, -501 and -424 ppm (Figure 3.2 a) which are similar to previously reported in the literature [39]. The NMR ignal of AC{TBA-V_{10}} was not visible since the hybrid had been washed with acetonitrile to remove excess POM and the remaining POM was well adsorbed on the carbon pores.

FTIR (Figure 3.2 b) was used to confirm the presence of Na-V_{10} and TBA-V_{10} in the hybrid materials. The FTIR spectra of decavanadates are quite similar and subtle differences can be observed depending on the nature of the counterions compensating the charge of V_{10}. The peak around 939 cm^{-1} can be assigned to the V=O bond while the absorption bands between 850 and 500 cm^{-1} can be attributed to various V—O vibrations. The key difference between Na-V_{10} and TBA-V_{10} can be observed in the region between 850–600 cm^{-1}. This is due to the presence of TBA-specific vibrational peaks [65]. In the hybrid materials, the signals between 850-500 cm^{-1} were not clearly visible due to the presence of AC and relatively low concentration of the POMs in the total mass. However, the adsorption of V_{10}-POMs on AC became evident due to the presence of a large peak at ca. 950 cm^{-1} which is absent in the spectrum of AC. It is also noteworthy that for both V_{10} salts, a blue shift in the V=O vibration peak takes place upon adsorption on the AC, which may stem from POM-carbon interactions.

It is well known that large crystals of POMs translate into slow diffusion of ions and poor conductivity which is one of the major problems associated with conventional battery materials. Therefore, the presence of such large crystals would lead to a suboptimal material for supercapacitors [66]. Consequently, XRD was mostly used in our work to rule out the presence of bulk POM microcrystals on carbon.

XRD is used to identify and characterise well-ordered crystal structures resulting in sharp diffraction peaks due to periodic arrangements of atoms. However, polyoxovanadates tend to form poorly crystalline or even amorphous solids with varying amounts of lattice water. Moreover, their synthesis is generally performed in aqueous media and the POMs are separated as hydrated salts with crystal

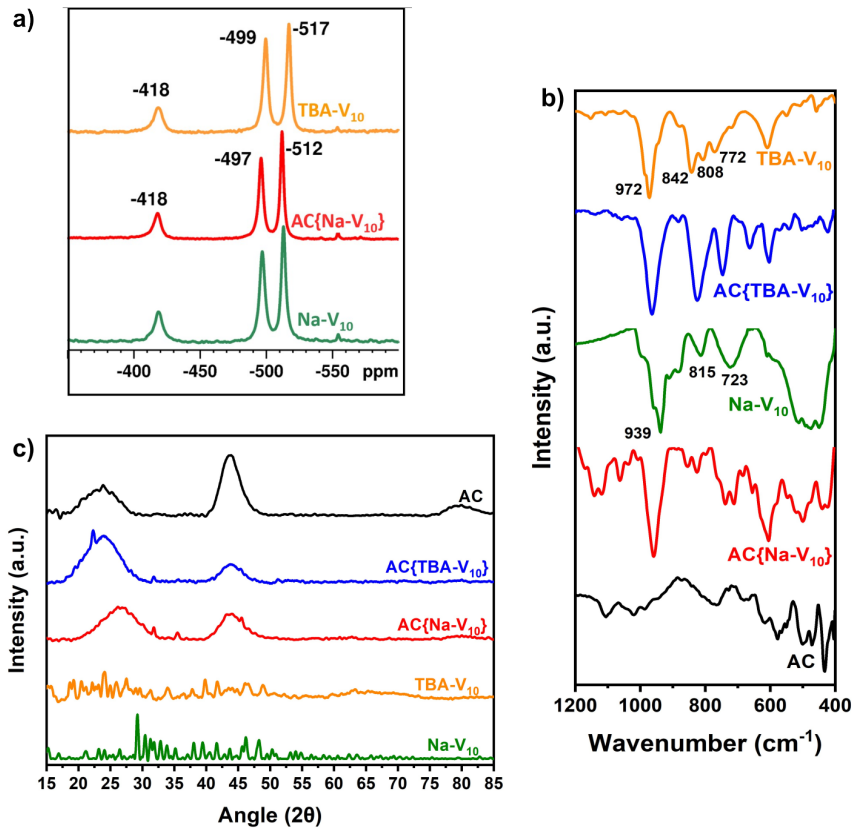

Figure 3.2: *a) NMR patterns of Na-V_{10}, AC{Na-V_{10}} and TBA-V_{10}, b) FTIR and c) XRD patterns of AC, V_{10}-POMs and their hybrid materials.*

lattice water. The drying of these POMs even at low temperatures can lead to loss of crystallinity and complete removal of this lattice water at temperatures around 120 °C can even lead to their decomposition into solid-state vanadium oxides [36, 67, 68]. Our syntheses of pure POMs was performed by precipitation methods which led to poor crystallisation. Moreover, the hybrid material was dried at 80 °C which would lead to removal of some of the lattice water leading to changes in the XRD patterns. Single crystals can be obtained and better characterised via XRD. However, since the objective of hybridising these POMs was to prevent their crystallisation, single-crystal XRD was not performed and instead we relied on NMR and FTIR patterns to identify the POMs.

Therefore, when it came to the systematic characterisation of AC{V_{10}-POM} nanocomposites, XRD was only used as a way to confirm the lack of extended crystallised domains of V_{10}-POMs in the hybrid. Figure 3.2 c. shows the XRD patterns of pristine AC, pure V_{10}-POMs, and the hybrid materials. Contrary to pure Na-V_{10} and TBA-V_{10} which had many sharp peaks indicating bulk crystallisation, the hybrid materials, AC{Na-$_{10}$} and AC{TBA-V_{10}} showed mostly broad peaks from carbons, indicating that there were no bulk microcrystals of the V_{10}-POMs in the samples. This was also verified through SEM of the AC{V_{10}-POM} electrodes (Figure 3.3). The small peaks in the XRD pattern of the hybrid materials may be due to the presence of some impurities which can be also seen at ca. -555 ppm.

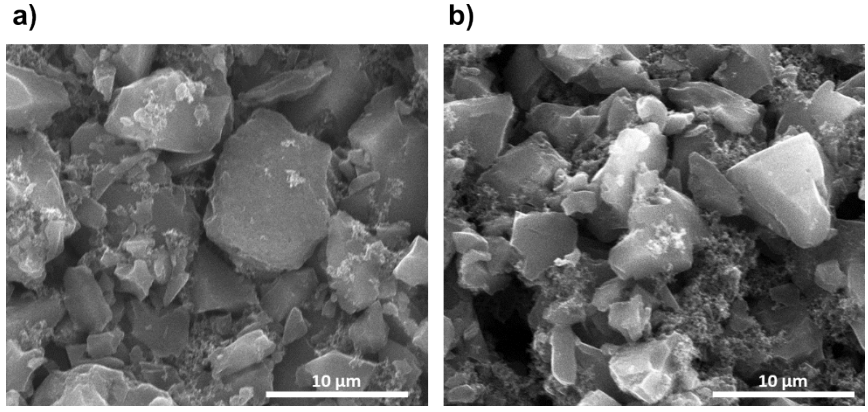

Figure 3.3: *SEM images of a) AC{Na-V_{10}} and b) AC{TBA-V_{10}} powders.*

The effect of adsorption of the V_{10}-POMs on the porous structure of AC was evaluated by **BET** N_2 adsorption and desorption as shown in Figure 3.4 a. The three curves can be classified as Type I isotherms as per the IUPAC classification, signifying a microporous structure. The adsorption of the V_{10}-POMs into the micropores of the AC can be confirmed by the reduction in the total pore volume (Table 3.1) which was recorded as 1.36 cm^3 g^{-1} for pristine AC, 0.78 cm^3 g^{-1} for AC{Na-V_{10}} and 0.45 cm^3 g^{-1} for AC{TBA-V_{10}}. The BET N_2 adsorption/desorption isotherms recorded the surface area of AC as 2136 m^2 g^{-1}. The surface area of AC{Na-V_{10}} and AC{TBA-V_{10}} was reduced to 1232 m^2 g^{-1} and 493 m^2 g^{-1}, respectively, which was expected due to the combination of two reasons: i) the partial blocking of pores by the POM adsorption (especially with bulky TBA counterions) and ii) the higher mass of the V_{10} POMs in comparison with AC, which is detrimental when normalising per mass.

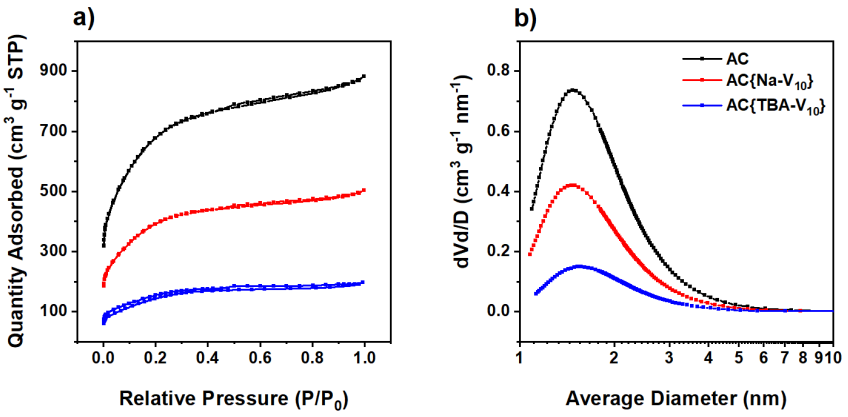

Figure 3.4: *a) N_2 adsorption/desorption isotherms and b) differential pore volume vs. pore width for AC (black), AC{Na-V_{10}} (red) and AC{TBA-V_{10}} (blue) powders.*

Table 3.1: *Porosity properties of AC, AC{Na-V_{10}} and AC{TBA-V_{10}}.*

Sample	S_{BET}[a] (m^2 g^{-1})	V_{Total}[b] (cm^3 g^{-1})	V_{micro}[c] (cm^3 g^{-1})
AC	2136	1.36	0.41
AC{Na-V_{10}}[d]	1232	0.78	0.24
AC{TBA-V_{10}}[d]	493	0.45	0.03
AC{Na-V_{10}}[e]	1647	1.06	0.33
AC{TBA-V_{10}}[e]	851	0.78	0.06

[a] Specific surface area determined by BET method. [b] Total pore volume.
[c] Micropore volume. [d] Normalised by total mass. [e] Normalised by mass of AC.

The decline in surface area of AC{Na-V_{10}} (42%) and total pore volume (43%) was similar to the drop in micropore volume (42%). This could be explained if we consider Na-V_{10} being predominantly adsorbed on AC micropores. However, some V_{10} may be present on the surface of AC since the hybrid was not washed. Interestingly, in case of the AC{TBA-V_{10}} hybrid material, a significant drop in surface area (77%) and total pore volume (67%) was observed. Moreover, its micropore volume dropped by 92%. Since AC{TBA-V_{10}} was washed during synthesis, it was assumed that the POM was completely adsorbed on AC micro pores. Upon normalisation of micropore volume by the mass of only AC (instead of the total sample mass), the same trend is observed. Table 3.1 gives the surface area, total pore volume and micropore volume of pristine AC and AC{V_{10}-POM}

hybrid materials, with all values normalised by the total mass of the material as well as by the mass of AC in the sample. If the POM is adsorbed in the micropores of the sample, a reduction in micropore volume should be seen irrespective of the mass normalisation, as is evident in the case of AC{Na-V_{10}} and AC{TBA-V_{10}} hybrid materials.

The thermal properties of the materials were studied by **TGA** (Figure 3.5 a). The pristine AC underwent a slight weight loss of 1.8% before 500 °C due to the removal of adsorbates. Thereupon, the large drop in its mass (inflection point at 640 °C) signified its total combustion and at 900 °C only 1.3% of weight was left as ashes. One sharp peak at 640 °C corresponding to its combustion can be seen from the dw/dT curve (Figure 3.5 b).

In case of AC{Na-V_{10}} hybrid, 2% of weight loss was observed at around 100 °C possibly due to the presence of small amount of crystal lattice water. The decomposition takes place in two distinct steps: first a sharp decrease at 300 °C takes place followed by a broader one centred at 480 °C and ending at 500 °C. Complete decomposition occurred with 23% of the original weight remaining in ashes. The AC{TBA-V_{10}} hybrid material also decomposed at approximately 480 °C but with three distinct steps, and with 22% of its initial weight remaining in ashes. Thus, the V cluster acts as a catalyst for the oxidation of AC at temperatures above 200 °C and the presence of V_{10}-POMs in AC lowers its combustion temperature. This behaviour has also been previously observed for other AC-POM hybrid materials [69, 70]. We consider that the V_{10}-POM decomposed in air to vanadium pentoxide (V_2O_5).

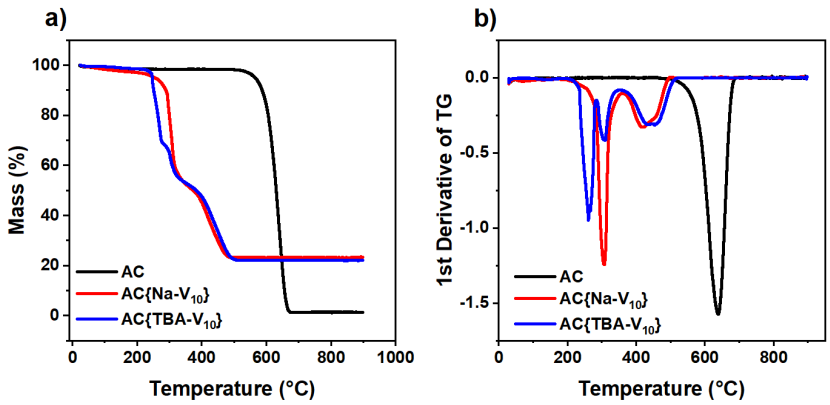

Figure 3.5: *a) TGA and b) corresponding dW/dT curves of pure AC and AC{V_{10}-POM} hybrid materials.*

In addition sodium reacted with CO_2 present in air to form sodium carbonate: $Na_6[V_{10}O_{28}] \rightarrow 5V_2O_5 + 3Na_2O \rightarrow 5V_2O_5 + 3Na_2CO_3$. Meanwhile, in the case of AC{TBA-V_{10}}, 1 mol V_{10} would form 5 mol V_2O_5. Using these assumptions and the TGA weight loss, the hybrid materials AC{Na-V_{10}} and AC{TBA-V_{10}} were calculated to contain 21% and 40.85% (w-w) of Na-V_{10} and TBA-V_{10} POMs respectively, which were close to the estimated values (by weight difference).

3.5 Electrochemical characterisation

3.5.1 Estimation of operable voltage range

Figures 3.6 a and c show the CVs of pure Na-V_{10} and TBA-V_{10} as well as AC{Na-V_{10}} and AC{TBA-V_{10}} hybrids in three-electrode configuration in a Swagelok cell with 1 M $NaClO_4$ in acetonitrile as the electrolyte. Carbon cloth loaded with AC served as the counter electrode and $Ag/AgNO_3$ as reference electrode. The supporting electrolyte used for the home-made assembly of the reference electrode was 0.1 M $TEABF_4$ and 0.01 M $AgNO_3$ in acetonitrile. The hybrid materials were characterised over an extended voltage range between -2.5 V and 1.4 V to establish the electrochemical activity range.

It was observed that for both AC{V_{10}} hybrid electrodes, the safe operational voltage range was between 2.1 V on the negative side and 1.1 V on the positive side, measured from the open circuit potential (OCP = 0.1 V). Beyond these limits, there is a sharp increase in current over small voltage changes due to spurious reactions such as electrolyte or substrate decomposition. This was also tested via CVs of pristine AC electrodes (Figure 3.6 b).

The exact electron activity in hybrid materials is difficult to ascertain due to the broad and sometimes overlapping peaks of the POMs and the AC. However, it is known that pure V_{10} allows all 10 electrons to participate in the electrochemical reactions [71]. This capability was assumed to be translated to the hybrid materials as well. However, V K-edge X-ray absorption near edge structure (XANES) experiments would need to be performed to confirm the precise electron participation in the redox activity of these hybrid materials. In the meantime, the best experiments to be carried out are tests of the electrochemical performance of final cells.

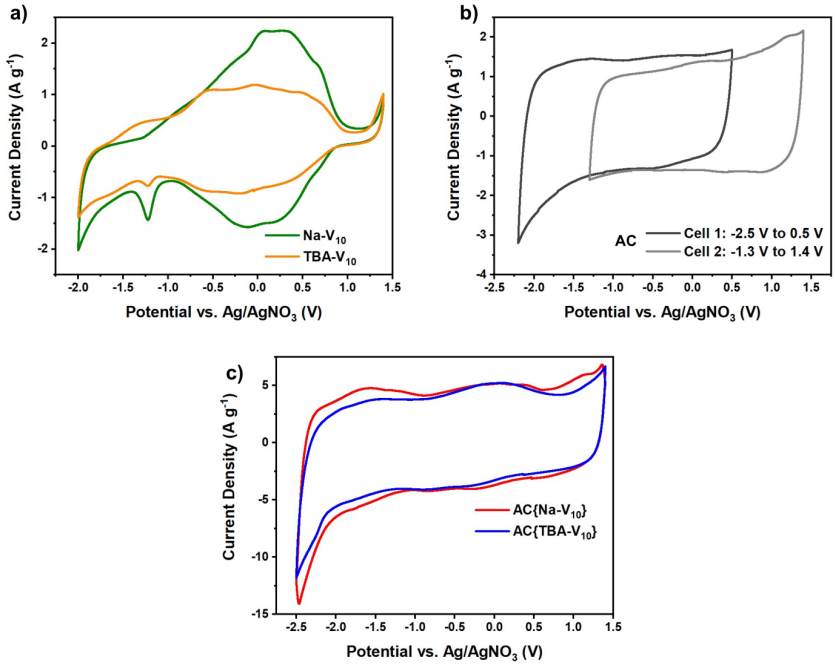

Figure 3.6: *CVs of a) pure Na-V_{10} and TBA-V_{10} electrodes at 20 mV s^{-1}, b) AC electrodes in different voltage ranges at 10 mV s^{-1} and c) AC{Na-V_{10}} and AC{TBA-V_{10}} hybrid electrodes at 20 mV s^{-1}. All electrodes were tested in three-electrode configuration with Ag/$AgNO_3$ reference electrode, AC loaded carbon cloth as counter electrode and 1 M $NaClO_4$ in acetonitrile electrolyte.*

3.5.2 Charge control mechanism

It has been previously reported that intercalation of Li^+ and Na^+ into the V_{10} crystal structure is possible because the reduction of POM is balanced by the cation's positive charge [39]. However, in our hybrid materials, V_{10} is present as isolated anionic clusters with a variable number of Na^+ ions depending on its oxidation state and with no diffusion restrictions, as it will be shown below. Therefore, intercalation is not anticipated in this case, but an interaction between POM-Na^+ to form ion pairs is expected. It has been previously observed for other dispersed POM clusters that the absence of microcrystals with an extended structure allows for faradaic processes to behave in a fast and reversible manner [16, 66], that are kinetically matched with a capacitive material. This leads to an overall capacitive or pseudocapacitive performance. The capacitive nature of the present hybrid materials was verified by Dunn's Method as the slope derived from fitting the

current of oxidation and reduction peaks was close to 1.

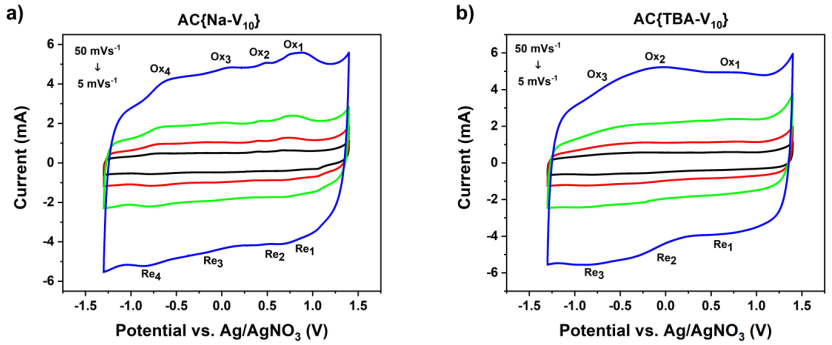

Figure 3.7: *Redox peaks selected for determining b-value of AC{Na-V_{10}} and AC{TBA-V_{10}} hybrid electrodes.*

The type of charge storage mechanism of a material can be determined by estimating what fraction of the total capacity of the electrode can be associated to either of two characteristic mechanisms, namely, "surface-capacitive" (typical of supercapacitors) and which to "ion-diffusion controlled" (typical of batteries). According to Dunn [59], the current response at any given potential can be expressed as a function of the scan rate used for measuring the CV according to Equation 3.1:

$$i = av^b \tag{3.1}$$

Where i is the maximum peak current, at a scan rate of v, and a and b are constants. For capacitive or fast charge storage mechanism, $b = 1$ as current is linearly proportional to scan rate. In case of ion-diffusion controlled charge storage mechanism, the current response would deviates from this linearity such that $b = 0.5$, i.e. current being proportional to the square root of the scan rate. Equation 3.1 can be written as:

$$log\, i = log\, a + b\, log\, \nu \tag{3.2}$$

The value of b for each redox peak can be calculated from the slope of the plot of $log\, i$ vs. $log\, \nu$. Overall, redox pairs for AC{V_{10}} hybrid materials are not very well defined in the corresponding CVs. For AC{Na-V_{10}} 4 pairs could be distinguished while for AC{TBA-V_{10}} only 3 pairs could be clearly identified. Figure 3.8 shows linear regressions for this type of double-log plots for various redox peaks of our hybrids. The R^2 values are given in Table 3.2 and are close to 1 indicating

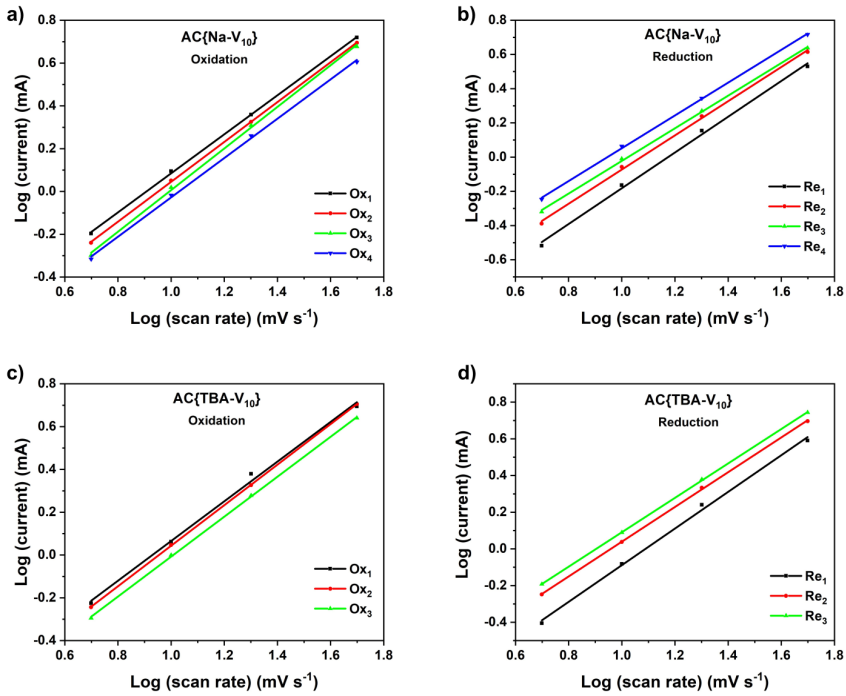

Figure 3.8: *b-value determination for oxidation and reduction peaks of AC{Na-V_{10}} and AC{TBA-V_{10}} electrodes.*

proper fitting. In addition, b values are identical to 1.0 within experimental error, indicating the fast charge storage mechanism not limited by diffusion which is typical of supercapacitors. These results are in great contrast with the ion-diffusion controlled reaction mechanism dominating POMs in crystallised extended structures. It has been proven that the adsorption of POMs on carbon pores allows direct availability of the electroactive moieties on the electrode-electrolyte interface for fast electron transfer and ion-pair formation [15].

Table 3.2: *Values of b and regression coefficient (R^2) derived from fitting current of oxidation O_x and reduction R_e peaks at scan rates of 5, 10, 20 and 50 mV s^{-1}.*

		O_{x1}	R_{e1}	O_{x2}	R_{e2}	O_{x3}	R_{e3}	O_{x4}	R_{e4}
AC{Na-V_{10}}	b	0.91	1.00	0.93	1.00	0.97	0.95	0.92	0.96
	R^2	0.999	0.996	1.000	0.998	0.999	0.999	0.999	0.999
AC{TBA-V_{10}}	b	0.93	1.00	0.95	0.95	0.93	0.94	-	-
	R^2	0.995	0.996	1.000	1.000	1.000	1.000	-	-

3.5.3 Symmetric cells

Symmetric coin cells were assembled to measure the capacitance of the hybrid electrode. A pseudo-rectangular shape with curved corners was observed in the CP curves of the AC coin cell (Figure 3.9 a). This profile, not strictly canonical, was possibly due to the difference in solvation of $NaClO_4$ in acetonitrile as well as the different size of the anion and cation and their compatibility with the pore size of activated carbon [72, 73]. The CPs of the AC{V_{10}} hybrid coin cells show an increase in area and broad peaks that can be assigned to V_{10}-POM activity. The same is observed when the cells are polarised over an extended scan rate range (Figure 3.9 c and d).

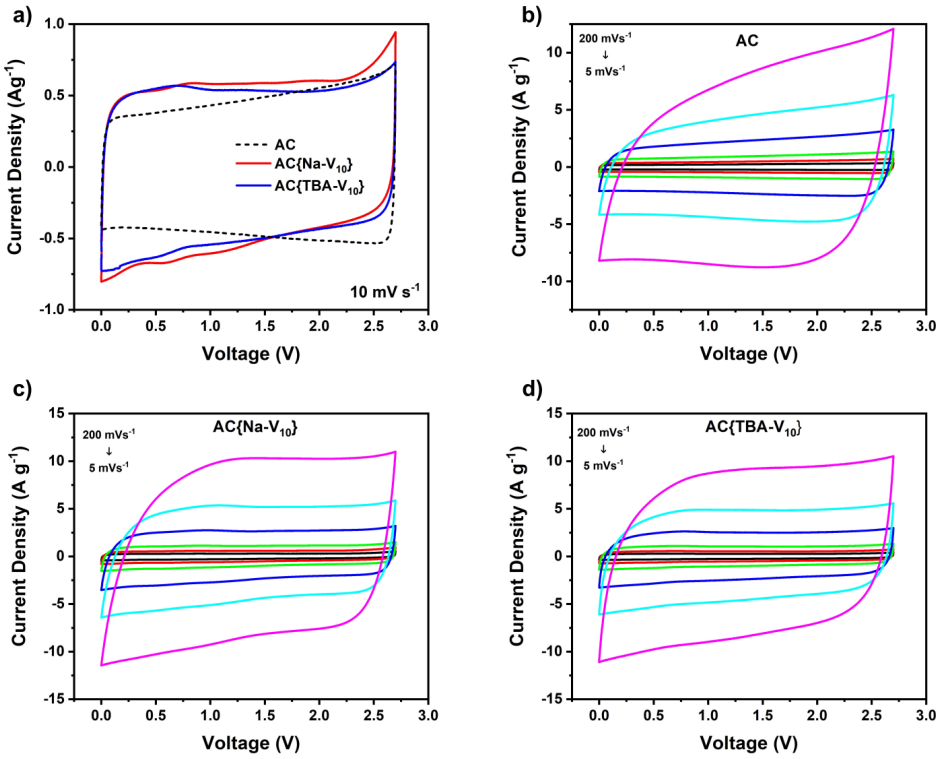

Figure 3.9: *a) Cyclic Polarisation of hybrid and AC electrodes and in 2-electrode symmetric configuration at scan rate of 10 mV s^{-1}, b), c) and d) Cyclic Polarisation of AC, AC{Na-V_{10}}, and AC{TBA-V_{10}} at various scan rates.*

The unusually good gravimetric capacitance of our hybrid materials at high rates was also demonstrated through GCD experiments. Electrode capacitance was calculated from the discharge curves and normalised with respect to active material mass in the electrode. The capacitance of the electrode (C_g) was calculated by Equation 2.7. These results are shown in Figure A.4 a, where it can be seen that the AC{TBA-V_{10}} electrode had better gravimetric capacitance than AC only at low current densities while at higher current densities it performed similar to AC electrodes. This is a practical realisation that the "kinetic match" between POMs redox activity and AC capacitive polarisation has limits. The AC{TBA-V_{10}} symmetric cell had gravimetric electrode capacitance of 70, 82, 91, 96, 101 and 112 F g^{-1} at current densities of 20, 10, 5, 2, 1, and 0.1 A g^{-1}. On the other hand, AC{Na-V_{10}} symmetric cell performed better with electrode capacitances of 79, 90, 97, 103, 106 and 116 at 20, 10, 5, 2, 1, and 0.1 A g^{-1} due to slightly lower mass of Na-cation in comparison with TBA-cation.

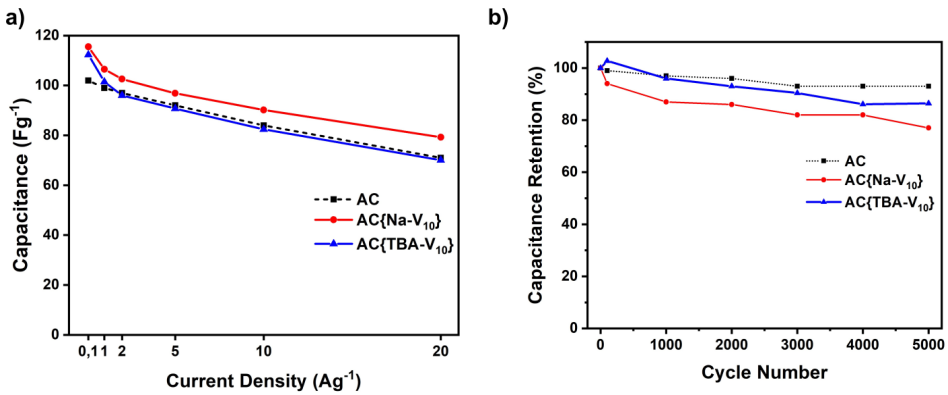

Figure 3.10: *a) Gravimetric capacitance of AC, AC{Na-V_{10}} and AC{TBA-V_{10}} electrodes at various current densities and b) Capacitance retention of symmetric cells over 5,000 cycles.*

The cell specific energy and power were calculated from Equations 2.10 and 2.11, respectively. The maximum specific energy of AC{Na-V_{10}} and AC{TBA-V_{10}} symmetric cells was found to be 29.2 and 28.4 Wh kg^{-1} as compared to 25.7 Wh kg^{-1} for AC at specific power of 68 W kg^{-1} in all three cases.

The electrodes were cycled at a current density of 5 A g^{-1}. After 100 cycles, the AC{Na-V_{10}} retained 94% of its initial capacitance. Meanwhile the capacitance retention of AC{TBA-V_{10}} electrode was found to be slightly over 100%, possibly due to the activation of the electrode upon cycling as a result of better access of electrolyte ions to the active material. After 1,000 cycles the capacitance retention of AC{Na-V_{10}} and AC{TBA-V_{10}} electrodes was found to be 87% and 96%, respectively and after 5,000 cycles it was 77% and 86% (Figure A.4 b).

Despite the significant improvement in metrics such as gravimetric capacitance, energy density and capacitance retention, it was observed that there could be a possibility to further improve the capacitance of the hybrid electrodes. Therefore, it was important to understand the processes of each electrode in a symmetric cell during the charge and discharge steps. Thus, the variation of the potential of both positive and negative electrodes vs. a reference electrode was studied in a symmetrical Swagelok cell and the results are shown in Figure 3.11 a and b. The positive electrode reached 1.4 V and the negative -1.3 V vs. reference. This was not favourable, because the positive limit was beyond the previously established 1.2 V safety limit, and the spikes detected at positive potential limits in Figure 3.6 a (three-electrode) and Figure 3.9 a (two-electrode) show that there may be spurious reactions at the AC surface when the electrodes were subjected to this higher than 1.2 V positive potential. In order to avoid this detrimental condition, we went on to design and set up asymmetric cells making a more efficient use of our hybrid materials.

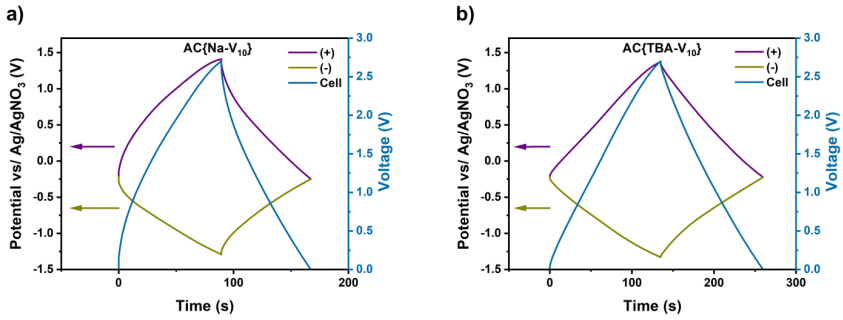

Figure 3.11: *Variation of the potential of both positive and negative electrodes, as well as the symmetric supercapacitor voltage during galvanostatic charging and discharging at 1 mA current.*

3.5.4 Asymmetric cells

The results from symmetric cells demonstrated better cyclability over the previous studies on V_{10} materials [43, 71] and proved our hypothesis for V-POMs to obtain better gravimetric capacitance than pristine AC electrodes. Nevertheless, both the capacitance and cycling of these materials could be further enhanced in asymmetric cells.

If we recall from Figures 3.6 b and c, a spiking current was observed when the positive electrode potential was pushed beyond approximately 1.2 V vs. the reference. This trend was also observed in pure activated carbon electrodes and, as mentioned before, it may be attributed to spurious reactions taking place with the electrolyte or with functional groups attached to the carbon. More importantly, it was clear that the V_{10}-POM provides more activity on the negative potentials which remained untapped in symmetric cells as the electrode potential did not extend beyond -1.3 V vs. the reference. This could be rectified in an asymmetric cell configuration by balancing the AC{V_{10}-POM} hybrid electrodes with AC. The cells were mass balanced and assembled with AC as the positive electrodes and AC{V_{10}-POM} hybrids as negative electrodes in 1 M $NaClO_4$ in acetonitrile electrolyte. The mass ratio was optimised as per Equation 3.3 [74]:

$$Q = C_{g+} m_+ U_+ = C_{g-} m_- U_- \tag{3.3}$$

The amount of charge (Q) stored in the positive and negative electrode must be the same. This is not a problem in symmetric cells where positive and negative electrodes are essentially identical and of equal mass. However, asymmetric supercapacitors need to be mass balanced to fully utilise the active materials and the voltage range. To understand the optimum mass ratio, capacitances of pure AC and symmetric AC{V_{10}-POM} hybrid cells were compared at a current density of 1 A g^{-1}. As a result, AC{V_{10}-POM}:AC mass ratio of approximately 1:1.1 was selected to prepare asymmetric cells.

Similar to the Section 3.5.3 symmetric cell study, voltage profile of each electrode vs. the reference was analysed in Swagelok cells with AC as positive and AC{V_{10}-POM} hybrid electrodes as negative. In both cases during charging, the positive electrode reaches a potential of approximately 1.1 V vs. reference electrode (Figure 3.12 a and b). Since the negative electrode potential is safely pushed down to -1.6 V in the asymmetric cells (as compared to -1.3 V in symmetric cells), the hybrid electrodes were able to effectively shift the working voltage range and improve the

utilisation of the redox activity of the V_{10}-POMs.

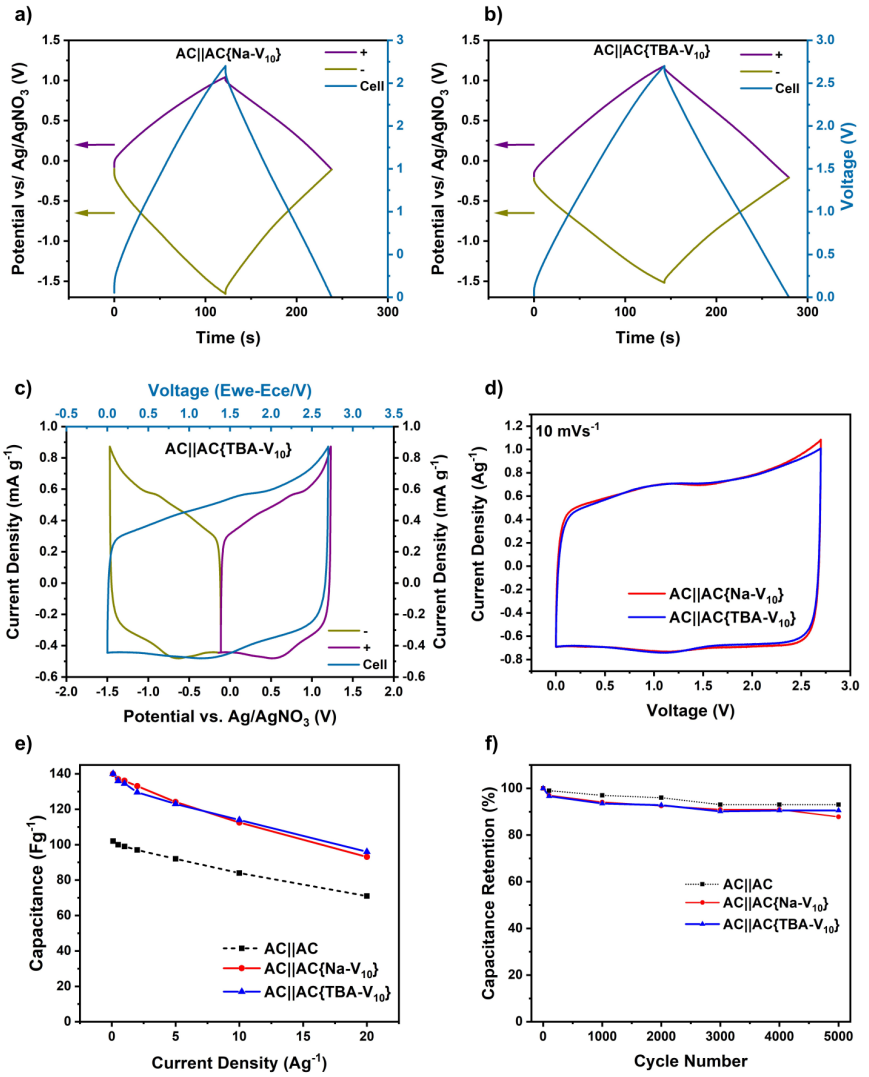

Figure 3.12: *a) and b) Variation of the potential of both positive and negative electrodes, as well as the asymmetric supercapacitor voltage during galvanostatic charging and discharging at 1 mA current. c) CVs of working positive (AC) and negative (AC{TBA-V_{10}}) electrodes and CP of the AC{TBA-V_{10}}||AC cell at 10 mV s^{-1}. d) CPs of AC{Na-V_{10}}||AC, and AC{TBA-V_{10}}||AC cells at scan rate of 10 mV s^{-1}. e) Gravimetric capacitance of AC, AC{Na-V_{10}}||AC, and AC{TBA-V_{10}}||AC cells at various current densities. f) Capacitance retention of AC, AC{Na-V_{10}}||AC, and AC{TBA-V_{10}}||AC cells over 5,000 cycles. In all cases the electrolyte was in 1 M $NaClO_4$ in acetonitrile.*

To test the performance of the asymmetric device, the electrodes were assembled in a coin cell. Figure 3.12 d shows the 2-electrode CP curves of AC{Na-V_{10}}||AC, and AC{TBA-V_{10}}||AC cells at 10 mV s^{-1}. The CP curves of the asymmetric cells were more rectangular in shape as compared to the symmetric cells and redox peaks can be seen more prominently. These improvements were further verified by the GCD results (Figure 3.12 e) in which the asymmetric cells far outperformed the symmetric cells as seen in Figure 3.13. The electrode capacitance for asymmetric cells was calculated from Equation 2.7, considering the active material mass of only the negative (AC{V_{10}-POM}) hybrid electrode. The AC{Na-V_{10}}||AC cell featured gravimetric capacitances of 93, 113, 124, 133, 136, 137 and 140 F g^{-1} and AC{TBA-V_{10}}||AC cell had 96, 114, 123, 130, 135, 136 and 140 F g^{-1} at 20, 10, 5, 2, 1, 0.5 and 0.1 A g^{-1} current densities, respectively (normalised by the mass of negative electrode). Both AC{Na-V_{10}}||AC and AC{TBA-V_{10}}||AC cells demonstrated the same maximum specific energy of 35.5 Wh kg^{-1} both at specific power of 68 W kg^{-1}.

The capacitance retention of the asymmetric cells also improved in comparison with the symmetric cells. For instance, both cells retained 97% of their initial capacitance after 100 cycles. After 1,000 cycles the capacitance retention was found to be 94% and 93% for AC{Na-V_{10}}||AC and AC{TBA-V_{10}}||AC cells respectively. Even after 5,000 cycles AC{Na-V_{10}}||AC cell retained 88% of its original capacitance whereas the AC{TBA-V_{10}}||AC cell performed even better by retaining 91% of its original capacitance (Figure 3.12 f).

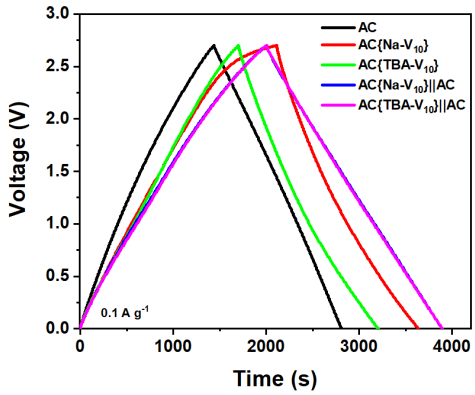

Figure 3.13: *Charge-discharge profiles of AC, AC{Na-V_{10}} and AC{TBA-V_{10}} electrodes in symmetric and asymmetric coin cells at 0.1 A g^{-1}.*

3.5.5 Volumetric capacitance

The gravimetric capacitance of POMs is generally limited due to their high molecular mass and in many cases their contributions are represented by volumetric capacitance. Therefore we also evaluated the volumetric capacitance of the symmetric and asymmetric cells using Equation 2.9.

The hybrid electrodes demonstrated clear superiority over pure AC electrodes when compared by the metric of volumetric capacitance as in this instance, the heavy mass of the V_{10}-POMs was not a limiting factor (Figure 3.14).

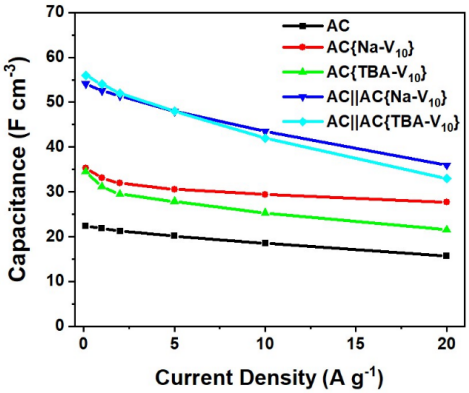

Figure 3.14: *Volumetric capacitance comparison of all AC and AC{V_{10}} electrodes in symmetric and asymmetric coin cells.*

The electrode thickness was measured by SEM images of the cross sections (Figure 3.15) by mounting the electrodes at 70° to horizontal and the measured thickness was multiplied by a correction factor of 1.06.

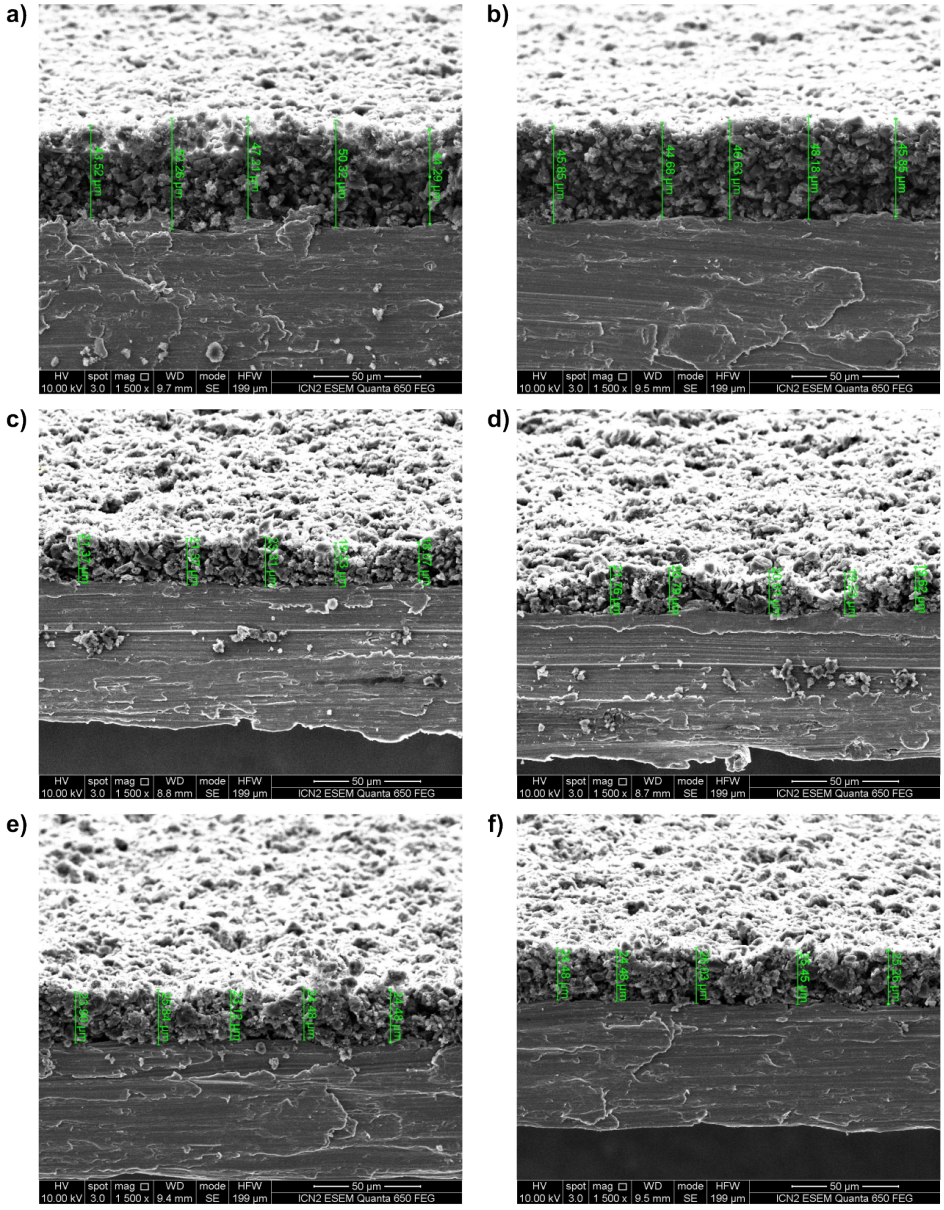

Figure 3.15: *SEM cross sections of a) and b) AC, c) and d) AC{Na-V_{10}}, e) and f) AC{TBA-V_{10}} electrodes at 70° to the horizontal.*

3.6 Discussion

V_{10}-POMs adsorbed onto porous AC have demonstrated high gravimetric capacitance and rate capabilities in organic electrolytes. The hybrid electrodes were tested in symmetric and asymmetric configurations and performed better in asymmetric configuration due to their capability to i) provide higher charge and ii) allow for an increased working voltage range thanks to a 0.3 V overpotential on the negative electrode. In asymmetric configuration after 5,000 cycles, the AC{V_{10}}||AC and AC{TBA-V_{10}}||AC electrodes could retain 88% and 91% of their capacitance, respectively. Furthermore, the asymmetric electrodes also demonstrated high specific energies of up to 35.5 Wh kg^{-1} at 68 W kg^{-1}. The gravimetric capacitance could be improved by further increasing the mass ratio between the positive and negative electrodes.

While AC{V_{10}-POM} hybridisation leads to less POM concentration in the electrode as compared to a pure V_{10}-POM electrode, it results in better utilisation of the V_{10}-POMs which are truly dispersed at a nanometric scale and therefore can react fast in a kinetically matched way with respect to AC. This leads to improved cyclability, allows for faster rates and provides better electrochemical activity compared to previously reported active materials based on bulk POM microcrystals. BET analysis demonstrated that the V_{10}-POMs were adsorbed onto the micropores of AC) which was the key to enhancing their cyclability.

Finally, our more general and important conclusion deals with the demonstration of high cyclability through the design of hybrid electrodes based on nanoclusters. The use of free (not crystallised) and dispersed electroactive nanoclusters like the present decavanadate polyoxoanions adsorbed on the pores of activated carbon allows for the harnessing of the (battery-like) electroactivity of the inorganic nanoclusters but at a rate and with the extended cyclability typical of supercapacitors. This clearly shows the way towards the development of energy storage devices with sizeable energy storage and substantially extended cycle life.

4

Hybrid carbon-tetradecavanadophosphate electrodes for energy storage

4.1 Introduction

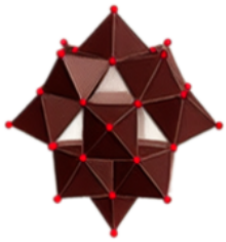

Figure 4.1: *Molecular structure representation of PV_{14}. Red dots represent oxygen atoms and V atoms occupy the centre of the polyhedra.*

$Na_5[H_4PV_{14}O_{42}]$ or PV_{14} is a hetero-polyoxovanadate with a bicapped Keggin structure, with phosphorus as a heteroatom located in a tetrahedral site at the centre of the polyanion. While limited literature is available for Vanadium based polyoxometalates in general, even fewer studies have been carried out for PV_{14} for its use as an electrochemical energy storage material. However, ex-situ XPS studies have indicated that PV_{14} is capable of transferring approximately 18 electrons during charge/discharge process. In addition it has been observed that the pristine POM's electron reaction is both diffusion-controlled and surface-controlled at high scan rates [21]. These two factors make PV_{14} an promising candidate as an active material in supercapacitors and batteries. However, the pristine POM investigated as an anode material in a sodium-ion battery demonstrated very poor cyclability of 87% after 120 cycles which is not surprising for crystalline POM electrodes. To resolve this issue, PV_{14} was also investigated in an aqueous redox-flow battery as a catholyte with high power and capacity as well as minimal capacity loss [41]. The information from these two studies indicates that while PV_{14} can be a promising material

for supercapacitors due to its relatively low mass, high electrochemical equivalent and high electron transfer capabilities, improving its cyclability would be the key challenge to overcome. The solution to this issue could be hybridising PV_{14} with AC by adsorbing the POM in AC pores, as we demonstrated for V_{10} in the previous chapter. It is already known that isolating POMs by anchoring them into AC pores allows better electrolyte accessibility to the active species, prevents them from dissolving into the electrolyte thereby improving their cyclability and enables fast electron transfer (a hard challenge in the case of extended crystalline materials) [15]. However, as we will explain below, implementing this "easy solution" proved itself an arduous task.

In this chapter we first describe the synthesis and characterisation of the different AC{PV_{14}} hybrid materials via common techniques such as XRD, FTIR, NMR, etc. We will discuss how, during the characterisation process, we discovered and proved the partial decomposition of the PV_{14}-POM into other vanadate species. We then will describe our attempts to find out the reasons and to eliminate this degradation of the POM specific to our hybridisation process. Finally, since the degraded hybrid materials contained electroactive PV_{14} and V_{10} species, we carried out and present here electrochemical tests in three-electrode Swagelok cells and two-electrode coin cells to measure the performance of these bi-composite electrodes.

4.2 Preparation of Sodium tetradecavanadophosphate (PV_{14}) and AC{PV_{14}} hybrids

4.2.1 Sodium tetradecavanadophosphate (PV_{14})

Pure real formula PV_{14} was prepared using the methodology from Selling et. al. [75]. $NaVO_3$ (61 g) was dissolved in DI water (350 ml) by boiling the solution. Hydrogen peroxide (H_2O_2) (50 drops) was added to the hot solution to oxidise V^{4+} to V^{5+}. The solution was boiled for another hour to decompose excess H_2O_2 and then cooled to room temperature. Small impurities were vacuum filtered through a fine porosity membrane and 85.4% (w/w) phosphoric acid (H_3PO_4, 14.3 g) was added to the filtered $NaVO_3$ solution. The pH of this solution was lowered to 2.3 with concentrated HCl and stirred for 24 h. The pH was readjusted to 2.3 and stirred for another 24 h. NaCl was added to this as saturated solution (350 ml). The crystals were collected by vacuum filtration and washed with cold DI water (50 ml) and dried in air.

Table 4.1: *Details of different AC{PV_{14}} hybrid syntheses.*

Sample Name	AC dispersed in 100 ml H_2O (g)	$NaVO_3$ dispersed in 100 ml H_2O (g)	H_3PO_4 (ml)	Hybrid Material Weight (g)	% POM adsorbed by mass
AC{PV_{14}-39}	2.0	2.0	0.28	3.27	39%
AC{PV_{14}-52}	2.0	6.1	0.85	4.17	52%
AC{PV_{14}-47W}	2.0	6.1	0.85	3.75	47%
AC{PV_{14}-80}	2.0	17.5	2.52	9.79	80%

4.2.2 In-situ preparation AC{PV_{14}} hybrids

The in-situ syntheses of different AC{PV_{14}} hybrids were performed in a similar manner as those of AC{Na-V_{10}} hybrids. The ratios of $NaVO_3$ to H_3PO_4 were maintained as per the pure PV_{14} synthesis. AC (2 g) was dispersed in DI water (100 ml) by bath sonication for 30 min and then stirred. Meanwhile $NaVO_3$ (as per Table 4.1) was separately dissolved in DI water (100 ml) by boiling the solution. The $NaVO_3$ solution was slowly cooled down to room temperature, added to the AC dispersion and stirred. H_3PO_4 (as per Table 4.1) was added to the AC-$NaVO_3$ dispersion. Concentrated HCl was added dropwise to reduce the pH to 2.3. The dispersion was stirred for approximately 24 h after which the pH was readjusted and then stirred again for 24 h. The AC{PV_{14}} hybrids were isolated through vacuum filtration. Due to the sensitivity of PV_{14} to the pH of the solution, the isolated hybrids were not washed except in the case of AC{PV_{14}-47W}. The AC{PV_{14}-47W} sample followed the same synthesis as AC{PV_{14}-52}, however it was washed with 325 ml acetonitrile to try and remove some excess POM without affecting the pH or introducing reactive species. The solids were dried in vacuum oven at 80 °C overnight. The final quantities of hybrid materials are provided in Table 4.1.

4.2.3 Ex-situ preparation of AC{PV_{14}} hybrid

AC (2 g) was dispersed in DI water (100 ml) by bath sonication for 30 min and then stirred. Meanwhile $NaVO_3$ (6.1 g) was separately dissolved in DI water (100 ml) by boiling the solution. The $NaVO_3$ solution was slowly cooled down to room temperature and H_3PO_4 (0.85 ml) was added to it. Concentrated HCl was added dropwise to reduce the pH to 2.3. The solution was stirred for approximately 24 h after which the pH was readjusted and then stirred again for 24 h (sample A). After the formation of PV_{14}, this solution was added to the AC dispersion and stirred for 6 h after which the pH was readjusted. The dispersion was stirred for another

10-12 h, and the pH was observed to be stable (Sample B). This dispersion was vacuum filtered and the filtration solution was collected as Sample C. The isolated solid hybrid material was dried at 80 °C in a vacuum oven overnight to remove excess water (Sample D).

4.3 Electrode preparation and cell assembly

The AC{PV_{14}-39} and AC{PV_{14}-52} slurries were prepared by mixing the hybrid material, carbon black and PVDF in the ratio 80:10:10 in NMP. The AC electrodes were prepared by mixing AC (YP-80F), CSP and PVDF in the ratio 90:5:5 in NMP. The pure PV_{14} electrodes were prepared by mixing the PV_{14}-POM, CSP and PVDF in the ratio 70:20:10 in NMP. The slurries were stirred for 6 h, bar coated onto aluminium foil and dried in vacuum at 80 °C to evaporate NMP. Any remaining water from the POMs was assumed to be extracted by NMP and then evaporated during the drying process. Electrodes of 14 mm (coin cells) and 10 mm (Swagelok cells) diameter were cut and pressed (3 t, 5 s) and assembled in symmetrical coin cells in an argon filled glove box with a Whatman 4 separator and 1 M $NaClO_4$ in acetonitrile as electrolyte.

4.4 Characterisation of AC{PV_{14}} hybrid materials

As described in detail in Chapter 3, the diffraction patterns of V-POMs can be quite variable depending on the extent of lattice water molecules in the crystal structure leading to different levels of amorphisation of the POM. Thus, **XRD** was primarily used to confirm the presence or lack of extended crystallised domains of PV_{14}-POMs in the hybrid materials. Several different in-situ synthesis were made to adsorb PV_{14} on AC pores. The percentage of the POM adsorbed on AC is given in Table 4.1 and the corresponding XRD patterns are shown in Figure 4.2. Sample AC{PV_{14}-39} had the lowest concentration of precursor material $NaVO_3$ and subsequently PV_{14} and its diffraction pattern showed broad peaks indicating that there were no bulk microcrystals.

When the concentration of PV_{14} was increased (AC{PV_{14}-52}), clear sharp peaks were observed, indicating the presence of crystallised domains in the material. This would imply that rather than adsorbing into the pores of the carbon, a significant part of the POM remained on the surface of AC in the form of crystals. To remove these clusters we first attempted to wash the hybrid material with DI water which was acidified to pH 2.3 using HCl. But this resulted in the reaction of

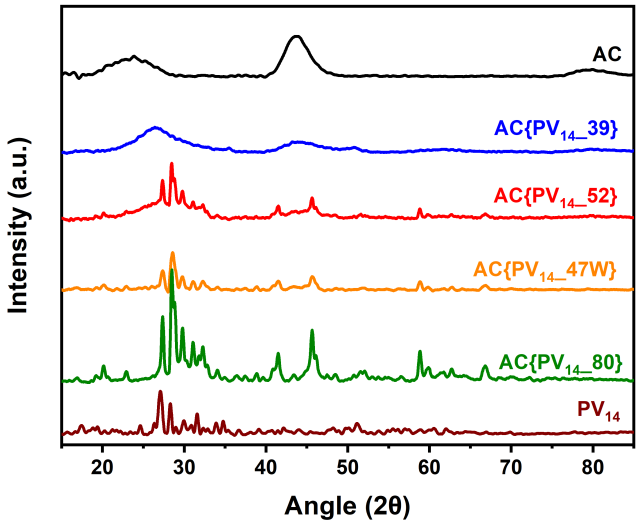

Figure 4.2: *XRD patterns of AC, PV_{14} and AC{PV_{14}} hybrid materials with different concentrations of PV_{14} adsorbed on carbon pores.*

the POM with the acid to produce other compounds which were visually verified due to the transition of the black hybrid material into a green-black material [76]. Therefore the other approach was to wash with an organic solvent like acetonitrile. We initially attempted to wash the hybrid material until a colourless filtrate was obtained as it would indicate the removal of all un-adsorbed POM from AC surface. However due to the low solubility of the POM in acetonitrile, even after washing with 325 ml acetonitrile, a yellow-ish colour in the filtrate was observed. Thus we decided to stop the washing at this moment and continue the characterisation of this hybrid material (AC{PV_{14}_47W}). As expected, the material still showed sharp peaks indicating crystalline domains. The final AC{PV_{14}} hybrid material synthesised was AC{PV_{14}_80} with the POM constituting 80% of the total mass. The diffraction pattern of this material showed the clearest peaks and was very similar to the pure POM.

Since we know that large crystals or POM clusters translate into slow diffusion of ions and poor conductivity associated with conventional battery materials, it is expected that presence of large crystals could possibly lead to poor performance expected from supercapacitors [66]. However, our previous experimental experience also showed that V-POMs have much higher conductivity, and therefore small amounts of crystallinity or bulk micro-crystals may not significantly impede the

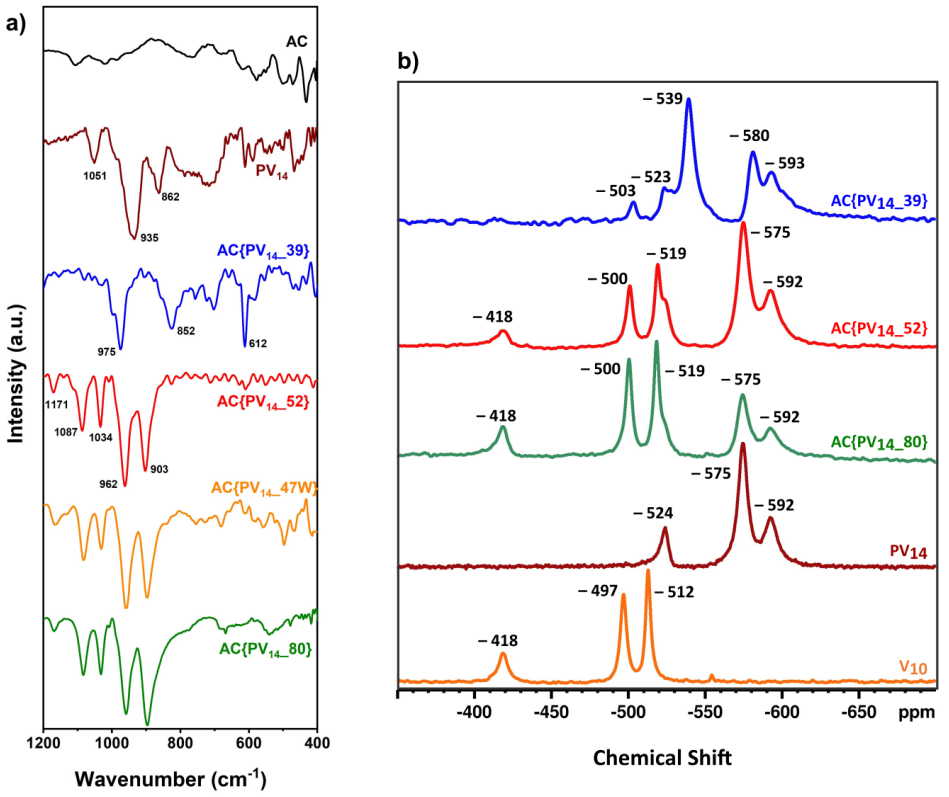

Figure 4.3: *a) FTIR and b) NMR patterns of AC{PV_{14}} hybrid materials.*

performance of the V-POMs. Thus, it was considered worthwhile continuing the initial exploration of hybrid materials and optimising the AC{PV_{14}} adsorption in the future.

FTIR was used to further evaluate the adsorption of PV_{14} on AC (Figure 4.3 a). The IR spectrum of pure PV_{14} shows a clear peak at 1051 cm^{-1} previously assigned to a P-O stretching vibrational mode [21, 65] while the other bands at 935 cm^{-1}, 862 cm^{-1}, etc. correspond to V-O vibrations. Interestingly the P-O stretching was not observed in AC{PV_{14}_39} and the pattern resembled closely to that of Na-V_{10}. In the remaining hybrid materials, the P-O peak was red shifted 1034 cm^{-1} and the additional peaks between 1200 and 1000 cm^{-1} could be due to the presence of different phosphates in the hybrid materials [77–79].

As a result of the discrepancies observed in FTIR studies, **^{51}V-NMR** was considered as an alternative method to verify the presence of PV_{14} as well as to identify any possible degradation of the POM. If the POM was well adsorbed on the AC pores, it would not be possible to perform a standard ^{51}V-NMR since the POM concentration would be too low and get masked by the carbon particles. However, in our case the presence of crystals on AC surface proved to be an advantage as the POM could be leeched and filtered out from AC in a D_2O solution. Figure 4.3 b shows the NMR spectra of all AC{PV_{14}} hybrid materials except AC{PV_{14}-47W}.

The NMR spectrum of pure PV_{14} crystals shows characteristic peaks at -524, -575 and -592 ppm [75, 80]. However, all the hybrid materials show two additional peaks at approx -418 and -497 ppm showing a clear partial degradation of PV_{14} into V_{10}. In addition, the compound AC{PV_{14}-39} shows the presence of pervanadyl species (VO_2^+) at -539 ppm [75]. This was unexpected as pervanadyl should be formed at pH values < 1.7. In addition, the PV_{14} POM is widely known to be extremely stable at a pH of 2.3 in previously reported literature [41, 75] and the same was observed during our synthesis of the pure PV_{14} POM. In fact, at appropriate concentrations, the POM has been known to spontaneously reassemble at pH 2.3 after decomposition in acidic or alkaline pH [41].

To understand the reason for this degradation and to possibly overcome it, we decided to keep the same same concentration of POM as in the case of AC{PV_{14}-52} but deviate from the in-situ synthesis to ex-situ. Since limited literature was available, our first hypothesis was that due to the presence of $NaVO_3$ in the hybrid dispersion with AC, $NaVO_3$ may be partially adsorbed on AC and then not react with H_3PO_4 to form PV_{14} species and instead form V_{10} species. By preparing PV_{14} ex-situ we might eliminate the presence of V_{10}. The concentration of the starting compound $NaVO_3$ was kept the same as in during the synthesis of AC{PV_{14}-52} because this material had allowed us to see clear NMR signals with low noise. Therefore a pure PV_{14} solution was prepared as described in Section 4.2.3 over a 65 h time period.

The results of this experiment are presented in Figure 4.4 a. Spectrum A shows the NMR of an an aliquot taken from this pure PV_{14} solution, which showed the presence of only PV_{14} species at pH 2.3. Spectrum B shows the NMR spectrum of the aliquot taken from the dispersion of AC and the previously made PV_{14} (after 65 h) with pH readjusted to 2.3. The solution still showed the presence of only PV_{14} species in the dispersion. Afterwards the dispersion was filtered (and not washed) to isolate the hybrid material. The filtrate was collected and its corresponding

spectrum is seen from Spectrum C which again, was consistent with that of pure PV_{14}. The solid was dried and dispersed in D_2O to leech out excess POM via filtration. As observed previously, the NMR spectrum deviated from that of the pure PV_{14}-POM and was similar to the ones observed from Figure 4.3 b. The corresponding SEM images from this synthesis are later presented in Figure 4.5 c, d and e. This means that the in-situ synthesis was not the issue and there must be another explanation.

PV_{14} is known to be stable at around 100 °C and the same was observed during the TGA of the hybrid material, as shown in the next section. Nevertheless, previous studies found that temperature can affect its crystal structure [68] and boiling the solution can result in its decomposition into V_2O_5 and V_{10} (in addition to residual dihydrogenphosphate ions) [75]. Therefore, to eliminate any external factors during the processing of the material in our lab, we performed a temperature study of pure PV_{14} and AC{PV_{14}_52} hybrid. Both materials were dried at room temperature (RT) of ca. 22-25 °C. Both materials were also dried in vacuum at 25 °C, 50 °C and 80 °C. The NMR spectra show that these drying conditions have no impact on PV_{14} crystals whereas the hybrid AC{PV_{14}_52} degraded under all drying conditions.

Since V_{10} and PV_{14} can exist in equilibrium during the formation of PV_{14}, it could not be ruled out that in certain conditions, the V_{10} species could be observed in the solution. Upon further investigation into the degradation of PV_{14} species, it was understood that the formation of stable PV_{14} required two main conditions:

1. An excess of phosphate in the solution to avoid precipitation into V_2O_5 [75],

2. The correct pH at a given concentration [80].

Initially, we had assume that condition 1 was being met in our syntheses as there is evidence of only PV_{14} species in both pure and hybrid solutions pre-isolation of the solid materials. This brought us to the conclusion that AC must have had a major role to play and that PV_{14} was likely degrading at the carbon surface. The reason for this could be the slightly basic pH of the AC YP-80F used. We hypothesise that even though the pH of the solution was kept at pH 2.3 for 48 hours, the pH inside the macro-/micro-pores of the AC was not significantly altered and only reduced to between pH 3-5, where V_{10} species are known to be stable [37]. This could be ascertained by treating the AC first with a strong acid such as concentrated HCl (also used to acidify the PV_{14} solution during synthesis) and then carrying out the hybridisation.

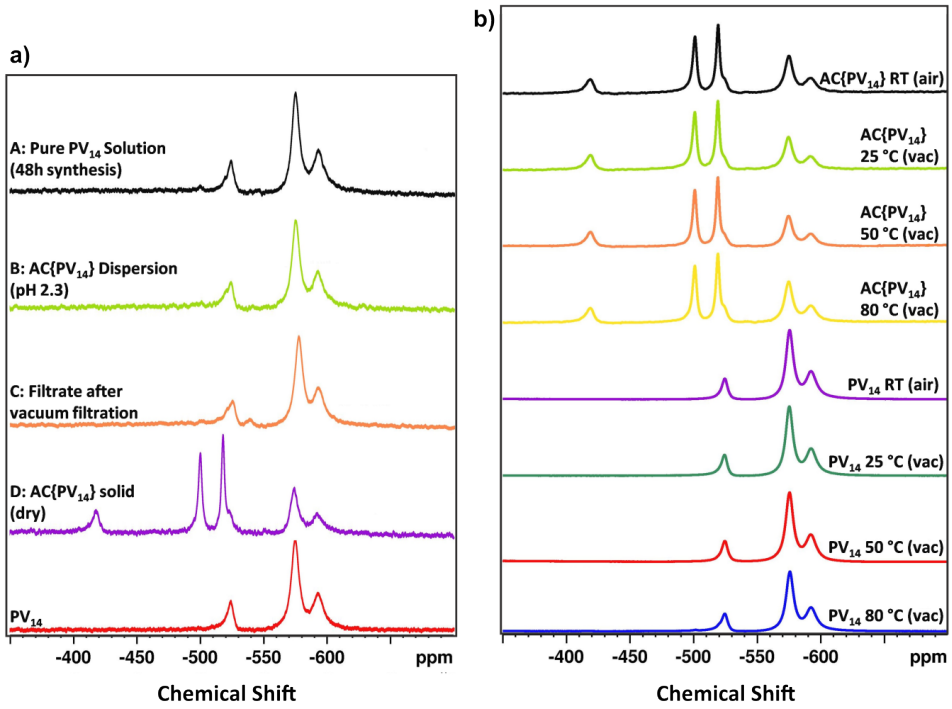

Figure 4.4: *NMR patterns of AC{PV_{14}} hybrid materials during various stages of synthesis.*

A similar challenge was mentioned by Domaille et. al. where both V_{10} and PV_{14} species were observed during the synthesis of pure PV_{14}-POM and the issue was resolved by lowering the pH of the solution to 1.7 [80]. As a result, modifying the present in-situ method by lowering the pH of the hybrid dispersion from 2.3 to 1.7 may also be a possible solution. Nevertheless, during this pH lowering process, a balance between the pH and phosphate concentration would be required to prevent the formation of pervanadyl species. These observations in the literature added strength to our hypothesis. However, due to time limitation, we decided to carry out these modified syntheses in future experiments.

At the same time, the hybrid materials prepared here contain Na-V_{10} and PV_{14} which are both electroactive species. Therefore, we decided to continue the examination of these materials in an attempt to explore whether a multi-component electrode containing both vanadates could lead to useful energy storage.

Figures 4.5 a and b show the **SEM** images of pure PV_{14} crystals dried under ambient air conditions. These were observed to be formed by agglomerates (ca. 50 to 200 μm) of hexagonal primary crystals a few microns in size. SEM images in Figures 4.5 c, d and e correspond to samples taken from the AC{PV_{14}} hybrid synthesis carried out for degradation analysis using NMR. In all cases, aliquotes were taken from solutions and dried on a silicon tab without filtration.

Figure 4.5 c shows the SEM of the dried droplet taken from the pure PV_{14} solution (synthesis A) and shows that the POM formed hollow cuboids. Figure 4.5 d corresponds to the dried aliquote taken from sample B dispersion (pH 2.3). It is clear that the phosphate impurities precipitate on AC. The final dried solid D: AC{PV_{14}} is shown in Figure 4.5 e and the impurities are clearly visible on carbon surface.

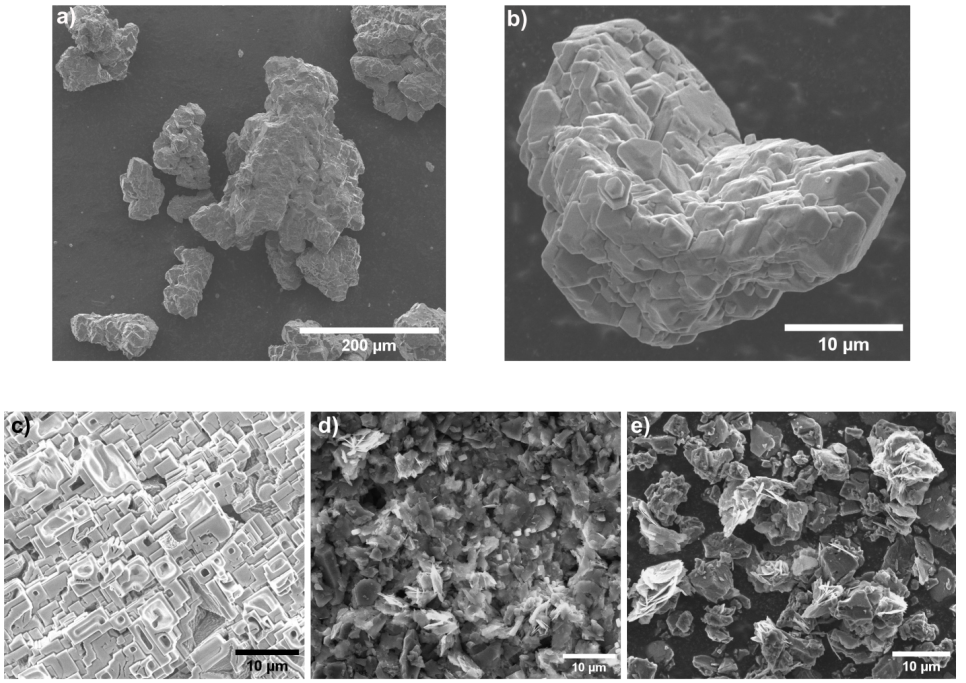

Figure 4.5: *SEM images of: a) and b) pristine PV_{14} crystals, c) dried droplet from PV_{14} solution A, d) dried droplet from AC{PV_{14}} dispersion B, and e) isolated solid AC{PV_{14}} powder D.*

Next, we compare the SEM images of the (AC{PV_{14}-52} and AC{PV_{14}-39}) hybrid powders prepared by in-situ method. Figures 4.6 a and b show the hybrid powder obtained after the synthesis of AC{PV_{14}-52} where multiple impurities of varying sizes can be detected interspersed between AC particles. Figure 4.6 c shows the SEM image of the AC{PV_{14}-52} electrode after the drying process. The same impurities can again be clearly seen which means they are insoluble in NMP. Interestingly, AC{PV_{14}-39} electrode did not show any sizeable amount of these phosphate impurities (at least not in significant amounts) (Figure 4.6 d), in good agreement with FTIR and NMR. At this point we might recall that AC{PV_{14}-39} sample was the only one prepared at greater dilution, and this might have led to a "failed" synthesis leading to a mixture of PV_{14}, V_{10} and pervanadyl ion in solution.

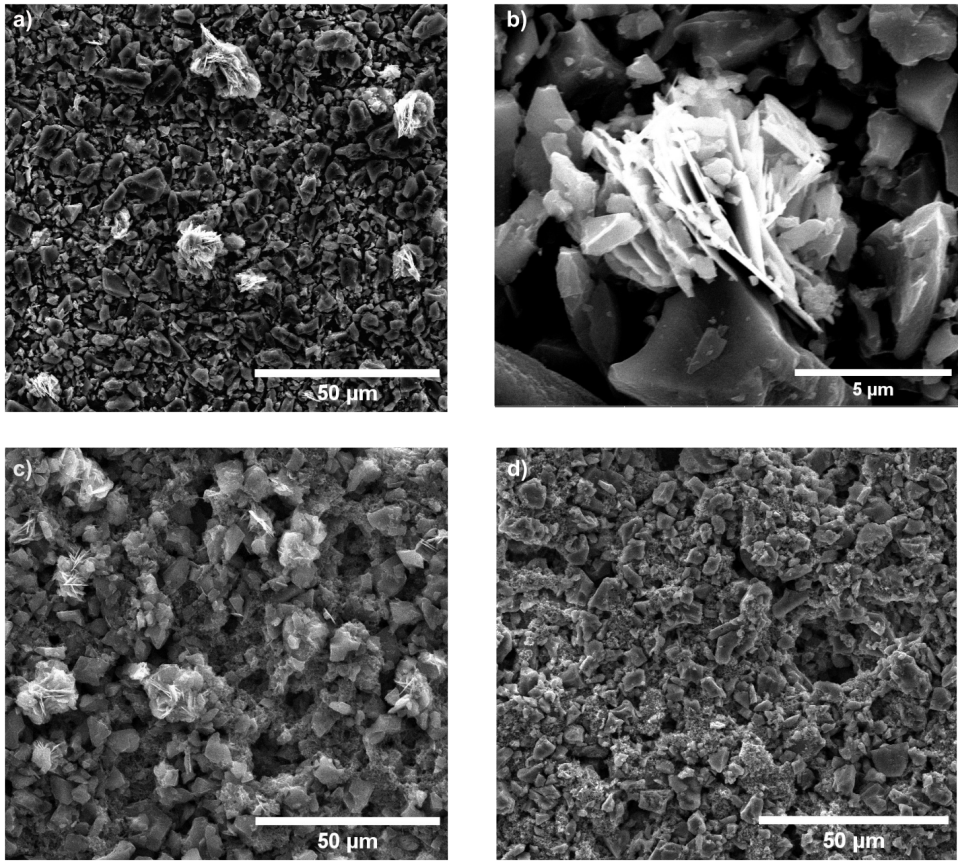

Figure 4.6: *SEM images of a) AC{PV_{14}-52} hybrid powder, b) crystal impurity present in AC{PV_{14}-52} powder, c) AC{PV_{14}-52} electrode, d) AC{PV_{14}-39} electrode.*

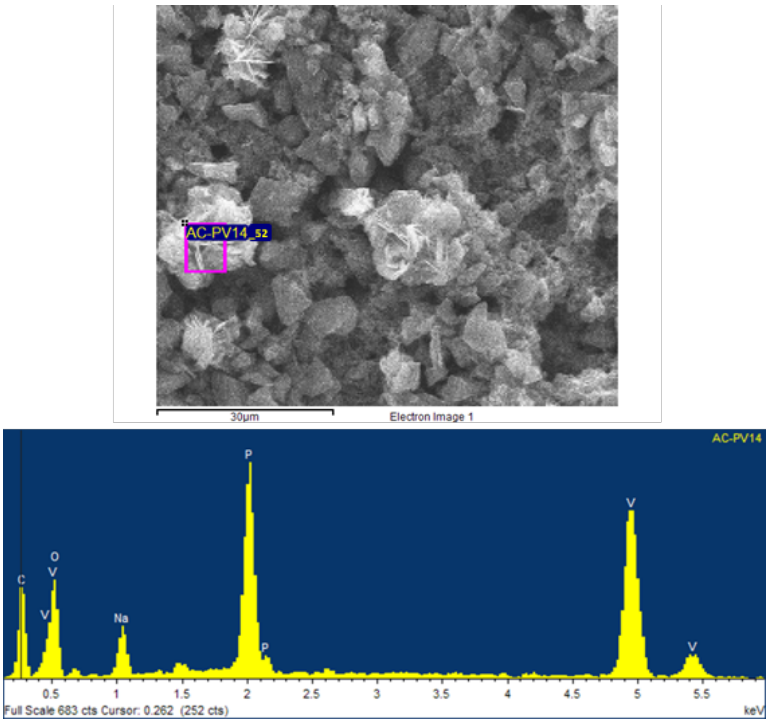

Figure 4.7: *EDX spectrum of the impurity in AC{PV_{14}-52} hybrid material.*

Table 4.2: *Quantitative analysis report for the EDX spectrum.*

Element	**C**	**O**	**Na**	**P**	**V**	**Total**
Weight%	50.28	33.19	2.80	6.06%	7.67	100

Figure 4.7 shows the EDX spectrum of the impurity observed in the PV_{14}-52} electrode and confirms the presence of phosphorous in the impurities.

The hybrid material AC{PV_{14}-52} was selected to study the thermal properties by **TGA** (Figure 4.8 a). The pristine AC underwent a slight weight loss of 1.8% before 500 °C due to the removal of adsorbates. The large drop in its mass centred at 640 °C marked its combustion and at 900 °C only 1.3% of weight was left as ashes. One sharp peak corresponding to its combustion can be seen from the dw/dT curve (Figure 4.8 b). In case of AC{PV_{14}-52} hybrid, 5% of weight loss was observed at around 200 °C, possibly due to the presence of small amount of crystallisation water and adsorbates on AC. Its decomposition takes place in 2 main steps with complete decomposition at 480 °C and 48% of the original weight remaining in ashes. It is

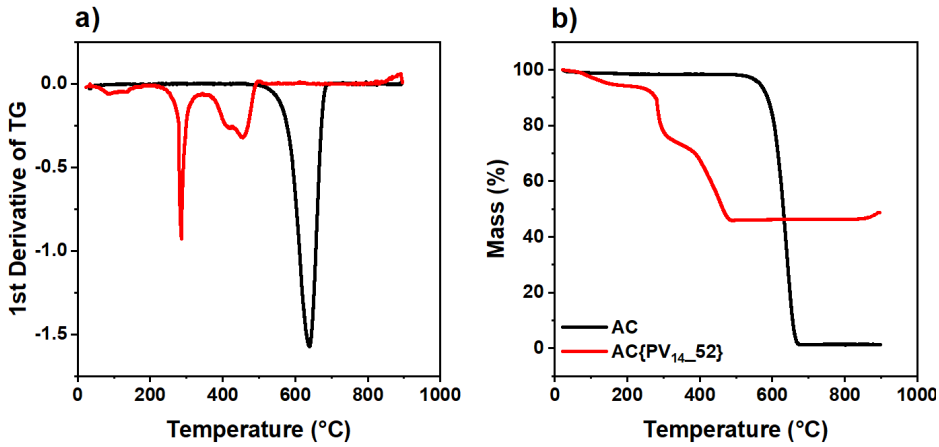

Figure 4.8: *a) TGA and b) corresponding dW/dT curves of pure AC and AC{PV_{14}-52}.*

clear that the V-cluster acts as a catalyst for the oxidation of AC at temperatures above 200 °C and the presence of PV_{14} and V_{10} POMs in AC lowers its combustion temperature. This behaviour has also been previously observed for other AC-POM hybrid materials [69, 70].

Due to the challenges associated with our AC{PV_{14}} hybrid synthesis namely, (i) partial degradation of PV_{14} into V_{10} and (ii) possible formation of Na_2HPO_4/Na_3PO_4 during synthesis, it was difficult to quantify the mass of POM adsorbed in the hybrid material using TGA.

The effect of adsorption of the degraded PV_{14}-POMs on the porous structure of AC was evaluated by **BET** N_2 adsorption and desorption for the sample AC{PV_{14}-52} as shown in Figure 4.9 a. The curves can be classified as Type I isotherms as per the IUPAC classification, signifying a microporous structure. The adsorption of "PV_{14}" into the micropores of the AC can be confirmed by the reduction in the total pore volume (Table 4.3) which was recorded as 1.36 cm^3 g^{-1} for pristine AC, and 0.53 cm^3 g^{-1} for AC{PV_{14}-52}. The BET N_2 adsorption/desorption isotherms recorded the surface area of AC as 2136 m^2 g^{-1}, while the surface area of AC{PV_{14}-52} was reduced to 652 m^2 g^{-1}, which was expected due to the combination of two reasons: i) the partial blocking of pores by the POM adsorption and ii) the higher mass of the V-POMs in comparison with AC, which can be problematic when normalising per mass.

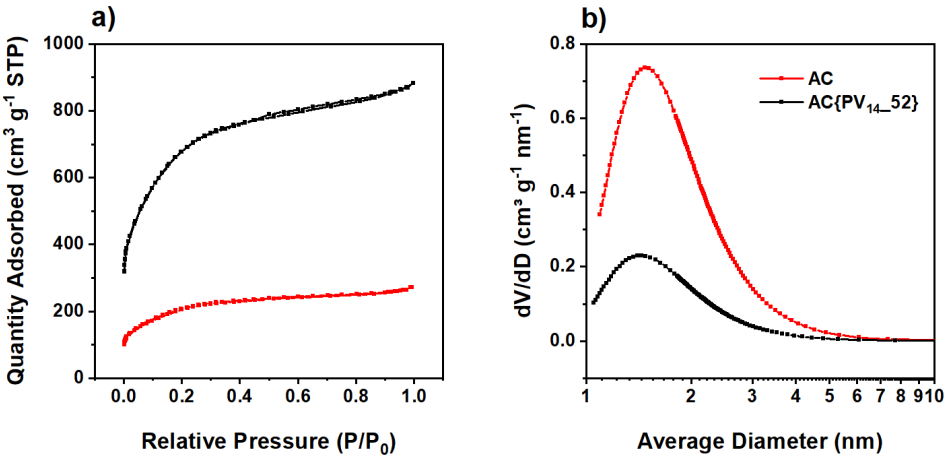

Figure 4.9: *a) N_2 adsorption/desorption isotherms and b) differential pore volume vs. pore width for AC (black) and AC{PV_{14}-52} (red) powders.*

Table 4.3: *Porosity properties of AC and AC{PV_{14}-52}.*

Sample	S_{BET}[a] (m^2 g^{-1})	V_{Total}[b] (cm^3 g^{-1})	V_{micro}[c] (cm^3 g^{-1})
AC	2136	1.365	0.41
AC{PV_{14}-52}[d]	652	0.53	0.11
AC{PV_{14}-52}[e]	1359	1.11	0.24

[a] Specific surface area determined by BET method. [b] Total pore volume.
[c] Micropore volume. [d] Normalized by total mass. [e] Normalized by mass of AC.

In comparison with pristine AC, a significant decline in surface area of AC{PV_{14}-52} (69%) and total pore volume (61%) was observed. On the other hand, its micropore volume dropped by 73%. Thus, a large amount of the "PV_{14}" POMs could be assumed to be adsorbed in AC pores. This was further supported by the fact that upon normalisation of micropore volume by the mass of only AC (instead of the total sample mass), a large drop in micropore volume (43%) was also observed. Thus, most of the "PV_{14}" POM could be considered adsorbed in the micropores of the sample since a reduction in micropore volume was detected irrespective of the mass normalisation. Table 4.3 provides the surface area, total pore volume and micropore volume of pristine AC and AC{PV_{14}-52} hybrid, with all values normalised by the total mass of the material as well as by the mass of AC in the sample.

4.5 Electrochemical characterisation

Figure 4.10 a shows the CVs of pristine AC and PV_{14} electrodes as well as the hybrid AC{V_{10}} and AC{PV_{14}-52} electrodes at 10 mV s^{-1}, while Figure 4.10 b shows the CVs of hybrid AC{PV_{14}-52} electrode at various scan rates in three-electrode configuration in a Swagelok cell with 1 M $NaClO_4$ in acetonitrile as the electrolyte. In both cases, carbon cloth loaded with AC served as the counter electrode and $Ag/AgNO_3$ as reference electrode. The supporting electrolyte for reference electrode was 0.1 M $TEABF_4$ and 0.01 M $AgNO_3$ in acetonitrile.

Four broad peaks can be seen from the CV of pristine PV_{14} electrode. In the CV of hybrid electrode, broadly 4 peaks could be ascertained, however, their positioning seems to be very different from that of the pristine electrode. It is well known that hybridisation may lead to some peaks becoming broader and difficult to distinguish from the pristine POM. However, upon closer examination, the CV profile of the AC{PV_{14}} hybrid was quite similar to that of the AC{V_{10}} hybrid. This was not surprising given the observations from the NMR spectra and confirmed the partial degradation of PV_{14} into V_{10} during the hybridisation.

Nevertheless, as mentioned before, both POMs are electroactive in nature and capable of providing fast electron transfer in organic electrolytes. Hence, symmetric cells of AC{PV_{14}} hybrids were assembled and their performance was first tested in 1 M $NaClO_4$ in acetonitrile. To this end, AC{PV_{14}-52} was first tested in a

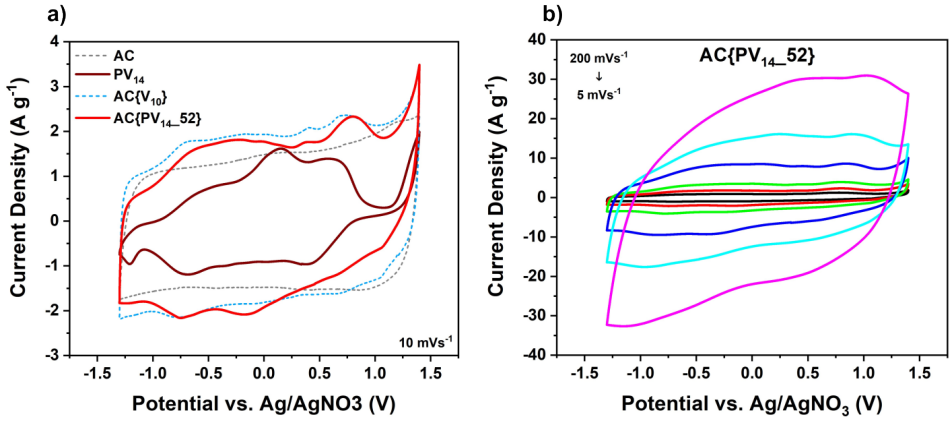

Figure 4.10: *a) 3-electrode CVs of pristine AC and PV_{14} electrodes as well as hybrid AC{V_{10}} and AC{PV_{14}-52} electrodes, b) 3-electrode CVs of AC{PV_{14}-52} electrode at scan rates of 200, 100, 50, 20, 10 and 5 mV s^{-1}.*

symmetric 3-electrode configuration in a Swagelok cell to understand the processes in each electrode during the charge and discharge steps. The variation of the potential of both positive and negative electrodes vs. the reference electrode can be seen from Figure 4.11 a, which shows that the positive electrode reached 1.4 V and the negative -1.3 V vs. reference.

To test the performance of the electrodes in a device, all AC{PV_{14}} hybrid electrodes were assembled in coin cells and their cyclic polarisation is shown in Figure 4.11 b. Broad peaks and an increase in area can be observed due to POM activity in all electrodes when compared to that of pristine AC. However, a deviation from the shape of AC electrode is also seen in case of AC{PV_{14}} hybrid electrodes possibly due to the modification of the porous structure of AC as a result of adsorption of the POMs. In addition, the difference in solvation of $NaClO_4$ in acetonitrile as well as the different size of the anion and cation, and their compatibility with the pore size of the hybrids, could lead to this distorted CP shape [72, 73].

The gravimetric electrode capacitance of all AC{PV_{14}} hybrids improved at low current densities. However, this improvement fades at higher current densities since the concentration of crystalline POMs and impurities in the hybrid materials were also high (except for AC{PV_{14}-39}). This explanation may indicate why AC{PV_{14}-39} electrode showed the best gravimetric capacitance followed by AC{PV_{14}-52} and AC{PV_{14}-80}. Interestingly, washing the AC{PV_{14}-52} with large amounts of acetonitrile to result in AC{PV_{14}-47W} did not show any improvement. This may be explained due to the fact that these inorganic POMs and the impurities have extremely low solubility in acetonitrile. Therefore, the washing process did not get remove surface-grown microcrystals in the hybrid material. The symmetric cells with AC{PV_{14}-52}, AC{PV_{14}-47W}, and AC{PV_{14}-80} show maximum specific energies of 34, 30 and 27 Wh kg^{-1}, all at the specific power of 68 W kg^{-1}. AC{PV_{14}-39} demonstrated the maximum specific energy of 33 Wh kg^{-1} at a specific power of 81 W kg^{-1}.

The capacitance retention of AC{PV_{14}-39} and AC{PV_{14}-52} was tested over 5,000 cycles. After 100 cycles, a small increase in capacitance was observed for AC{PV_{14}-39} electrode, likely due to the improved penetration of electrolyte into the carbon pores. Meanwhile, AC{PV_{14}-52} electrode retained 91% of its capacitance over 100 cycles. After 2,000 cycles there is a drastic drop in capacitance of both electrodes and they retain only 81% of their capacitance. After 5,000 cycles, this figure further reduces to 73% and 72% for AC{PV_{14}-39} and AC{PV_{14}-52},

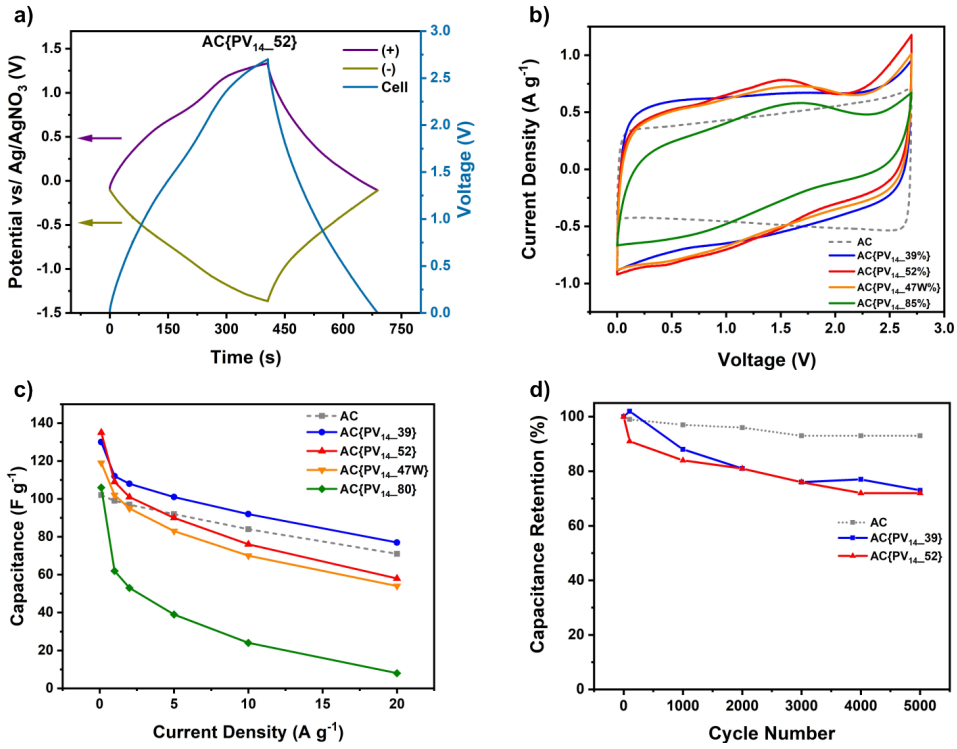

Figure 4.11: *a) Variation of the potential of both positive and negative electrodes, as well as the symmetric supercapacitor voltage during GCD measurements at 1 mA for AC{PV_{14}-52} b) CP of hybrid and AC electrodes in two-electrode symmetric configuration at scan rate of 10 mV s^{-1}, c) Gravimetric capacitance of AC, and hybrid AC{PV_{14}} symmetric cells, d) Capacitance retention of AC and AC{PV_{14}} symmetric cells over 5,000 cycles. In all cases the electrolyte was 1 M $NaClO_4$ in acetonitrile.*

respectively. Thus, the cyclability of the hybrid materials improved significantly over previous studies. But, the cells were not able to show even better capacitance retention since the POMs were partially adsorbed on the AC micropores and also precipitated on the surface of AC as bulk micro-crystals. Hence, the hybrid material cannot be expected to perform in the same manner as other similar AC-POM hybrids (also synthesised and tested in this thesis). It is also quite likely that as a result of these bulk micro-crystals, these un-adsorbed POMs could eventually dissolve into the electrolyte creating shuttle ions upon repeated cycling. Therefore, as seen in previous studies, it leads to reduced capacitance over time.

AC{PV_{14}-39} and AC{PV_{14}-52} electrodes were also compared on a volumetric basis (Equation 2.9). The volumetric capacitance of the AC{PV_{14}} hybrid electrodes was observed to be more than twice that of AC electrodes at 0.1 A g^{-1} as shown in Figure 4.12.

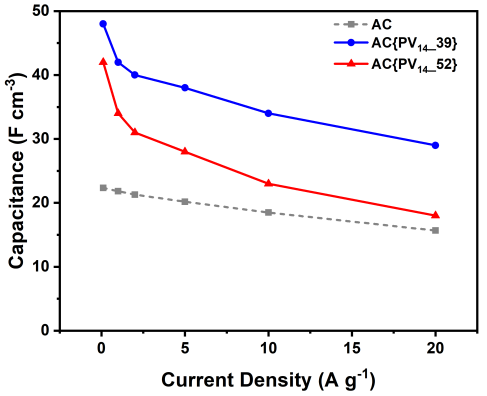

Figure 4.12: *Volumetric capacitance of AC{PV_{14}-39} and AC{PV_{14}-52} electrodes over 0.1, 1, 2, 5, 10 and 20 A g^{-1}.*

The average electrode thickness was measured by mounting the electrodes at 70° to horizontal and the measured thickness was multiplied by a correction factor of 1.06 (Figure 4.13).

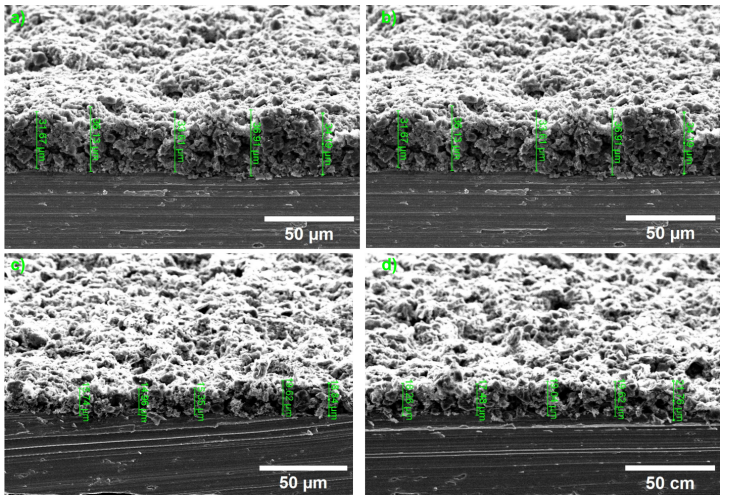

Figure 4.13: *Cross sections of electrodes before cycling: a) and b) AC{PV_{14}-39}, c) and d) AC{PV_{14}-52}.*

4.6 Discussion

Hybridisation of the PV_{14}-POM was found to be a complicated process due to the combined sensitivity of the POM towards both pH and phosphate concentrations. The addition of AC leads to the disturbance of these factors and results in the formation of other species such as decavandates ($[H_xV_{10}O_{28}]^{(6-x)-}$), pervanadyl ($VO_2{}^+$), and possibly sodium dihydrogen phosphate as byproducts.

The quantification of the amount of each species present was also found to be a challenging task and outside the scope of the main objectives of this work. Despite these challenges, the partially degraded AC{PV_{14}} hybrid materials did show an overall improvement in specific capacitance. However, this advantage was diminished at high current densities due to the presence of impurities and the absence of nano-dispersed POM ions. Thus, our work allows us to conclude that the partial decomposition of PV_{14} into V_{10} and P-containing impurities was not as detrimental to the performance of the resulting hybrid electrodes as it was the fact of getting microcrystal of extended POM phases grown on the surface of AC, turning the activity of these compounds sluggish and less durable.

The cyclability of the mixed AC{PV_{14}} hybrid cells was also improved compared to previous literature using pure POMs. For example, the material AC{PV_{14}-52} could retain 84% of its initial capacitance after 1,000 cycles and 72% after 5,000 cycles. Therefore, the hybridisation approach could extend the life-span of these materials.

Future work would involve modifying the synthesis process to stabilise PV_{14} and allow its better adsorption into AC pores. In addition, the hybrid electrodes should be tested in asymmetric configuration to allow complete utilisation of the POM's electroactivity.

Part II

Electrodes to Devices: High Mass Loaded Electrodes

Context

The focus in advancing EES technology often lies in the composition of the electrodes, particularly the properties of the active materials, their microstructure, and reactivity. However, many other parameters are important for the optimal design of battery cells with high energy storage capacity. Typically, electrodes are manufactured as thin coated layers (ca. 25 μm) [44] on thin current collectors (in the best cases reduced down to 10 μm) [81], a design common in both rechargeable batteries and supercapacitors. Although this is a well-established approach, it is not ideal due to the presence of large amounts of non-active or non-energy storing materials such as current collector, binder and separator. This only leads to heavier devices, with reduced energy density but also increased costs. So, the question arises, "how did this current design become the industry-standard to develop electrodes for modern rechargeable batteries as we know them?"

The standard way to manufacture Li-ion batteries, includes the use of inks for making thin coatings. This process was developed as a result of practicality and not-strictly scientific reasons (which is illustrative of how technologies evolve). First of all, it should be noted that lab scale cells work better with thinner electrodes. Thick electrodes typically hinder the transport of electrolyte ions due to tortuosity and lead to low specific capacities and energies, especially at fast rates. Secondly, the safest way to transfer knowledge from lab to industry is to translate the lab procedures at industrial scales. Third, we should be aware that industries can be reluctant to modify their production lines to allow new developments.

In the late 1980s, Sony developed a strong interest in producing rechargeable batteries for their consumer electronics. At the same time, while Li-ion technology was gaining momentum, other battery technologies were quickly falling out of favour. Meanwhile, magnetic tape for cassettes were also quickly becoming obsolete due to the rise of compact discs. Then, in a clever move, someone realised that Sony's manufacturing lines, which were originally designed for coating audio tapes with magnetic slurry, could be repurposed for producing Li-ion batteries. Leveraging their multi-disciplinary expertise, Sony combined their knowledge of battery technology with existing cassette-tape manufacturing equipment and skilled personnel to mass-produce thin coatings for Li-ion electrodes, just as it had been done on a smaller scale in laboratories [82].

Since then, rechargeable cylindrical Li-ion batteries have continued to use suboptimal configurations of layered materials, consisting of a current collector, graphite, separator, $LiCoO_2$, and another current collector, all rolled up inside. For

various reasons, much like the persistence of QWERTY keyboards, rechargeable Li-ion batteries and other imperfect technologies continue to dominate in order to maintain an edge in a fiercely competitive market. And yet, inside a traditional "heavy-duty" saline or even an alkaline primary battery, the electrodes are made of pastes with active materials comprising a significantly larger percentage of the total mass.

Then, wouldn't it be reasonable to try to implement thick electrodes or paste electrodes to rechargeable batteries in general? For example, it has been demonstrated that if batteries using cathodes and anodes with 25 μm thickness were stacked together, then the electrode component was responsible for 56% of the total cell volume. However, if the battery with the same volume, but having electrodes with 200 μm thickness was designed, the electrode component occupied 88% of the total volume. This makes it clear that batteries having high mass loaded electrodes are capable of generating much more energy inside the same volume as conventionally thin-electrode batteries [44].

What prevents the development of extremely high mass loaded electrodes? We must also take a look at why this standard process of coating "inks" onto the current collectors, could not be scaled up to develop thicker coatings. Increasing electrode thickness has traditionally led to performance issues, as simply making electrodes thicker using conventional formulations tends to be detrimental to their performance. Conversely, achieving better performance usually involves creating highly complex nanostructures, which are difficult to scale and implement. Therefore, it is crucial to conduct fundamental studies to understand the factors limiting thick electrodes.

Carbon-based supercapacitor electrodes are typically only a few microns thick, resulting in a low ratio of active (energy-storing) to non-active (binder, current collector, separator, casing, etc.) components. To reduce costs and create more compact energy storage devices with high power densities, it is essential to increase the loading of active materials by developing thicker or higher mass loading electrodes, while minimising the proportion of non-active components [83–85]. Industry standards usually define a thick electrode as having a mass loading > 10 mg cm^{-2}, but such electrodes often suffer from low capacitance due to poor charge transfer kinetics, reduced structural stability, and high tortuosity [86]. Additionally, delamination from the current collector can increase internal resistance within the cell [83]. Common approaches to improve mass loading involve one or more of the strategies that we have collected in Figure 4.14.

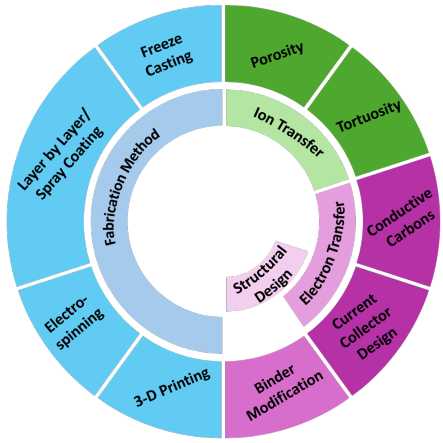

Figure 4.14: *Different factors to be considered for the design of effective thick electrode.*

Part II of the thesis brings up and tries to answer the following questions:

1. What are the best scalable methods to prepare thick electrodes for supercapacitors, and up to what mass loading?

2. Do different commercial carbon additives and flexible binders improve the capacitance and mechanical strength of thick electrodes?

3. What is the role of porosity and tortuosity in influencing the capacitance of thick electrodes?

4. What are the metrics that should be used to measure the impact of increasing mass loadings?

5. Can commercial 3-D frameworks enhance the gravimetric capacitance of thick electrodes?

6. Can adding polyoxometalates to carbon improve the thick electrode capacitance? and lastly,

7. Is there a possibility for a fundamental design change (outside of Figure 4.14) that could lead to the creation of improved thick electrodes?

In **Chapter 5**, we attempt to address questions 1 to 6. Thus we will present our studies on several fabrication techniques that we have used to develop scalable thick electrodes, such as spray coating and freeze-casting, while considering porosity,

tortuosity and impact of conductive additives and binders. Then we will analyse a commercial 3-D current collector developed through electrospinning techniques and finally we will describe our efforts to incorporate V-POMs as redox active materials to improve the charge storage and transfer of some of the thick electrodes fabricated.

Chapter 6 focuses on question 7. As it is already known, and will be experimentally verified, many of the methods reported in literature (as well as those discussed in Chapter 5) still require large amounts to non-active components such as binders and conductive additives. If we look at redesigning conventional electrodes to contain large amounts of active materials, flow cells could come to mind, but commercial flow cells suffer from low concentration of electroactive species. To address this, we propose a novel approach: non-flowing yet internally flowable electrodes in the form of "Nanopastes." To the best of our knowledge, these nanopastes have been presented for the first time as binder-free and non-flowable electrodes by our laboratory and its spin-off company Napptilus Battery Labs. Since the electrode formation is redesigned, the type of device used to test these materials also needed to be reinvented. The assembly and design parameters of such a prototype device that works by creating a pressure system is described in Chapter 6. This chapter collects our preliminary studies on nanopaste electrodes in an attempt to build large bulk electrodes.

A series of difficulties, not surprisingly linked to the novelty of the concept and the necessity of developing specialised techniques for the proper characterisation of these unconventional composite electrodes, presently hindered their comprehensive study. Nevertheless, we ultimately decided to include these preliminary results as part of the work carried out in this thesis aiming at a first qualitative indication of the way ahead for nanopaste electrodes.

5

Scalable techniques for the fabrication of thick electrodes

5.1 Introduction

Various strategies have been pursued and described in the literature to develop thick electrodes that could perform comparably to thin ones. These methods include creating hierarchical porous composites through pyrolysis [87–90], designing advanced current collectors [91–94], adding conductive materials [90, 95–97], and modifying binders [98–101]. Enhancing the conductivity of activated carbon (AC)-based supercapacitors by adding carbon additives, such as carbon blacks (CSP or C65), nanofibers (NFs), and carbon nanotubes (CNTs), has been a long-standing area of research [102–104]. While AC is highly porous and offers good capacitance, its conductivity is relatively low [105]. For example, a 500 μm thick CNT based supercapacitor with a gel-filled electrolyte achieved an areal capacitance of 2662 mF cm^{-2} at a scan rate of 2 mV s^{-1} and 2038 mF cm^{-2} at 10 mV s^{-1} [106]. In another study, a supercapacitor utilising a PANI−incorporated ultra-thick carbon nanotube fibre demonstrated a high specific capacitance of 335 F g^{-1} and a volumetric capacitance of 523.3 F cm^{-3} at 1 A g^{-1} [107]. A flexible electrode composed of Cobalt-Bismuth Oxybromide and CNTs with a mass loading of 15 mg cm^{-2} exhibited a capacity of 61 mAh g^{-1} at 1 A g^{-1} after 3,000 cycles [108].

Another approach to improving thick electrode performance involves enhancing ion transfer throughout the electrode's bulk by reducing tortuosity through pore engineering, which has shown promising results [109, 110]. Various techniques can optimise the electrode's nano/micro pore structure to facilitate better ion

transfer [84, 111, 112]. For instance, freeze-casting or lyophilisation can create nanochannels and reduce tortuosity, leading to improved electrolyte saturation [86, 113, 114]. An example is an approx. 1 mm thick cellulose-based asymmetric supercapacitor with a RuO_2/cellulose carbon aerogel anode that achieved an areal capacitance of 4284 mF cm^{-2} at 2 mA cm^{-2} [115]. Another study demonstrated enhanced ionic transfer in low-tortuosity graphene electrodes produced through a two-step tape-casting/freeze-casting method [111].

In addition to improving conductivity and optimising porosity, different coating and electrode formulation methods may also enhance the performance of thick electrodes. Conventional knife-casting methods often result in poor adhesion between carbon particles and increased series resistance over cycles, leading to reduced capacitance [116]. Thicker slurries may not ensure good dispersion of carbon particles and binder, but fine inks sprayed onto collectors in a controlled manner can improve dispersion, enhance carbon particle contact [104, 117], and efficiently control electrode thickness [118, 119].

Despite various attempts to address the challenges associated with thick electrodes, few reports exist on thick electrodes with good rate capability that can be produced using scalable methods. This study takes a multi-faceted approach to developing high mass loading multi layer electrodes (up to 0.6 mm) by testing different coating methods, conductive additives, and binders. Scalable techniques like spray coating and freeze-casting were explored, and the effects of carbon additives like CSP and CNTs, as well as binders like carboxymethylcellulose (CMC) and PVDF-HFP, were analysed and compared. This research aims to provide insights into the barriers hindering the performance of thick electrodes and help define strategies for their design.

5.2 Spray-coated and freeze-casted electrodes

5.2.1 Methodology

Preparation of spray-coated electrodes

In the case of using CMC as a binder, a mixture of AC(YP-50F):Conductive Carbon:CMC in 85:10:5 ratio was made in DI water as per Table 5.1 and stirred for 12 h until a spray-able slurry was obtained. The slurries of AC:CSP:PVDF-HFP (80:10:10 and 75:10:15) were prepared by stirring with NMP for 12 h. It is well known that binders can block AC pores and hence cause a reduction in the

capacitance of electrodes. Thus, binder mass was kept as low as possible while maintaining structural stability of the coatings for both CMC and PVDF-HFP binders.

The spray-coating process is described in Figure 5.1. For the AC (CSP/CNT) CMC electrodes, the aluminium current collector was placed on a heating plate with a constant temperature maintained at 60 °C ± 5 °C. The slurry was loaded into a spray gun, and coatings were produced by controlling the number of sprays (4, 15, 35 and 50, resulting in electrode mass between 1–2, 6–8, 10–14, and 17–24 mg, respectively). The deposit was allowed to dry for 30 s between each coating to prevent solvent concentration and subsequent cracking. The coated film was then pressed at 3 t (10 s) in a mechanical press and dried overnight at 100 °C. This helped maintain consistency in mass and volume between different coatings and samples.

In the case of PVDF-HFP as the binder, only CSP was used as the conductive material. The spray process was the same as previously mentioned except for a few differences. For example, the coatings were produced at a constant heating temperature of 75 °C ± 5 °C, and the slurry was sprayed 3 times and 27 times to obtain coatings of different thicknesses and mass loadings.

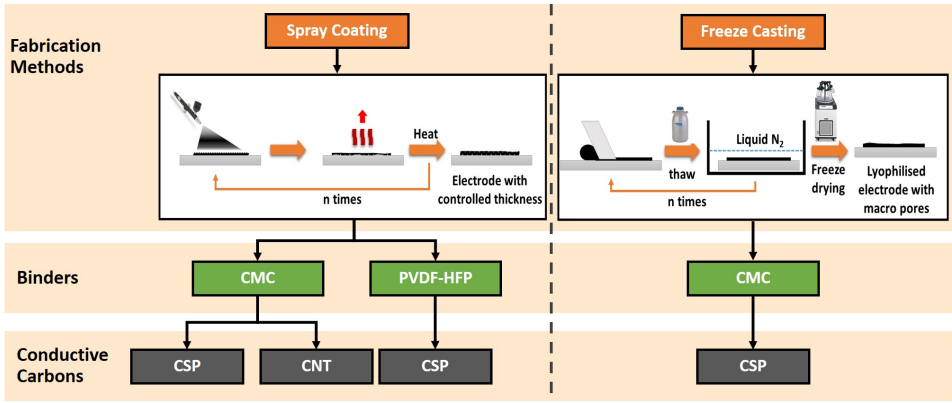

Figure 5.1: *Electrode-making processes through spray-coating and freeze-casting. Image reprinted with permission from our own publication [120].*

To test the limits of the spray-coating process, even thicker electrodes (0.6 mm) with AC:CNT:CMC (85:10:5) as well as AC:CSP:PVDF-HFP (80:10:10) were developed with mass loading of 31 and 30 mg cm^{-2}, respectively. The electrode names have a number as a prefix to differentiate different coatings on the basis of mass. Electrodes with active material mass loadings of approximately 1 mg cm^{-2}

have a prefix of 1, while those between 4 and 6 mg cm^{-2} have a prefix of 2, 6-9 mg cm^{-2} have a prefix of 3, 11-17 mg cm^{-2} have a prefix of 4 and 30-31 mg cm^{-2} have a prefix 5. (Table 5.1). Electrodes of 14 mm diameter were cut and pressed at 1 t for 5 s, and their thickness was measured using a micrometer. Symmetric CR2032 coin cells were assembled using a 16 mm cellulose separator.

Preparation of freeze-casted electrodes

The AC, CSP and CMC were dispersed in a ratio of 85:10:5 in DI water for 12 h. The slurry was coated onto the Al current collector using a casting blade and then frozen in a container with liquid nitrogen. To obtain a thicker coating, the slurry was subsequently coated and frozen three times. The coatings were then placed in a lyophiliser (Telstar Crodos) at -50 °C (0.802 mbar) for 24 h to completely remove water (Figure 5.1). The electrodes were not pressed except for the cell "3B_LYO_5%CMC" (1 t, 5 s) and their thickness was measured using a micrometer. Symmetric CR2032 coin cells with electrodes of 14 mm diameter were cut and assembled using a 16 mm cellulose separator.

Table 5.1: *Description of various coatings developed for spray- and freeze-casting.*

	Composition	Solid/Solvent Ratio	Fabrication Method	No. of Coatings	Mass Loading (mg cm^{-2})
1_CSP_5%CMC	AC:CSP:CMC (85:10:5)	1:13	Spray-Coating	4	0.9
2_CSP_5%CMC				15	3.6
3_CSP_5%CMC				35	6.5
4_CSP_5%CMC				50	11.1
1_CNT_5%CMC	AC:CNT:CMC (85:10:5)	1:15	Spray-Coating	4	1.1
2_CNT_5%CMC				15	5.5
3_CNT_5%CMC				35	8.9
4_CNT_5%CMC				50	15.5
5_CNT_5%CMC				60	31.0
1_CSP_10%PVDF HFP	AC:CSP:PVDF HFP (80:10:10)	2:7	Spray-Coating	3	0.9
4_CSP_10%PVDF HFP				27	16.7
5_CSP_10%PVDF HFP				40	30.1
1_CSP_15%PVDF HFP	AC:CSP:PVDF HFP (75:10:15)	2:7	Spray-Coating	3	0.5
4_CSP_15%PVDF HFP				27	13.8
2_LYO_5%CMC	AC:CSP:CMC (85:10:5)	2:5	Freeze-Casting	1	4.9
3A_LYO_5%CMC				3	7.0
3B_LYO_5%CMC				3	8.2

*AC(YP-50F) was used in all compositions described in this table.

5.2.2 Morphology characterisation

Figures 5.2 and 5.3 present the cross-sectional views of spray-coated thin and thick electrodes. For the spray-coated electrodes, comparisons were made between those with thicknesses ranging from 20-30 μm (prefix 1 | a & c) and those between 317-333 μm (prefix 4 | b & d). For freeze-casted electrodes, the thinnest (271 μm, 2_LYO_5%CMC) and thickest (647 μm, 3A_LYO_5%CMC) were selected for comparison as shown in Figure 5.4.

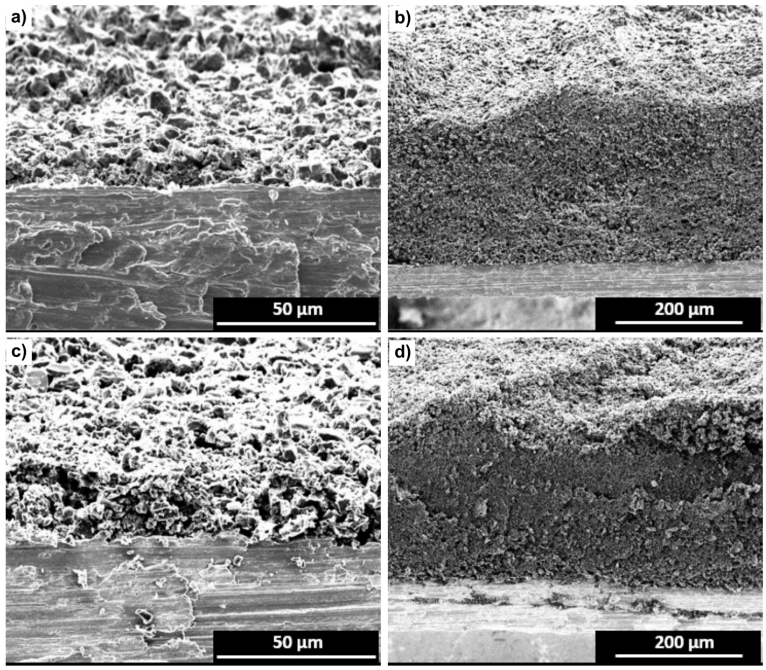

Figure 5.2: *Cross-sectional SEM images of a) 1_CSP_5%CMC, b) 4_CSP_5%CMC, c) 1_CNT_5%CMC, d) 4_CNT_5%CMC electrodes.*

All electrodes displayed smooth surfaces and good contact with the current collectors. As electrode thickness increased, some thick electrodes exhibited slight unevenness on the top surface due to variability that arises from the manual coating process. Nevertheless, the overall structural integrity of the electrodes was maintained despite the increase in thickness, and a compact carbon layering was observed in all spray-coated electrodes.

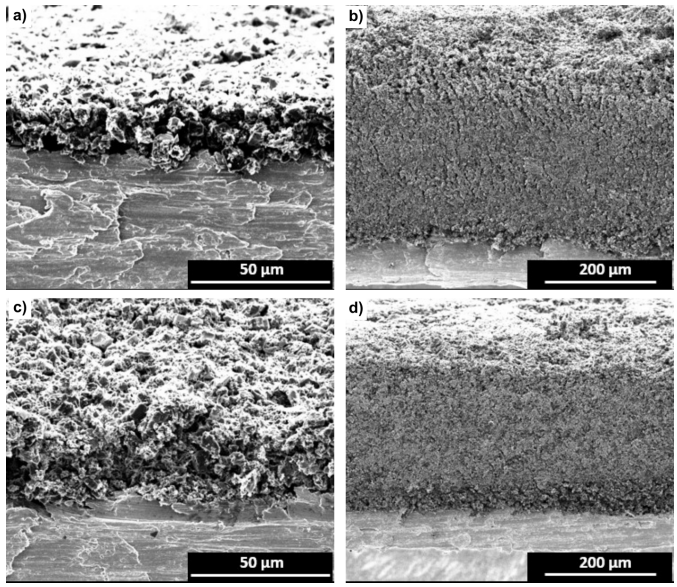

Figure 5.3: *Cross-sectional SEM images of a) 1_CSP_10%PVDF-HFP, b) 4_CSP_10%PVDF-HFP, c) 1_CSP_15%PVDF-HFP, d) 4_CSP_15%PVDF-HFP electrodes.*

For the thin freeze-casted electrode (Figure 5.4 a), no distinct macro-pore structure was evident. In contrast, the thicker freeze-casted electrodes displayed a characteristic macro-pore structure typical of the freeze-drying process. This macrostructure appeared more open and accordion-like, with nano-channels potentially improving electrolyte penetration. However, the macro-pores were unevenly distributed and randomly oriented, resulting in dead-end pores likely due to the casting of multiple layers as well as a certain variability of temperatures during the process.

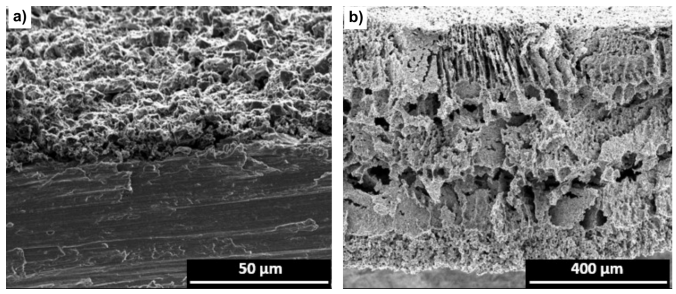

Figure 5.4: *Cross-sectional SEM images of a) 2_LYO_5%CMC, b) 3A_LYO_5%CMC electrodes.*

5.2.3 Porosity analysis

The porosity of an electrode is important for understanding its microstructure as well as for understanding its mechanical properties. The total porosity (P) of an electrode is given by the ratio of the bulk or geometric density of the coated film, including void space (ρ_g), to the theoretical or true density of the solid compounds of the coating (ρ_t).

$$P = \frac{\rho_g}{\rho_t} \cdot 100 \tag{5.1}$$

ρ_g and ρ_t are given by:

$$\rho_g = \frac{E_m}{d} \tag{5.2}$$

and

$$\frac{1}{\rho_t} = \sum \frac{\omega_i}{\rho_i} \tag{5.3}$$

Here, E_m is the electrode mass loading (g cm^{-1}), d is the electrode thickness (cm), ω_i is the mass fraction of each material of the electrode and ρ_i is the density of each component material.

Table 5.2: *True densities of coating materials.*

Material	True Density (g cm^{-3})
AC(YP-50F)	0.27 [121]
Carbon SuperP	0.16 [122]
Multiwalled Carbon Nanotubes	2.1 [123]
CMC	1.60 [124]
PVDF HFP	1.78 [125]

All electrodes exhibited porosity values greater than 80% (Table 5.3). In case of spray-coated electrodes, the porosity was higher in thinner electrodes ($\geq$ 85%) but it decreased with increasing thickness. Conversely, electrodes produced using the freeze-casting method maintained very high porosity even at greater thicknesses due to their more open structure. Figure 5.5 shows the variation of electrode porosity with its thickness and capacitance. The capacitance values were calculated from CP curves at 10 mV s^{-1} and given in detail in the Section 5.2.5.

The thickest freeze-cast electrode ($\simeq$600 μm) had the highest porosity of all at 96%. When this thick electrode was pressed, it likely destroyed the macro-pore

structure and the porosity decreased to 85%. Nevertheless, the increase in areal capacitance indicated that the remaining porosity was sufficient to allow adequate electrolyte infiltration and ion transfer (Figure 5.5 a). In fact, the application of pressure led to an improvement in areal capacitance most likely due to an improved contact between carbon particles.

The variation in gravimetric and volumetric capacitance with porosity and thickness is illustrated in Figures 5.5 b and c). Focusing on gravimetric capacitance, thinner electrodes (up to 300 μm) demonstrated higher performance, with porosity playing a minor role. However, for volumetric capacitance, more compact (spray-coated) electrodes performed better and the capacitance was almost independent of thickness for values <200 μm. It was observed that porosity values between 80-90% were desirable for ensuring good contact between carbon grains and enhancing the capacitance of thick electrodes.

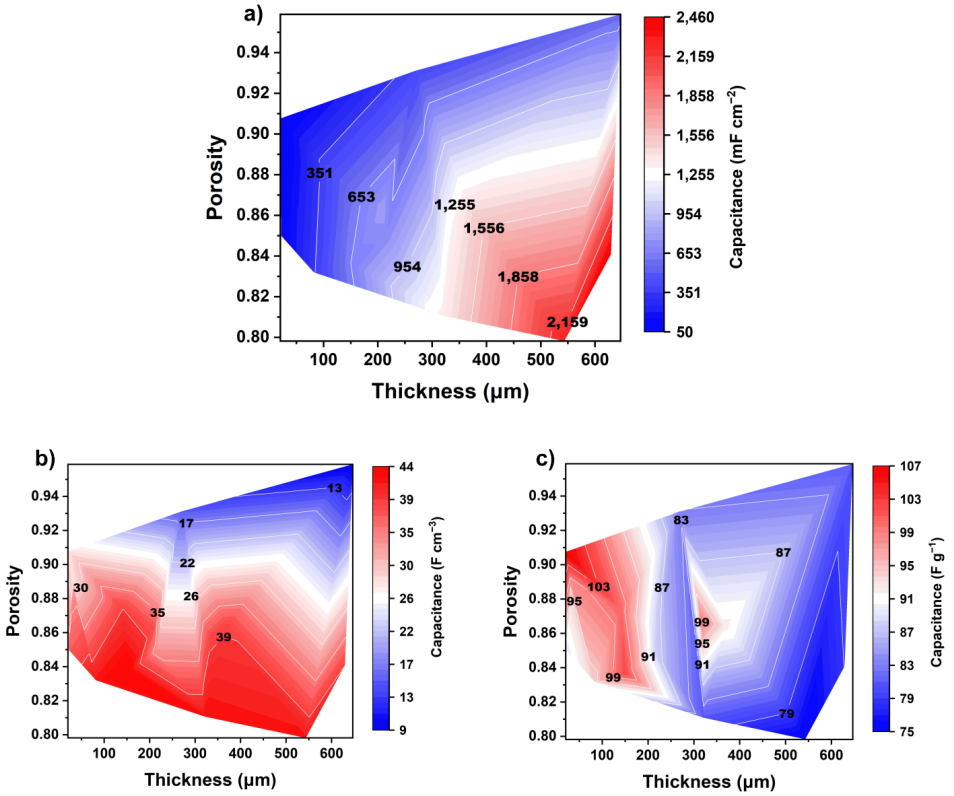

Figure 5.5: *Dependence of electrode a) areal, b) volumetric and c) gravimetric capacitances (at 10 mV s^{-1}) on thickness and porosity.*

5.2.4 Electrochemical impedance spectroscopy and tortuosity

Electrochemical impedance spectroscopy (EIS) is a technique used for understanding the kinetics of the charge–discharge process as well as the pore structure of electrodes. The EIS experiment was conducted over a frequency range from 500 kHz to 50 MHz with a 10 mV perturbation amplitude using a BioLogic VMP3 potentiostat controlled by the EC-Lab software. The equivalent circuit was obtained by fitting the impedance spectra using a simplified transmission-line model with constant-phase elements (TLM-Q, Ma3) that neglected the charge transfer across the electrode/electrolyte interface (i.e. blocking conditions) [126].

EIS can provide comprehensive insights into the kinetics of the charge-discharge process and the pore structure of electrodes [127, 128]. Figure 5.6 shows a semicircle followed by a transmission line behaviour for all electrodes. The high-frequency semicircle (previously noted in studies of both thick and thin electrodes), has been

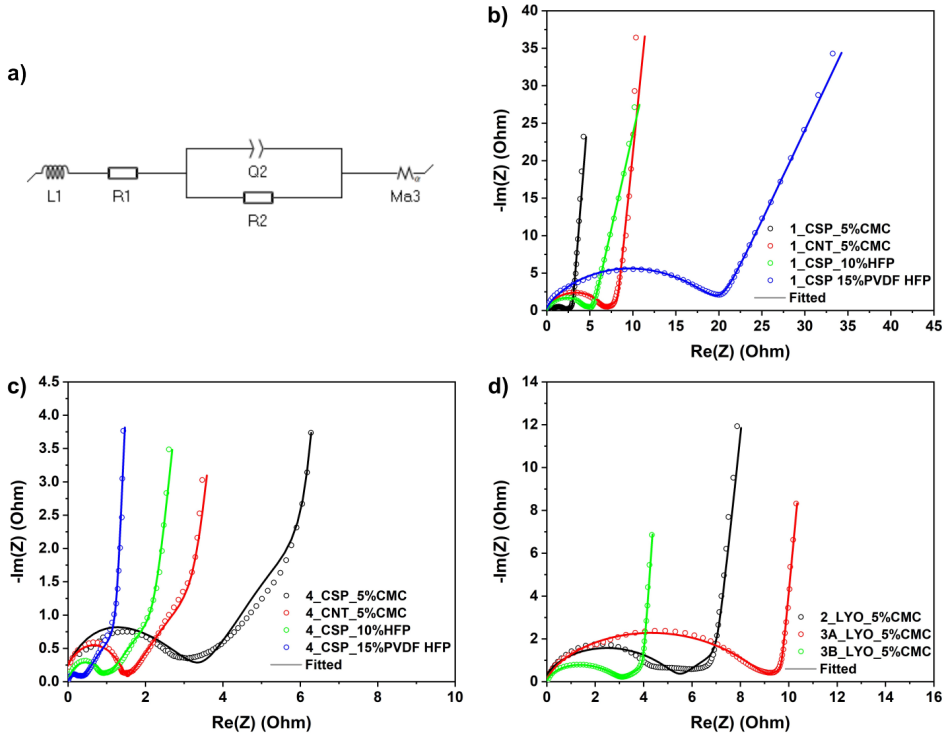

Figure 5.6: *a) equivalent circuit, and EIS fittings for b) thin electrodes, c) thick electrodes and d) freeze-casted electrodes.*

attributed to high resistance arising from various possible factors such as poor contact between the electrode and current collector [126, 129], electrolyte resistance within electrode pores [128], or redox processes involving hetero-atoms present in carbon materials [129]. In the case of thick electrodes, the smaller semicircle may indicate reduced interface charge loss (at the current collector interface) compared to thin electrodes [130, 131]. This contrary behaviour may arise due to the repeated pressing of electrode as well as a more compact packing within the coin-cell housing. A comparison of the thinnest and thickest electrodes (Figures 5.6 b and c) reveals that the resistance of 1_CSP_5%CMC cell was lower than that of 1_CNT_5%CMC, while 4_CSP_5%CMC had higher resistance than 4_CNT_5%CMC. This discrepancy might be due to CSP offering slightly better charge transfer between AC particles than CNTs in thin electrodes, resulting in lower resistance. However, for thick electrodes, CNTs provided, firstly very long 1-D electron-conducting pathways (tens of microns) and secondly, better mechanical strength and (as a result) slightly better adhesion to the current collector, leading to lower resistance in CNT-based thicker electrodes.

Regardless of the underlying cause of these electrochemical responses, it has been established that as long as the transmission line (TL) behaviour is observable, both the ionic resistance and the tortuosity of the electrodes can be determined [126]. Therefore, we considered the proposed circuit as a valid approach for estimating electrode tortuosity and linking it to electrochemical performance. The components $R1$, $R2$, and $Q2$ collectively represent the electrode's internal resistance. $Ma3$ is the modified restricted diffusion element that represents ion diffusion within the electrode together with the capacitive charging of the surfaces, modelled with constant phase elements to account for non-ideal behaviour that arise from geometric effects. The slope of the line at intermediate frequencies differed for different thicknesses, indicating a longer ion diffusion process in the thicker electrodes [128]. The model also includes the diffusion resistance $Rd3$, which represents the total ion transport resistance or R_{ion}. The inductor $L1$ represents a negligible inductance in the electrode [132]. Therefore, the electrolyte flow through the electrode pores can be determined by tortuosity (τ), calculated using Equation 5.4 [111].

$$\tau = \frac{R_{ion} \cdot A \cdot \kappa \cdot P}{2d} \tag{5.4}$$

Where A, d, P respectively are surface area, thickness, and porosity of the electrode and κ is the conductivity (0.05614 S cm^1) of 1 M $TEABF_4$ in acetonitrile.

The tortuosity values for the electrodes are provided in Table 5.3. The thin electrodes with a lower binder percentage showed lower tortuosity values (when CMC is used as the binder). However, as the binder percentage increases from 5% to 10% to 15%, tortuosity nearly doubles, irrespective of the binder type. Conversely, an increase in electrode thickness results in a decrease in tortuosity, and in some cases, the observed values were below 1 (tortuosity for through-pores). This may be due to the presence of dead-end pores, which would increase the surface area and consequently a reduction in tortuosity [133]. The study by Nguyen et al. suggests that ions do not need to percolate all the way to the current collector as long as they reach the active surface of the electrode. Thus, dead-end pores may not only increase the active area of the electrode but also provide more accessible paths for ions, leading to a reduction in tortuosity, potentially even to values below one (indicating greater accessibility than straight pores). It is important to note that the layer-by-layer deposition method used in this work may contribute to the formation of these pores. Similarly, dead-end pores may also result from the addition of conductive carbon and binder materials. The results indicated that electrodes prepared with CSP exhibited lower tortuosity compared to other spray-coated electrodes. Additionally, freeze-casted electrodes showed very low tortuosity values due to the presence of micropores and a more open structure. However, as illustrated in Figures 5.4 a and b, these pores were not aligned or well-ordered, potentially leading to the formation of dead-end pores and resulting in tortuosity values < 1.

Table 5.3: *Porosity and tortuosity values for all electrodes.*

Electrode	Mass loading (mg cm^{-2})	Thickness (μm)	Porosity (%)	Tortuosity
1_CSP_5%CMC	0.9	31	89	2.5
1_CNT_5%CMC	1.1	31	89	4.6
1_CSP_10%PVDF-HFP	0.9	23	85	4.3
1_CSP_15%PVDF-HFP	0.5	21	91	8.1
2_CSP_5%CMC	3.6	82	83	1.0
2_CNT_5%CMC	5.5	141	87	0.7
2_Lyo_5%CMC	4.9	271	93	0.9
3_CSP_5%CMC	6.5	151	84	0.8
3_CNT_5%CMC	8.9	210	86	0.7
3A_Lyo_5%CMC	7.0	647	96	0.1
3B_Lyo_5%CMC	8.2	215	85	0.4
4_CSP_5%CMC	11.1	317	87	1.0
4_CNT_5%CMC	15.5	369	86	0.5
4_CSP_10%PVDF-HFP	16.7	322	81	0.4
4_CSP_15%PVDF-HFP	13.8	333	86	0.3
5_CNT_5%CMC	31.1	629	84	0.2
5_CSP_10%PVDF-HFP	30.1	543	80	0.1

5.2.5 Electrochemical characterisation

Symmetric capacitor cells of all electrode coatings included in Table 5.1 were prepared with 1 M $TEABF_4$ in acetonitrile as electrolyte. Cyclic polarisation (CP) was carried out within the voltage range 0 <V< 2.7, at varying scan rates (2 mV s^{-1} < ν < 200 mVs^{-1}) to assess the capacitive behaviour and to determine the potential stability window. Since the electrodes varied very substantially in mass, it was preferred to first use CP curves to calculate cell capacitance (C_{cell}) from Equation 2.1. The gravimetric (C_g), areal (C_a), and volumetric electrode capacitance (C_v) were calculated from Equations 2.7, 2.8, 2.9.

Finally, GCD comparisons for thinnest and thickest electrodes were also performed to analyse the charging behaviour and to provide an additional estimate of the gravimetric capacitance. The upper limit of the current densities varied due to the 400 mA limitation of the potentiostat used. Gravimetric specific energy (Wh kg^{-1}) and power (W kg^{-1}) of the device were calculated from GCD curves at 1 A g^{-1} using equations 2.10 and 2.11, respectively.

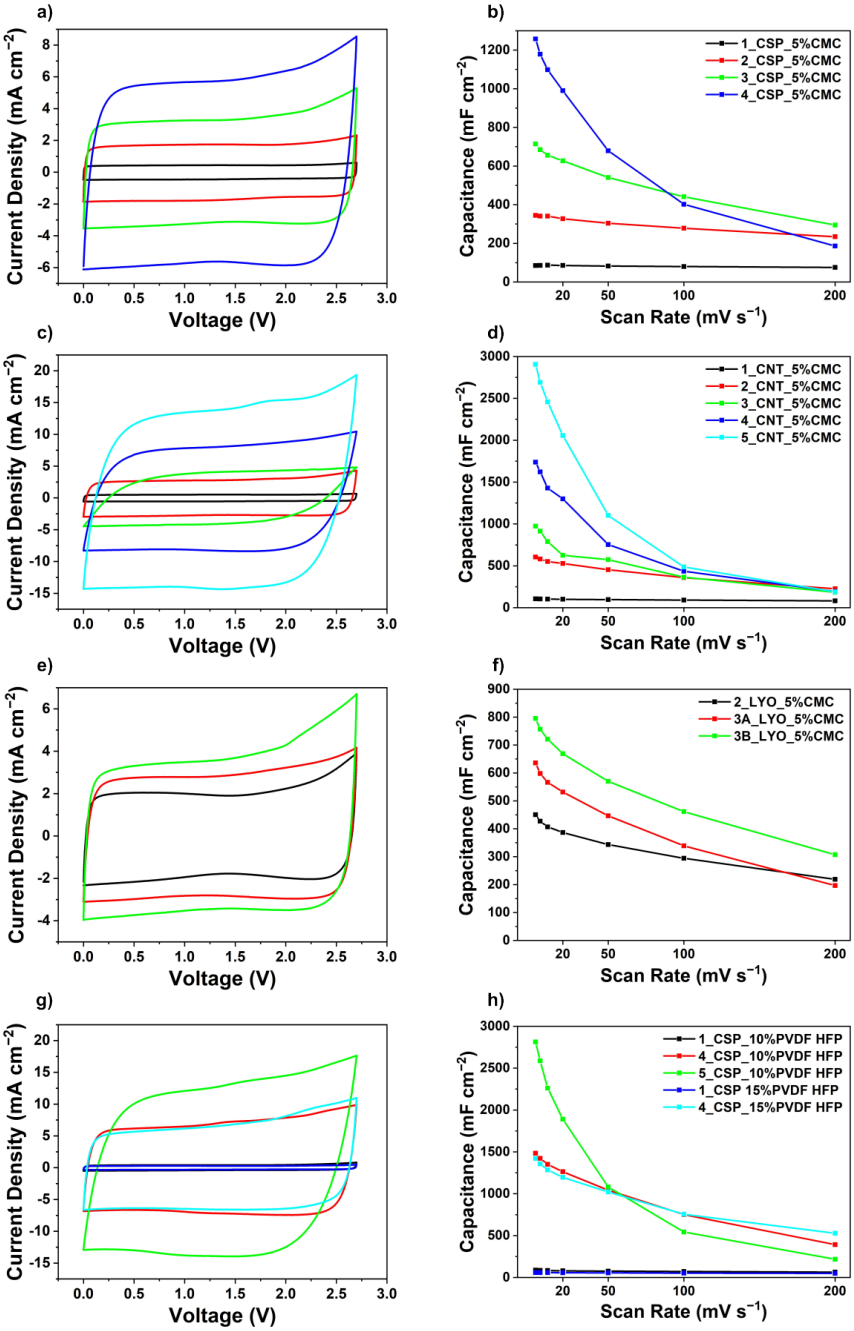

Figure 5.7: *a), c), e) and g) CP curves at 10 mV s^{-1} and b), d), f) and h) areal capacitance vs. scan rate graphs of electrodes, respectively with CSP and CMC, CNT and CMC, Lyophilised CSP and CMC, and CSP and PVDF-HFP.*

From the CP curves shown in Figure 5.7, we first take a look at the areal capacitances, which is one of the most common used parameters to evaluate the performance of thick electrodes. The left column of Figure 5.7 displays the CP curves for various electrodes with increasing thicknesses at a scan rate of 10 mV s^{-1}. The graphs indicate that as the electrode thickness increases, the area under the curves also expands, indicating a rise in areal capacitance. This is expected because the amount of active material is higher for the thick electrodes over the same current collector area. When comparing the two coating methods, it is evident that freeze-cast electrodes exhibited significantly lower capacitance than spray-coated electrodes. However, the freeze-casted and pressed electrode (3B_LYO_5%CMC) demonstrated better areal capacitance and rate capability than its unpressed counterpart (3A_LYO_5%CMC). This suggests that while the macro-pore structure improves electrolyte percolation, it also reduces the contact between carbon particles, resulting in poor conductivity.

The right column of Figure 5.7 depicts the variation of the areal capacitances of a decreasing capacitance with increasing scan rate. Thicker electrodes in general showed extremely high areal capacitance at low scan rates, but the capacitance of thick spray-coated electrodes dropped sharply for scan rates above 20 mV s^{-1}. In contrast, the thin spray-coated electrodes maintained their areal capacitances even at higher scan rates.

The thickest electrode, composed of CNTs as the conductive carbon and 5% wt CMC as the binder (5_CNT_5%CMC, $\simeq$600 μm & 28 mg cm^{-2}), exhibited the highest areal capacitance of 2459 F cm^{-2}, at 10 mV s^{-1}. A comparable electrode with similar mass loading and thickness (5_CSP_10%PVDF-HFP), using 10% wt PVDF-HFP as the binder, had a slightly lower capacitance of 2261 F cm^{-2} also at 10 mV s^{-1}. However, both types of electrodes under-performed at high scan rates. Figure 5.10 a illustrates the variation in areal capacitance (mF cm^{-2}) with changes in mass loading (mg) and thickness (μm) for all electrodes. Additionally, Figures 5.8 and 5.9 show the dependencies of volumetric and gravimetric capacitance on the volume and mass of the electrodes, respectively. Volumetric capacitance improved with thickness for slow scan rates. However, the rate capability behaviour (rate of decreasing capacitance as the scan rate is increased) got worse as the thickness of the electrodes increased. In the case of gravimetric normalisation of capacitance, the qualitative picture is the same but values for electrodes of different thicknesses are more similar (clustered together in the plots) for thinner electrodes.

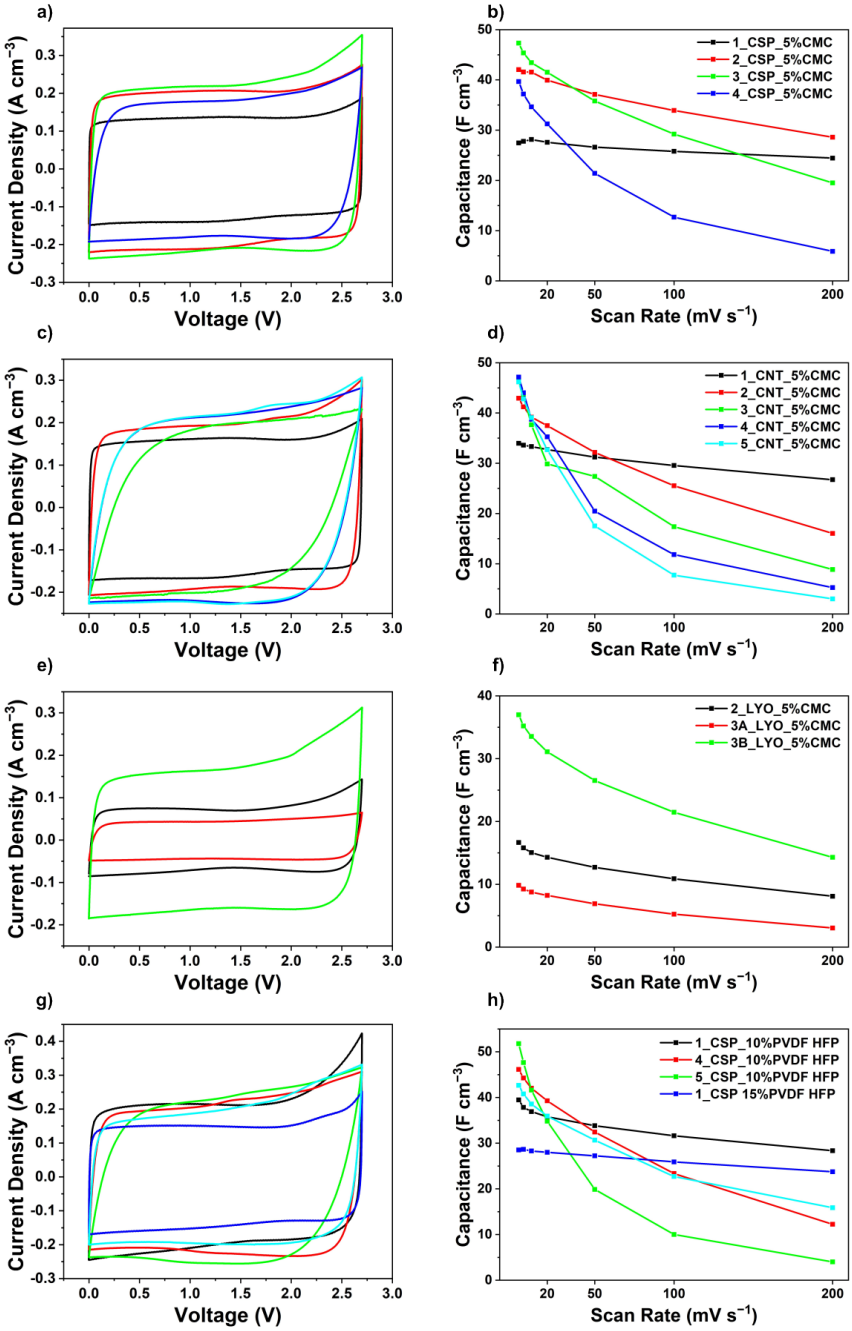

Figure 5.8: *a), c), e) and g) CP curves at 10 mV s^{-1} and b), d), f) and h) volumetric capacitance vs. scan rate graphs of electrodes, respectively with CSP and CMC, CNT and CMC, Lyophilised CSP and CMC, and CSP and PVDF-HFP.*

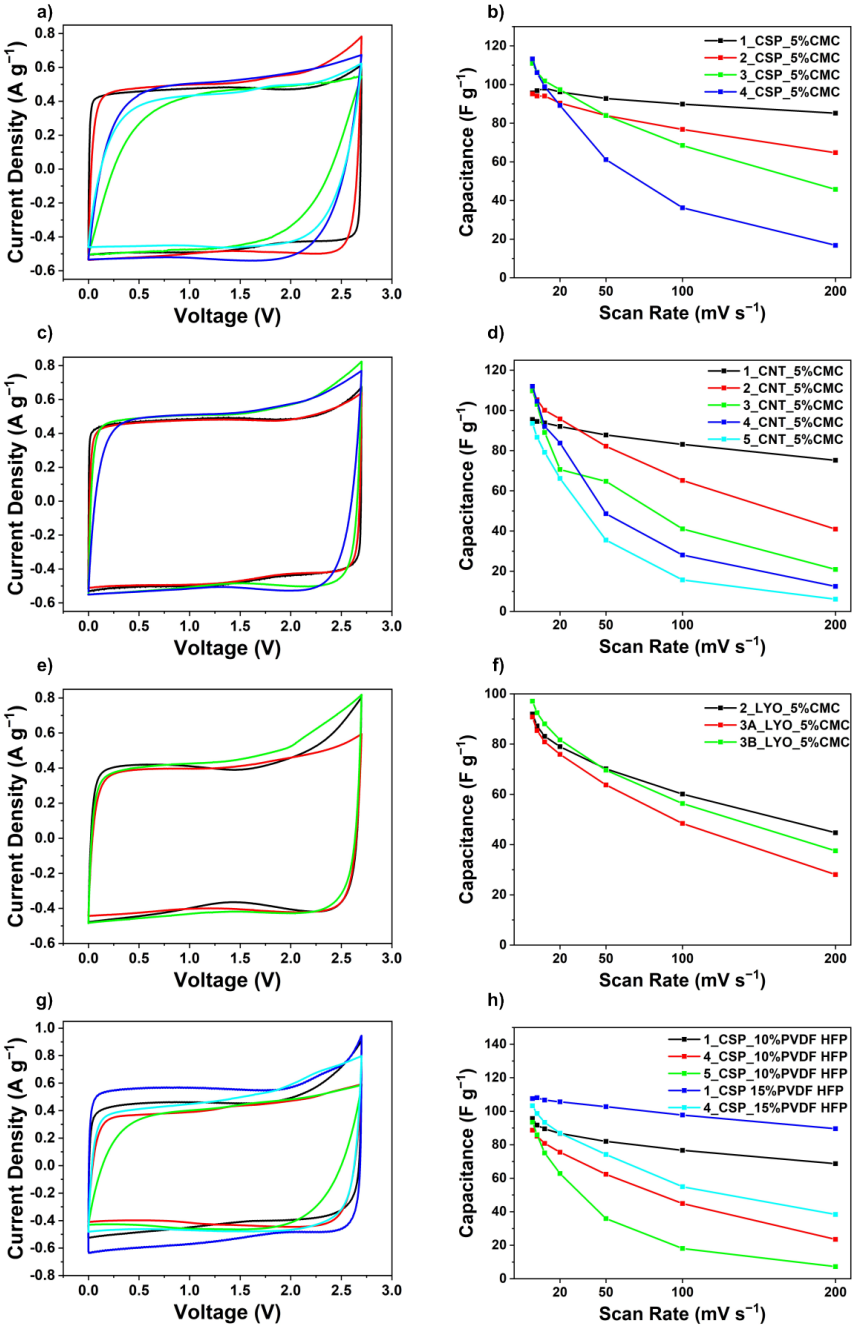

Figure 5.9: *a), c), e) and g) CP curves at 10 mV s^{-1} and b), d), f) and h) gravimetric capacitance vs. scan rate graphs of electrodes, respectively with CSP and CMC, CNT and CMC, Lyophilised CSP and CMC, and CSP and PVDF-HFP.*

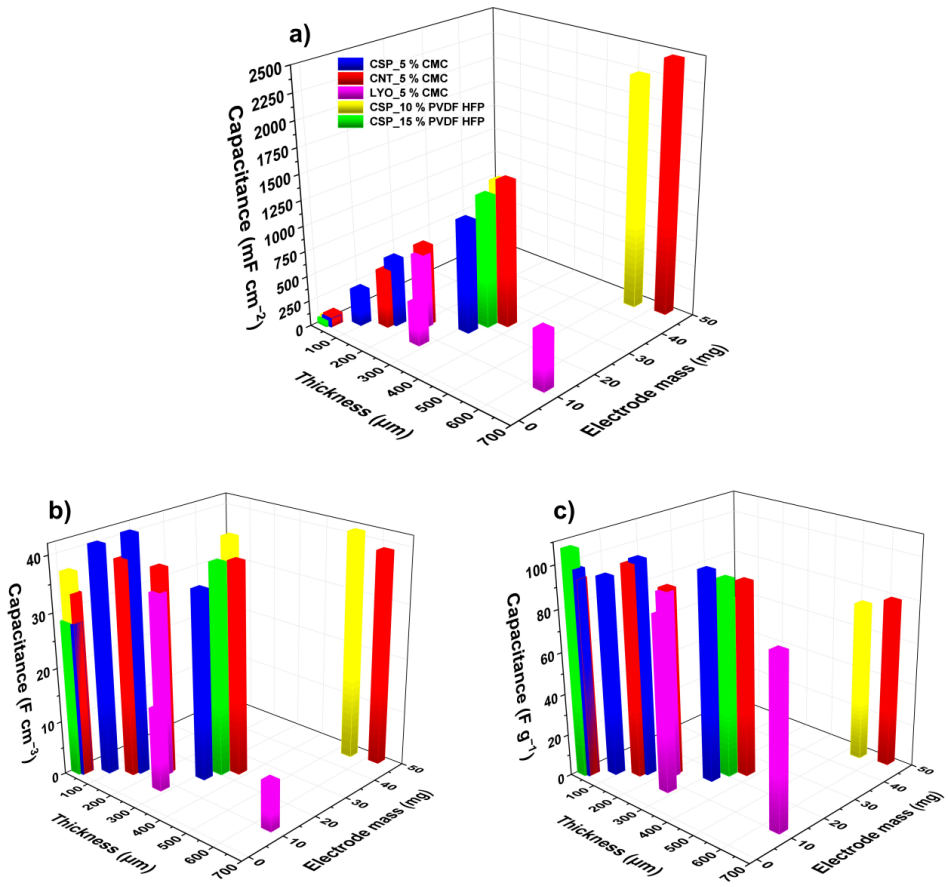

Figure 5.10: *a) Areal, b) volumetric and c) gravimetric capacitances (at 10 mV s^{-1}) of various electrodes as a function of thickness and mass.*

Figure 5.11 a presents the GCD curves of "low" mass loaded or "thin" electrodes (prefix 1) and "high" mass loaded or "thick" electrodes (prefix 4) prepared using spray-casting method. As mentioned earlier, the electrodes with higher mass loading could not be subjected to the same high current densities due to the potentiostat limitations. However, their performance at lower current densities provides a trend that is indicative for capacitance at high current densities as well.

For all electrodes, the gravimetric capacitance is comparable at very low current densities (similar to CP observations at low scan rates). It was also noted that generally, the PVDF-HFP based electrodes had slightly lower capacitances than CMC based electrodes, possibly due to the blocking of pores from larger amounts

of binder. For current densities greater than 2 A g^{-1}, there is a rapid decline in the specific capacitance of these thick electrodes. For example, there is a 40% decline in capacitance for CMC based thick electrodes in going from 2 to 5 A g^{-1} discharge, while the capacitance change is only 2% on average in case of their thinly-coated counterparts. The low mass loaded electrodes maintain a stable capacitance even at 20 A g^{-1}.

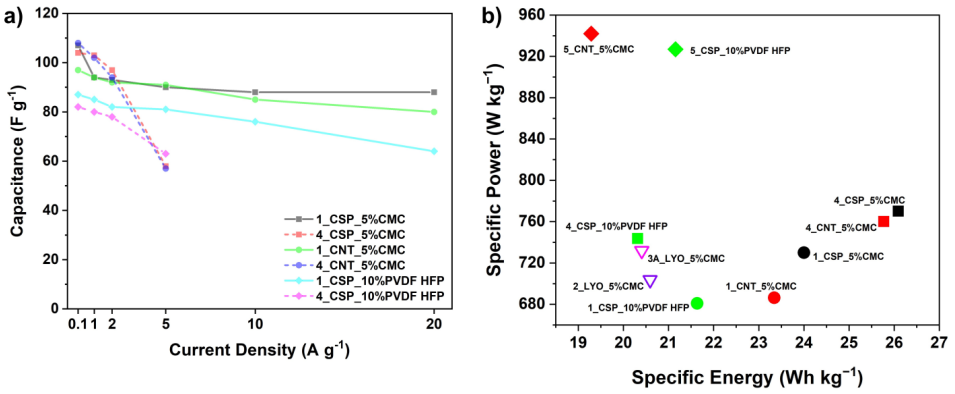

Figure 5.11: *a) GCD comparison of spray-coated low and high mass loaded electrodes and b) Ragone plot of electrodes with specific energy and specific power measured at 1 A g^{-1}. Here, circles represent spray-coated thin electrodes with average mass loading 1 mg cm^{-2}, squares represent spray-coated thick electrodes with average mass loading of 14 mg cm^{-2}, diamond shapes indicate spray-coated thick electrodes with average mass loading of 31 mg cm^{-2}, and inverted triangles depict freeze-casted electrodes.*

The specific energy vs. power for selected electrodes at a current density of 1 A g^{-1} is presented in Figure 5.11 b. Due to the methodology adopted during the initial testing process, the energy and power comparisons were only made on a gravimetric basis. However, since this study uses all three metrics for comparing the performance of thick electrodes, comparison of energy and power on a gravimetric basis can be used as an indicator for the overall performance of these electrodes. It is clear that the increase in mass loading of the electrodes is directly proportional to the device power. The thickest electrodes achieved the highest specific power at 942 W kg^{-1}, outperforming the thinner electrodes. If we consider that by increasing the mass loading (and thickness) of the electrode, we could not fully utilise the active material, the charging would take place only in outer shells of the electrode (especially if we consider the presence of dead-end pores). This would lead to higher gravimetric power values seen for the thicker electrodes. On the other hand, energy values for devices with different thicknesses, carbon additives, and binders were

generally comparable up to a mass loading of approximately 15 mg cm^{-2}. However, when the mass loading is doubled to around 31 mg cm^{-2}, the device energy reduces sharply. Finally, one general conclusion we can extract from our work is that, with the procedures followed as described, the spray-coated electrodes outperformed freeze-cast electrodes.

5.2.6 Impact of conductive carbons and binders on electrode thickness and performance

The impact of the carbon additives on electrode capacitance can be deduced from Figures 5.7, 5.8, and 5.9. Electrodes with CNTs exhibited slightly higher areal and volumetric capacitance compared with those based on CSP as conductive additive. This was likely due to better dispersion with CMC binder. Interestingly, while CNT-containing electrodes had a higher overall areal capacitance than CSP-containing electrodes, the slope of their capacitance versus scan rate was also steeper. This means that CSP-based electrodes experienced less of a capacitance decline as the scan rate increased.

Additionally, it was observed that even though CNT-containing electrodes offered better bonding and mechanical strength with CMC, CSP-containing electrodes of similar thicknesses showed higher gravimetric capacitance (Figure 5.9). This suggests that carbon-to-carbon inter-particle contact may be more effective in thick CSP electrodes, although their thickness is limited due to their poorer mechanical strength, which can lead to crack formation at relatively high thicknesses (unlike CNT-based electrodes).

Overall, thick electrodes using CMC as a binder outperformed those with PDF-HFP in terms of gravimetric capacitance (Figure 5.11 a). However, thick electrodes with PVDF-HFP were slightly more flexible and had better mechanical strength than those with CMC. In addition, increasing the PVDF-HFP binder content from 10% to 15% had minimal effect. Thick electrodes with 15% PVDF-HFP performed slightly better at high scan rates, likely due to improved adherence to the current collector. Nevertheless, it is well known that using excessive binder can obstruct carbon pores and decrease capacitance, as supported by tortuosity analysis [133]. However, in this particular case, the improvement in gravimetric capacitance for thick electrodes may be attributed to better adherence to the current collector. At the same time, the minor discrepancies in manual coating processes can also play some role in the quality of contact between the current collector and electrode.

5.3 Modification of current collector: NOVAC's universal current collector (UCC)

5.3.1 Methodology and morphology characterisation

The spin coated current collector called "universal current collector" or UCC was fabricated and provided by NOVAC S.r.l. The thickness of the coating was 100 μm. The UCC cross-section is shown in Figures 5.12 a and b, and was prepared by a patented process by NOVAC (briefly described):

- The current collector composed of an aluminium foil over which a "conductive" glue composed of proprietary PVDF and carbon additive blend (10-50 μm thickness) was knife-casted.
- The next layer composed of a proprietary woven/non-woven fabric made by spin coating.
- The layers were consolidated using a rolling press and the final product was dried to eliminate the solvent in the conductive glue.

In order to understand the morphology of the commercial UCC, we first examined its surface and cross-section using SEM. As mentioned before, all cross-sections were obtained by freeze drying the electrodes to obtain a regular (or smooth) surface for examination. Moreover, the cross-sections were mounted on a 70° support and hence, the obtained thickness was multiplied by a correction factor of 1.06 to obtain the correct values.

The cross-sections of a pristine UCC is shown in Figures 5.12 a and b. The average thickness of the current collector was observed to be approximately 12.6 μm. The thickness of conductive glue and carbon fibres was approximately 100 μm. Figure 5.12 c shows the top-view of the arrangement of the carbon fibres on the conductive glue. These fibres were unevenly distributed forming a denser network in one area and sparser in others. Moreover, sometimes they were embedded in the carbon glue. The diameters of these fibres ranged from 6 to 10 μm.

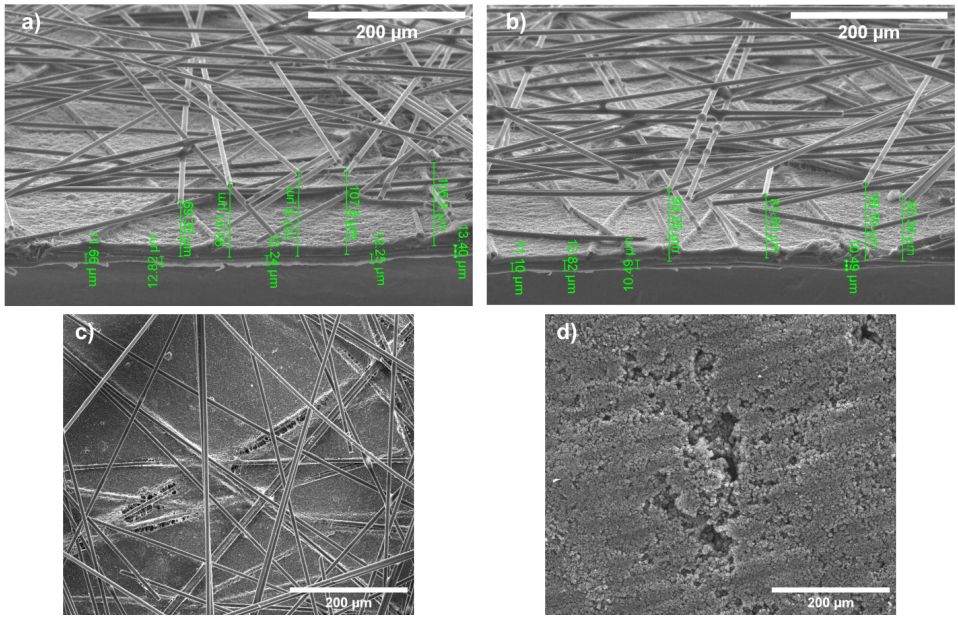

Figure 5.12: *a) and b) Cross sections of pristine UCC provided by NOVAC, c) Top view of UCC and d) Top view showing imperfections of a once through knife-casted process.*

Coating procedure: AC & PVDF-HFP

A slurry of AC(YP-50F):PVDF-HFP (1:0.1) with limited NMP was prepared. CSP was not used in the first attempt since the fibres were expected to not only provide mechanical support but also to improve conductivity between AC particles. The coating was dried at 100 °C overnight in a vacuum oven.

Figure 5.12 d shows the top view of the "once through" knife-casted UCC electrode. Clearly the UCC was not well optimally coated, and "holes" or empty spaces in the electrode were observed. To avoid this, the UCC was "twice coated" with a casting knife with 100 μm setting and then spray coated with the same ink (but with additional NMP). The multi-coating procedure was developed in 2 sequential steps:

1. Knife-casting (100 μm) was performed twice followed by partial drying at 65 °C for 1 min.

2. 7 sprays using the same composition (1:13 solid:NMP ratio) at 65 °C ± 5 °C with each spray coating partially dried for 30-40 s.

This was done to a) avoid empty/unfilled areas in the coating, b) cover all UCC

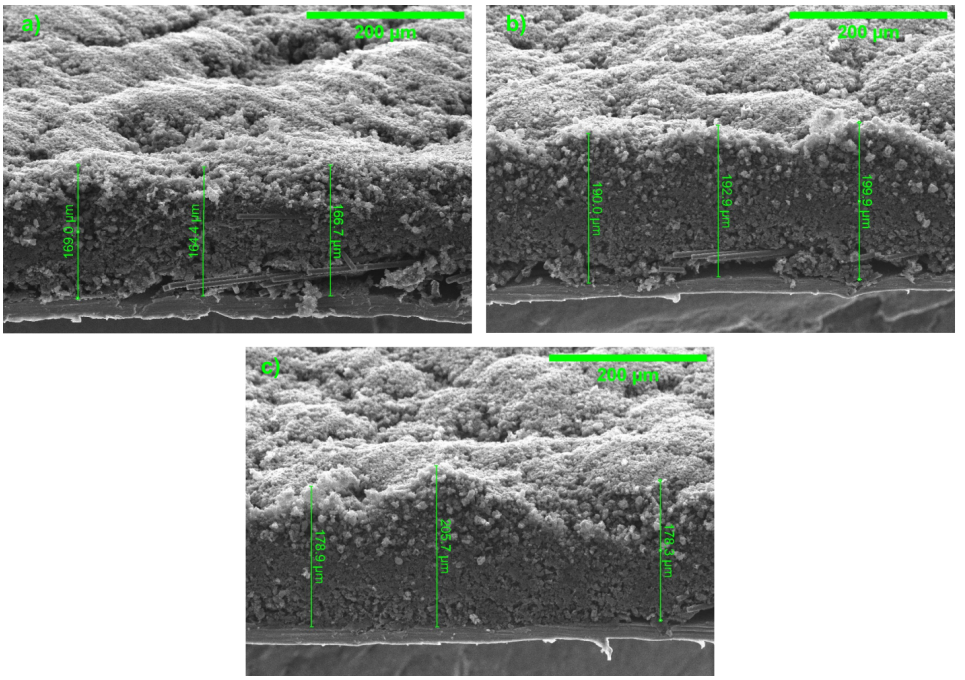

Figure 5.13: *a), b) and c) Cross sections of UCC_AC_10%PVDF-HFP electrodes at a 70° mounting angle.*

fibres, and c) create a uniform surface.

The resulting electrode had an active material mass loading of 7.8 mg cm^{-2} and its cross sections are shown in Figures 5.13 a, b, and c. Even after this modification, the electrode did not exhibit uniform thickness. We attribute this to the variability arising from the manual spray-coating process.

Coating procedure: AC, CSP & PVDF-HFP

Another electrode with AC, CSP and PVDF-HFP (85:5:10) was prepared by the same method of knife-casting + spray-coating (Figure 5.14 a, b, and c) to assess if the conductive carbon could also contribute to the improvement in electrode capacitance. The coating procedure was the same as before with the UCC "twice coated" using a casting knife with 100 μm setting, and then 7 times spray coated with the same ink (but with additional NMP) each with 30-40 s interval and keeping the temperature of the heating plate at 65 °C.

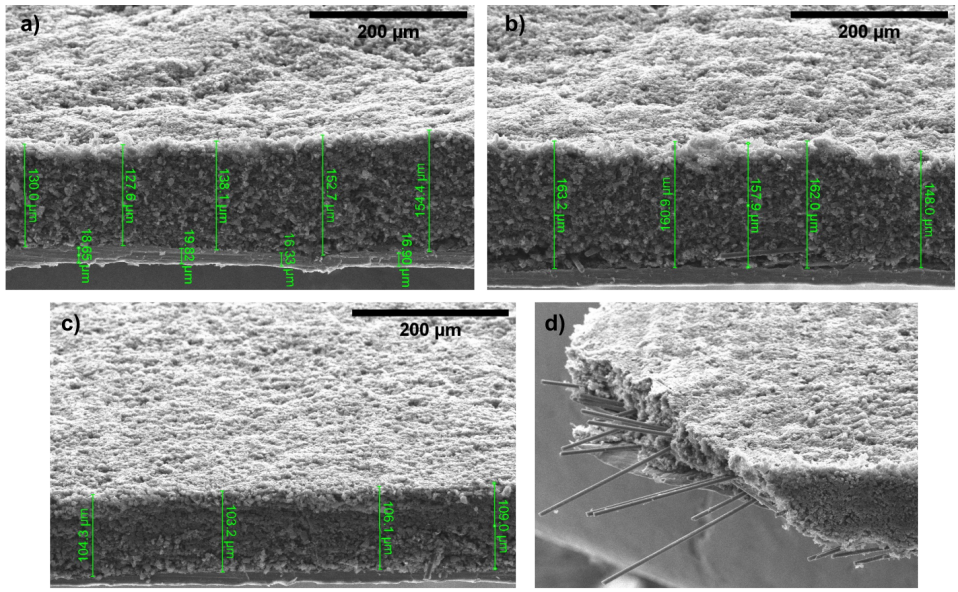

Figure 5.14: *a), b) and c) Cross sections of UCC_AC-CSP_10%PVDF-HFP electrodes at a 70° mounting angle, d) naturally broken edge of UCC_AC-CSP_10%PVDF-HFP electrode showing carbon-fibres embedded in electrode structure and uniformly covered by the spray-coating process.*

This electrode had an active material mass loading of 6.7 mg cm^{-2} and a much more even cross section. Figure 5.14 d shows the image of a naturally broken edge of the UCC_AC-CSP_10%PVDF-HFP electrode. The uniform top surface can be observed without any gaps or holes in the electrode. But even more interestingly, we can see how the AC and CSP fill in the spaces between the carbon fibres. As mentioned earlier, these conductive fibres are unevenly spaced with relatively large distancing between them. The impact of this design on the electrochemical performance is examined in the next section.

5.3.2 Electrochemical characterisation of UCC

The blank (uncoated) UCC current collectors were first assembled in a symmetric coin cell to evaluate if the conductive glue or the carbon fibres could provide additional capacitance. The cells were tested with 1 M $TEABF_4$ electrolyte and their CP curves demonstrated negligible electrode capacitance (< 2 F g^{-1}/5 mV s^{-1}).

To compare the performance of the UCC-electrodes with the spray coated electrodes from Section 5.2, we calculated the gravimetric (red curves) and volumetric

capacitance (blue curves) from the CV curves (Figure 5.15 b). Both gravimetric and volumetric capacitances of UCC_AC-CSP_10%PVDF-HFP were slightly higher than that of UCC_AC_10%PVDF-HFP due the presence of additional conductive carbon in the former.

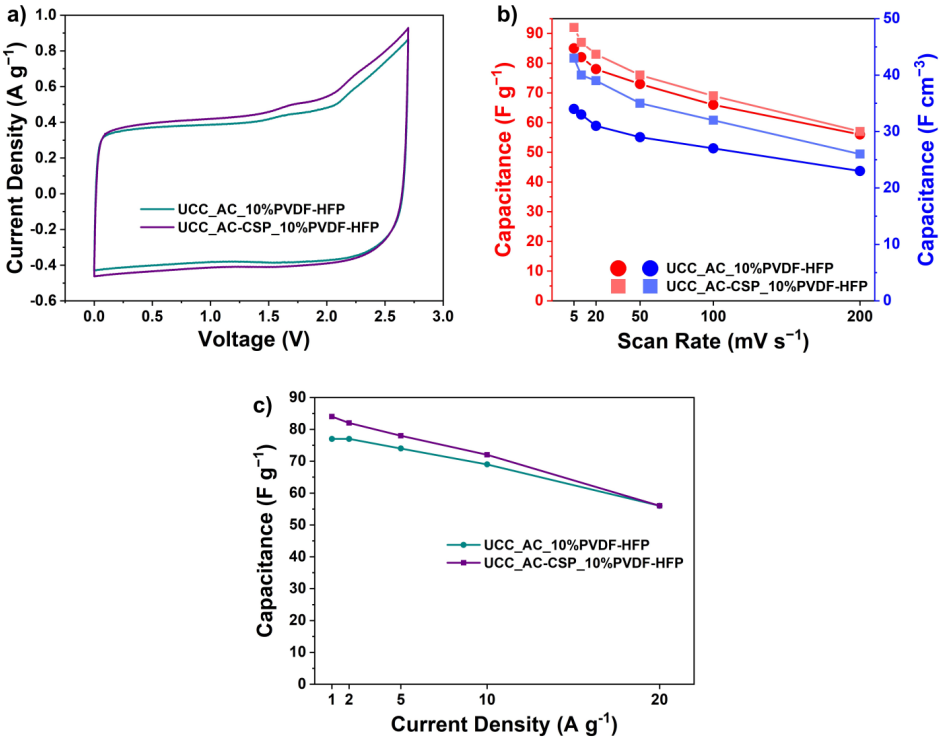

Figure 5.15: *a) CP curves of UCC electrodes at 10 mV s^{-1}, b) Gravimetric (red) and volumetric capacitance (blue) of UCC electrodes at varying scan rates, c) Dependence of gravimetric capacitance of UCC electrodes on current density.*

Since the two electrodes had relatively comparable mass loadings, we obtained the capacitance from the GCD curves at 1, 2, 5, 10 and 20 A g^{-1}. Similar to the results from CVs, the gravimetric capacitance of UCC_AC-CSP_10%PVDF-HFP electrode was higher than that of UCC_AC_10%PVDF-HFP electrode (Figure 5.15 c). This difference in capacitance became narrower with the increase in current density until 20 A g^{-1}, where the capacitance of both electrodes was equal. This showed that in case of this specialised current collector, the conductive carbon only had benefit at low current densities, while at higher current densities, they had similar performance.

Overall, the use of UCC did not lead to an improvement in capacitance of the electrodes. However, the UCC provided additional mechanical strength to the thicker electrodes, which may be more useful when approaching thicknesses 500 μm or more. Since the UCC does not improve conductivity, the existing design would only add to the amount of non-active components of the electrodes, which is not desirable.

5.4 Redox active thick electrodes

The results from the different coating strategies and modification of the current collector lead us to a few observations:

1. Higher tortuosity and porosity may not always lead to superior thick electrode performance due to the presence of dead-end pores.
2. Conductive carbons can only provide a limited improvement towards the development of thick electrodes.
3. The modification of the current collector may add to larger inactive components to the device and apart from providing better mechanical strength, it may not necessarily provide better conductivity.

The experience with V-POMs leads us to speculate that they may be useful in improving the charge storage and performance of the thick electrode. Since ours and other literature methods have proved that these V-POMs are "fast charging/discharging" POMs, and immobilising them in AC pores provides substantial improvement in their capacitance retention, we decided to carry out some experiments on thick electrodes based on decavanadate POMs to bridge and connect Part 1 and Part 2 of the thesis. We chose to use the AC{Na-V_{10}} hybrid material since it demonstrated some of the best results as thin coatings in Part I.

5.4.1 Methodology

AC{Na-V_{10}} (developed in Chapter 3), CSP, and PVDF-HFP were mixed in 80:10:10 ratio in NMP (total solid to solvent ratio 1:5) for 12 h. We used PVDF-HFP as binder since it provides flexibility to the thick electrodes and prevents crack formation. The slurry was then spray coated 15 times to develop relatively thick electrodes loaded with 5 mg cm^{-2} active material (Th_AC{Na-V_{10}}). Since the AC used in this case was YP-80F, we developed a similar "blank" spray coated

electrode with AC(YP-80F), CSP and PVDF-HFP (80:10:10) (Th_AC(80F)). The active material mass loading of this electrode was 3.8 mg cm^{-2}. While the coating strategy was the same, due to the heavier mass of the V_{10}-POM, the mass loading of the AC{Na-V_{10}} electrode was higher even though the spray inks were prepared and coated in the same way. In principle, one could think that this may prove to be detrimental for the already heavy POM-based electrodes when normalising per mass. However, as we will describe below, this was not the case. The electrodes were assembled in a symmetric coin cell with 1 M $NaClO_4$ in acetonitrile electrolyte.

5.4.2 Electrochemical characterisation

Figure 5.16 shows the CP and GCD results of the thick electrodes: Th_AC(80F) and Th_AC{Na-V_{10}}. Even though the mass loading of the hybrid electrode was slightly higher than for the AC electrode, its CP curve showed an increase in area (with signs of POM activity) even after mass-normalisation. The capacitance measured from the CP at 10 mV s^{-1} for Th_AC(80F) electrode was 77 F g^{-1} whereas that for Th_AC{Na-V_{10}} electrode was 110 F g^{-1} (a 43% improvement).

To evaluate the device performance, we carried out GCD experiments at various current densities. The Th_AC{Na-V_{10}} electrode outperformed the pristine AC electrode with capacitance of 114, 106, 101, 93, 81 and 36 F g^{-1} at 0.1, 1, 2, 5, 10 and 20 F g^{-1}, respectively. The difference in capacitance between the Th_AC(80F) and Th_AC{Na-V_{10}} electrodes was more pronounced at lower current densities and became smaller at the highest current density of 20 A g^{-1}. This can be attributed to one or more of the following factors:

- As observed previously in this chapter, the thick electrodes suffer larger performance drop at high current densities when compared with conventional thin electrodes of the same material.
- The faradaic capacity of POMs is generally more fully utilised at lower current densities as compared to high current densities.
- The small difference in active material mass loading has a greater impact at lower current densities but it becomes more evident at high current densities.
- The inherent variability in the hand-made assembly of the cells (a less obvious but sometimes an important factor).

Since we did not have "thin-electrodes" casted using the mixture of AC(YP-80F), CSP and PVDF-HPF, we compared the results of Th_AC(80F) and Th_AC{Na-V_{10}}

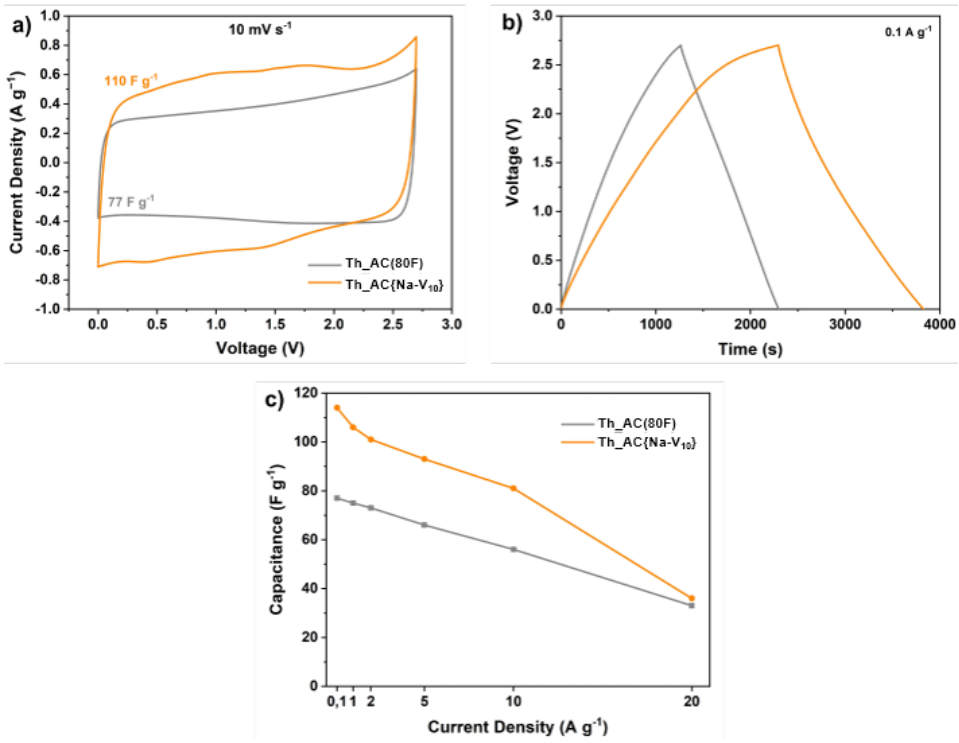

Figure 5.16: *Comparative performances of a symmetric supercapacitor cell made with two of our Th_AC{Na-V_{10}} electrodes and a symmetric cell with "blank" Th_AC(80F) electrodes, a) CP curves b) GCD curves, and c) specific capacitances at different discharge current densities. Th stands for thick.*

electrodes with the thin electrodes developed in Chapter 3 (AC and AC{Na-V_{10}}). The binder used in case of AC and AC{Na-V_{10}} electrodes was PVDF, so the comparison is not strictly rigorous, but it still gives us an indication of how the cell performance changes with an increase in mass loading.

Table 5.4 provides a comparison between "thin" and "thick" AC(80F) and AC{Na-V_{10}} electrodes. It is evident that for pristine AC electrodes at low current densities, when the mass loading increases from 1 to 3.8 mg cm^{-2}, there is an approximate drop of 25% in gravimetric capacitance. On the other hand, upon a 5-fold increase of mass loading in AC{Na-V_{10}} electrodes, there is a negligible loss in gravimetric capacitance, which is not usually expected for AC-POM hybrid electrodes.

Table 5.4: *Comparison of gravimetric capacitances between thin and thick electrodes.*

A g^{-1}	Pristine AC electrodes			AC{Na-V_{10}} Hybrid Electrodes		
	AC(80F)[a]	Th_AC(80F)[b]	Decrease in Capacitance	AC{Na-V_{10}}[a]	Th_AC{V_{10}}[b]	Decrease in Capacitance
	($F\ g^{-1}$)			($F\ g^{-1}$)		
0.1	102	77	25%	116	114	1%
1	99	75	24%	106	106	0%
2	97	73	25%	103	101	2%
5	92	66	28%	97	93	4%
10	84	56	33%	90	81	10%
20	71	33	54%	79	36	55%

[a] 10% PVDF binder, [b] 10% PVDF-HFP binder.

5.5 Discussion

Traditionally, thin single-layer electrodes have been fabricated to ensure electrolyte impregnation of an electronically conductive carbon network (Figure 5.17). However, this approach limits the potential of bulk electrodes, which can offer significantly higher device capacity and energy density. The ideal scenario, illustrated in Figure 5.17 d, involves achieving porosity throughout the multilayer thick electrodes. While our work demonstrates that this goal is achievable, it also highlights the numerous challenges that must be overcome. For instance, the freeze-casted electrodes led to multilayer structures with significant dead-end porosity (similar to Figure 5.17 c) and poor performance. In contrast, multilayer spray-coated thick electrodes showed much better areal capacitance compared to thin electrodes. However, since this improvement did not hold when normalised by mass, there is still room for improving our thick electrodes. Furthermore, when capacitance is normalised by volume, thick electrodes made using the multi-spray method exhibited higher volumetric capacitance than thin electrodes, but only at low scan rates. This suggests that while electrolyte penetration in thick electrodes may be adequate, other factors can limit ionic diffusion at higher rates. Overcoming these challenges should be our next collective objective.

Using CMC as a binder with CNTs as conductive carbon, produced electrodes with good mechanical strength. However, they were not particularly flexible. In contrast, thick electrodes made with the PVDF-HFP copolymer binder had good mechanical strength and flexibility. However, these electrodes required a higher binder content, increasing the proportion of non-active components in the supercapacitor. Since the areal capacitance of thick electrodes using either CMC or PVDF-HFP was similar, CMC with CNTs may be considered a better choice for developing thick electrodes due to its environmental friendliness, water solubility,

and the fact that a smaller amount is required. But if flexibility is to be included, then CSP and PVDF-HFP may be used for equally good results.

These thick electrodes showed increased areal capacitance with greater mass loading and thickness, but this trend did not extend to gravimetric capacitance at high scan rates. While thick electrodes exhibited high gravimetric capacitance at low scan rates, thin electrodes outperformed them at higher scan rates and maintained their performance more effectively. However, focusing solely on areal capacitance (as is often done for thick electrodes) can be misleading. Volumetric capacitance may offer a more accurate assessment of material performance as it considers the entire bulk of the electrode, which is crucial for practical device design. Nonetheless, volumetric capacitance does not account for the utilisation of active material, which can be better understood through gravimetric capacitance analysis. Therefore, a thorough evaluation of gravimetric, areal, and volumetric capacitance is necessary for each specific device to assess the performance of thick electrodes in order to ensure compact cells and optimal utilisation of active material.

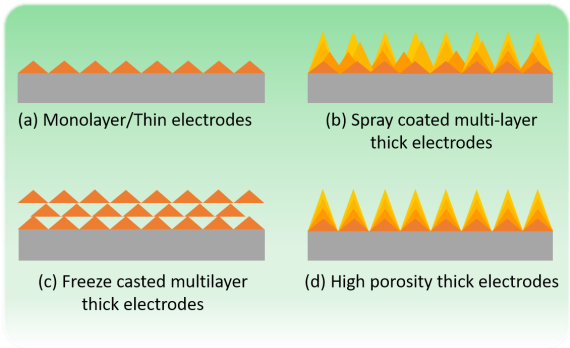

Figure 5.17: *Schematic representation of multilayer electrode structures exemplifying different microstructures, each leading to different porosities and electrode–electrolyte active areas.*

Porosity estimates and tortuosity analyses using impedance measurements were conducted to assess the pore structure and current collector-electrode-electrolyte interface of the electrodes. It was noted that dead-end pores in thick electrodes might be contributing to anomalously low tortuosity values. Thus, techniques like electron tomography, small angle X-ray scattering and X-ray computed tomography could be useful for further investigation of the pore structure. Although freeze-casted electrodes exhibited high porosity, they did not show high capacitance, indicating that a higher level of porosity does not automatically lead to better

performance. Instead, a balance is necessary between porosity and the contact between carbon particles within the electrode material. Ideally, a well-ordered pore structure with good carbon particle contact, as illustrated in Figure 5.17, would enhance performance across all metrics discussed in this study.

Additionally, modification of the current collector may help improve mechanical strength of thick electrodes. However their development should incorporate conductive pathways to reduce the amount of "non-active" components in the electrode. Moreover, relatively lightweight POMs such as polyoxovanadates, can be used to improve the capacitance of thick electrodes.

6

Nanopaste electrodes

6.1 Introduction

To flow or not to flow

The concept of improving active material loading in electrochemical energy storage cells is a well-researched topic. From solid "thick electrodes" to flow cells, many conventional methods have been explored. Yet, none of the strategies have been successfully commercialised. The title of this section is taken by our perspective article [3], where we analyse the challenges to design bulk electrodes for massive energy storage, from conventional batteries to Redox Flow Batteries and everything in between. The main challenge lies in increasing electrolyte accessibility to the bulk of the active electrode sites without losing electrical conductivity. This is generally believed to be the most important factor for enhancing power and cyclability without losing capacity and energy density in these thick electrode systems. However, solving this challenge is easier said than done and many difficulties arise frequently. For example, nano-confinement of liquids in 2D solids (Figure 6.1) was proposed to improve ionic transport; however, on repeated cycling, it leads to electrode exfoliation. On the other hand, the so called "semisolid" flow cells, have been successful in improving active material concentrations, but proper flow mechanism of these highly viscous fluids is still under development [3, 134].

Within this context, the field could evolve towards electroactive bulk "nanopastes" (Figure 6.1), which (in theory) could work as effectively as thick solid electrodes and would not need to be pumped. This alternative design could strongly contribute towards lower battery manufacturing costs due to an increased energy density since the mass of inactive components such as binders and, most importantly, current

collectors would be minimised. However, this would need an optimal balance between electron percolation through the solid particles of the paste plus electrolyte/ions percolation through the electrolyte part of the paste. In essence, solid and liquid networks should coexist, as illustrated in the nanopaste scheme in Figure 6.1.

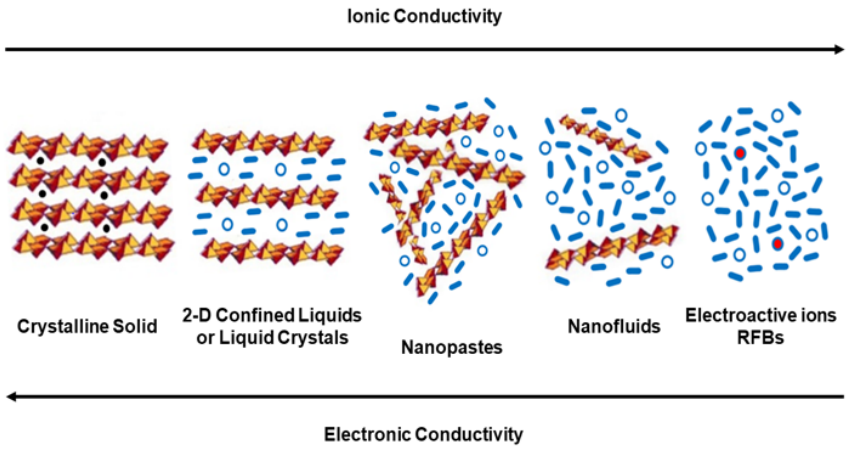

Figure 6.1: *Schematic comparative diagram of the stages involved in moving from compact solid electrode materials to dilute nanofluids and RFB solutions [3].*

These nanopastes could be extremely important for upcoming battery gigafactories since "pastes" are already well known by the battery industry for primary conventional cells. Therefore, the same concept could be translated to large-scale rechargeable batteries. Like for primary batteries, nanopastes could be developed with an internal electrolyte system in which the electrolyte would be nano-confined within solid electroactive particles. In this chapter we will explore proof-of-concept or preliminary experiments that pursue this idea. The nanopastes were developed using AC as a primary capacitive material. Conductive carbons such as carbon superP (CB), ketjen black (KB) and multi-walled carbon nanotubes (CNTs), were added to improve inter-grain conductivity (similar to conventional solid electrodes) in different aqueous and organic electrolytes (Section 6.2). These configurations were tested in a piston cell, described in Section 6.3 and 6.4.

6.2 Preparation of nanopastes

Carbon mixtures were first prepared by dispersing various amounts of carbons in 200 ml of water, stirring overnight and collected with vacuum filtration, which was followed by drying at 100 °C in a vacuum oven for 12 h. Pastes were prepared through manual mixing method by taking a designated amount of carbon solids and slowly adding electrolyte while mixing with a spatula. After a paste-like consistency was reached, the beaker was covered with parafilm and the material was sonicated in a bath sonicator with ice cold water for 3-5 min.
The nanopastes using AC, conductive carbons and 1 M H_2SO_4 were prepared as per Table 6.1.

Table 6.1: *Formulations of nanopastes with different carbon masses and 1 M H_2SO_4 electrolyte volume.*

Electrode Material	AC (g)	CB (g)	CNT (g)	KB (g)	1 M H_2SO_4 (ml)
$(AC)_{1g}$ (1 M $H_2SO_4)_{2ml}$	1	-	-	-	2
$(AC)_{1g}$ (1 M $H_2SO_4)_{3ml}$	1	-	-	-	3
$(AC)_{1g}$ $(CB)_{0.1g}$ (1 M $H_2SO_4)_{2.8ml}$	1	0.1	-	-	2.8
$(AC)_{1g}$ $(CB)_{1g}$ (1 M $H_2SO_4)_{8ml}$	1	1	-	-	8
$(AC)_{1g}$ $(CB)_{0.05g}$ $(CNT)_{0.2g}$ (1 M $H_2SO_4)_{4.3ml}$	1	0.05	0.2	-	4.3
$(AC)_{1g}$ $(KB)_{0.1g}$ (1 M $H_2SO_4)_{3.1ml}$	1	-	-	0.1	3.1

The nanopaste with AC and 1 M Na_2SO_4 was prepared as per the formulation in Table 6.2.

Table 6.2: *Formulations of nanopastes with 1 M Na_2SO_4.*

Electrode Material	AC (g)	1 M Na_2SO_4 (ml)
$(AC)_{1g}$ (1 M $Na_2SO_4)_{2ml}$	1	2

The nanopaste with AC, CB (or CSP) and 1 M $TEABF_4$ in acetonitrile was prepared as per the formulations in Table 6.3. The same formulation was used in two cells with 0.5 g and 1 g of nanopaste in each electrode.

Table 6.3: *Formulations of nanopastes with 1 M $TEABF_4$ electrolyte.*

Electrode Material	AC (g)	CSP (g)	1 M $TEABF_4$ (ml)
$(AC)_{1g}$ $(CB)_{0.1g}$ (1 M $TEABF_4)_{3.3ml}$	1	0.1	3.3

A nanopaste was also prepared using the AC{Na-V_{10}} hybrid material prepared in Chapter 3. The conductive additive used were CNTs and electrolyte was 1 M $TEABF_4$ in acetonitrile. This AC{Na-V_{10}} nanopaste was prepared as per the formulation in Table 6.4.

Table 6.4: *Formulations of AC{Na-V_{10}} nanopastes with 1 M $TEABF_4$ electrolyte.*

Electrode Material	AC{Na-V_{10}} (g)	CNT (g)	1 M $TEABF_4$ (ml)
$(AC\{Na\text{-}V_{10}\})_{1g}$ $(CNT)_{0.1g}$ $(1\ M\ TEABF_4)_{1.8ml}$	1	0.1	1.8

6.3 Piston cell design

For the electrochemical characterisation of paste electrodes, it was necessary to design an ad-hoc cell which would provide air-tightness and allow for the application of a certain pressure to the paste electrode samples. The "piston cell" used in the work described here was designed by Verónica Fabián Puerta for her PhD work at ICN2 in collaboration with Napptilus Battery Labs. The device fabrication was carried out both in the Mechanical Workshop Facility at ICN2 as well as with the help of external workshop services.

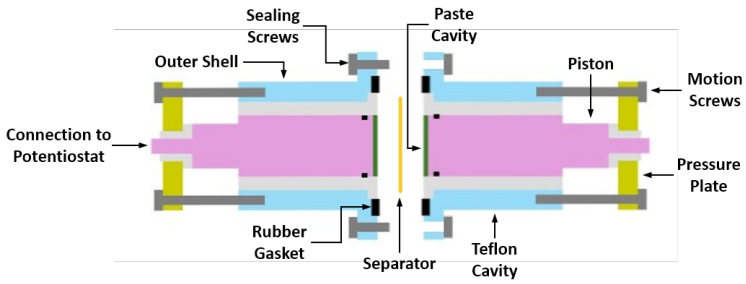

Figure 6.2: *Schematic design of a piston cell*[i]*. O-rings in black, nanopaste electrodes in green and separator in orange.*

This piston cell is a 2-electrode cell developed to contain and test the electrochemical performance of a paste-like or semi-solid electroactive materials with high viscosity and low electrolyte content. The cell consists of two identical stainless steel (304) outer shells that each contain a movable 'piston' surrounded by a Teflon cavity

[i]Figure assembled by Prof. Pedro Gómez-Romero based on a figure provided by Verónica Fabián Puerta.

to allow easy movement of the piston (Figure 6.2). A rubber gasket on each side is provided to seal the cell and prevent electrolyte leakage. The paste is deposited on each cavity along with a separator and closed with six screws and bolts (Figure 6.3). The movable pistons perform the dual role of exerting pressure on the paste as well as acting as current collectors.

6.4 Piston cell assembly

The cell assembly was performed as follows:

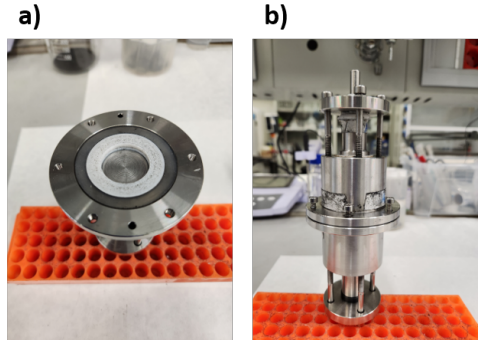

Figure 6.3: *Photographs of a) half electrode part and b) fully assembled piston cell.*

- The pistons were retracted to at least 1 cm depth to allow paste filling (Figure 6.3 a). Generally, 1 g of total paste was transferred to each electrode.
- After this, a Whatman 4 paper separator of 42.5 mm diameter was soaked with 0.5 ml of electrolyte and then placed on one of the piston sides. This was done to prevent the separator from absorbing the electrolyte from the paste.
- The other part of the piston cell with paste was placed vertically on top of the first part with separator and closed using screws (Figure 6.3 b).
- Then the pistons on the end of the cell were moved by equally turning each screw on both sides by 180° until a slight resistance on the movement was observed. Afterwards, the screws were rotated at a 90° angle until further pressure was felt, but were stopped before any electrolyte leakage. This type of slow but methodical movement of the pistons allowed for an approximately equal pressure on both electrodes. This was verified by measuring the depth of the cell through a Vernier caliper during disassembly and cleaning.

6.5 Morphological characterisation

The characterisation techniques used to understand the true nature and microstructure of nanopastes were limited and hence, different types of SEM were primarily deployed to understand nanopaste structure and to empirically observe solid-electrolyte interactions. First, solid mixtures of AC with different conductive carbons were observed to see the comparative size and morphology of different carbon particles at various magnifications. However, the structure of the nanopaste would be very different depending on the amount of electrolyte and pressure applied to the cell. Hence, two preliminary tests using Environmental SEM and Cryo-SEM were performed with the nanopaste containing AC, CSP and CNT in order to see their distribution within the nanopaste. The electrolyte used in these cases was 0.5 M Na_2SO_4 to avoid corrosion inside the microscope and the paste composition was: $(AC)_{1g}$ $(CB)_{0.05g}$ $(CNT)_{0.15g}$ $(0.5\ M\ Na_2SO_4)_{2.3ml}$.

Figure 6.4 displays SEM photographs of several of the carbons mixtures prepared showing how conductive carbon particles are dispersed between AC particles when they are simply mixed together. The size of AC particles is in microns whereas the conductive carbons are only a few nanometres in size. While this allows for good conductivity between AC particles in thinly layered solid electrodes, one wonders if the particle size variation by a factor of 10^3 is ideal for nanopastes? The answer to this question may not be so obvious as the interaction with electrolyte and pressure become crucial factors. Nevertheless, it seems clear that larger amounts of conductive carbons would lead to performance improvement. Furthermore, it could be interesting to combine carbons with particle sizes of different orders of maginitude. For example, commercially available solutions could be AC with CB and CNT in appropriate volumes. On the other hand, AC particle size could be varied with ball milling, and bespoke conductive carbons of different orders of magnitude may also be developed.

Figure 6.5 shows SEM images of the real nanopaste $(AC)_{1g}$ $(CB)_{0.05g}$ $(CNT)_{0.15g}$ $(0.5\ M\ Na_2SO_4)_{2.3ml}$ (pressed paste electrode) with different humidity levels. A specific area was observed as the solvent (in this case water) evaporates. We can confirm that there are cavities present in between carbon particles and contact between them is not ideal. This may be resolved with addition of more conductive carbon and/or reducing the amount of electrolyte. Since the carbons cannot be properly observed with high humidity levels, Cryo-SEM was also attempted. Figure 6.6 shows Cryo-SEM of a cross-section of the same composition nanopaste at

different magnifications. As the electrolyte is frozen between carbon particles, it is again difficult to observe the morphology of the nanopaste. Thus, under our experimental conditions and constrains, Cryo-SEM was not found to be a very useful method to study our nanopastes.

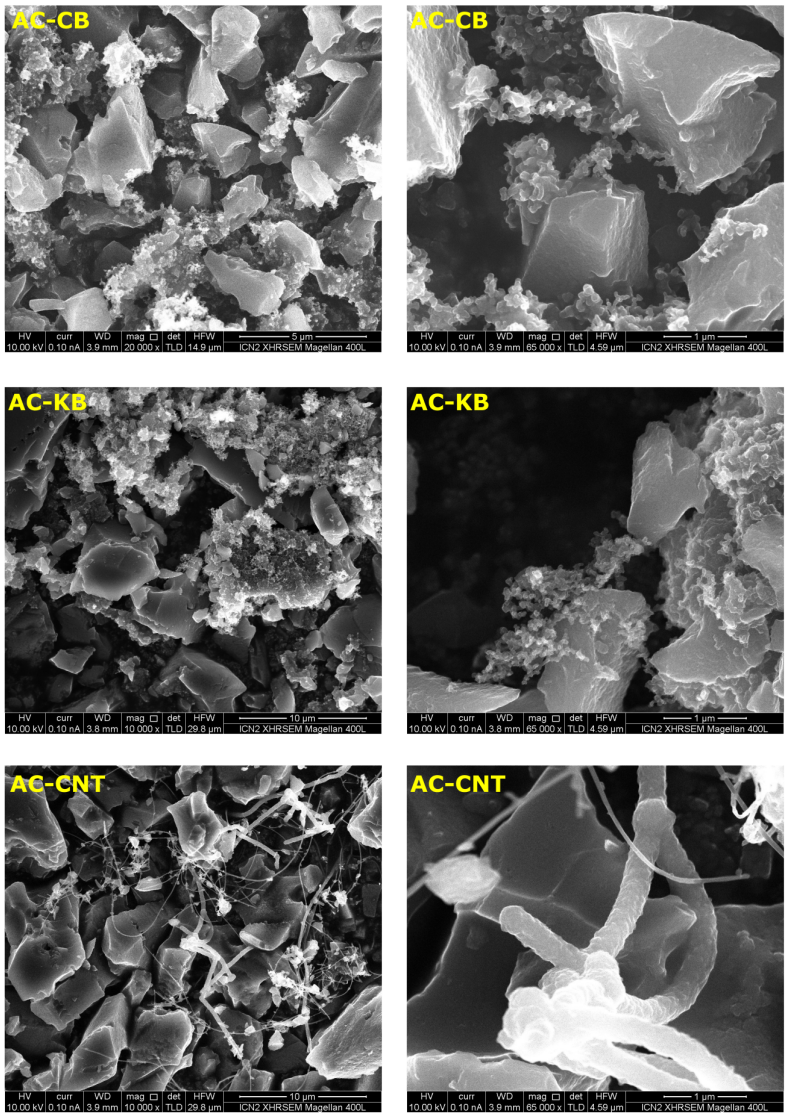

Figure 6.4: *SEM images of AC-CB, AC-KB and AC-CNT solid mixtures in 9:1 ratio. Here CB is alternatively used for CSP.*

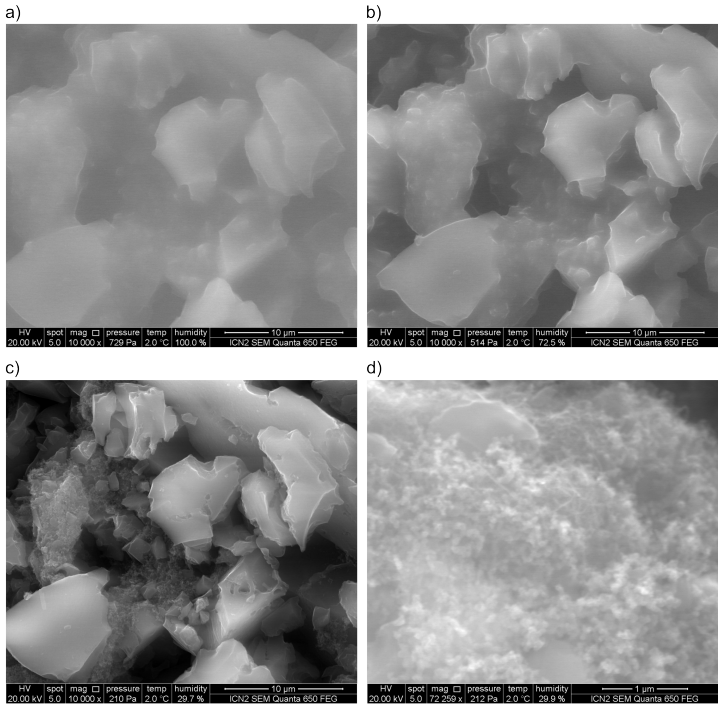

Figure 6.5: *Environmental SEM images of AC-CB-CNT nanopaste with 0.5 M Na_2SO_4 at a) 100%, b) 72%, c) and d) 30% humidity levels.*

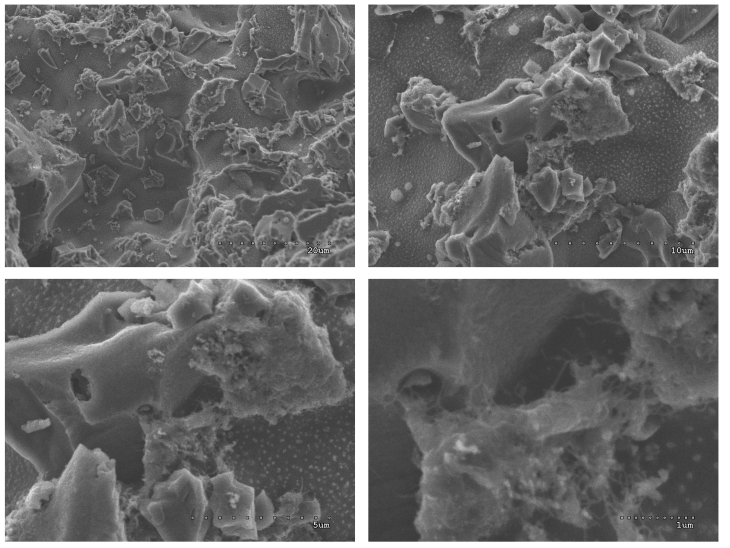

Figure 6.6: *Cryo-SEM images of AC-CB-CNT nanopaste with 0.5 M Na_2SO_4.*

6.6 Electrochemical measurements

The nanopastes were prepared as per Section 6.2 and assembled in a piston cell as described in Sections 6.3 and 6.4. Figure 6.7 shows a disassembled piston cell with nanopaste after electrochemical testing.

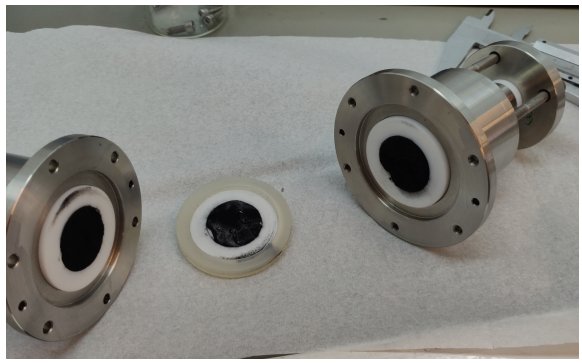

Figure 6.7: *A disassembled piston cell with nanopaste after electrochemical testing.*

6.6.1 1 M H_2SO_4 electrolyte

AC - 1 M H_2SO_4

The first set of experiments were aimed at understanding how to optimise solid to electrolyte ratio. Hence, 1:2 and 1:3 (wt/vol) ratio of AC and 1 M H_2SO_4 electrolyte were tested. In both cases, the CPs at 10 mV s^{-1} were not rectangular, which would be expected from purely supercapacitive materials. Instead, a tilted "flower-petal" like shape was observed (as shown in Figure 6.8 a). This indicates high internal resistance of the electrode. Moreover, increasing the amount of electrolyte did not translate in better performance. In fact, it led to lower capacitance as the electrolyte-richer paste did not perform as well as the original paste (Figure 6.8 b). This could be attributed to poor contact between the carbon particles due to larger amounts of electrolyte and hence poor contact between AC-AC particles leading to poorer electrical conductivity. This represents the opposite scenario to conventional solid electrodes, where electrode resistance is low due to the strong electrical contact between AC-AC particles, and between the AC particles and the current collector. Thus, maintaining a right ratio of active material and electrolyte was one of the most important factors for developing these nanopastes.

AC - CB - 1 M H_2SO_4

The next set of experiments evaluated the effects of the addition of CB (or CSP) conductive material to lower resistance and improve capacitance of the electrode. As in the case of conventional bar-coated thin electrodes, conductive carbons were expected to improve the performance of the nanopastes. CB particles are a good candidate for nanopastes due to their spherical shape and small size (< 1 nm). However, adding even a small amount of CB required more electrolyte to reach a paste-like texture due to the large volume of CB particles. The AC-CB mixture was prepared in a 1:1 and 1:0.1 (wt/wt) ratio to measure their impact on electrode resistance.

As seen from Figure 6.8 c, both CPs change to a more rectangular, supercapacitor-like shape due to lower resistance. This was also confirmed with an improvement in overall capacitance as compared to only AC containing paste (Figure 6.8 d). As expected, a more rectangular CP shape and better capacitance was observed in the paste with higher amount of CB. This AC to CB ratio would need to be further optimised to get better performance of nanopaste electrodes. But as a general conclusion we confirmed that the addition of CB, despite the associated incorporation of more electrolyte to the paste, leads to a better performance probably associated to an improved inter-particle connection and greater conductivity.

Other Carbons - 1 M H_2SO_4

The success of CB in improving paste performance led to additional experiments with other conductive carbons. CNT and KB were chosen due to:

(i) Long range of CNTs which could be combined with small spherical CSP particles and would add another dimension of conductivity to the nanopastes,

(ii) Nano-size and lower density of KB, which could replace CB and reduce electrode resistance [112].

The formulation was prepared as per Table 6.1. The AC-CB-CNT nanopaste electrode showed a minor improvement in capacitance in comparison with only AC paste (Figure 6.8 d). In the case of AC-KB, slightly lower capacitance was observed. Nevertheless, since the AC to carbon additive ratios were not optimised, KB may still be a promising material for improving paste conductivity in a different composition.

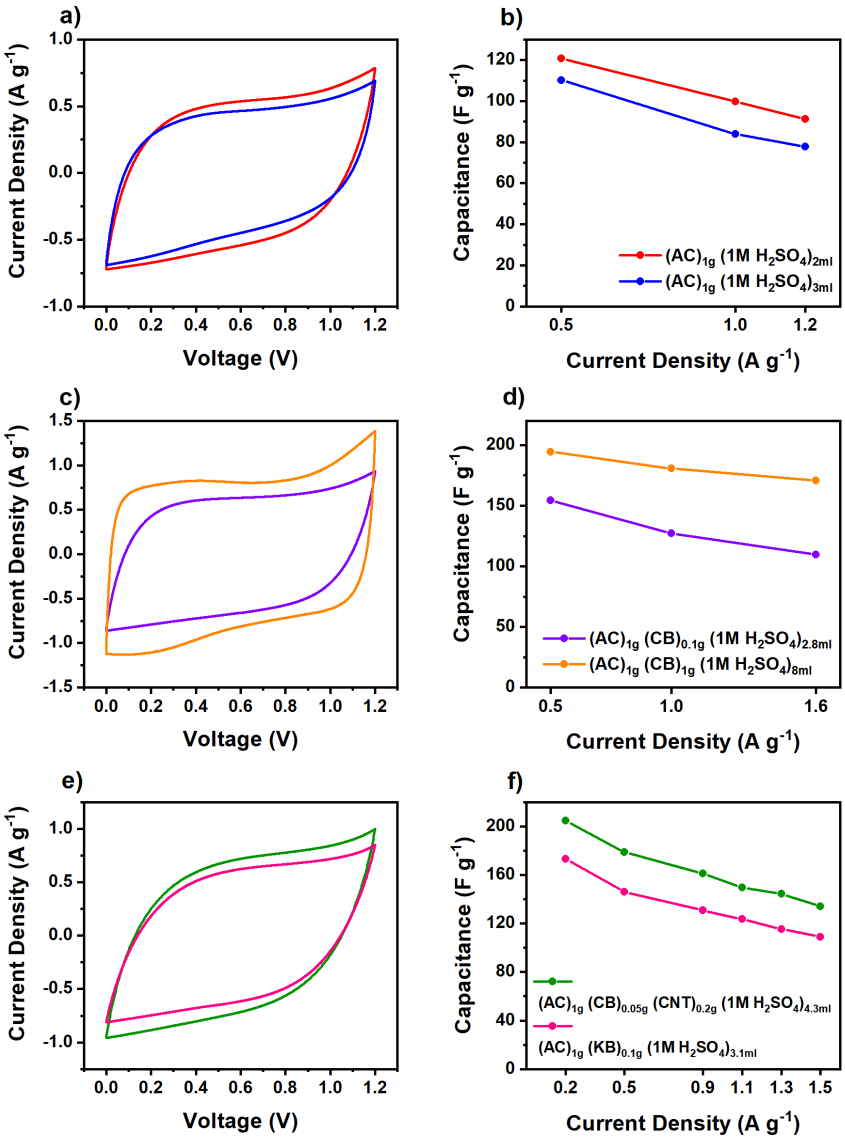

Figure 6.8: *CP at 10 mv s^{-1} and GCDs at various current densities for different paste compositions with 1 M H_2SO_4 electrolyte, as indicated.*

6.6.2 1 M Na_2SO_4 and 1 M $TEABF_4$ electrolyte

AC - 1 M Na_2SO_4

Alternative sodium-based electrolytes were also tested for nanopaste formulations. Paste electrodes containing 1 M Na_2SO_4 electrodes were prepared and assembled as per Table 6.2. The electrodes had much lower capacitance values (Figure 6.9 b), which was expected due to the larger ionic size of (solvated) Na^+ in Na_2SO_4 solutions and greater (proton) ionic conductivity of aqueous sulphuric acid through the well-known Grotthus mechanism.

AC - CB - 1 M $TEABF_4$

To extend our comparative study to other electrolytes, 1 M $TEABF_4$ in acetonitrile was tested as it is a well-known organic electrolyte for AC-based supercapacitors. Furthermore, the voltage window can be extended up to 2.7 V in acetonitrile, which in theory would improve the specific energy of the cell. The electrolyte was tested with AC and CB in two configurations: (i) 1 g of total paste per electrode and (ii) 0.5 g of total paste per electrode as shown in Figures 6.9 c and f. Unsurprisingly, the cell with lower mass loading performs slightly better than the other due to lower overall resistance. The future work could involve assessing this difference in nanopaste electrode mass loading with a higher ratio of conductive carbon.

AC{Na-V_{10}} - CNT - 1 M $TEABF_4$

A nanopaste with the hybrid material AC{Na-V_{10}} prepared in Chapter 3 was tested to extend the utilisation of decavanadates to a novel thick electrode. The addition of V_{10}-POM improved the overall gravimetric capacitance and rate capabilities of the electrode (Figure 6.10). Redox peaks were not observed in the CP at 10 mv s^{-1}. Moreover, the stability of V_{10}-POM in an environment with high electrolyte concentration would need to be studied.

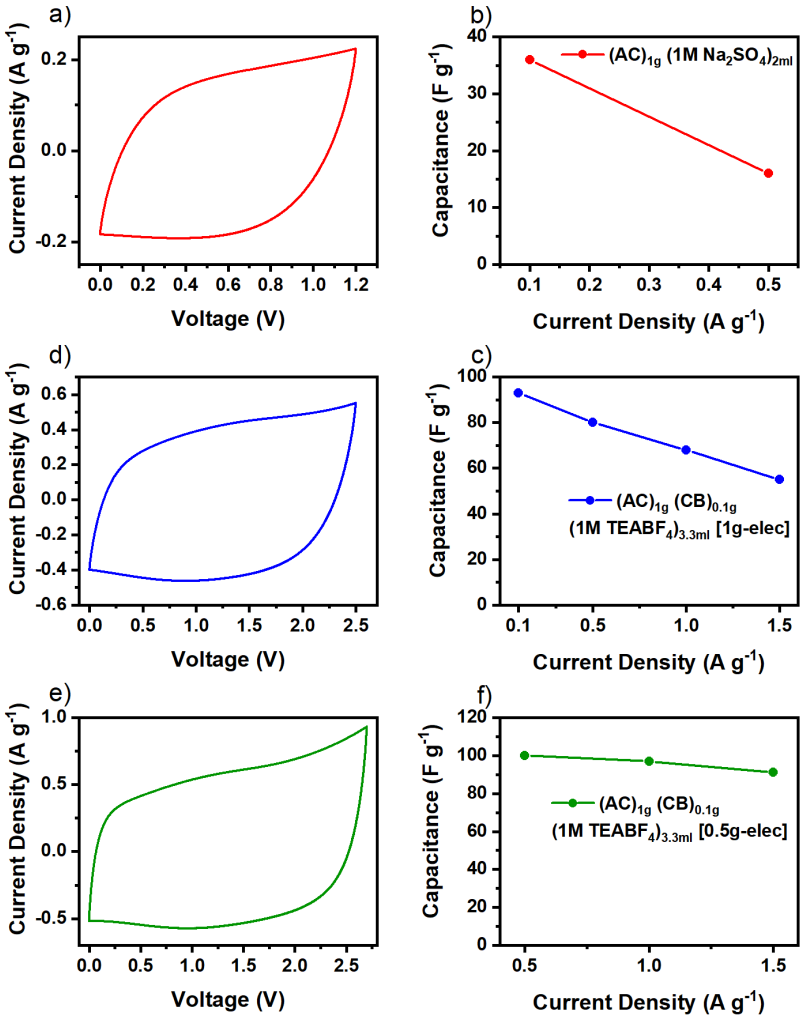

Figure 6.9: *CP at 10 mv s^{-1} and GCDs at various current densities for different paste compositions with 1 M Na_2SO_4 and 1 M $TEABF_4$ in MeCN electrolyte.*

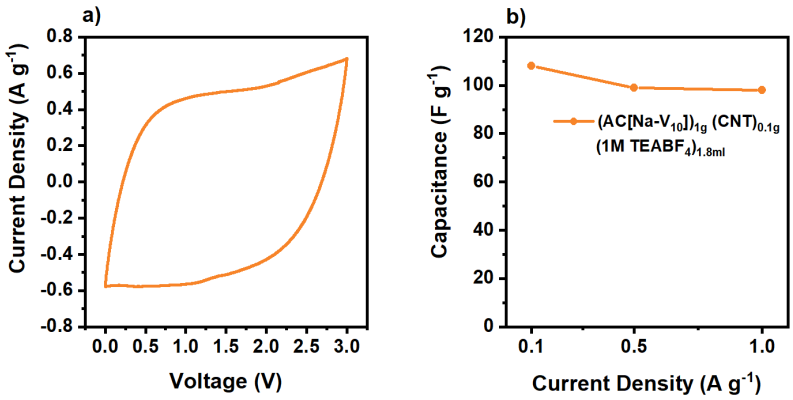

Figure 6.10: *a) CP at 10 mv s^{-1} and GCDs at various current densities for nanopaste composed with AC{Na-V_{10}} hybrid material, CNT and 1 M $TEABF_4$ in MeCN electrolyte.*

6.7 Challenges

The piston cell proved to be a moderately adequate first attempt solution to contain the pastes while providing the option to apply pressure to improve contact between individual carbon particles. However, it lacked certain features to test this novel electrode concept, which led to major difficulties impeding electrochemical characterisation. For example, the primary challenge was ensuring reliable replication of results. Figure 6.11 shows the CVs at 10 mV s^{-1} and GCDs at 0.5 A g^{-1} of two identical cells repetitively assembled on different days with the same composition and mass loading. Although all measurements were carried out immediately after cell assembly, the CP of Cell 1 had larger area than Cell 2 which was similarly reflected in the GCDs. In terms of final capacitance results, not much difference was observed in this case with Cell 1 having a specific capacitance of 121 F g^{-1} and Cell 2 with 120 F g^{-1}. However, this example was a good indicator of the typical variability in studying the reproducibility of the results.

At this point, it should be remarked that similar variations in reproducibility can be also found in conventional coin cell studies. Mass loading, electrode mass balancing, cell assembly with accurate electrode placement and quantity of electrolyte can play a major role in replicating results [135, 136]. In case of piston cells, these errors were not as significant because the mass loading was much higher, electrode placement is always accurate in paste cavity and electrolyte is mixed with active material. Therefore, the difference must arise due to variability in pressure exerted on the cell by the movement of pistons, whereas in coin cells pressure is not

a major factor as it can be easily made consistent using spacers and springs.

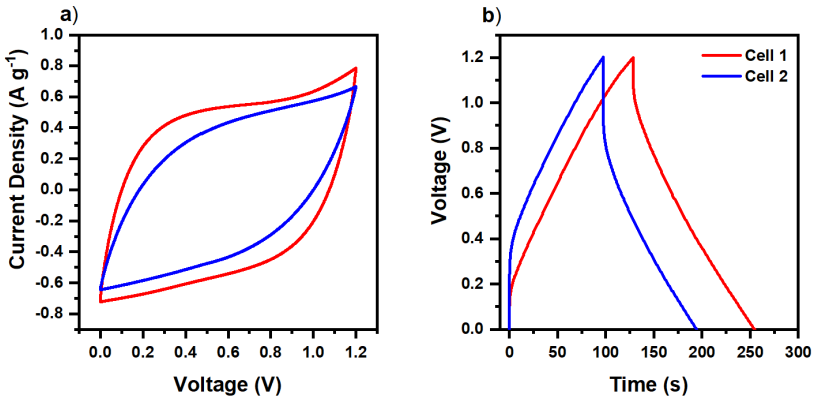

Figure 6.11: *a) CPs at 10 mV s^{-1} and b) GCDs at 0.5 A g^{-1} (cycle 3) of two different (repetitive) cell assemblies with same paste composition of $(AC)_{1g}$ (1 M $H_2SO_4)_{2ml}$.*

Furthermore, this piston cell did not allow measuring the pressure applied to the cell in real time during each step. This uncertainty not only posed a problem in replication of results with same composition, but also for comparing different compositions accurately. Since each paste composition consisted of different types and quantities of carbons as well as varying electrolyte amounts, different pastes had different volume even if the mass per electrode was kept the same. Therefore, it was not possible to set or apply an optimal pressure on each electrode with this device. Similarly, standardising electrode volume instead of electrode mass would also not provide the desired outcome due to the reasons mentioned above. Moreover, during cell assembly electrolyte leakage was sometimes observed if too much pressure was applied to the cell. This would change the composition of the paste and impact the results.

The independent movement of the two pistons also proved to be a difficulty in ensuring equal pressure on both electrodes. Without accurate pressure or distance measurement, it could be very likely that the two electrodes would not be of equal thickness if pistons were not moved the same distance. This could lead to unequal pressure on the two electrodes. While care was taken during movement of the pistons, electrode thickness could only be verified during post-mortem analysis of the cell using a Vernier caliper. Occasionally, some experiments ended up showing unequal electrode thicknesses, in which case the results were discarded.

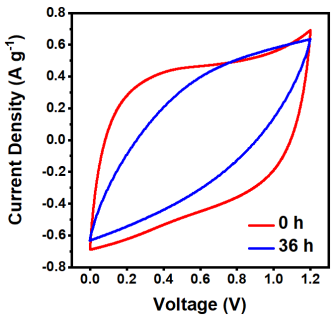

Figure 6.12: *CVs of $(AC)_{1g}$ (1 M $H_2SO_4)_{3ml}$ after assembly and after 36 h.*

Another great challenge was ensuring the "air-tightness" of the piston cell. Despite cell design catered to prevent evaporation using gaskets and seals, slight electrolyte evaporation was still observed when the cell was left running for several days. For example, CVs of $(AC)_{1g}$ (1 M $H_2SO_4)_{3ml}$ were analysed after cell assembly and then after 36 h (Figure 6.12). It was seen that the CVs changed to more resistive curves most likely due to electrolyte evaporation. In general, the evaporation rate of organic electrolyte was observed to be very high (Figure 6.13). This hindered the analysis of the cyclability of nanopaste electrodes. To reduce electrolyte evaporation, all cells were wrapped in parafilm and tests were performed immediately after assembling the cells.

Thus, the reliability of results was found to be extremely dependent on cell assembly. With these considerations, each cell assembly was carefully monitored. In case of electrolyte leakage, unequal cell volume, etc., the results were discarded. Therefore, the presented results were generally seen to be reliable for comparing different paste compositions over a short time period.

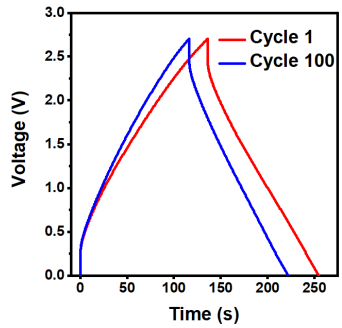

Figure 6.13: *Charge-discharge of 1^{st} and 100^{th} cycle of $(AC)_{1g}$ $(CB)_{0.1g}$ (1 M $TEABF_4)_{3.3ml}$ [0.5 g-electrode] cell.*

A different obstacle emerged while deciding the parameters to normalise the capacitance. The standard measure of normalisation for electrode materials is the active material mass in the electrode. Alternatively, area and volume of electrode are also considered for thick electrodes, as discussed in Chapter 5. In case of nanopastes, binders materials were absent, but larger amount of electrolyte was needed as compared to solid electrodes, due to the fact that the carbons absorbed a lot of electrolyte.

One option presented was to normalise with mass of the total electrode bulk, which includes conductive carbons as well the electrolyte mass. However, for such thick electrodes, the performance would be very difficult to compare with existing state-of-the-art technologies. If area was chosen for normalisation, then due to

the extremely high mass loading, the performance would be superior but it would not reflect the utilisation of the material. Meanwhile, volumetric normalisation would be challenging as the volume can only be studied after disassembling the cell. Thus, a decision was made to stay with the status-quo of normalising all parameters by active material mass for simplicity. Indeed, once the issues related to cell design and characterisation are resolved, this would need to be assessed and perhaps normalisation with both, total electrode mass and volume, should be preferred for a final cell.

This leads to self-critique of the work where total electrode mass (including electrolyte and conductive carbons) of 1 g (unless specified) was chosen to be transferred to each electrode. This raises the obvious question that the active material (AC) mass loading of all paste compositions would be different. As we know from the case of solid electrodes, varying the mass loading of the same electroactive material, can vary the results. The best practices for laboratory testing is to have 1-2 mg cm^2 of active material and keep similar conductive carbon ratios while comparing different materials. But this was a difficult task to achieve for nanopastes due to practical limitations at the time. Therefore, 1 g per electrode was selected for transferring the paste quantity, creating slight inconsistency in the measurement methods. While, this issue was recognised from the start, it was consciously kept on the back-end of priorities due to the other major challenges already mentioned such as pressurisation, electrolyte evaporation, etc. Due to these issues not being resolved until the completion of the thesis work, further tests were not performed.

6.8 Future improvements

6.8.1 Cell design

To make the cell completely sealed and to prevent electrolyte evaporation, the piston cell design would need to be completely overhauled. The cell cannot be fully air-tight due to its inherent design that allows ease of opening, closing, pressurising and re-use. The currently available commercial sealable (and single-use) options such as coin-cells and pouch cells were initially tested for nanopastes but proved to be difficult in containing the "paste" like consistency. Cylindrical cells are popular for primary batteries and could be an interesting candidate for paste electrodes as well. However, filling and separating pre-prepared pastes into a cylindrical cell was found to be extremely challenging in a non-mechanised environment. Therefore, a

completely new design would be needed to resolve all the above mentioned problems.

At the same time, some of the challenges mentioned in Section 6.7 can be mitigated by minor design improvements. For example, the 4 screws on each size of the piston (Figure 6.2) can be replaced with springs for uniform control. The movement of the pistons could be controlled by attaching a "micrometre-type" set up with a graduated sleeve, thimble and a rachet stop to ensure precise movement on each piston. This would help knowing the electrode thickness before disassembly. A dynamometric key could also be used if the right pressure for each paste is predetermined. Thin film flexible pressure sensors could also be used inside the cell to measure the pressure subjected to the paste. However, external connections might facilitate electrolyte leakage and/or evaporation. Moreover, the sensors would have to be tolerant to the electrolyte.

6.8.2 Nanopaste preparation

Manual method of paste preparation through short-duration sonication may not ensure electrolyte permeation throughout the bulk of the solid particles. As a simple alternative, a homogeniser equipment such as Dispermat may be used for speeding up the process of dispersing carbons as well as making pastes with non-volatile electrolytes. Planetary centrifugal mixer could also be useful for proper dispersion of carbons and electrolyte. To avoid electrolyte evaporation during paste preparation, a temperature-controlled environment would be advisable as one among many solutions.

6.8.3 Nanopaste characterisation

Techniques for characterising conventional solid electrodes are widely available and well known. However, some of them such as SEM, are not directly suitable for nanopaste characterisation. Moreover, nanopastes require study of parameters that may not be necessary in the case of conventional electrodes. For example, to properly characterise different paste compositions, a Rheometer for rheology measurements should be used. This would help identify the correct viscosity of different nanopastes. In addition, studying the solid-electrolyte interaction would be even more prominent for nanopaste electrodes. NMR dipolar cross-relaxation could be used for understanding nano-confined fluids with the matrix solids [137], while low frequency NMR to study the intra-/inter-molecular motion, diffusion processes, as well as dynamic, thermodynamic and structural properties of fluids.

Such studies could not only provide an insight into the nanopastes but also assist in improving the formulations and performance of such nanopastes.

After the cell design is improved, electrochemical characterisation results could be normalised by total mass of the electrode as well as by cell volume, providing a more practical and industrial outlook for this technology. Once the above-mentioned improvements are managed, the role of conductive carbons and their right formulations could be studied systematically with more reliability.

6.9 Discussion

A proof-of-concept study to develop and test nanopastes was carried out. Nanopastes can be useful to develop a new line of thick electrodes that are in between conventional flowable and non-flowable technologies. This preliminary study helped understand electrochemical behaviour of several nanopaste formulations and their performance with different conductive carbons and electrolytes.

Nanopastes can perform as ultra-thick electrodes with very high mass loading and without any binder. Their capacitance critically depends on a multitude of factors such as the amount of conductive carbon in the electrode, ratio of carbons to electrolyte or rheology of the nanopaste, pressure applied to the electrode bulk, etc.

Finally, in addition to the specific problems and possible solutions discussed in this chapter, we should consider this experience as a demonstration of the need to co-develop material components and cells in a concerted way when it comes to disruptive technologies like the ones we are implementing.

Part III

Devices to Applications

Context

The end of the 20^{th} Century witnessed the general adoption of Li-ion batteries to feed consumer electronics. It was a specific storage technology for a technological sector with specific demands, mostly lightweight and compactness. Durability and price were not important since the products that those batteries cater to, are expensive and intended to be replaced every few years. The first quarter of the 21^{st} Century is witnessing an increasing wealth of applications for electrochemical energy storage technologies, each with its own specific demands but, generally speaking, with safety, durability and cost at the top of their priority list.

The first stages of the new energy storage outbreak took place by taking "off-the-shelf" batteries (i.e. Li-ion batteries at the time) and putting them to work everywhere, from electric vehicles (EVs) to stationary energy storage. Also, different EESS technologies like redox-flow batteries were taking over specific niches of applications. As discussed in Chapter 1, the different applications may have varying requirements such as response time, time of storage, weight or volume restrictions, mobility, minimum life-time, costs, etc. The storage time vs. applications is given

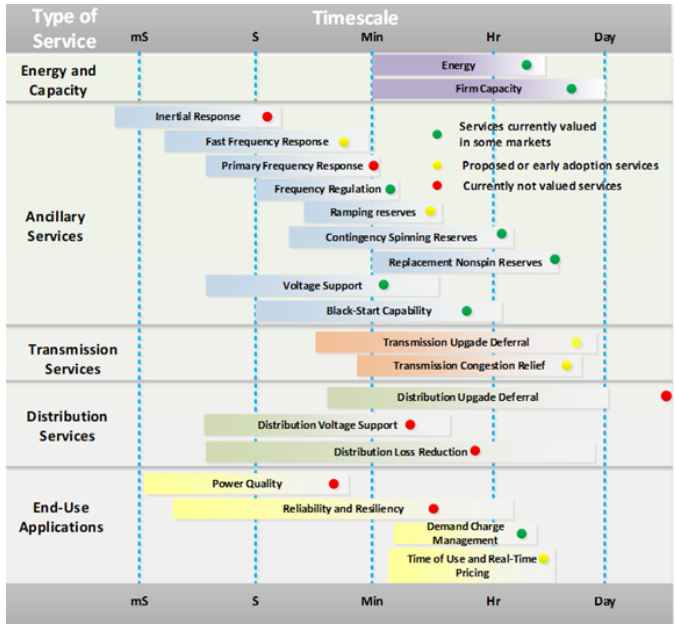

Figure 6.14: *Types of services and timescale for stationary grid applications. Green = currently valued in some markets, yellow = early adoption/proposed, and red = currently not valued [138].*

by Figure 6.14.

This trend of different storage technologies for different applications will necessarily keep growing in the future. Furthermore, it would be desirable to have co-designing processes among materials, components, devices, systems and novel applications, as we analysed in a recent "perspective" article [3]. In this section of the thesis (**Chapter 7**) we analyse one such application which is frequency regulation that could benefit from the development of novel materials and devices, namely that of frequency regulation in grids.

7

Frequency regulation of wind power plants by electrochemical energy storage

7.1 Introduction

The rising share of renewable energy (RE), particularly wind, has raised concerns about reduced grid inertia and the challenges of managing disturbances due to the variable nature of these energy sources. As offshore wind technology becomes more commercially viable, the proportion of wind energy in the power mix is only poised for further expansion. However, wind turbines (WTs) lack the ability to provide inertia because they are decoupled from the grid through converters [139]. Grid inertia is crucial for maintaining frequency stability by supplying power over a short duration, giving the system time to stabilise before additional generation comes online or a load is shed [140].

The decommissioning of numerous nuclear and thermal power plants worldwide, along with increasing costs and supply-chain challenges related to gas imports, has heightened concerns about the future grid stability [141]. Therefore, as RE based energy generation increases, providing ancillary services becomes even more important.

This section of the thesis, examines the energy storage story from an application point of view. As mentioned in Chapter 3, AC-POM hybrid materials function well in the energy/power realm between supercapacitors and batteries. These materials are ideal for applications requiring repeated cycling, high power and slightly larger energy applications in comparison with conventional carbon-based double-layer supercapacitors. The application fields that require such configurations in the

current market are frequency regulation and electric vehicle acceleration. In this section, we examine the former, due to its utmost importance for our current energy system.

To this end, the 1^{st} and major part of Chapter 7 takes a look at how a battery can perform frequency regulation services in a high wind penetration environment. Generally thermal generators or pumped hydro (if available) have the capability of providing small amounts of ramping support, but are slow in response. Over the years, other complementary strategies such as simultaneous wind–battery control have been proposed to enhance grid support since it would reduce dependence on a single type of generator. However, further research is needed to conduct a comprehensive sensitivity analysis on the impact of different WT control strategies and to compare these with battery energy storage systems. Therefore, we examine WT control strategies that incorporate a battery, evaluating their individual effects on frequency regulation during grid disturbances. We then assess the combined impact of these controls and adjust their response capabilities to develop improved control strategies that enhance frequency regulation.

In the 2^{nd} section of Chapter 7, we compare the parameters of a conventional Li-ion battery with our AC{V_{10}}||AC asymmetric cells developed in Sections 1 and 2. We extrapolate the experimental results and propose these hybrid materials as better alternatives to using Li-ion batteries or AC supercapacitors.

7.2 Impact of BESS-integration in frequency control of an electrical grid with wind power

7.2.1 State-of-the-art control strategies for frequency regulation in wind power plants

Traditionally, inertia control has been managed through governor control of synchronous machines and the use of swing or backup generators. Depending on the country, the grid frequency is either 50 or 60 Hz, and any imbalance between generation and load causes deviations from these standard values. The rate of change of frequency (ROCOF) is expressed by the swing equation [140].

$$\frac{df}{dt} = \frac{f_0}{2H_{sys} \cdot S_G}(P_m - P_e) \tag{7.1}$$

Where df/dt is the ROCOF, f_0 is the system frequency, while H_{sys}, S_G, P_m and P_e are the system inertia constant, generator rated power, mechanical power

and electrical power, respectively.

Wind power plants (WPPs) have traditionally not been involved in frequency regulation due to the operational characteristics of older permanent magnetic synchronous generator (PMSG) turbines, which function in maximum power point tracking (MPPT) mode and cannot adjust their speed to vary output power. Although coordinated PMSG wind turbine control strategies have been developed to simulate a combined inertia response from the turbines and generator to provide short-term frequency support, these strategies are still not widely adopted [142]. In contrast, newer variable-speed wind turbines (VSWTs) are capable of being externally controlled through various mechanisms to provide inertia response [143–147]. For instance, inertia control can inject energy into the system in response to the rate of change of frequency or ROCOF, while droop control is based on the difference between frequency levels [148, 149]. Additionally, deloading control involves shifting the wind turbine's operating point from optimal to reduced power output, which is achieved through adjustments in speed and pitch angle [150–153].

Wind turbine control strategies can also be integrated with other generators on the grid to enhance frequency regulation. For example, a coordinated control strategy with time-varying gains for inertia and droop control loops has been developed [154]. These control loop gains can be adjusted based on the desired frequency-response time, with initial gains determined by the wind speed and operating conditions of each WT within the farm. Additionally, a coordination strategy between WT droop control and synchronous machines, allows conventional generators to inject power immediately after the frequency drop [155]. This results in reduced frequency deviation but does not shorten the overall time needed to restore frequency to its threshold.

A hierarchical control system can also be designed to coordinate WTs and minimise the number of turbines required for frequency regulation [156]. This system employs three layers of wind farm management, wind farm control, and WT control to facilitate information sharing among wind farms, conventional power plants, and the system dispatch centre. The WT control layer is tasked with tracking the reference active power and communicating operational data—such as output power, available frequency control power, wind speed, rotor speed, and pitch angle—to the wind farm management layer. Among the active power control methods, rotor speed control is favoured over pitch angle control due to its faster response and reduced mechanical wear. As a result, rotor speed control is considered

to provide higher reserve power quality. However, the sensitivity of WT responses to variations in inertia and droop constants has not been thoroughly investigated. Given the diversity of WT control models in the literature, it is crucial to compare their performance and assess their sensitivity across different scenarios. detailed models have been developed to compare the performance of an actual wind power plant using various inertial controller gains [157]. However, the gains should be extensively varied and contrasted with alternative frequency control methods.

More recently, energy storage systems, particularly batteries and supercapacitors, have gained prominence as a viable option for providing primary frequency support. Batteries are not only capable of responding within seconds but can also sustain power delivery over extended periods, potentially reducing or even eliminating the need for secondary or tertiary reserves in many situations [158–160]. Furthermore, batteries can store excess energy produced by wind power plants, which can then be used for frequency regulation. As a result, the combination of frequency regulation and renewable energy arbitrage has become a key focus area for wind power plant operators [161].

In traditional power grids, inertia is typically provided by synchronous generators in thermal power plants through governor control. When a frequency drop occurs, these synchronous machines supply additional power to stabilise the system. However, their response time is relatively slow, even taking a few seconds to react. In contrast, EESS like batteries and especially supercapacitors offer nearly instantaneous output and can deliver energy over a longer duration compared to the inertia and droop responses of wind turbines. Numerous studies have demonstrated that battery energy storage system (BESS) control strategies are well-suited for frequency regulation in systems with high wind power penetration [162–171].

The impact of various aggregated and distributed energy storage technologies in a wind farm has been studied and evaluated [163]. For example, a control strategy involving BESS and wind turbine pitch angle control, where the pitch control is activated only when the battery's state of charge (SoC) falls below 40%. The synchronous generator responds at 30% SoC to recharge the battery and restore SoC levels to 50% has been proposed [162]. Another example of SoC-based control scheme coordinates the response time between generators and BESS to manage wind frequency deviations [166]. Li-ion battery control has also been used to mitigate damping power associated with inter-area low-frequency oscillations in a wind power plant [164]. The concept of treating a WPP and a BESS as a virtual power plant to provide both energy and frequency regulation in energy markets has

been explored, with a cooperation strategy that deploys BESS during periods of insufficient generation from the WPP, taking into account battery cycle numbers and energy change functions to extend battery life [169]. The combination of batteries and supercapacitors has also been widely studied for frequency regulation, offering faster responses and reducing both battery size and overall costs [168, 172–178].

7.2.2 Frequency Support from wind turbine control and BESS

As previously discussed, wind turbines can regulate themselves during rapid frequency changes using various methods. In our study, we focused on inertia and droop control strategies because they can inject sufficient momentary power into the grid without the need to deload the WT, thereby avoiding stress on the turbine blades.

Inertia response: For variable-speed wind turbines (VSWTs), the rotating mass is mechanically decoupled from the grid, meaning the kinetic energy (KE) cannot provide a direct inertia response similar to synchronous generators for frequency balancing. However, doubly-fed induction generators (DFIGs) can be operated to slow down, releasing this KE into the grid for a few seconds, thereby providing inertia support for up to 10 s. This brief period allows sufficient time for the synchronous generator to activate its governor control and further stabilise the frequency within 30 s (primary control). Following this, slower secondary and tertiary controls are engaged to restore frequency levels to their threshold values [179].

$$E_k = \frac{1}{2} J \omega^2 \tag{7.2}$$

Where E_k is the kinetic energy, J is the moment of inertia of wind rotor and ω is the rotational speed. The inertia constant H (Equation 7.3) represents the time duration for which the wind generator can provide nominal power (S) by using kinetic energy.

$$H = \frac{J\omega^2}{2S} \tag{7.3}$$

Droop control: This method is widely used by wind generators to mimic the behavior of conventional generator governors by adjusting the active power output of a wind turbine in proportion to changes in frequency.

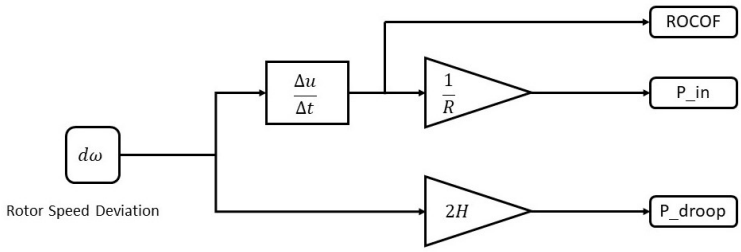

Figure 7.1: *Frequency regulation block with inertia and droop controls [53].*

$$\Delta P = \frac{f_{nom} - f_{meas}}{R} \tag{7.4}$$

Where f_{nom}, f_{meas} and R are nominal frequency, measured frequency and droop constant, respectively. The default inertia constant was selected as 5.04 and the droop constant as 0.05. These were later modified to observe the best response (please see the Figure 7.1).

Battery control: Unlike synchronous generators, batteries have the capability to both inject and absorb power from the grid within seconds. Battery control algorithms can be designed to inject the appropriate amount of power into the grid immediately when a frequency drop is detected. This response can be based on two factors: (i) frequency deviations in the grid and (ii) the rate of change of frequency (ROCOF) within the system.

The state of charge (SoC) of the battery at a given time (t) is defined as the ratio of the available energy to the battery's rated energy:

$$SoC(t) = \frac{E(t)}{E_{rated}} \tag{7.5}$$

Where $E(t)$ represents the energy stored in the battery at time t, and E_{rated} is the battery's rated energy capacity. The operation of the BESS is limited by:

$$SoC_{min} \leqslant SoC(t) \leqslant SoC_{max} \tag{7.6}$$

7.2.3 Sensitivity analysis

To assess the response sensitivity of the WT control and a battery, an existing Kundur two-area system model was modified (Figure 7.2). The Simscape–MATLAB model contains a grid system with a synchronous machine acting as a swing generator (M2), a DFIG wind turbine, and a load in Area 1. An additional 200 MW load was connected via a breaker, which was switched at time intervals of 50 s and 100 s, resulting in a frequency drop and subsequent rise. Area 2 included two synchronous machines (M3 and M4) and another load. A constant wind speed was maintained throughout the limited simulation period. The parameters of the model are detailed in Table 7.1. The sensitivity of the system's response to frequency disturbances was analysed for both under-frequency and over-frequency scenarios. Various cases were explored to examine the frequency response of the WT and the BESS.

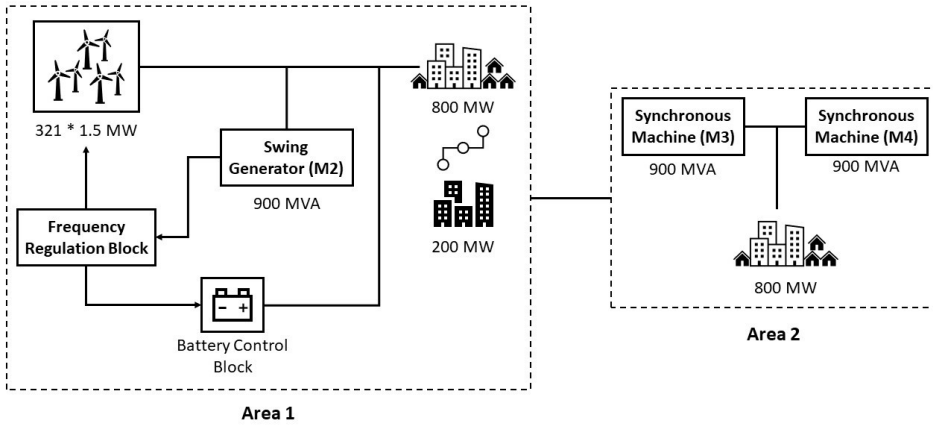

Figure 7.2: *Modified two area model [53].*

Table 7.1: *Parameters of modified two area model.*

Parameter	Value
Wind turbine nominal power	1.5 MW
Number of wind turbines	321
Wind speed	10 m s^{-1}
Grid frequency	60 Hz
Initial load	1600 MW
Rated power of synchronous machines	900 MVA

The parameters for the battery were set according to Table 7.2 [168, 180–182], with an assumed energy rating higher than necessary to ensure that the BESS could provide sufficient energy throughout the entire simulation period.

Table 7.2: *BESS parameters.*

Parameter	Value
Rated power	300 MW
Rated capacity	50 MWh
Efficiency	95%
SoC_{max}	80%
SoC_{min}	20%

No control

The response of the WT was initially analysed without any frequency control to establish a baseline. At 50 s, a load switch was activated which connected additional 200 MW load to the system. This caused a significant frequency drop and the frequency attempted to stabilise after a few seconds, with the frequency nadir at 59.4 Hz, as seen in Figure 7.3 a. To supply additional power and regulate the frequency, the synchronous generators (M2, M3, M4) kicked in but with a delayed response of a few seconds to reach the adequate power levels, as seen in Figure 7.3 c. When this additional load was removed at 100 s, the frequency increased and eventually stabilised around 60 Hz after a brief period of time.

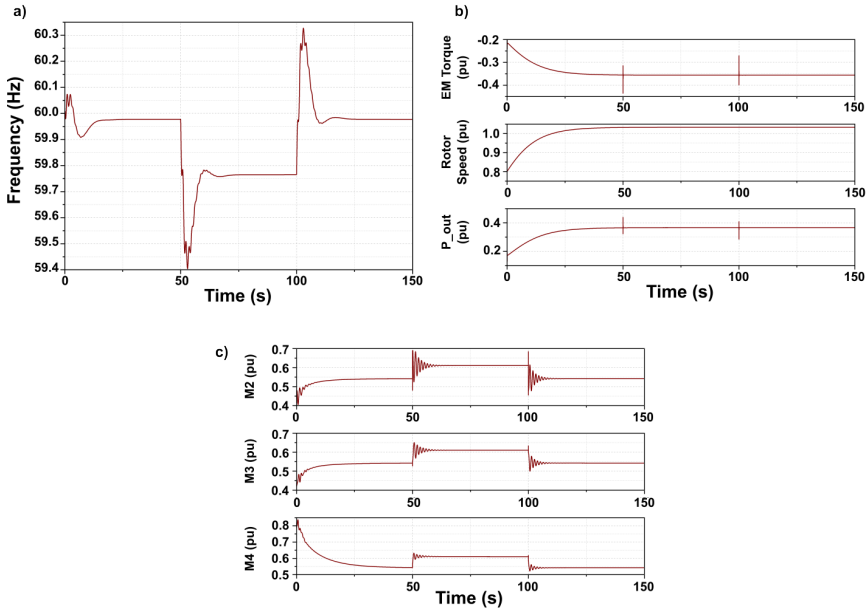

Figure 7.3: *Behaviour of a) grid frequency, b) wind turbines, and c) synchronous machines during no frequency control [53].*

Inertia and droop control

To optimise the WT's response, the inertia and droop constants were adjusted to determine the most effective settings. Figures 7.4 a and b show the frequency responses with the default inertia constant (H = 5.04) and droop constant (R = 0.05) compared against scenarios with modified values to assess system stability. In all cases, at 50 s the frequency settled at a higher value compared to the baseline scenario, with the frequency nadir being higher when using the default constants (A). Increasing the inertia constant and decreasing the droop constant resulted in increased WT output power for frequency regulation. The smallest frequency drop was observed in scenarios C and D. However, due to the limited duration of additional power supply from the WT, a second frequency drop occurred (in scenarios C and D), leading to a final frequency lower than that in the default scenario (A), which could potentially introduce further instability. Based on the analysis presented in Table 7.3 and Figure 7.4, scenario B emerged as the optimal choice for frequency response using only inertia and droop control. The WT control effectively mitigates a significant initial drop, allowing the synchronous machines enough time to stabilise the frequency.

Table 7.3: *Inertia and droop constant values for frequency control through WT*

	Inertia Constant (H)	Droop Constant (R)
A	5.04	0.05
B	10.08	0.025
C	13.104	0.019
D	0	0.019

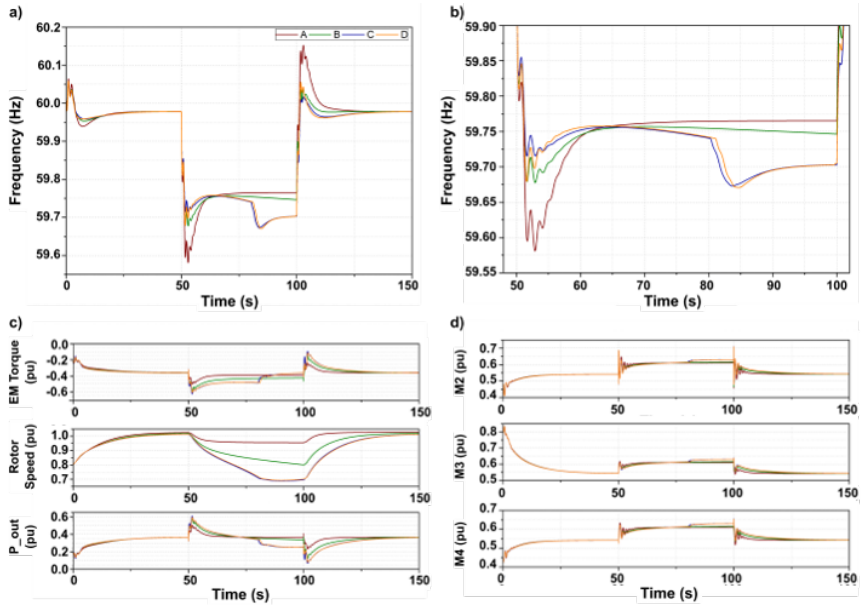

Figure 7.4: *Variation in a) and b) grid frequency, c) wind turbines, and d) synchronous machines response during different inertial and droop control scenarios.*

Battery control

In this scenario, the inertia and droop controls were disabled, leaving the battery solely responsible for frequency support. The battery's response was governed by both frequency deviation and ROCOF, with variations in the control gains. With lower gains (A), the battery response to the frequency drop was slower which allowed the synchronous machines to assist in balancing the system. However, when battery sensitivity was increased (scenario C), at 50 s, the battery reacted swiftly, supplying power immediately and preventing any significant frequency drop. The frequency was stabilised more quickly and at a higher level than only WT inertia and droop control. The output from the synchronous machines showed no significant increase

in output, indicating that they did not contribute to frequency support as the battery provided all the necessary power. At 100 s, the battery absorbed the surplus energy and brought the frequency close to 60 Hz. This suggested that by adjusting the gains or battery responses, the battery's sensitivity to frequency fluctuations can be optimised (refer Figure 7.5 and Table 7.4).

Table 7.4: *Battery gain multipliers.*

	Frequency Deviation Multiplier	ROCOF Multiplier
A	50×10^6	10×10^6
B	50×10^8	10×10^8
C	50×10^9	10×10^9

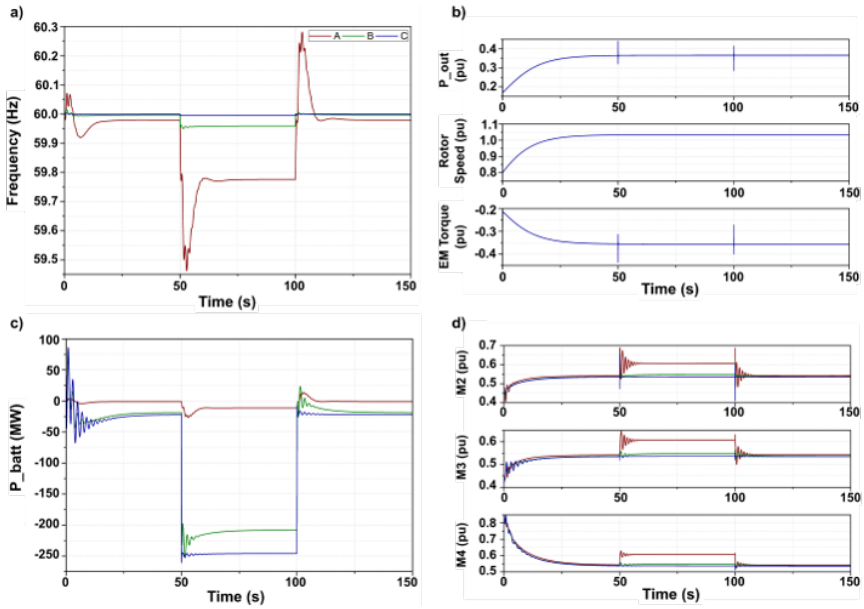

Figure 7.5: *Variation in a) grid frequency, b) wind turbines, c) battery and d) synchronous machines response during different battery control scenarios.*

All controls

In this scenario, both inertia and droop control, as well as battery control, were activated. The optimal H and R values from only "Inertia and Droop Control" were chosen to maximise the wind turbine's support, with the battery providing additional assistance as needed. The battery ramp rates were adjusted in a manner similar to those in the case of only battery control. In scenario A, the battery control gains were too low, preventing the battery from responding, so frequency regulation was managed solely by the wind turbine and synchronous machines, with no output from the battery. Conversely, in scenario C, where battery control gains were set too high, neither the wind turbine nor the synchronous machines contributed to frequency regulation.

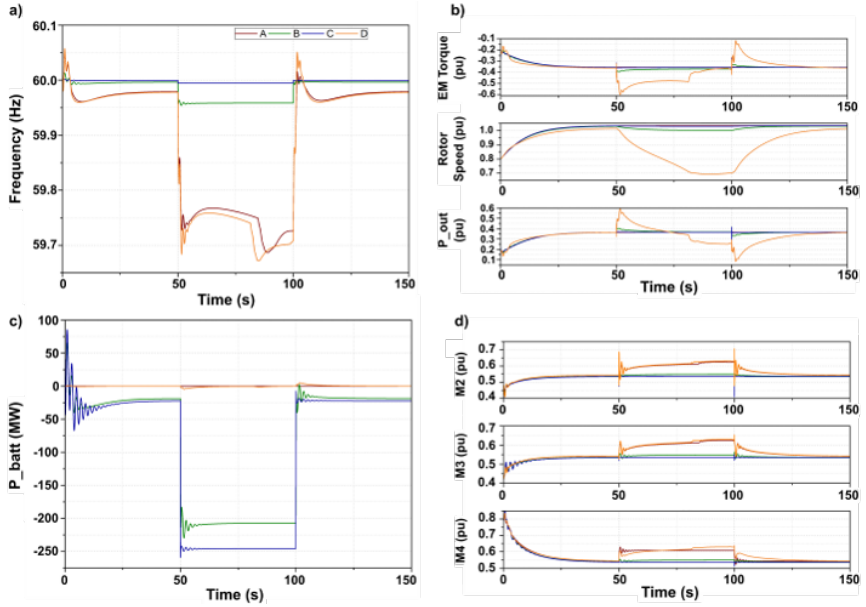

Figure 7.6: *Variation in a) grid frequency, b) wind turbines, c) battery and d) synchronous machines response during different wind-battery combined control parameters.*

By decreasing the battery's sensitivity—thus lowering its response capabilities—the inertia and droop controls engage first, with the battery providing a smaller amount of power. The minimal contribution from the synchronous machines indicates that the combination of wind turbine control and the battery alone can effectively manage frequency imbalances (see Table 7.5 and Figure 7.6).

Table 7.5: *WT control and BESS gain parameters.*

	H	R	Frequency Deviation Multiplier	ROCOF Multiplier
A	13.104	0.019	50×10^6	10×10^6
B	13.104	0.019	50×10^8	10×10^8
C	13.104	0.019	50×10^9	10×10^9
D	0	0.019	50×10^9	10×10^9

7.2.4 Impact of wind-battery hybrid control strategies

The frequency control schemes utilising either individual or combined wind-battery systems offered superior frequency regulation compared to traditional generators. The effectiveness of these schemes is dependent on control parameters and varies with the sensitivity of the frequency regulation strategies.

In the case of only WT control (using inertia and droop), using a highly sensitive wind turbine control strategy can potentially lead to further frequency destabilisation, as illustrated in Figure 7.4 a. Under control strategies C and D, the initial frequency drop is significantly smaller, reaching 59.72 Hz and 59.67 Hz, respectively, compared to scenario A. However, after 80.5 s, the WT is unable to supply additional power, causing the frequency to experience a secondary drop to 59.67 Hz in both cases. In such situations, slightly compromising the frequency nadir could result in a more stable WT response.

When only a battery energy storage system (BESS) is connected, the system's response depends on the control strategy. It can either keep the frequency close to 60 Hz or, with low sensitivity allow it to drop to 59.45 Hz. In the medium-sensitivity scenario (B), the BESS limits the frequency drop to 59.55 Hz, as shown in Figure 7.5 a. Highly sensitive control could lead to the battery being constantly engaged with the grid, potentially affecting its longevity. While this study does not focus on the long-term performance of the BESS, it is important to note that battery lifespan is influenced by several factors. It is well known that adjusting battery cycling, depth of discharge levels [183], and charge-discharge protocols can extend battery life [184–188]. Although Li-ion batteries are the most widely deployed and have shown improvements in cyclability [189, 190], they still have relatively short cycle lives (10^3 cycles) compared to supercapacitors (10^6 cycles) [191]. As future energy systems incorporate larger shares of variable renewables, more frequent frequency disturbances are expected, increasing the demand on batteries and potentially shortening their lifespan. Further research is needed to explore

the relationship between different battery applications, their longevity and other characteristics.

The optimal approach would combine the strengths of both WT and BESS responses to avoid relying on a single control method. Figures 7.6 a and b demonstrate that by limiting the battery's response, WTs can also contribute, providing mutual support. Operators can optimise sensitivity based on the WT and battery ratings and the required level of support [192]. This approach would reduce mechanical stress on the WTs, improve battery longevity, and lessen the need for conventional spinning reserves.

7.3 Comparison of Li-ion batteries with AC{V_{10}-POM} hybrid material devices

We now follow the steps of this bottom up integration of materials, devices into applications by comparing our AC{V_{10}-POM}||AC asymmetric cells with conventional Li-ion technologies in terms of energy and power as well as cyclability. As mentioned throughout this thesis, the field of AC-POM hybrid materials is driven by two main motivations:

1. Improving stability or cyclability of POMs, and

2. Increasing the specific energy of the AC-based (double-layer) supercapacitors.

However, very few times can these benefits be seen directly translated into applications. And yet, looking at these novel materials from an application point of view is necessary as their performance enhancement should benefit practical use. As mentioned before, AC-POM based hybrid supercapacitors can inject high power and sustain it for longer periods of time due to the higher energy storage capabilities of the POMs. While the energy stored per kg of active material may be lower than Li-ion batteries, depending on the application, these hybrid supercapacitors may prove to be more advantageous for this specific one.

Batteries can only be operated between approx. 80% and 20% SoC and suffer from low cycle life. On the other hand, supercapacitors can be fully charged and discharged, and operate up to 10,000 cycles. Our hybrid supercapacitors can retain approx. 90% of their capacitance in 5,000 cycles. While, experimental validation would be required, it would be safe to extrapolate that these materials could sustain 10,000 cycles before end of life.

Many Li-ion technologies are available commercially, but for wind power applications, chemistries such as Graphite/$LiFePO_4$ and $Li_4Ti_5O_{12}$/$LiMO_2$ (LTO) with longer cycle life would be preferred due to the constant charging and discharging of the battery. For example, LTO based batteries offer higher cyclability ($\sim$ 5,000 cycles) than graphite/$LiMO_2$ ($\sim$ 3,000) but provide slightly lower gravimetric energy. To make our comparison we use the study by Stroe et. al. who demonstrated the use of LTO batteries for 6,200 partial charge-discharge cycles at 25 °C for frequency support in a wind power plant [193].

- Model Requirements (oversized system): 300 MW/50 MWh
- LTO battery gravimetric energy: 75 Wh kg^{-1}
- Kg of LTO active material required to meet specifications: 666 Tons
- Gravimetric energy AC{V_{10}}||AC supercapacitor: 35 Wh kg^{-1}
- Specifications of AC{V_{10}}|| AC supercapacitor (666 Tons of active material): 443 MW/23 MWh
- Specifications of symmetric AC supercapacitor (666 Tons of active material): 443 MW/17 MWh.

As per the model requirements specified in Section 1.1.3, the Li-ion battery is capable of providing approx. 10 min at full rating. As per the scenario of using only battery for frequency regulation, the maximum power required at a time from the battery would be 250 MW for 50 s, which is within the capabilities of the battery. At the same time, if the same amount of AC{V_{10}} material is used, it can provide 443 MW for 3 min or the required 250 MW for 5.5 min which is sufficient for the system requirements.

However the main advantage comes from the cyclability. While the LTO battery can be used for only 6,500 partial charge discharge cycles [193], the AC{V_{10}}||AC supercapacitor can work for approx. 10,000 cycles before end of life. Since the major capacity fade for AC-POM hybrid materials was observed before 1,000 cycles, we performed both linear and logarithmic regression to approximate the capacitance retention at 6,500 and 10,000 cycles.

7.3.1 Regression analysis and cyclability forecasting of asymmetric cell AC{V_{10}}||AC

Linear regression and forecasting

Linear regression was performed using experimental data up to 5,000 cycles as shown in Chapter 3. The R^2 value was not observed to be close to 1 and hence the goodness of fit for the model could not be ensured. As per this model, the cyclability was projected as 86% at 6,500 cycles and 80% at 10,000 cycles (Figure 7.7).

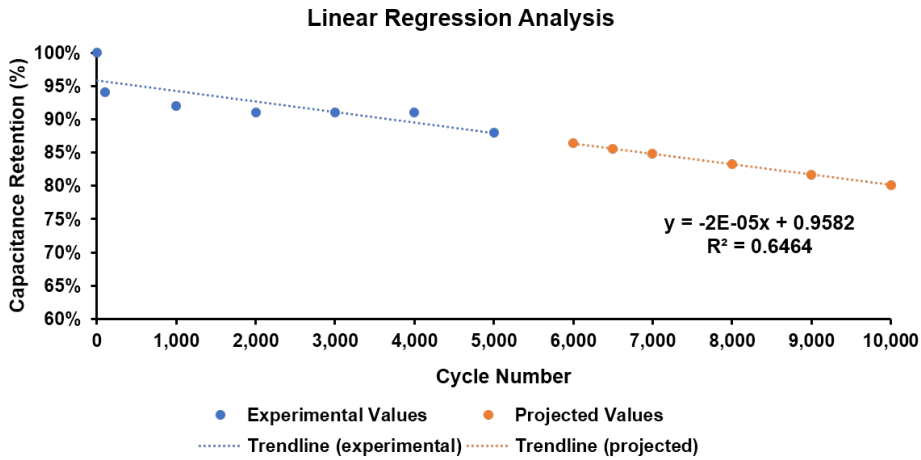

Figure 7.7: *Forecasting capacitance retention of AC{V_{10}}||AC asymmetric cells using linear regression.*

Logarithmic regression and forecasting

Since the cycling data for energy storage materials follows a logarithmic trend (maximum capacitance loss before 100 and 1,000 cycles), we utilised a logarithmic regression model. Using this, the R^2 was observed to be 0.94, indicating a good fit. As per this model, the cyclability was projected as 89% at 6,500 cycles and 88% at 10,000 cycles (Figure 7.8).

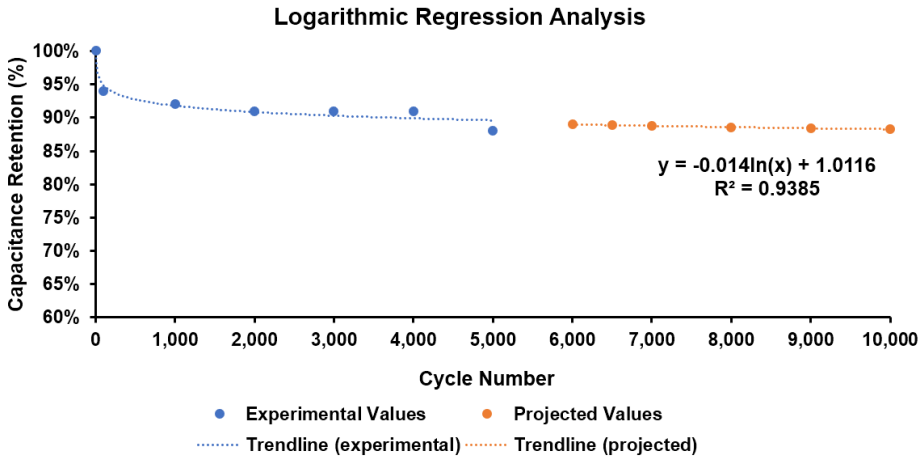

Figure 7.8: *Forecasting capacitance retention of AC{V_{10}}||AC asymmetric cells using logarithmic regression.*

The predictions showed 80% and 88% capacitance retention using linear and logarithmic regression, respectively, at 10,000 full charge-discharge cycles. While these values may not be perfectly accurate, they can provide a reasonable estimate of the performance of these materials. Hence, we can predict that our AC{V_{10}}||AC supercapacitor would be able to provide frequency regulation services for the model before its end of life.

7.4 Discussion

A control strategy for the hybrid system was designed to enable both the wind turbine and battery to contribute to frequency regulation. This approach ensured that the battery does not react to every minor frequency fluctuation. The battery is inherently more responsive to frequency variations compared to inertia and droop control, but excessive sensitivity can negatively impact the battery's long-term health. On the other hand, if the battery's sensitivity is too low, it cannot adequately support frequency regulation, forcing the synchronous machines to provide inertia. An oversized battery system would result in higher costs, while an undersized one would fail to deliver adequate response. Therefore, the battery energy storage system must be appropriately sized to supply the necessary power during frequency drops. Novel energy storage devices based on hybrid materials such as AC$\{V_{10}\}$, which have higher gravimetric energy and power than previously developed AC-tungstate/molybdate materials, as well as good cyclability compared to Li-ion batteries, can provide the right specifications for frequency regulation applications.

8

Conclusions and Perspectives

8.1 Conclusions

This thesis has presented a multi-disciplinary approach for the integrated development of electrochemical energy storage systems. The main conclusion of this thesis are:

Concerning hybrid materials for improved capacitance and specific energies, AC{V-POM} hybrids were first studied:

1. Activated carbon-sodium decavanadate ($Na_6[V_{10}O_{28}]$ or Na-V_{10}) based hybrid materials were first developed and in-situ synthesis method for adsorption of Na-V_{10} on AC was demonstrated for the first time.

2. The Na-cation was substituted with TBA-cation (forming $[(C_4H_9)_4N]_3H_3[V_{10}O_{28}]$ or TBA-V_{10}) to perform the synthesis in organic media and eliminate the presence of water molecules from the crystal structure. The presence of Na-V_{10} impurities and further purification of sample to obtain pure TBA-V_{10} did not allow in-situ synthesis and instead the AC{TBA-V_{10}} hybrid material was formed via ex-situ synthesis.

3. Symmetric cells of AC{Na-V_{10}} and AC{TBA-V_{10}} were tested in 1 M $NaClO_4$ in acetonitrile electrolyte. The electrochemical analysis (CVs, CPs and GCDs) demonstrated that the hybrid electrode gravimetric capacitance (112 and 116 F g^{-1} at 0.1 A g^{-1}, respectively) improved with respect to AC (102 F g^{-1}). This was achieved for the first time in an organic electrolyte thanks to the use of polyoxovanadates instead of polyoxotungstates or polyoxomolybdates. Even

at high current densities of 20 A g^{-1}, the AC{Na-V_{10}} exhibited higher capacitance (79 F g^{-1}) than AC (71 F g^{-1}), while AC{TBA-V_{10}} was comparable (70 F g^{-1}).

4. The electrochemical study of log(current) as a function of log(scan rate) in CVs demonstrated a linear dependence, indicative of storage mechanism not limited by diffusion and typical of surface capacitive storage. This was true for both AC{Na-V_{10}} and AC{TBA-V_{10}} hybrids in organic electrolytes. This allows kinetic matching of the fast reversible redox activities of V_{10}-POMs with capacitive materials.

5. The entire electrochemical activity of the V_{10}-POM was not utilised in a symmetric configuration and hence, asymmetric cells AC{Na-V_{10}}||AC and AC{TBA-V_{10}}||AC were assembled with 1 M $NaClO_4$ in acetonitrile. Both asymmetric cells with hybrid electrodes as anodes and carbon as cathodes showed further improvement in gravimetric electrode capacitances (140 F g^{-1} at 0.1 A g^{-1}), and energy (35.5 Wh kg^{-1} at 68 W kg^{-1}) with respect to AC electrodes (25.7 Wh kg^{-1}).

6. The symmetric AC{Na-V_{10}} and AC{TBA-V_{10}} hybrid supercapacitors with two identical electrodes showed improvement in gravimetric electrode capacitance by 14% and 10% over AC electrodes, respectively. On the other hand, both asymmetric AC{Na-V_{10}}||AC and AC{TBA-V_{10}}||AC cells showed a 37% improvement in gravimetric electrode capacitance at 0.1 A g^{-1}, which was maintained even at high current densities of 20 A g^{-1}(35%).

7. While the capacitance of the electrodes was improved in asymmetric configuration as per our objectives, the electrochemical window of the V_{10}-POM did not seem to be fully utilised with balanced asymmetric cells from CV and GCPL studies. Therefore, it could not be established if all 10 electrons participated in redox reactions.

8. Most importantly, the adsorption of V_{10} clusters onto AC pores greatly improved the structural stability of V_{10}-POMs and prevented their decomposition upon cycling. Both symmetric and asymmetric cells were capable of cycling beyond 5,000 full charge-discharge cycles with maximum capacitance retention of 91%. As per our review of literature, this has been the best case until now demonstrating high capacitance retention of the decavanadate POMs in either batteries or supercapacitors.

9. Next, in-situ synthesis of AC{PV_{14}} for the adsorption of $Na_5[H_4PV_{14}O_{42}]$ (or PV_{14}) in AC micropores was attempted in various concentrations. The complex chemistry of the PV_{14}-POM resulted in its partial decomposition into V_{10} and other by-products upon contact with AC.

10. The decomposition products of AC{PV_{14}} hybrids were identified through NMR, FTIR, SEM as decavanadate, phosphates and pervanadyl ion.

11. Finally, the partially decomposed AC{PV_{14}-39} and AC{PV_{14}-52} hybrid electrodes in symmetric configuration with 1 M $NaClO_4$ acetonitrile electrolyte showed high gravimetric capacitances of 130 and 117 F g^{-1}, respectively at 0.1 A g^{-1} (higher than AC and AC{Na-V_{10}} electrodes).

Furthermore, thick electrodes made of AC and conductive carbons were developed using scalable methods and a new concept of nano-pastes was introduced.

12. We demonstrated the possibility of developing thick solid electrodes up to a thickness of 629 μm using a spray coating process. These AC electrodes demonstrated high conductivity and mechanical strength through the use of CSP and CNT with flexible binders such as CMC and PVDF-HFP.

13. The maximum thickness of 629 μm and mass loading of 31 mg cm^{-2} was achieved by combining AC and CNT with CMC. Electrodes with AC, CSP and PVDF-HFP could also achieve a similar mass loading of 30 mg cm^{-2} and 543 μm thickness. Slurries using CMC with CSP were found to be easier to spray compared to slurries with CNTs.

14. Lyophilisation was also tested by layer-over-layer casting to develop electrode with 674 μm thickness and 12.6 mg cm^{-2} mass loading.

15. The thick electrodes demonstrated high porosities of over 80%. However, tortuosity values > 1 implied the presence of dead-end pore.

16. The spray coated "thickest" electrodes with AC, CNT and CMC achieved the highest areal capacitance values of 2,459 mF cm^{-2} (629 μm), while their "thinner" counterparts (31 μm) showed 103 mF cm^{-2}. The volumetric capacitances were comparable (39 and 37 F cm^{-3}, respectively), while gravimetric capacitances reduced from 94 F g^{-1} in the thin electrode to 79 F g^{-1} in the thick electrode (at 10 mV s^{-1}).

17. Concerning rate capabilities across all compositions, thin spray coated electrodes suffered a low capacitance loss (gravimetric, volumetric and areal) of approximately 10% in going from 2 mV s^{-1} to 200 mV s^{-1}. On the other hand, their thicker counterparts suffered a reduction of over 80% across all capacitance metrics.

18. The "thin" and "thick" freeze-casted electrodes showed unsatisfactory electrode capacitance across all metrics (83.1 and 80.9 F g^{-1}; 15.0 and 8.8 mF cm^{-2}; 407 and 567 F cm^{-3}, respectively) due to poor contact between carbon particles, and a disconnected macroporosity among layers resulting from a suboptimal lyophilisation process.

19. The thick electrodes developed using AC{Na-V_{10}} hybrid material (5 mg cm^{-2}) experienced no loss in gravimetric capacitance (114 F g^{-1}) with respect to their thinner counterparts in symmetric configuration at current densities of 0.1 A g^{-1}. Moreover, capacitance of the hybrid electrode was superior to that of pristine thick AC electrodes (102 A g^{-1}). However, both thick electrodes showed poor rate capability (55% lower capacitance at 20 A g^{-1}).

20. We successfully proved the concept for novel nanopaste electrodes with extremely high active material mass loadings ranging from 30 to 50 mg cm^{-2} with an integrated electrolyte and without binders.

21. The nanopaste electrodes using carbon materials and 50 mg cm^{-2} mass loadings demonstrated high gravimetric capacitance of 150 F g^{-1} in 1 M H_2SO_4 and 81 F g^{-1} in 1 M $TEABF_4$ in acetonitrile electrolytes at 0.1 A g^{-1}.

22. We also prepared AC{Na-V_{10}} hybrid material based nanopastes in 1 M $TEABF_4$ in acetonitrile with gravimetric electrode capacitance of 136 F g^{-1} at 0.1 A g^{-1}.

The AC{V_{10}} hybrid materials and cells were selected for the application of frequency regulation due to the combination of high gravimetric energy, power and extended cyclability.

24. Electrochemical energy storage systems provide superior frequency regulation support compared to synchronous machines or wind power plant controls such as inertia and droop control.

25. As per the model specifications, an LTO-battery with 300 MW/50 MWh would be needed as an oversized energy storage system. The AC{V_{10}}||AC hybrid supercapacitor developed using the same amount of active material as the battery could provide 443 MW/23 MWh. For comparison, an AC supercapacitor would provide 443 MW power but only 17 MWh.

26. The AC{V_{10}} hybrid materials were also found to be better suited for frequency regulation than Li-ion batteries due to their full charge-discharge capabilities, long cycle life (>80% retention after 10,000 cycles) and intermediate gravimetric energy densities between batteries and supercapacitors.

8.2 Future work

This thesis has demonstrated the integrated development of hybrid nano-materials, hybrid devices, and applications. Due to the wide scope of the experimental work, this thesis focused on key proof of concept studies and essential electrochemical analyses. Thanks to these positive results, many detailed and extensive studies can be done on these materials and devices.

Optimising the adsorption of V-POMs on AC as well as preventing the partial degradation of PV_{14} is a first step to further improve these materials. Additionally, experiments on extending the voltage range should be performed for the AC{V-POM} hybrid materials. In-situ XANES experiments could be performed to identify the oxidation states of V atoms. Also some controlled electrochemical experiments (chronoamperometry) could be performed to establish the number of electrons exchanged at each potential and correlate this with in-situ XANES results.

Going beyond Na^+ cations used in this thesis, it would be interesting to study the possible use of these same polyoxovanadate nanoclusters for multivalent ion batteries such as Zn^{2+} or Al^{3+}.

The concept of hybridisation in thick or high mass loaded electrodes also opens up a new avenue of research, especially if we consider nanopastes. Currently, efforts are

being made to improve the devices for nanopaste containment and characterisation, and future work will focus on their composition, characterisation, pressure impact, and cyclability.

The initial results from integrating AC{V-POM} hybrid materials with high power requiring applications such as frequency regulation also present interesting pathways to analyse and understand these materials. For example, cycling behaviour of these materials, including partial charge-discharge can be studied using impedance models. Feedback from the impedance models could then be used to predict frequency regulation (or even EV acceleration) capabilities of these materials under various scenarios. Moreover, a detailed techno-economic and life-cycle analysis could also be performed for feasibility assessment of these hybrid materials.

A

Appendix

A.1 Impurities during synthesis of TBA-V_{10}

The FTIR spectra of the un-purified TBA-V_{10} did not match the FTIR spectra of the purified compound. The spectra were close to that of Na-V_{10} showing that the Compound A may also contain some Na-V_{10}. Moreover, the spectra of filtered impurity (Compound B) was quite similar to that of Na-V_{10} (Figure A.1).

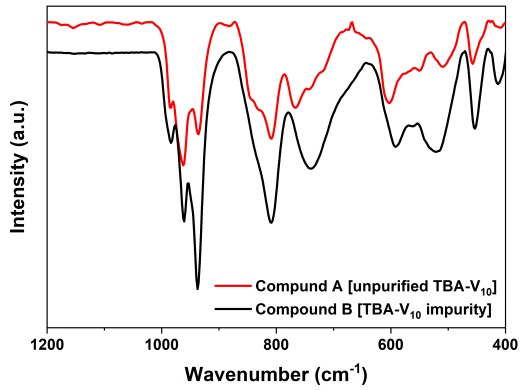

Figure A.1: *Infrared spectra of unpurified TBA-V_{10} compounds during synthesis.*

A.2 Preliminary studies of the performance of AC{V_{10}} symmetric cells in different electrolytes

We first performed an initial test for selecting a non-Li electrolyte to evaluate the capacitance of AC{V_{10}} hybrid materials. We prepared symmetric coin cells as described in Chapter 3, with a variety of common electrolytes used for supercapacitors namely, 1 M $TEABF_4$ and 1 M $NaClO_4$ in acetonitrile, 1 M $NaClO_4$ in PC, and 1 M $NaClO_4$ in a proprietary H_2O/acetonitrile mix electrolyte.

The electrode capacitance values from CP were calculated using Equation 2.1 and presented in Table A.1. We first tested AC{Na-V_{10}} hybrid material in 1 M $TEABF_4$ in acetonitrile since it is a common supercapacitor electrolyte. However, the electrode capacitance was not satisfactory. We then tested the electrodes in Na-based electrolytes, particularly 1 M $NaClO_4$ in acetonitrile and 1 M $NaClO_4$ in PC. The gravimetric capacitance of the hybrid electrode improved in these two electrolytes. We also tested in 1 M $NaClO_4$ in EC:PC as well as 1 M $NaClO_4$ in a proprietary hybrid electrolyte, but the capacitance was low. Table A.1 shows the capacitance calculated from the CP curves at 10 mV s^{-1} for AC{Na-V_{10}} and AC{TBA-V_{10}} symmetric coin cells. Overall, the capacitance of the AC{Na-V_{10}} hybrid materials was better in 1 M $NaClO_4$ in acetonitrile.

As mentioned in Chapter 3, the hybrid material AC{TBA-V_{10}} was prepared by substituting the Na^+ for an organic cation in order to test its compatibility

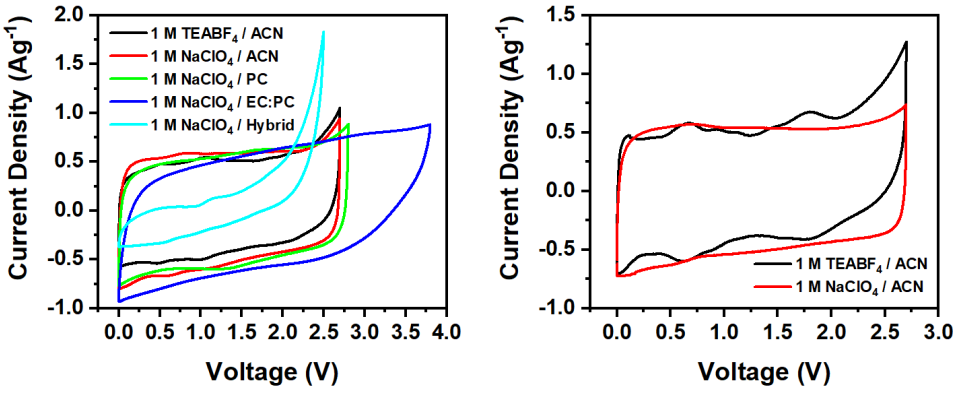

Figure A.2: *CP at 10 mv s^{-1} of AC{Na-V_{10}} and AC{Na-V_{10}} electrodes in various electrolytes.*

Table A.1: *Capacitance of AC{Na-V_{10}} and AC{TBA-V_{10}} hybrid electrodes in various electrolytes.*

	Electrolyte	Voltage (V)	Gravimetric Capacitance (F g^{-1}) from CP (10 mV s^{-1})
AC{Na-V_{10}}	1 M $TEABF_4$ in MeCN	2.7	92
	1 M $NaClO_4$ in MeCN	2.7	111
	1 M $NaClO_4$ in PC	2.8	108
	1 M $NaClO_4$ in EC:PC	3.8	104
	1 M $NaClO_4$ in Hybrid E	2.5	34
AC{TBA-V_{10}}	1 M $TEABF_4$ in MeCN	2.7	98
	1 M $NaClO_4$ in MeCN	2.7	106

with the electrolyte as well as to improve the stability of the material which could have resulted in an improved gravimetric capacitance. The electrode was tested in symmetric coin cells in 1 M $TEABF_4$ in acetonitrile and 1 M $NaClO_4$ in acetonitrile. The performance of the electrode in both electrolytes was quite similar (Table A.1) and it showed slightly better performance than AC{Na-V_{10}}. Hence, to keep a coherence in the comparisons between the two materials, 1 M $NaClO_4$ in acetonitrile electrolyte was selected for all analysis.

A.3 Capacities of AC{V_{10}} hybrid electrodes

The capacity of the symmetric and asymmetric cells assembled using hybrid materials was calculated by Equation 2.12 and is presented in Table A.2.

Table A.2: *Capacities of of AC{Na-V_{10}} and AC{TBA-V_{10}} symmetric and asymmetric electrodes in 1 M $NaClO_4$ in acetonitrile.*

Current Density (A g^{-1})	Gravimetric Capacitance (F g^{-1})				
	AC	AC{Na-V_{10}}	AC{TBA-V_{10}}	AC{Na-V_{10}}||AC	AC{TBA-V_{10}}||AC
0.1	38	43	42	52	53
1	37	39	37	50	49
2	35	38	36	49	47
5	32	34	33	44	42
10	27	31	29	38	34
20	18	24	23	29	23

A.4 Cyclic voltammograms of AC, AC{Na-V_{10}} and AC{TBA-V_{10}} electrodes at various scan rates

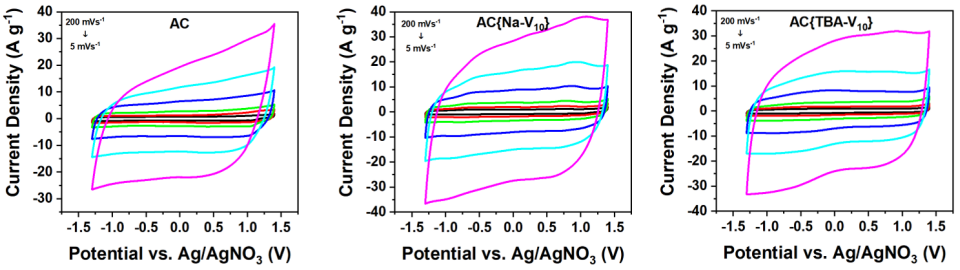

Figure A.3: *Cyclic Voltammograms of AC, AC{Na-V_{10}} and AC{TBA-V_{10}} in three-electrode configuration at 5, 10, 20, 50, 100 and 200 mV s^{-1} with $Ag/AgNO_3$ reference electrode, AC loaded carbon cloth as counter electrode and 1 M $NaClO_4$ in acetonitrile.*

A.5 Charge-discharge curves of symmetric coin cells

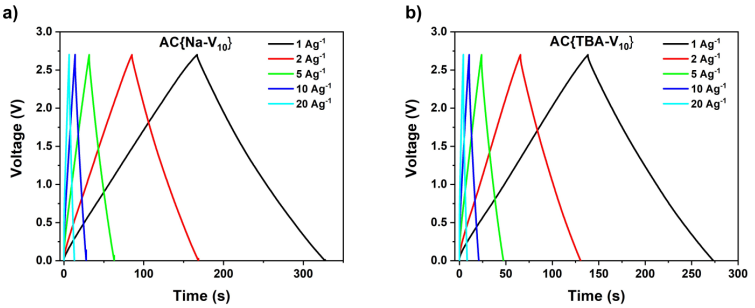

Figure A.4: *Charge-discharge curves of a) AC{Na-V_{10}} and b) AC{TBA-V_{10}} hybrid electrodes at at various current densities in symmetric coin cell configuration.*

A.6 Cyclic polarisation and charge-discharge curves of asymmetric coin cells

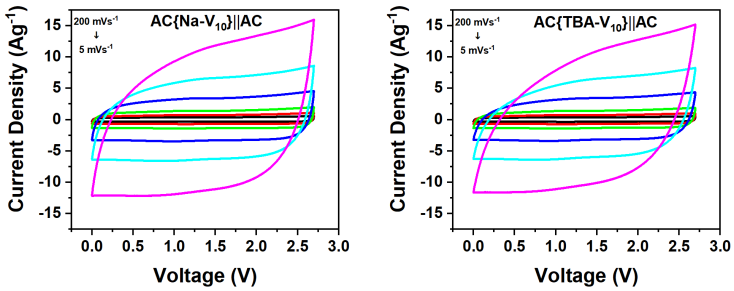

Figure A.5: *CPs of AC{Na-V_{10}}||AC and AC{TBA-V_{10}}||AC asymmetric coin cells with 1 M $NaClO_4$ in acetonitrile at scan rates of 5, 10, 20, 50, 100 and 200 mV s^{-1}.*

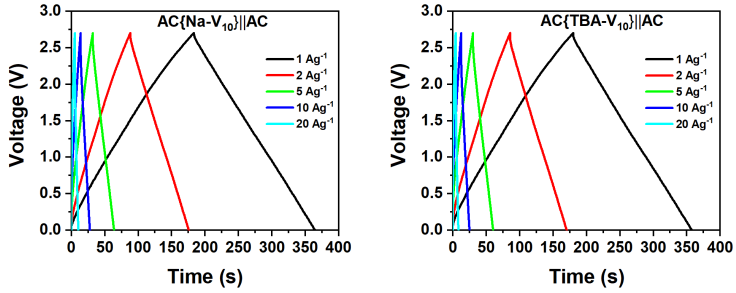

Figure A.6: *GCD profiles of AC{Na-V_{10}}||AC and AC{TBA-V_{10}}||AC asymmetric coin cells with 1 M $NaClO_4$ in acetonitrile at various current densities.*

Bibliography

[1] *Renewable capacity highlights*, Tech. Rep. (International Renewable Energy Agency (IRENA), 2024).

[2] I. E. A. (IEA), *Grid-scale storage* (2023), last accessed 08 September 2024.

[3] A. Pokhriyal, D. Rueda-García, and P. Gómez-Romero, *To flow or not to flow. a perspective on large-scale stationary electrochemical energy storage*, Sustainable Energy Fuels **7**, 5473 (2023).

[4] M. S. Kiai, O. Eroglu, and N. Aslfattahi, *Metal-ion batteries: Achievements, challenges, and prospects*, Crystals **13** (2023).

[5] Y. Li, X. Zhao, Y. Gao, *et al.*, *Design strategies for rechargeable aqueous metal-ion batteries*, Science China Chemistry **67**, 165 (2024).

[6] L. Elbinger, M. Enke, N. Ziegenbalg, J. C. Brendel, and U. S. Schubert, *Beyond lithium-ion batteries: Recent developments in polymer-based electrolytes for alternative metal-ion-batteries*, Energy Storage Materials **65**, 103063 (2024).

[7] H. Aziam, B. Larhrib, C. Hakim, N. Sabi, H. Ben Youcef, and I. Saadoune, *Solid-state electrolytes for beyond lithium-ion batteries: A review*, Renewable and Sustainable Energy Reviews **167**, 112694 (2022).

[8] K. Mongird, V. Viswanathan, J. Alam, C. Vartanian, V. Sprenkle, and R. Baxter, *Energy Storage Grand Challenge Cost and Performance Assessment 2020*, Tech. Rep. December (U.S. Department of Energy, 2020).

[9] S. Ugarte, J. Larkin, B. van der Ree, V. Swinkels, M. Voogt, N. Friedrichsen, J. Michaelis, A. Thielmann, and R. Wietschel, *Energy Storage: Which Market Designs and Regulatory Incentives are needed?*, Tech. Rep. (Directorate General for Internal Policies Policy Department A: Economic and Scientific Policy, 2015).

[10] B.E.Conway, *Electrochemical Supercapacitors: Scientific Fundamentals and Technological Applications* (Springer New York, NY, 1999).

[11] Z. S. Iro, C. Subramani, and S. Dash, *A brief review on electrode materials for supercapacitor*, International Journal of Electrochemical Science **11**, 10628 (2016).

[12] N. R. Chodankar, H. D. Pham, A. K. Nanjundan, J. F. S. Fernando, K. Jayaramulu, D. Golberg, Y.-K. Han, and D. P. Dubal, *True meaning of pseudocapacitors and their performance metrics: Asymmetric versus hybrid supercapacitors*, Small **16**, 2002806 (2020), https://onlinelibrary.wiley.com/doi/pdf/10.1002/smll.202002806 .

[13] T. Brousse, D. Bélanger, and J. W. Long, *To be or not to be pseudocapacitive?*, Journal of The Electrochemical Society **162**, A5185 (2015).

[14] D. P. Dubal, O. Ayyad, V. Ruiz, and P. Gómez-Romero, *Hybrid energy storage: the merging of battery and supercapacitor chemistries*, Chem. Soc. Rev. **44**, 1777 (2015).

[15] J.-J. Zhu, R. Benages-Vilau, and P. Gomez-Romero, *Can polyoxometalates enhance the capacitance and energy density of activated carbon in organic electrolyte supercapacitors?*, Electrochimica Acta **362**, 137007 (2020).

[16] M. R. Horn, A. Singh, S. Alomari, S. Goberna-Ferrón, R. Benages-Vilau, N. Chodankar, N. Motta, K. K. Ostrikov, J. MacLeod, P. Sonar, P. Gomez-Romero, and D. Dubal, *Polyoxometalates (poms): from electroactive clusters to energy materials*, Energy Environ. Sci. **14**, 1652 (2021).

[17] M. T. Pope, M. Sadakane, and U. Kortz, *Celebrating polyoxometalate chemistry*, European Journal of Inorganic Chemistry **2019**, 340 (2019), https://chemistry-europe.onlinelibrary.wiley.com/doi/pdf/10.1002/ejic.201801543 .

[18] P. Gómez-Romero and M. Lira-Cantú, *Hybrid organic-inorganic electrodes: The molecular material formed between polypyrrole and the phosphomolybdate anion*, Advanced Materials **9**, 144 (1997), https://onlinelibrary.wiley.com/doi/pdf/10.1002/adma.19970090210 .

[19] Y. Ji, L. Huang, J. Hu, C. Streb, and Y.-F. Song, *Polyoxometalate-functionalized nanocarbon materials for energy conversion, energy storage and sensor systems*, Energy Environ. Sci. **8**, 776 (2015).

[20] A. Bijelic, M. Aureliano, and A. Rompel, *Polyoxometalates as potential next-generation metallodrugs in the combat against cancer*, Angewandte Chemie International Edition **58**, 2980 (2019), https://onlinelibrary.wiley.com/doi/pdf/10.1002/anie.201803868 .

[21] C.-C. Lin, W.-H. Lin, S.-C. Huang, C.-W. Hu, T.-Y. Chen, C.-T. Hsu, H. Yang, A. Haider, Z. Lin, U. Kortz, U. Stimming, and H.-Y. Chen, *Mechanism of sodium ion storage in na7[h2pv14o42] anode for sodium-ion batteries*, Advanced Materials Interfaces **5**, 1800491 (2018).

[22] J. Suárez-Guevara, V. Ruiz, and P. Gomez-Romero, *Hybrid energy storage: high voltage aqueous supercapacitors based on activated carbon–phosphotungstate hybrid materials*, J. Mater. Chem. A **2**, 1014 (2014).

[23] A. K. Cuentas-Gallegos, R. Martínez-Rosales, M. Baibarac, P. Gómez-Romero, and M. E. Rincón, *Electrochemical supercapacitors based on novel hybrid materials made of carbon nanotubes and polyoxometalates*, Electrochemistry Communications **9**, 2088 (2007).

[24] D. P. Dubal, B. Ballesteros, A. A. Mohite, and P. Gómez-Romero, *Functionalization of polypyrrole nanopipes with redox-active polyoxometalates for high energy density supercapacitors*, ChemSusChem **10**, 731 (2017), https://chemistry-europe.onlinelibrary.wiley.com/doi/pdf/10.1002/cssc.201601610 .

[25] J. Suárez-Guevara, V. Ruiz, and P. Gómez-Romero, *Stable graphene–polyoxometalate nanomaterials for application in hybrid supercapacitors*, Phys. Chem. Chem. Phys. **16**, 20411 (2014).

[26] D. P. Dubal, J. Suarez-Guevara, D. Tonti, E. Enciso, and P. Gomez-Romero, *A high voltage solid state symmetric supercapacitor based on graphene–polyoxometalate hybrid electrodes with a hydroquinone doped hybrid gel-electrolyte*, J. Mater. Chem. A **3**, 23483 (2015).

[27] P. Gómez-Romero, M. Chojak, K. Cuentas-Gallegos, J. A. Asensio, P. J. Kulesza, N. Casañ-Pastor, and M. Lira-Cantú, *Hybrid organic–inorganic nanocomposite materials for application in solid state electrochemical supercapacitors*, Electrochemistry Communications **5**, 149 (2003).

[28] M. Lira-Cantú and P. Gómez-Romero, *Electrochemical and chemical syntheses of the hybrid organicinorganic electroactive material formed by phosphomolybdate and polyaniline. application as cation-insertion electrodes*, Chemistry of Materials **10**, 698 (1998), https://doi.org/10.1021/cm970107u .

[29] A. Cuentas-Gallegos, M. Lira-Cantú, N. Casañ-Pastor, and P. Gómez-Romero, *Nanocomposite hybrid molecular materials for application in solid-state electrochemical supercapacitors*, Advanced Functional Materials **15**, 1125 (2005), https://onlinelibrary.wiley.com/doi/pdf/10.1002/adfm.200400326 .

[30] J. Vaillant, M. Lira-Cantu, K. Cuentas-Gallegos, N. Casañ-Pastor, and P. Gómez-Romero, *Chemical synthesis of hybrid materials based on pani and pedot with polyoxometalates for electrochemical supercapacitors*, Progress in Solid State Chemistry **34**, 147 (2006), advanced Functional Nanomaterials - from NanoscaleObjects to Nanostructered Inorganic and Hybrid Materials.

[31] J.-J. Zhu and P. Gomez-Romero, *Polyoxometalate intercalated mxene with enhanced electrochemical stability*, Nanoscale **14**, 14921 (2022).

[32] J.-J. Zhu, A. Hemesh, J. J. Biendicho, L. Martinez-Soria, D. Rueda-Garcia, J. R. Morante, B. Ballesteros, and P. Gomez-Romero, *Rational design of mxene/activated carbon/polyoxometalate triple hybrid electrodes with enhanced capacitance for organic-electrolyte supercapacitors*, Journal of Colloid and Interface Science **623**, 947 (2022).

[33] D. C. Crans, *Enzyme interactions with labile oxovanadates and other polyoxometalates*, Comments on Inorganic Chemistry **16**, 35 (1994), https://doi.org/10.1080/02603599408035851 .

[34] K. Y. Monakhov, W. Bensch, and P. Kögerler, *Semimetal-functionalised polyoxovanadates*, Chem. Soc. Rev. **44**, 8443 (2015).

[35] M. Aureliano, N. I. Gumerova, G. Sciortino, E. Garribba, C. C. McLauchlan, A. Rompel, and D. C. Crans, *Polyoxidovanadates' interactions with proteins: An overview*, Coordination Chemistry Reviews **454**, 214344 (2022).

[36] M. Anjass, G. A. Lowe, and C. Streb, *Molecular vanadium oxides for energy conversion and energy storage: Current trends and emerging opportunities*, Angewandte Chemie International Edition **60**, 7522 (2021), https://onlinelibrary.wiley.com/doi/pdf/10.1002/anie.202010577 .

[37] H.-Y. Chen, G. Wee, R. Al-Oweini, J. Friedl, K. S. Tan, Y. Wang, C. L. Wong, U. Kortz, U. Stimming, and M. Srinivasan, *A polyoxovanadate as an advanced electrode material for supercapacitors*, ChemPhysChem **15**, 2162 (2014), https://chemistry-europe.onlinelibrary.wiley.com/doi/pdf/10.1002/cphc.201400091 .

[38] H.-Y. Chen, J. Friedl, C.-J. Pan, A. Haider, R. Al-Oweini, Y. L. Cheah, M.-H. Lin, U. Kortz, B.-J. Hwang, M. Srinivasan, and U. Stimming, *In situ x-ray absorption near edge structure studies and charge transfer kinetics of na6[v10o28] electrodes*, Phys. Chem. Chem. Phys. **19**, 3358 (2017).

[39] S. Hartung, N. Bucher, H.-Y. Chen, R. Al-Oweini, S. Sreejith, P. Borah, Z. Yanli, U. Kortz, U. Stimming, H. E. Hoster, and M. Srinivasan, *Vanadium-based polyoxometalate as new material for sodium-ion battery anodes*, Journal of Power Sources **288**, 270 (2015).

[40] M. H. Anjass, M. Deisböck, S. Greiner, M. Fichtner, and C. Streb, *Differentiating molecular and solid-state vanadium oxides as active materials in battery electrodes*, ChemElectroChem **6**, 398 (2019), https://chemistry-europe.onlinelibrary.wiley.com/doi/pdf/10.1002/celc.201801406 .

[41] J. Friedl, M. V. Holland-Cunz, F. Cording, F. L. Pfanschilling, C. Wills, W. McFarlane, B. Schricker, R. Fleck, H. Wolfschmidt, and U. Stimming, *Asymmetric polyoxometalate electrolytes for advanced redox flow batteries*, Energy Environ. Sci. **11**, 3010 (2018).

[42] L. E. VanGelder, A. Kosswattaarachchi, P. L. Forrestel, T. R. Cook, and E. M. Matson, *Polyoxovanadate-alkoxide clusters as multi-electron charge carriers for symmetric non-aqueous redox flow batteries*, Chem. Sci. **9**, 1692 (2018).

[43] M. Ghosh, D. Sorsche, R. Binte Ahmed, and M. Anjass, *Stabilizing decavanadate cluster as electrode material in sodium and lithium-ion batteries*, ChemSusChem **16**, e202300631 (2023), https://chemistry-europe.onlinelibrary.wiley.com/doi/pdf/10.1002/cssc.202300631 .

[44] Y. B. Sim, B. K. Park, and K. J. Kim, *Reasonable design of thick electrodes in lithium-ion batteries*, Frontiers in Batteries and Electrochemistry **2** (2023).

[45] D. P. Dubal, D. Rueda-Garcia, C. Marchante, R. Benages, and P. Gomez-Romero, *Hybrid Graphene-Polyoxometalates Nanofluids as Liquid Electrodes for Dual Energy Storage in Novel Flow Cells*, The Chemical Record , 1 (2018).

[46] Z. Qi and J. Gary M. Koenig, *Review Article: Flow battery systems with solid electroactive materials*, Journal of Vacuum Science & Technology B, Nanotechnology and Microelectronics: Materials, Processing, Measurement, and Phenomena **35**, 040801 (2017).

[47] V. Presser, C. R. Dennison, J. Campos, K. W. Knehr, E. C. Kumbur, and Y. Gogotsi, *The electrochemical flow capacitor: A new concept for rapid energy storage and recovery*, Advanced Energy Materials **2**, 895 (2012).

[48] M. Duduta, B. Ho, V. C. Wood, P. Limthongkul, V. E. Brunini, W. C. Carter, and Y. M. Chiang, *Semi-solid lithium rechargeable flow battery*, Advanced Energy Materials **1**, 511 (2011).

[49] V. Fabian Puerta, D. Rueda Garcia, R. Benages Vilau, P. Gomez Romero, J. Aibar Sala, and R. Terradas Robledo, *Hybrid paste electrodes and cell stacking for high power electrical energy storage devices* (31/08/2020 PCT/ES2020/070523).

[50] P. Gomez-Romero, J. Aibar Sala, E. Alarcon, R. Terradas Robledo, D. Rueda-garcia, V. Fabian Puerta, M. Saad, and R. Betolaza, *Hybrid paste electrodes and cell stacking for high power electrical energy storage devices* (31/08/2020 PCT/ES2020/070523).

[51] O. Alšauskas, Y. Chen, J. Dallard, J. Dallard, A. Dasgupta, S. Dhir, M. Drtil, E. F. Musa Erdogan and, D. Fischer, V. Franza, Y. Y. Kim, T. Lombardo, V. O'Riordan, C. Paillard, A. Pastore, N. Papastefanakis, M. Schoenfisch, L. Staas, R. Taniguchi, G. Tonolo, A. Vautrin, , and G. Vittoria, *Batteries and Secure Energy Transitions, World Energy Outlook Special Report*, Tech. Rep. (International Energy Agency (IEA), 2023).

[52] M. Mann, S. Babinec, and V. Putsche, *Energy Storage Grand Challenge Energy Storage Market Report*, Tech. Rep. (U.S. Department of Energy, 2020).

[53] A. Pokhriyal, J. L. Domínguez-García, and P. Gómez-Romero, *Impact of battery energy system integration in frequency control of an electrical grid with wind power*, Clean Technologies **4**, 972 (2022).

[54] A. Serrano, E. Foxhall, and N. Bohra, *Texans asked to conserve energy as demand was expected to put strain on electric grid*, The Texas Tribune .

[55] C. Hao, *Texas power company warns of catastrophic failure if storage issues go unresolved*, Governing .

[56] L. Kearney, *Ercot asks texas power generators to delay outages in expected heat next week*, Reuters .

[57] R. S. Macomber, *A Compltete Introduction to Modern NMR Spectroscopy* (John Wiley Sons, 1998).

[58] V. Petrić and Z. Mandić, *On the need for simultaneous electrochemical testing of positive and negative electrodes in carbon supercapacitors*, Electrochimica Acta **384**, 138372 (2021).

[59] J. Wang, J. Polleux, J. Lim, and B. Dunn, *Pseudocapacitive contributions to electrochemical energy storage in tio2 (anatase) nanoparticles*, The Journal of Physical Chemistry C **111**, 14925 (2007).

[60] T. Brousse, O. Crosnier, D. Bélanger, and J. W. Long, *1 - capacitive and pseudocapacitive electrodes for electrochemical capacitors and hybrid devices*, in *Metal Oxides in Supercapacitors*, Metal Oxides, edited by D. P. Dubal and P. Gomez-Romero (Elsevier, 2017) pp. 1–24.

[61] J. W. Gittins, Y. Chen, S. Arnold, V. Augustyn, A. Balducci, T. Brousse, E. Frackowiak, P. Gómez-Romero, A. Kanwade, L. Köps, P. K. Jha, D. Lyu, M. Meo, D. Pandey, L. Pang, V. Presser, M. Rapisarda, D. Rueda-García, S. Saeed, P. M. Shirage, A. Ślesiński, F. Soavi, J. Thomas, M.-M. Titirici, H. Wang, Z. Xu, A. Yu, M. Zhang, and A. C. Forse, *Interlaboratory study assessing the analysis of supercapacitor electrochemistry data*, Journal of Power Sources **585**, 233637 (2023).

[62] V. Ruiz, J. Suárez-Guevara, and P. Gomez-Romero, *Hybrid electrodes based on polyoxometalate–carbon materials for electrochemical supercapacitors*, Electrochemistry Communications **24**, 35 (2012).

[63] J. Suárez-Guevara, V. Ruiz, and P. Gomez-Romero, *Hybrid energy storage: high voltage aqueous supercapacitors based on activated carbon–phosphotungstate hybrid materials*, J. Mater. Chem. A **2**, 1014 (2014).

[64] W. G. Klemperer, *Tetrabutylammonium isopolyoxometalates*, in *Inorganic Syntheses* (John Wiley Sons, Ltd, 1990) pp. 74–85, https://onlinelibrary.wiley.com/doi/pdf/10.1002/9780470132586.ch15 .

[65] K. Nomiya, K. Kato, and M. Miwa, *Preparation and spectrochemical properties of soluble vanadophosphate polyanions with bicapped-keggin structure*, Polyhedron **5**, 811 (1986).

[66] Y. Ji, L. Huang, J. Hu, C. Streb, and Y.-F. Song, *Polyoxometalate-functionalized nanocarbon materials for energy conversion, energy storage and sensor systems*, Energy Environ. Sci. **8**, 776 (2015).

[67] S. Greiner, *Novel Decavanadate Compounds for Lithium-Ion Batteries: En Route Towards a New Class of High-performance Energy Materials* (Springer Spektrum Wiesbaden, 2020).

[68] S. Uematsu, Z. Quan, Y. Suganuma, and N. Sonoyama, *Reversible lithium charge–discharge property of bi-capped keggin-type polyoxovanadates*, Journal of Power Sources **217**, 13 (2012).

[69] C. Bosch-Navarro, B. Matt, G. Izzet, C. Romero-Nieto, K. Dirian, A. Raya, S. I. Molina, A. Proust, D. M. Guldi, C. Martí-Gastaldo, and E. Coronado, *Charge transfer interactions in self-assembled single walled carbon nanotubes/dawson–wells polyoxometalate hybrids*, Chem. Sci. **5**, 4346 (2014).

[70] J. W. Jordan, G. A. Lowe, R. L. McSweeney, C. T. Stoppiello, R. W. Lodge, S. T. Skowron, J. Biskupek, G. A. Rance, U. Kaiser, D. A. Walsh, G. N. Newton, and A. N. Khlobystov, *Host–guest hybrid redox materials self-assembled from polyoxometalates and single-walled carbon nanotubes*, Advanced Materials **31**, 1904182 (2019).

[71] H.-Y. Chen, J. Friedl, C.-J. Pan, A. Haider, R. Al-Oweini, Y. L. Cheah, M.-H. Lin, U. Kortz, B.-J. Hwang, M. Srinivasan, and U. Stimming, *In situ x-ray absorption near edge structure studies and charge transfer kinetics of na6[v10o28] electrodes*, Physical Chemistry Chemical Physics **19**, 3358 (2017).

[72] F. Béguin, V. Presser, A. Balducci, and E. Frackowiak, *Carbons and electrolytes for advanced supercapacitors*, Advanced Materials **26**, 2219 (2014), https://onlinelibrary.wiley.com/doi/pdf/10.1002/adma.201304137 .

[73] B. Pal, S. Yang, S. Ramesh, V. Thangadurai, and R. Jose, *Electrolyte selection for supercapacitive devices: a critical review*, Nanoscale Adv. **1**, 3807 (2019).

[74] C. Peng, S. Zhang, X. Zhou, and G. Z. Chen, *Unequalisation of electrode capacitances for enhanced energy capacity in asymmetrical supercapacitors*, Energy Environ. Sci. **3**, 1499 (2010).

[75] A. Selling, I. Andersson, L. Pettersson, C. M. Schramm, S. L. Downey, and J. H. Grate, *Multicomponent polyanions. 47. the aqueous vanadophosphate system*, Inorganic Chemistry **33**, 3141 (1994), https://doi.org/10.1021/ic00092a021 .

[76] N. I. Gumerova and A. Rompel, *Polyoxometalates in solution: speciation under spotlight*, Chem. Soc. Rev. **49**, 7568 (2020).

[77] N. I. of Standards and Technology, *Phosphoric acid, octadecyl ester*, Tech. Rep. CAS Registry Number: 2958-09-0 (U.S. Department of Commerce, Washington, D.C., 29.06.1965).

[78] P. Campos, A. Albuquerque, R. Angélica, and S. Paz, *Ftir spectral signatures of amazon inorganic phosphates: Igneous, weathering, and biogenetic origin*, Spectrochimica Acta Part A: Molecular and Biomolecular Spectroscopy **251**, 119476 (2021).

[79] M. Klähn, G. Mathias, C. Kötting, M. Nonella, J. Schlitter, K. Gerwert, and P. Tavan, *Ir spectra of phosphate ions in aqueous solution: predictions of a dft/mm approach compared with observations*, The Journal of Physical Chemistry A **108**, 6186 (2004), https://doi.org/10.1021/jp048617g .

[80] P. J. Domaille, *The 1- and 2-dimensional tungsten-183 and vanadium-51 nmr characterization of isopolymetalates and heteropolymetalates*, Journal of the American Chemical Society **106**, 7677 (1984), https://doi.org/10.1021/ja00337a004 .

[81] P. Zhu, D. Gastol, J. Marshall, R. Sommerville, V. Goodship, and E. Kendrick, *A review of current collectors for lithium-ion batteries*, Journal of Power Sources **485**, 229321 (2021).

[82] A. Stephan, L. D. Anadon, and V. H. Hoffmann, *How has external knowledge contributed to lithium-ion batteries for the energy transition?*, iScience **24**, 101995 (2021).

[83] E. Stojanovska and A. Kilic, *Carbon nanofibers as thick electrodes for aqueous supercapacitors*, Journal of Energy Storage **26**, 100981 (2019).

[84] M. Cronau, A. Paulus, L. P. Pescara, M. Kroll, D. Renz, J. A. Mekontso, A. Marx, and B. Roling, *What Limits the Rate Capability of Ultrathick Composite Electrodes in Lithium-Ion Batteries? A Case Study on the Thickness-Dependent Impedance of LiCoO2 Cathodes*, Batteries Supercaps **5**, e202200194 (2022).

[85] Y. Kuang, C. Chen, D. Kirsch, and L. Hu, *Thick Electrode Batteries: Principles, Opportunities, and Challenges*, Advanced Energy Materials **9**, 1901457 (2019).

[86] F. Wu, M. Liu, Y. Li, X. Feng, K. Zhang, Y. Bai, X. Wang, and C. Wu, *High-Mass-Loading Electrodes for Advanced Secondary Batteries and Supercapacitors*, Electrochemical Energy Reviews **4**, 382 (2021).

[87] F. Wang, J. Y. Cheong, J. Lee, J. Ahn, G. Duan, H. Chen, Q. Zhang, I.-D. Kim, and S. Jiang, *Pyrolysis of Enzymolysis-Treated Wood: Hierarchically Assembled Porous Carbon Electrode for Advanced Energy Storage Devices*, Advanced Functional Materials **31**, 2101077 (2021).

[88] S. Guo, H. Li, X. Zhang, H. Nawaz, S. Chen, X. Zhang, and F. Xu, *Lignin carbon aerogel/nickel binary network for cubic supercapacitor electrodes with ultra-high areal capacitance*, Carbon **174**, 500 (2021).

[89] W. Zhang, M. Li, L. Zhong, J. Huang, and M. Liu, *A family of MOFs@Wood-Derived hierarchical porous composites as freestanding thick electrodes of solid supercapacitors with enhanced areal capacitances and energy densities*, Materials Today Energy **24**, 100951 (2022).

[90] Q. Zhang, Z. Yu, P. Du, and C. Su, *Carbon Nanomaterials Used as Conductive Additives in Lithium Ion Batteries* (2010).

[91] Y. Yue and H. Liang, *3D Current Collectors for Lithium-Ion Batteries: A Topical Review*, Small Methods **2**, 1800056 (2018).

[92] G.-F. Yang, K.-Y. Song, and S.-K. Joo, *Ultra-thick Li-ion battery electrodes using different cell size of metal foam current collectors*, RSC Advances **5**, 16702 (2015).

[93] L. Liu, H. Zhao, Y. Wang, Y. Fang, J. Xie, and Y. Lei, *Evaluating the Role of Nanostructured Current Collectors in Energy Storage Capability of Supercapacitor Electrodes with Thick Electroactive Materials Layers*, Advanced Functional Materials **28**, 1705107 (2018).

[94] Z. Yang, J. Tian, Z. Ye, Y. Jin, C. Cui, Q. Xie, J. Wang, G. Zhang, Z. Dong, Y. Miao, X. Yu, W. Qian, and F. Wei, *High energy and high power density supercapacitor with 3D Al foam-based thick graphene electrode: Fabrication and simulation*, Energy Storage Materials **33**, 18 (2020).

[95] Y. Kuang, C. Chen, G. Pastel, Y. Li, J. Song, R. Mi, W. Kong, B. Liu, Y. Jiang, K. Yang, and L. Hu, *Conductive Cellulose Nanofiber Enabled Thick Electrode for Compact and Flexible Energy Storage Devices*, Advanced Energy Materials **8**, 1802398 (2018).

[96] L. Yu, L. Hu, B. Anasori, Y.-T. Liu, Q. Zhu, P. Zhang, Y. Gogotsi, and B. Xu, *MXene-Bonded Activated Carbon as a Flexible Electrode for High-Performance Supercapacitors*, ACS Energy Letters **3**, 1597 (2018).

[97] Y. Fu, H. Liu, H. Liang, L. Sun, and Y. Bu, *Mesoporous carbon rods capable of fast transport of axial electrons and radial ions for ultra-thick supercapacitor electrodes*, Electrochimica Acta **404**, 139768 (2022).

[98] T. M. Higgins, S.-H. Park, P. J. King, C. J. Zhang, N. McEvoy, N. C. Berner, D. Daly, A. Shmeliov, U. Khan, G. Duesberg, V. Nicolosi, and J. N. Coleman, *A Commercial Conducting Polymer as Both Binder and Conductive Additive for Silicon Nanoparticle-Based Lithium-Ion Battery Negative Electrodes*, ACS Nano **10**, 3702 (2016).

[99] Y. Shi, X. Zhou, and G. Yu, *Material and Structural Design of Novel Binder Systems for High-Energy, High-Power Lithium-Ion Batteries*, Accounts of Chemical Research **50**, 2642 (2017).

[100] L. Ibing, T. Gallasch, P. Schneider, P. Niehoff, A. Hintennach, M. Winter, and F. M. Schappacher, *Towards water based ultra-thick Li ion battery electrodes – A binder approach*, Journal of Power Sources **423**, 183 (2019).

[101] J. Landesfeind, A. Eldiven, and H. A. Gasteiger, *Influence of the Binder on Lithium Ion Battery Electrode Tortuosity and Performance*, Journal of The Electrochemical Society **165**, A1122 (2018).

[102] N. Jäckel, D. Weingarth, A. Schreiber, B. Krüner, M. Zeiger, A. Tolosa, M. Aslan, and V. Presser, *Performance evaluation of conductive additives for activated carbon supercapacitors in organic electrolyte*, Electrochimica Acta **191**, 284 (2016).

[103] G. Wang, Z. Shao, and Z. Yu, *Comparisons of different carbon conductive additives on the electrochemical performance of activated carbon*, Nanotechnology **18**, 205705 (2007).

[104] M. Kaempgen, C. K. Chan, J. Ma, Y. Cui, and G. Gruner, *Printable Thin Film Supercapacitors Using Single-Walled Carbon Nanotubes*, Nano Letters **9**, 1872 (2009).

[105] L. Liu, X. Wang, V. Izotov, D. Havrykov, I. Koltsov, W. Han, Y. Zozulya, O. Linyucheva, V. Zahorodna, O. Gogotsi, and Y. Gogotsi, *Capacitance of coarse-grained carbon electrodes with thickness up to 800μm*, Electrochimica Acta **302**, 38 (2019).

[106] X. Li, J. Shao, S.-K. Kim, C. Yao, J. Wang, Y.-R. Miao, Q. Zheng, P. Sun, R. Zhang, and P. V. Braun, *High energy flexible supercapacitors formed via bottom-up infilling of gel electrolytes into thick porous electrodes*, Nature Communications **9**, 2578 (2018).

[107] S. Lee, J.-G. Kim, H. Yu, D.-M. Lee, S. Hong, S. M. Kim, S.-J. Choi, N. D. Kim, and H. S. Jeong, *Flexible supercapacitor with superior length and volumetric capacitance enabled by a single strand of ultra-thick carbon nanotube fiber*, Chemical Engineering Journal **453**, 139974 (2023).

[108] B. Long, Q. Zhang, T. Duan, T. Song, Y. Pei, X. Wang, C. Zhi, X. Wu, Q. Zhang, and Y. Wu, *Few-Atomic-Layered Co-Doped BiOBr Nanosheet: Free-Standing Anode with Ultrahigh Mass Loading for "Rocking Chair" Zinc-Ion Battery*, Advanced Science **9**, 2204087 (2022).

[109] J. Liu, Z. Wang, Q. Liu, S. Li, D. Wang, and Z. Zheng, *Rational design of freestanding and high-performance thick electrode from carbon foam modified with polypyrrole/polydopamine for supercapacitors*, Chemical Engineering Journal **447**, 137562 (2022).

[110] S. M. Jung, D. L. Mafra, C.-T. Lin, H. Y. Jung, and J. Kong, *Controlled porous structures of graphene aerogels and their effect on supercapacitor performance*, Nanoscale **7**, 4386 (2015).

[111] D. Dang, Y. Wang, S. Gao, and Y.-T. Cheng, *Freeze-dried low-tortuous graphite electrodes with enhanced capacity utilization and rate capability*, Carbon **159**, 133 (2020).

[112] Y. Wang, X. Fu, M. Zheng, W.-H. Zhong, and G. Cao, *Strategies for Building Robust Traffic Networks in Advanced Energy Storage Devices: A Focus on Composite Electrodes*, Advanced Materials **31**, 1804204 (2019).

[113] M.-A. Shahbazi, M. Ghalkhani, and H. Maleki, *Directional Freeze-Casting: A Bioinspired Method to Assemble Multifunctional Aligned Porous Structures for Advanced Applications*, Advanced Engineering Materials **22**, 2000033 (2020).

[114] R. Amin, B. Delattre, A. P. Tomsia, and Y.-M. Chiang, *Electrochemical Characterization of High Energy Density Graphite Electrodes Made by Freeze-Casting*, ACS Applied Energy Materials **1**, 4976 (2018).

[115] L. E, W. Gan, J. Sun, Z. Wu, C. Ma, W. Li, and S. Liu, *High-Performance Supercapacitor Device with Ultrathick Electrodes Fabricated from All-Cellulose-Based Carbon Aerogel*, Energy Fuels **35**, 8295 (2021).

[116] S. Kumagai, K. Mukaiyachi, and D. Tashima, *Rate and cycle performances of supercapacitors with different electrode thickness using non-aqueous electrolyte*, Journal of Energy Storage **3**, 10 (2015).

[117] M. A. Garakani, S. Bellani, V. Pellegrini, R. Oropesa-Nuñez, A. E. D. R. Castillo, S. Abouali, L. Najafi, B. Martín-García, A. Ansaldo, P. Bondavalli, C. Demirci, V. Romano, E. Mantero, L. Marasco, M. Prato, G. Bracciale, and F. Bonaccorso, *Scalable spray-coated graphene-based electrodes for high-power electrochemical double-layer capacitors operating over a wide range of temperature*, Energy Storage Materials **34**, 1 (2021).

[118] Y. Guo, W. Li, H. Yu, D. F. Perepichka, and H. Meng, *Flexible Asymmetric Supercapacitors via Spray Coating of a New Electrochromic Donor–Acceptor Polymer*, Advanced Energy Materials **7**, 1601623 (2017).

[119] M. Karakaya, J. Zhu, A. J. Raghavendra, R. Podila, S. G. Parler, J. P. Kaplan, and A. M. Rao, *Roll-to-roll production of spray coated N-doped carbon nanotube electrodes for supercapacitors*, Applied Physics Letters **105**, 263103 (2014).

[120] A. Pokhriyal, R. M. González-Gil, L. N. Bengoa, and P. Gómez-Romero, *Nanostructured thick electrode strategies toward enhanced electrode–electrolyte interfaces*, Materials **16** (2023).

[121] Kurary, *Kurary coal yp series* (2019).

[122] T. Scientific, *Product specification carbon black, super p conductive, 99+*.

[123] S. Aldrich, *Product specification carbon nanotube, multi-walled* ().

[124] *Product specification sodium carboxymethyl cellulose*.

[125] S. Aldrich, *Product specification poly(vinylidene fluoride-co-hexafluoropropylene)* ().

[126] J. Landesfeind, J. Hattendorff, A. Ehrl, W. A. Wall, and H. A. Gasteiger, *Tortuosity determination of battery electrodes and separators by impedance spectroscopy*, Journal of The Electrochemical Society **163**, A1373 (2016).

[127] H. D. Yoo, J. H. Jang, J. H. Ryu, Y. Park, and S. M. Oh, *Impedance analysis of porous carbon electrodes to predict rate capability of electric double-layer capacitors*, Journal of Power Sources **267**, 411 (2014).

[128] B.-A. Mei, O. Munteshari, J. Lau, B. Dunn, and L. Pilon, *Physical interpretations of nyquist plots for edlc electrodes and devices*, The Journal of Physical Chemistry C **122**, 194 (2018).

[129] T. S. Mathis, N. Kurra, X. Wang, D. Pinto, P. Simon, and Y. Gogotsi, *Energy Storage Data Reporting in Perspective—Guidelines for Interpreting the Performance of Electrochemical Energy Storage Systems*, Advanced Energy Materials **9**, 1902007 (2019).

[130] J. Yu, C. Yu, W. Guo, Z. Wang, S. Li, J. Chang, X. Tan, Y. Ding, M. Zhang, L. Yang, Y. Xie, R. Fu, and J. Qiu, *Decoupling and correlating the ion transport by engineering 2D carbon nanosheets for enhanced charge storage*, Nano Energy **64**, 103921 (2019).

[131] G. Dhakal, D. R. Kumar, S. Sahoo, and J.-J. Shim, *Litchi seed biowaste-derived activated carbon supporting matrix for efficient symmetric and asymmetric supercapacitors*, Carbon **208**, 277 (2023).

[132] D. I. Abouelamaiem, G. He, T. P. Neville, D. Patel, S. Ji, R. Wang, I. P. Parkin, A. B. Jorge, M.-M. Titirici, P. R. Shearing, and D. J. Brett, *Correlating electrochemical impedance with hierarchical structure for porous carbon-based supercapacitors using a truncated transmission line model*, Electrochimica Acta **284**, 597 (2018).

[133] T.-T. Nguyen, A. Demortière, B. Fleutot, B. Delobel, C. Delacourt, and S. J. Cooper, *The electrode tortuosity factor: why the conventional tortuosity factor is not well suited for quantifying transport in porous Li-ion battery electrodes and what to use instead*, npj Computational Materials **6**, 123 (2020).

[134] K. B. Hatzell, M. Boota, and Y. Gogotsi, *Materials for suspension (semi-solid) electrodes for energy and water technologies*, Chem. Soc. Rev. **44**, 8664 (2015).

[135] G. M. Koenig, D. Gupta, and Y. Kim, *Perspective—expected variation in reported coin cell capacities due to current collector mass distribution*, Journal of The Electrochemical Society **167**, 120529 (2020).

[136] R. Dugas, J. D. Forero-Saboya, and A. Ponrouch, *Methods and protocols for reliable electrochemical testing in post-li batteries (na, k, mg, and ca)*, Chemistry of Materials **31**, 8613 (2019).

[137] J.-H. Chen, C. Liu, S. M. Althaus, and M. Boudjatit, *Nuclear magnetic resonance dipolar cross-relaxation interaction between nanoconfined fluids and matrix solids*, ACS Omega **7**, 45189 (2022).

[138] G. the Grid, *Summary of potential energy storage services and required response times and durations*.

[139] K. S. Ratnam, K. Palanisamy, and G. Yang, *Future low-inertia power systems: Requirements, issues, and solutions - a review*, Renewable and Sustainable Energy Reviews **124**, 109773 (2020).

[140] P. Denholm, T. Mai, R. W. Kenyon, B. Kroposki, and M. O'Malley, *Inertia and the Power Grid:A Guide Without the Spin*, Technical Report NREL/TP-6A20-73856 (National Renewable Energy Laboratory, Golden, CO, 2020).

[141] A. Jazeera, *Europe faces gas supply disruption after russia imposes sanctions* (2022).

[142] Z. Wu, W. Gao, J. Wang, and S. Gu, *A coordinated primary frequency regulation from permanent magnet synchronous wind turbine generation*, in *2012 IEEE Power Electronics and Machines in Wind Applications* (2012) pp. 1–6.

[143] A. Attya, J. Dominguez-Garcia, and O. Anaya-Lara, *A review on frequency support provision by wind power plants: Current and future challenges*, Renewable and Sustainable Energy Reviews **81**, 2071 (2018).

[144] A. Fernández-Guillamón, E. Gómez-Lázaro, E. Muljadi, and Ángel Molina-García, *Power systems with high renewable energy sources: A review of inertia and frequency control strategies over time*, Renewable and Sustainable Energy Reviews **115**, 109369 (2019).

[145] Z. Wu, W. Gao, T. Gao, W. Yan, H. Zhang, S. Yan, and X. Wang, *State-of-the-art review on frequency response of wind power plants in power systems*, Journal of Modern Power Systems and Clean Energy (2018).

[146] J. F. Conroy and R. Watson, *Frequency response capability of full converter wind turbine generators in comparison to conventional generation*, IEEE Transactions on Power Systems **23**, 649 (2008).

[147] U. Akram, M. Nadarajah, R. Shah, and F. Milano, *A review on rapid responsive energy storage technologies for frequency regulation in modern power systems*, Renewable and Sustainable Energy Reviews **120**, 109626 (2020).

[148] F. Díaz-González, M. Hau, A. Sumper, and O. Gomis-Bellmunt, *Participation of wind power plants in system frequency control: Review of grid code requirements and control methods*, Renewable and Sustainable Energy Reviews **34**, 551 (2014).

[149] F. M. Gonzalez-Longatt, *Effects of the synthetic inertia from wind power on the total system inertia: simulation study*, in *2012 2nd International Symposium On Environment Friendly Energies And Applications* (2012) pp. 389–395.

[150] W. Yao and K. Y. Lee, *A control configuration of wind farm for load-following and frequency support by considering the inertia issue*, in *2011 IEEE Power and Energy Society General Meeting* (2011) pp. 1–6.

[151] X. Zhu, Y. Wang, L. Xu, X. Zhang, and H. Li, *Virtual inertia control of dfig-based wind turbines for dynamic grid frequency support*, in *IET Conference on Renewable Power Generation (RPG 2011)* (2011) pp. 1–6.

[152] P. Li, H. Li, D. Han, T. Shang, Y. Deng, Y. Tao, W. Lv, and Q.-H. Yang, *Packing Activated Carbons into Dense Graphene Network by Capillarity for High Volumetric Performance Supercapacitors*, Advanced Science **6**, 1802355 (2019).

[153] R. G. de Almeida and J. A. Pecas Lopes, *Participation of doubly fed induction wind generators in system frequency regulation*, IEEE Transactions on Power Systems **22**, 944 (2007).

[154] Y.-K. Wu, W.-H. Yang, Y.-L. Hu, and P. Q. Dzung, *Frequency regulation at a wind farm using time-varying inertia and droop controls*, IEEE Transactions on Industry Applications **55**, 213 (2019).

[155] J. M. Mauricio, A. Marano, A. Gomez-Exposito, and J. L. Martinez Ramos, *Frequency regulation contribution through variable-speed wind energy conversion systems*, IEEE Transactions on Power Systems **24**, 173 (2009).

[156] C. Shao, Z. Li, R. Hao, Z. Qie, G. Xu, and J. Hu, *A wind farm frequency control method based on the frequency regulation ability of wind turbine generators*, in *2020 5th Asia Conference on Power and Electrical Engineering (ACPEE)* (2020) pp. 592–596.

[157] Y.-L. Hu and Y.-K. Wu, *Inertial response identification algorithm for the development of dynamic equivalent model of dfig-based wind power plant*, IEEE Transactions on Industry Applications **57**, 2104 (2021).

[158] A. Poullikkas, *A comparative overview of large-scale battery systems for electricity storage*, Renewable and Sustainable Energy Reviews **27**, 778 (2013).

[159] H. C. Hesse, M. Schimpe, D. Kucevic, and A. Jossen, *Lithium-ion battery storage for the grid—a review of stationary battery storage system design tailored for applications in modern power grids*, Energies **10** (2017).

[160] O. Palizban and K. Kauhaniemi, *Energy storage systems in modern grids—matrix of technologies and applications*, Journal of Energy Storage **6**, 248 (2016).

[161] S. S. Behnam Zakeri, *Electrical energy storage systems: A comparative life cycle cost analysis*, Renewable and Sustainable Energy Reviews **42**, 569 (2015).

[162] J. Dang, J. Seuss, L. Suneja, and R. G. Harley, *Soc feedback control for wind and ess hybrid power system frequency regulation*, in *2012 IEEE Power Electronics and Machines in Wind Applications* (2012) pp. 1–7.

[163] W. Li and G. Joos, *Comparison of energy storage system technologies and configurations in a wind farm*, in *2007 IEEE Power Electronics Specialists Conference* (2007) pp. 1280–1285.

[164] J. Sun, L. Sheng, Y. Sun, Z. Zhou, and R. Fu, *Stability simulation analysis of a hybrid wind-battery system*, in *Theory, Methodology, Tools and Applications for Modeling and Simulation of Complex Systems*, edited by L. Zhang, X. Song, and Y. Wu (Springer Singapore, Singapore, 2016) pp. 154–163.

[165] L. Liang, J. Zhong, and Z. Jiao, *Frequency regulation for a power system with wind power and battery energy storage*, in *2012 IEEE INTERNATIONAL CONFERENCE ON POWER SYSTEM TECHNOLOGY (POWERCON)* (2012) iEEE International Conference on Power System Technology (POWERCON), Auckland, NEW ZEALAND, OCT 30-NOV 02, 2012.

[166] M. Toge, Y. Kurita, and S. Iwamoto, *Supplementary load frequency control with storage battery operation considering soc under large-scale wind power penetration*, in *2013 IEEE Power Energy Society General Meeting* (2013) pp. 1–5.

[167] T. Ono and J. Arai, *Frequency control with dead band characteristic of battery energy storage system for power system including large amount of wind power generation*, Electrical Engineering in Japan **185**, 1 (2013), https://onlinelibrary.wiley.com/doi/pdf/10.1002/eej.22485 .

[168] W. Li and G. Joos, *A power electronic interface for a battery supercapacitor hybrid energy storage system for wind applications*, in *2008 IEEE Power Electronics Specialists Conference* (2008) pp. 1762–1768.

[169] G. He, Q. Chen, C. Kang, Q. Xia, and K. Poolla, *Cooperation of wind power and battery storage to provide frequency regulation in power markets*, IEEE Transactions on Power Systems **32**, 3559 (2017).

[170] V. Y. Singarao, S. Nimmagadda, and V. Rao, *Economic comparison of deloaded-wind and wind-battery systems*, in *2014 Sixth Annual IEEE Green Technologies Conference* (2014) pp. 126–131.

[171] J. Tan and Y. Zhang, *Coordinated control strategy of a battery energy storage system to support a wind power plant providing multi-timescale frequency ancillary services*, IEEE Transactions on Sustainable Energy **8**, 1140 (2017).

[172] W. Li, G. Joos, and J. Belanger, *Real-time simulation of a wind turbine generator coupled with a battery supercapacitor energy storage system*, IEEE Transactions on Industrial Electronics **57**, 1137 (2010).

[173] N. Mendis, K. M. Muttaqi, and S. Perera, *Management of battery-supercapacitor hybrid energy storage and synchronous condenser for isolated operation of pmsg based variable-speed wind turbine generating systems*, IEEE Transactions on Smart Grid **5**, 944 (2014).

[174] S. Hajiaghasi, A. Salemnia, and M. Hamzeh, *Hybrid energy storage system for microgrids applications: A review*, Journal of Energy Storage **21**, 543 (2019).

[175] J. Fang, Y. Tang, H. Li, and X. Li, *A battery/ultracapacitor hybrid energy storage system for implementing the power management of virtual synchronous generators*, IEEE Transactions on Power Electronics **33**, 2820 (2018).

[176] J. Fang, H. Li, Y. Tang, and F. Blaabjerg, *On the inertia of future more-electronics power systems*, IEEE Journal of Emerging and Selected Topics in Power Electronics **7**, 2130 (2019).

[177] A. Tani, M. B. Camara, and B. Dakyo, *Energy management in the decentralized generation systems based on renewable energy—ultracapacitors and battery to compensate the wind/load power fluctuations*, IEEE Transactions on Industry Applications **51**, 1817 (2015).

[178] S. Zhang, Y. Mishra, and M. Shahidehpour, *Fuzzy-logic based frequency controller for wind farms augmented with energy storage systems*, IEEE Transactions on Power Systems **31**, 1595 (2016).

[179] S. M. Mohammad Dreidy, H. Mokhlis, *Inertia response and frequency control techniques for renewable energy sources: A review*, Renewable and Sustainable Energy Reviews **69**, 144 (2017).

[180] S. Zhan, P. Hou, P. Enevoldsen, G. Yang, J. Zhu, J. Eichman, and M. Z. Jacobson, *Co-optimized trading of hybrid wind power plant with retired ev batteries in energy and reserve markets under uncertainties*, International Journal of Electrical Power Energy Systems **117**, 105631 (2020).

[181] A. Atieh, S. Charfi, and M. Chaabene, *Chapter 8 - hybrid pv/batteries bank/diesel generator solar-renewable energy system design, energy management, and economics*, in *Advances in Renewable Energies and Power Technologies*, edited by I. Yahyaoui (Elsevier, 2018) pp. 257–294.

[182] X. Luo, J. Wang, M. Dooner, and J. Clarke, *Overview of current development in electrical energy storage technologies and the application potential in power system operation*, Applied Energy **137**, 511 (2015).

[183] X. Han, M. Ouyang, L. Lu, J. Li, Y. Zheng, and Z. Li, *A comparative study of commercial lithium ion battery cycle life in electrical vehicle: Aging mechanism identification*, Journal of Power Sources **251**, 38 (2014).

[184] S. S. Zhang, *The effect of the charging protocol on the cycle life of a li-ion battery*, Journal of Power Sources **161**, 1385 (2006).

[185] N. Zhang, N.-C. Yang, and J.-H. Liu, *Optimal sizing of pv/wind/battery hybrid microgrids considering lifetime of battery banks*, Energies **14** (2021).

[186] D.-I. Stroe, M. Świerczyński, A.-I. Stan, R. Teodorescu, and S. J. Andreasen, *Accelerated lifetime testing methodology for lifetime estimation of lithium-ion batteries used in augmented wind power plants*, IEEE Transactions on Industry Applications **50**, 4006 (2014).

[187] N. Bouchhima, M. Gossen, S. Schulte, and K. P. Birke, *Lifetime of self-reconfigurable batteries compared with conventional batteries*, Journal of Energy Storage **15**, 400 (2018).

[188] M. Alramlawi, A. Gabash, E. Mohagheghi, and P. Li, *Optimal operation of hybrid pv-battery system considering grid scheduled blackouts and battery lifetime*, Solar Energy **161**, 125 (2018).

[189] Z. Hou, L. Zhang, J. Chen, Y. Xiong, X. Zhang, and Y. Qian, *An aqueous rechargeable lithium ion battery with long cycle life and overcharge self-protection*, Mater. Chem. Front. **5**, 2749 (2021).

[190] H. Chen, T. N. Cong, W. Yang, C. Tan, Y. Li, and Y. Ding, *Progress in electrical energy storage system: A critical review*, Progress in Natural Science **19**, 291 (2009).

[191] R. Xiong, H. Chen, C. Wang, and F. Sun, *Towards a smarter hybrid energy storage system based on battery and ultracapacitor - a critical review on topology and energy management*, Journal of Cleaner Production **202**, 1228 (2018).

[192] *Wind energy and on-site energy storage. Exploring market opportunities*, Technical Report (Wind Europe, 2017).

[193] D.-I. Stroe, M. Swierczynski, A. Stan, R. Teodorescu, and S. Andreasen, *Performance-degradation model for li4ti5o12 -based battery cells used in wind power applications* (2012).

Acknowledgements

I recently stumbled upon the saying, "Life is all about the people that we meet and the food that we eat." Having lived in India and Spain—two countries full of warm-hearted people and culinary delights—I can certainly say that this rings true for me. The dream of earning this PhD was mine, but its achievement has only been possible due to my great mentors, supportive friends and loving family.

First I thank my supervisors Prof. Pedro Gómez Romero, Dr. José Luis Domínguez García and Dr. Rosa Maria González Gil for their guidance and support.

Pedro, from the depths of my heart, I thank you for taking a chance on me. Your efforts and time could have gone to much more experienced students, but I am grateful every day that you selected me as one of your students. You have gone above and beyond the role of a supervisor and truly been a mentor and a friend over these years. Even when things were not going so great, you always made me see the positives by remarking on my professional growth over the years. Your faith in me while going through the period of switching the PhD topic allowed me to keep pushing and believing in myself. You have been most generous with your time and advice and always kept an open door policy to your office. I learned from you that research is all about the effort to reinvent the wheel and contribute to new scientific knowledge. Your guidance has shown me the importance of taking risks in scientific work and effectively communicating ideas.

My gratitude also extends to my other supervisor José Luis. Thank you for accepting to collaborate in this PhD topic and helping me to attempt the crazy ambitious idea that we had. You had been always available for a call or meeting to help me clear my doubts and advise me. I thank you for your patience and kindness during these years when I was juggling multiple topics. This research work would not have been possible without your support.

Rosa, I have told you this many times and I will keep saying it, my real PhD started from the day you came to our group. You came in, with your cheerful attitude and immense knowledge on different syntheses, like the light at the end of a dark tunnel. Every time I hit a roadblock, you always had a solution. I'm honoured to have been one of your "little chickens". I take this opportunity to thank you again, and tell you that you really are a role model for women in science.

Leandro, how can I ever thank you for saving my experiments? Even though you were not officially involved in my project, you never said no when I asked for help and you became my go to person to ask questions about electrochemistry. I could always trust you for giving the right advice. You have gone above and beyond in helping me and for that I will forever be grateful. I have immensely enjoyed working with you and laughing at silly things happening in the lab. I also thank you for introducing me to "Mate", I didn't know what I had been missing for three decades of my life.

I extend my gratitude to the staff at ICN2, particularly Javier, Jessica, Marcos, and Francisco for helping me when I had doubts about material characterisation. Rafael thanks for handling my instrumentation requests and discussing piston cell modifications.

I must also mention two colleagues who helped me a lot when I first came to the group, Junjie (who is back in China) and Dani. Junjie, you were the most fun colleague to have had worked with. You trained me in making cells and I still apply your techniques to this day. Dani, I will fondly remember those early days struggling with nanopastes when I joined the group. At the time, it was a relief to see that an expert like you, was as frustrated with pastes as I was. Your knowledge of electrochemistry is unparalleled, and I'm just happy that, after all these years, I can finally understand your suggestions without it all sounding like Latin to me.

I want to extend my heartfelt thanks to my fellow members of the "1097 Neo Energy" WhatsApp group: Sharin, Shamim, Georgia, Andrea, Lipeng, Si Yu, Judith, and Aladdin. I'll always cherish our morning tea breaks and the laughs we shared over lunch. It's been wonderful to have office mates who understood both the joys and frustrations of our experiments. Getting to know you all outside of work has been a true pleasure, and you've each made a impact on my daily life. I'm grateful for all of you and wish you the very best in your careers. Sharin, I have enjoyed our morning sunlight exposure sessions and laughs. It was always a great way to start the day. Shamim, you are the most generous member of our group. I hope you will forgive me for being your worst swimming student yet. Thank you for always trying to bring people together and organising group activities. Andrea, thank you for sharing your "lab adventures" and making us cry with laughter. Lipeng, you have given us words of wisdom that are more powerful than the entirety of Confucius works: "Be a man". Thank you for this. I appreciate you and Si Yu for introducing us to a variety of new teas and amplifying our tea addiction. Georgia and Ceren, you came as exchange members to our group, but became such an important part

of it (and it was not just because you both became our alcohol suppliers). Ceren, I thank you especially, for your advice, kindness and Turkish coffee.

Over these years I became friends with some phenomenal people that I will cherish for life.

Viveka, we met at the beginning of the lockdown and I feel the universe had sent me a personal chai-maker in those terrible times. I already miss our sauna sessions, midnight walks around Vila and dumpling dinners. Laughing everyday with you at our fiascos was the best stress reliever.

Henglun, I met you through Viveka but you have become one of my friends that I can really count on. I have never met anyone with a more organised social life and I wish I can adopt some of your skills. Thank you for sharing my passion for walking tours. I will cherish our free museum days outings.

Ashwin and Nikki, I couldn't have had better partners in being lost in Spanish classes to being lost in Glühwein. Ashwin, I am so glad to have met you. You have become one of my most cherished friends and these years would not have been the same without you. I appreciate you for continuing on making plans that kept getting cancelled. I promise one day we will be able to find a schedule that works for everyone, although we might need to make reservations a year in advance. But most importantly thank you for entertaining us old ladies with your "happening" social life.

Saptam, I second you in saying I will miss our "chugli" sessions in the first floor corridor. Don't worry we will continue them at bars in Gracia.

George, Rini, Fran, Lydia, Carlos and Tijana, thank you for your friendship and companionship.

I also had a remarkable group of friends like family, supporting me from India. Archit, Ankit, Nishant, Vivek and Siddhant, thank you for your video calls, updates about your (and each others') lives and providing much needed comedic relief. But, also no thank you for asking "when will you finish your studying" on every call. I miss you guys every day.

Pooja, my dearest of friends, soul sister, the angel and devil on my shoulder combined, I could not have survives Spain without your thrice-a-week calls. Thank you for operating in the CET timezone no matter what part of the world you are in and making me laugh. Thank you for keeping me updated with the lives of your colleagues who I have never met. It has been the best TV-show/podcast with never ending seasons.

Mi familia española, Mamá, Papá, Marta, Abu y tíos, gracias por acogerme con los brazos abiertos en vuestra encantadora familia. A pesar de las barreras del idioma, me mostrastéis vuestro amor en innumerables momentos que me hicieron sentir como en casa en España. Os quiero mucho a todos.

Chacha Chachi, you are like my second set of parents and I thank you for your love and care and your belief in me. Maasi, Maama, Maami, Bua, Bhabi, Nana, Nani and Dadi, thank you for your unwavering love.

Anuroop and Nandini, my first pets, having you two as my younger siblings was the best gift that I got from our family. Thank you for keeping me entertained with your calls. Anuroop, you are the brother every sister dreams of. Thank you for taking care of everything at home so I never had to worry. Without your regular updates on happenings of our family, I would have been distressed and clueless.

Mom and dad, thank you for always giving me the opportunities to achieve my dreams. You have always trusted me in all my professional and personal decisions, letting me explore this world from a very young age and providing me a safe space to fall back on. Popsy, you inspired me to be ambitious, and Mommy you have been the best example of a strong woman that I hope I can be. Being an expat comes with unknown challenges, and I especially thank my Mom for always joking that I could have an easy life back at home and reminding me that I was pursing this academic journey because of my passion.

Kali and Simba, thank you for entertaining me with your antics and stupidity and providing instant stress relief whenever I watched you.

At the end I thank the most important person without whom I might not have considered a PhD in Spain, my husband Angel. *"Te dejo este mensaje, simplemente, para repetirte algo que yo sé que vos sabías."* From writing applications to finding mistakes in my thesis, you have been involved in this PhD almost as much as I have. Thank you for celebrating all my little successes, keeping me motivated, making numerous insane drives from Germany to Spain and for just being yourself.